R77-159
NAS9-14801

NASA CR-
151499

ENGINE HYDRAULIC STABILITY

FINAL REPORT

JULY 1977

Prepared for

National Aeronautics and Space Administration
Lyndon B. Johnson Space Center
Houston, Texas 77058

Rockwell International
Rocketdyne Division
6633 Canoga Avenue
Canoga Park, California 91304

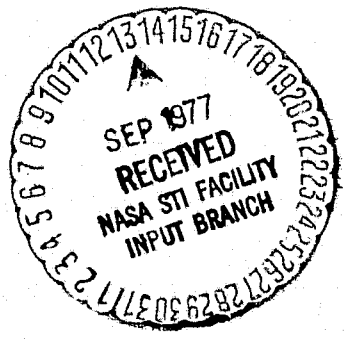

R77-159

ENGINE HYDRAULIC STABILITY

FINAL REPORT

CONTRACT NAS9-14801

JULY 1977

PREPARED FOR

NATIONAL AERONAUTICS AND SPACE ADMINISTRATION
LYNDON B. JOHNSON SPACE CENTER
HOUSTON, TEXAS 77058

PREPARED BY

R. C. KESSELRING
R. L. NELSON
K. M. SPROUSE

APPROVED BY

J. A. NESTLERODE
PROJECT ENGINEER
COMBUSTION STABILITY

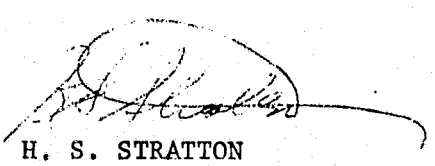

H. S. STRATTON
PROGRAM MANAGER
ROCKET TECHNOLOGY

ROCKWELL INTERNATIONAL
ROCKETDYNE DIVISION
6633 CANOGA AVENUE
CANOGA PARK, CALIF. 91304

FOREWORD

This document was prepared by Rocketdyne, a Division of Rockwell International Corporation, in accordance with DRLT-1204, Line Item No. 4 of the Data Requirements List of Contract NAS9-14801 with the National Aeronautics and Space Administration. The contract period of performance was December 1975 to July 1977. The NASA/JSC Technical Monitor was Mr. Ronald C. Pasadyn. The Rocketdyne Program Manager was Mr. R. D. Paster for the first ten months; he was replaced by Mr. H. S. Stratton for the remainder of the program. Mr. J. A. Nestlerode served as the Project Engineer and the Principal Engineer was Dr. R. C. Kesselring. Mr. R. L. Nelson was responsible for the model formulation and programming. Mr. K. M. Sprouse was responsible for the analytical descriptions of the injector modelling technique and the chamber pressure input.

This report has been assigned Rocketdyne Report No. R77-159.

ABSTRACT

An analytical injector model was developed specifically to analyze combustion instability coupling between the injector hydraulics and the combustion process. This digital computer dynamic injector model will, for any imposed chamber or inlet pressure profile with a frequency ranging from 100 to 3000 Hz (minimum) accurately predict/calculate the instantaneous injector flowrates.

The engine hydraulic stability computer model was developed using the "lumped parameter" technique. The model was formulated such that the equations governing fluid flow inside the injector were linearized and subsequently arranged in matrix form. The matrix is then solved in a frequency response format giving gains and phases for pressures and flowrates at various locations within the injector.

The injector system is described in terms of which flow segments enter and leave each pressure node. For each flow segment, a resistance, line lengths, and areas are required as inputs (the line lengths and areas are used in determining inertance). For each pressure node, volume and acoustic velocity are required as inputs (volume and acoustic velocity determine capacitance). The geometric criteria for determining inertances of flow segments and capacitances of pressure nodes was set. Also, a technique was developed for analytically determining time averaged steady-state pressure drops and flowrates for every flow segment in an injector when such data is not known. These pressure drops and flowrates are then used in determining the linearized flow resistance for each line segment of flow.

Model output includes both absolute and vector summations of the oscillatory injector flow (for a unit pressure perturbation) so as to facilitate interpretation of the model results. Graphical displays (plots) are also included.

The model was correlated with experimental data from three injectors - the Rocketdyne Lance XRL Booster injector, the Aerojet Space Shuttle OME Technology injector, and the Rocketdyne Space Shuttle OME Technology injector.

Each of these injectors experimentally exhibited hydraulic coupling in the 100- to 3000-Hz range. In addition, experimentally proven hardware fixes which successfully eliminated the instability, exist for each of the three "correlation" injectors.

The engine hydraulic stability computer model was run for each of the "correlation" injectors with both pre-fix and post-fix injector model input. Examination and analysis of the model output revealed that the computer model successfully predicted that the fixes applied to each correlation injector would increase combustor stability with respect to the instability mode actually observed.

The establishment of injector design criteria was attempted by conducting a sensitivity analysis with the model through a systematic study of various injector design variables using the model to constantly gauge the effects relative to injector gain (stability).

It is concluded that the engine hydraulic stability computer model is quite capable of predicting effects of proposed injector fixes and/or evaluating design options relative to one another.

The program was completed with the successful operation of the engineering model on the NASA/JSC Univac 1110, EXEC-8 computer system and by extensive documentation of the model in the form of a computer manual and final report.

CONTENTS

ILLUSTRATIONS

ILLUSTRATIONS (Continued)

ILLUSTRATIONS (Continued)

ILLUSTRATIONS (Continued)

TABLES

NOMENCLATURE

a	Sonic speed of hydraulic feed system
a_c	Sonic speed of gas in combustion chamber
A	Cross-sectional area
B	Boundary condition
C	Capacitance of pressure node
CR	Combustor contraction ratio
C_F	Thrust coefficient
D	Hydraulic diameter
D_{ch}	Diameter of combustion chamber
f	Fanning friction factor
F	Thrust
g_c	System units conversion factor (386 in.-lbm/lbf-sec^2)
G	Gain
h	Viscous momentum head loss
i, j	$\sqrt{-1}$
I	Inertance of the fluid element
J_m	Bessel function of the first kind, order m
K_f	Pipe friction head loss
K_t	Minor friction head loss
L	Length of pipe section, length between pressure nodes
m	Separation constant
P	Pressure
ΔP	Pressure change

r	Spatial co-ordinate
R	Time-averaged resistance
R_L	Linearized flow resistance
t	Time
v	Velocity
V	Volume of pressure node
$\dot{w}$	Mass flowrate
x	Spatial co-ordinate
Y_m	Bessel function of the second kind, order m

GREEK LETTERS

β	Complex pressure
θ	Spatial co-ordinate
λ	Acoustic wavelength
μ	Viscosity
ν	Acoustic frequency (sec^{-1})
ρ	Density
τ	Viscous surface force tensor
ϕ	Phase shift
Φ	Complex velocity
ω	Angular acoustic frequency
ω_b	Break frequency (R_L/I)

SUPERSCRIPTS

$\overline{\quad}$	Time-averaged value of variable
$\sim$	Perturbed or oscillatory component of variable

SUBSCRIPTS

$\vec{\quad}$	Vector
amp	Amplitude
BC	Boundary condition at a surface
d	Downstream
i	Individual flow or pressure node
IC	Initial condition (zero time)
m,n	Transverse acoustic mode in cylindrical combustor
rad	First radial mode at r = 0
ref	Reference disturbance
R	Reduced resistance
T	Total injector
TS	Total series
TP	Total parallel
u	Upstream
W	Combustor wall

SECTION I

INTRODUCTION AND SUMMARY

Combustion instability normally falls into one of three types: acoustic, feed-system coupled, or hybrid.

These types of instability have been classified according to the wavelength of the frequency compared to a characteristic dimension of the chamber. When the frequency is so low that pressure fluctuations are felt (in bulk) simultaneously throughout the chamber, the instability is directly related to the feed system effects and is commonly called "feed-system coupled" or "chug." When frequencies become great enough that wave motion within the chamber is involved, the instability is classified "acoustic" if feed system effects are minimal, and "hybrid or combined" if feed system effects are predominant. The most classic instabilities are chug and acoustic, but recently hybrid instabilities have been observed in a number of engines.

Generalized models dealing with acoustic and feed-system coupled instability are currently in use. Such a generalized model for hybrid instability, however, does not currently exist. Nonetheless, limited models developed for specific cases of hybrid instability have achieved success in the past. This program is concerned with the development of a generalized model whose emphasis is on the hybrid type of combustion instability.

Analytical models of acoustic instability describe the variation of burning rate with position in the combustion chamber. This is shown schematically in Fig. 1 where the portion of the engine system being considered analytically is enclosed by the heavy black line. The analytical model of acoustic instability employed most often at Rocketdyne is a modification of the Priem model.

As indicated in Fig. 2, the essence of the feed system model is a detailed one-dimensional treatment of the feed system and a simplified treatment of the combustion process and chamber dynamics. Rocketdyne recently completed such a generalized model under contract NAS9-14515 with NASA-JSC (Ref. 1). The feed-system model predicts relative stability and reveals the essential design

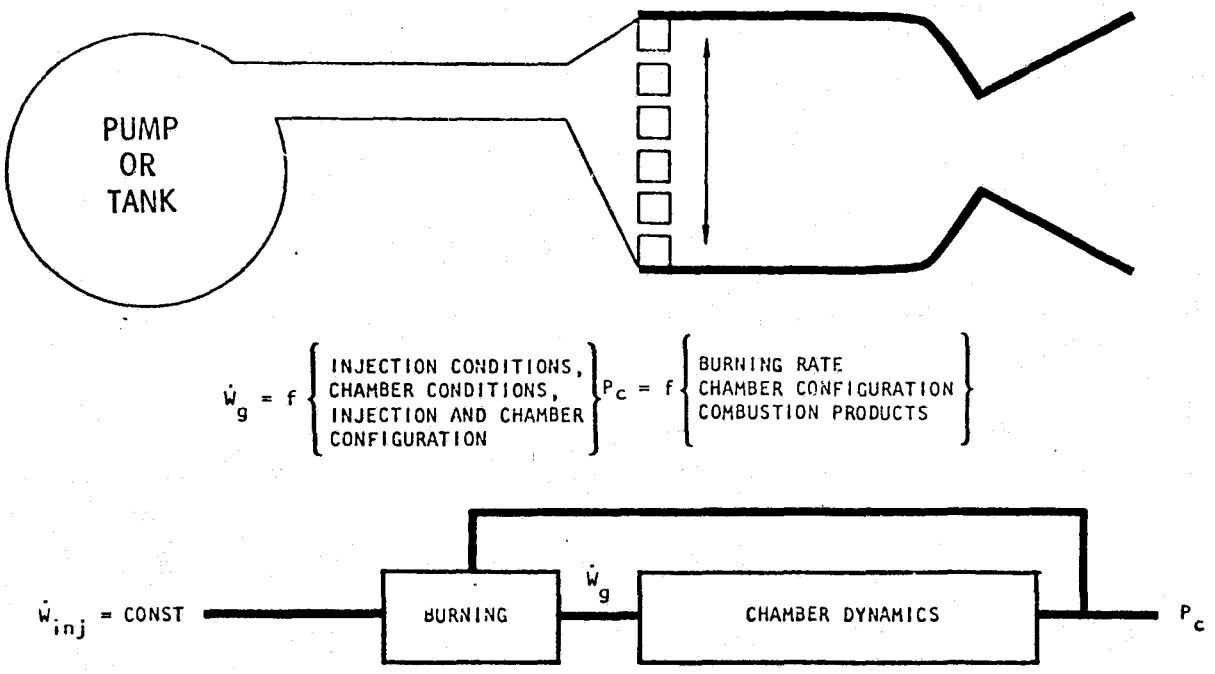

Figure 1. Acoustic Instability - Variations in Burning Rate

characteristics influencing that stability. An example of this is shown in Fig. 3. Fig. 3 is a Bode plot and is widely used for studying system stability. The y-coordinate, $\bar{\dot{w}}/2\ \Delta P$, is termed the gain, while the x-coordinate, f_b, is termed the break frequency. Lower gain systems are most stable (other factors equal). The effect of ΔP in lowering the gain is shown. Also shown is the effect of increasing orifice inertia or increased orifice L/D. Increasing the orifice L/D decreases the break frequency and enlarges the region of low gain. The resonant modes are determined by the overall feed system design details.

The complexity of hybrid instability is indicated in Fig. 4. Two- or three-dimensional aspects of both the feed system and the chamber acoustics must be taken into account. This is because constituent portions of the injector such as ring grooves or annular manifolds have characteristic frequencies which are close to the acoustic frequencies of the chamber itself. While this total model has not yet been solved analytically, engines exhibiting these phenomena have been analyzed and their problems resolved by limiting the analysis to the feed system, combustion process, chamber dynamics, or a simplified combination of the above.

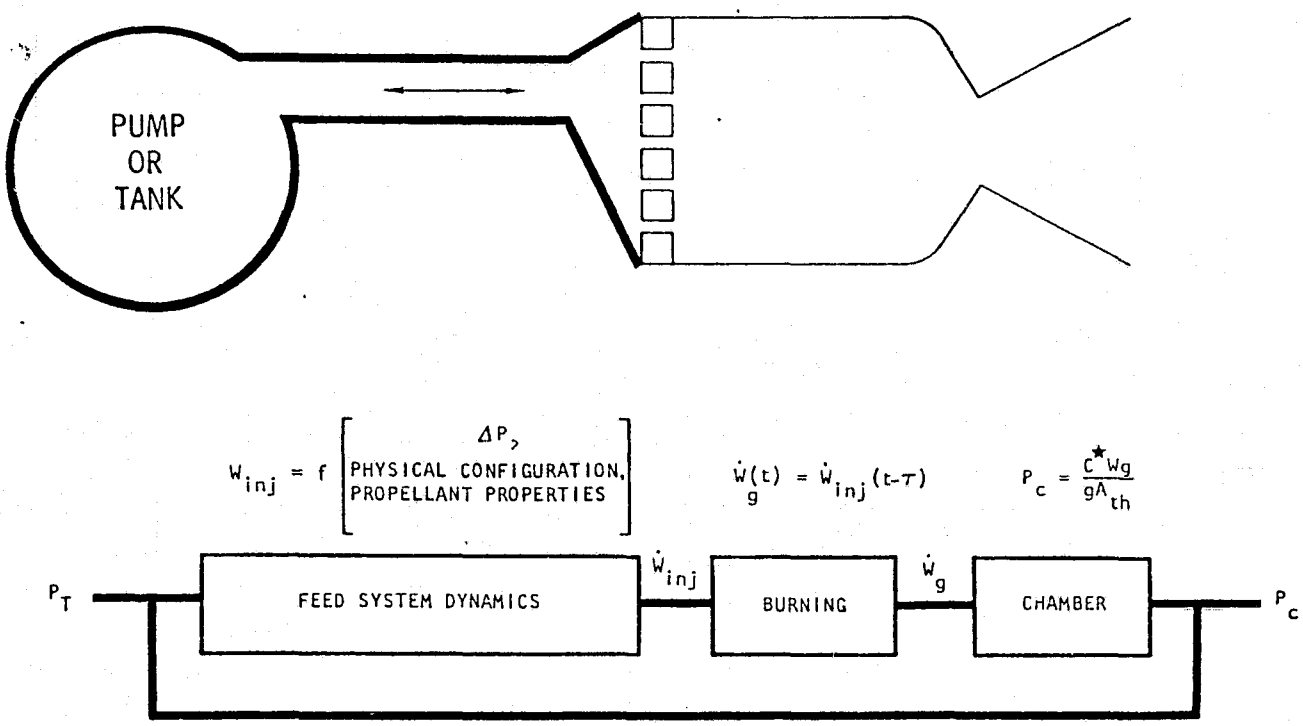

Figure 2. Feed System Coupled Oscillations-Variations in Injected Flowrate

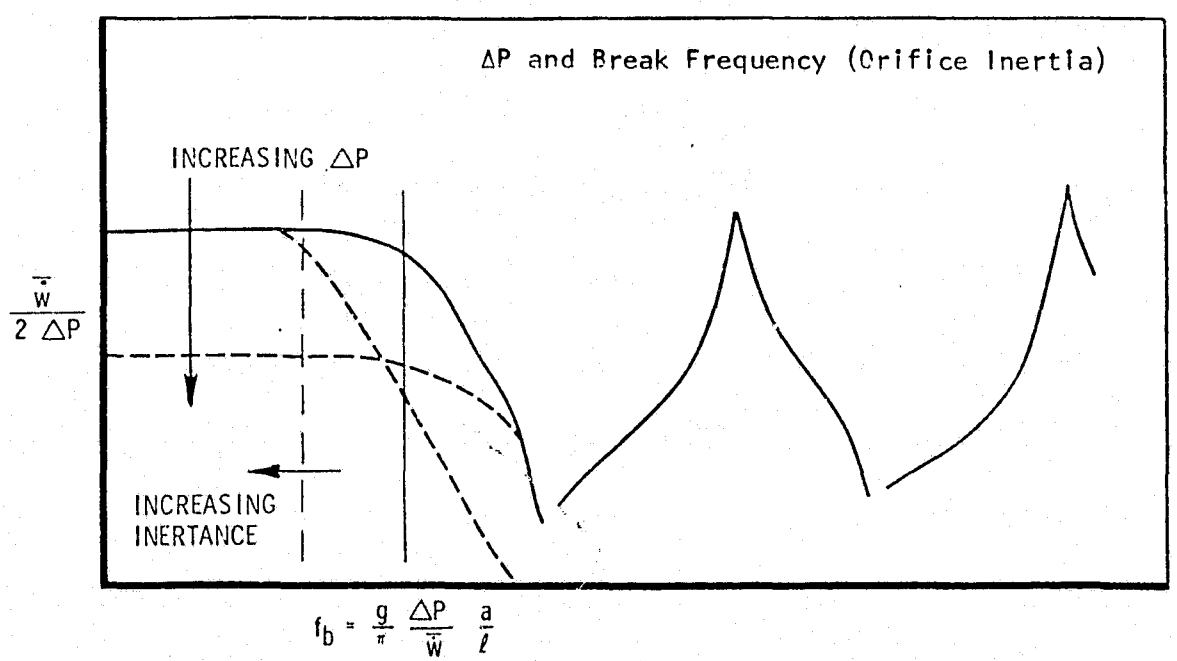

Figure 3. Evaluation of Feed System Modifications

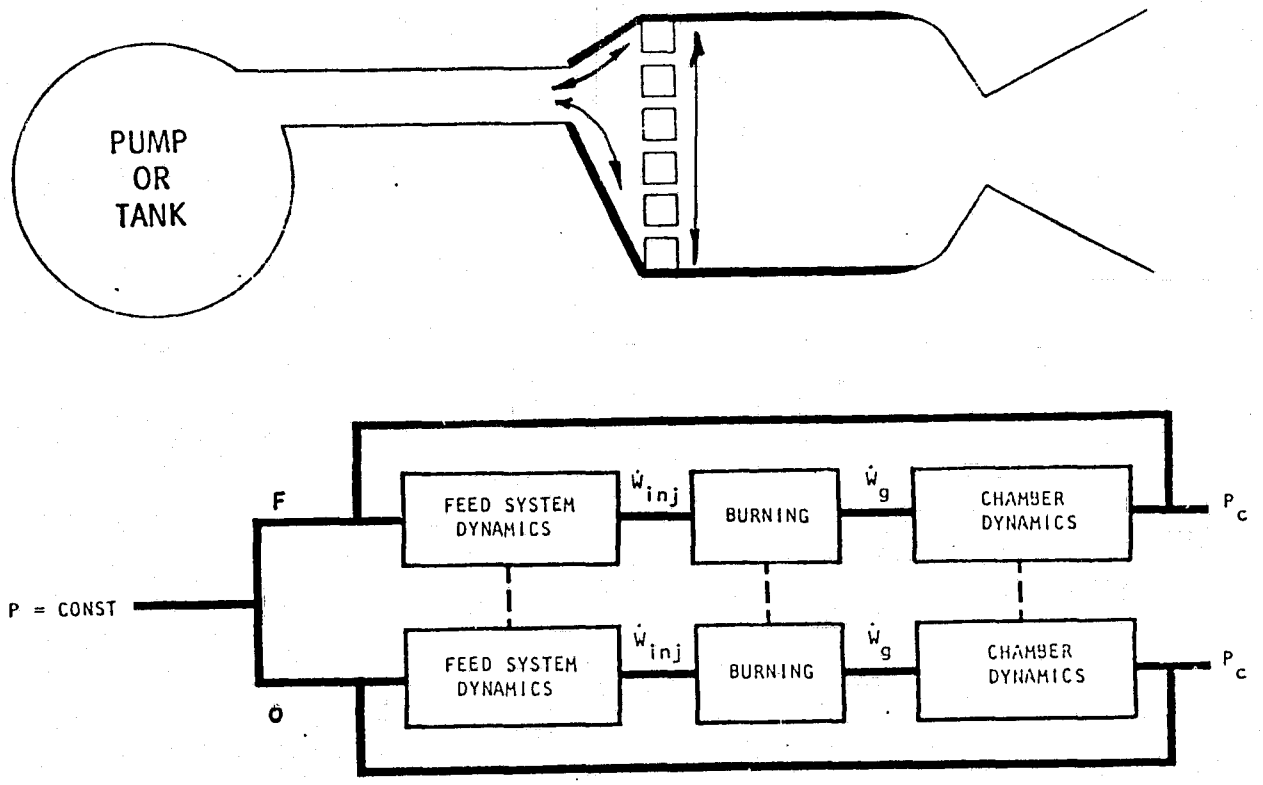

Figure 4. Hybrid Instability

The digital computer injector model developed during the subsequently described effort analyzes an injector in terms of its coupling potential with the chamber dynamics after the injector's multidimensional description has been input to the model. The model is an open-loop type model requiring that a combustion chamber pressure profile representing a specific acoustic mode of instability be imposed on the injector. The model predicts the injector response in terms of flowrate and pressure oscillations throughout the injector, and is capable of analyzing frequencies up to at least 3000 Hz.

This document is the final report of a 16-month analytical research program to develop generalized injector design criteria for the prevention of coupling between the injector hydraulics and the combustion process. This program was conducted in the following manner:

- Construction of a digital computer dynamic injector model which, for any imposed chamber or inlet pressure profile with a frequency ranging from 100 to 3000 Hz, accurately predicts/calculates the instantaneous injector flowrates.

- Correlation of the model with existing test cases which exhibited hydraulic coupling in the 100- to 3000-Hz range and verification that the model can predict characteristic differences in the frequency response of injectors which coupled and those which did not couple.

- A sensitivity analysis which consisted of a systematic variation of injector design variables using the model whose end objective was the establishment of generalized design criteria.

The analytical and test evaluation range of interest in this program is summarized below:

- Coupling problem in 100 to 3000 Hz frequency range
- Propellants - acid/amine, LOX/amine, acid/hydrocarbon, LOX/hydrocarbon
- Thrust - 25 to 50,000 lbf
- P_c - 100 to 1000 psia
- MR - maximum performance $\pm$20%
- Fuel temperature - 40°F to 0° subcooling at injected conditions
- Acid temperature - 40°F to 0° subcooling at injected conditions
- LOX temperature - -298°F to 0° subcooling at injected conditions
- Orifice size - 0.020 to 0.040 in. diameter
- Orifice ΔP - 25 to 50 psid (or 15% of P_c)

The specific end products of this effort are as follows:

1. A practical digital computer program (model) running on the NASA/JSC computer which describes the injector manifolding and orifice feed geometry and permits analysis of the injectors. hydraulic coupling characteristics. The model will be structured in a manner compatible with a total system stability model (NAS9-14315).

2. The necessary design criteria which will allow the injector designer to configure an injector such that hydraulic coupling will not occur.

3. Complete documentation consisting of the following:
   a. A final report describing the entire effort.
   b. A computer manual with appropriate sections for the user, the engineer, and the programmer.

The program was accomplished in four tasks:

Task I. Review Existing Models
Task II. Model Formulation
Task III. Model Correlation
Task IV. Sensitivity Analysis

In Task I - Review Existing Models, data was compiled on the modeling techniques employed in existing injector models. Three basic injector modeling techniques (lumped parameter, continuous parameter, and multidimensional wave solution, i.e., Green's functions) were evaluated for possible utilization in the generalized injector model to be developed in this program. To assist in the evaluation, a total of three injectors (all of which have exhibited hydraulic coupled instability) were defined in detail. The lumped parameter injector modeling technique was demonstrated to be capable of satisfactorily describing any of these "typical" injectors and was selected for utilization in Task II. Application of this technique to "typical" injector designs is simple, flexible, and state-of-the-art. Effort conducted in Task I resulted in the elimination of possible disadvantages previously believed associated with the lumped parameter technique (i.e., (1) computer core storage, (2) computation time, (3) limitation on injector description capability due to core storage limitation, and (4) accuracy due to description limitation.

In Task II - Model Formulation, the model was formulated such that the equations governing fluid flow inside the injector were linearized and

subsequently arranged in matrix form. The matrix is then solved in a frequency response format giving gains and phases for pressures and flowrates at various locations within the injector.

The injector system is described (using the lumped parameter technique) in terms of which flow segments enter and leave each pressure node. For each flow segment, a resistance, line lengths, and areas are required as inputs (the line lengths and areas are used in determining inertance). For each pressure node, volume and acoustic velocity are required as inputs (volume and acoustic velocity determine capacitance). The geometric criteria for determining inertances of flow segments and capacitances of pressure nodes was set. Also, a technique was developed for analytically determining time averaged steady-state pressure drops and flowrates for every flow segment in an injector when such data is not known. These pressure drops and flowrates are then used in determining the linearized flow resistance for each line segment of flow. The model was constructed to have an input option of any of three chamber instability mode shapes (first or second tangential or first radial). However, any general pressure profile input can be used by specifying the amplitude and sign of each of the individual input locations.

To provide a simple way to evaluate any specific injection configuration, summations were made of the oscillatory injector flow (for a unit pressure perturbation). These summations include: (1) a summation of all the absolute values of injector flowrate, (2) a vector summation of all injector flowrates (attempt to include phase angle), and (3) and (4) the previous two cases except that each injector flow is multiplied by the relative amplitude of the chamber pressure that it feeds before making the summations. In addition to printout of the summation of injector flows (both absolute and vector), the ease of interpreting the output of the engine hydraulic stability computer model was also enhanced by a graphical display of the amplitudes of ring groove flows, ring groove pressures, injector flows, and chamber pressure inputs around each ring groove.

In Task III - Model Correlation, three "correlation" injectors were selected for utilization. These were the Rocketdyne Lance XRL Booster Injector, the Aerojet Space Shuttle OME technology injector, and the Rocketdyne Space Shuttle OME technology injector. Each of these injectors experimentally exhibited hydraulic coupling in the 100- to 3000-Hz range. In addition, experimentally proven hardware fixes, which successfully eliminated the instability, exist for each of the three "correlation" injectors.

The engine hydraulic stability computer model was run for each of the "correlation" injectors with both pre-fix and post-fix injector model input. Examination and analysis of the model output revealed that the computer model successfully predicted that the fixes applied to each correlation injector would increase combustor stability with respect to the instability mode actually observed.

In Task IV - Sensitivity Analysis, a systematic variation of injector design variables was made, using the computer model for the Aerojet and Rocketdyne OME technology injectors, to gauge the effects on injector gain. The variables investigated included (1) model frequency, (2) orifice resistance, (3) orifice inertance, (4) ring groove area, and (5) the presence of dams. For the Rocketdyne injector, injector gain was observed to be simply related to orifice resistance, orifice inertance, and frequency through a term called the break frequency. However, for the Aerojet injector, complications caused by the possibility of the pie manifolds acting as Helmholtz resonsators precluded the establishment of any simple relationship for the injector gain. Results of these sensitivity analyses showed that individual injector design parameters (i.e., orifice characteristics, ring groove area, etc.) could not be characterized as promoting or retarding coupling. Instead, the interaction between all constituent injector flow passages must be analyzed together. It was concluded, therefore, that the development of generalized design criteria is premature to its use in place of the parametric application (to a specific injector) of the engine hydraulic stability model. The engine hydraulic stability computer model, however, was concluded to be quite capable of predicting the relative effects of proposed fixes and/or evaluating design options of a particular injector concept.

The program was concluded with the conversion of the engineering model from Rocketdyne's IBM 370 computer to the NASA/JSC Univac 1110, EXEC-8 computer system and successful operation of the engineering model at NASA/JSC. Model documentation in the form of the present final report and a computer manual constituted the end products of the contract.

The work performed within all of the foregoing tasks is presented in this document. The presentation of the subject matter is organized as a task-by-task description rather than a detailed discussion of the computer program. The latter is extensively described in a separate companion document entitled "Engine Hydraulic Stability Model Computer Manual" (Ref. 2).

SECTION II

REVIEW OF EXISTING MODELS

The development of the fundamental equations describing fluid flow in the injector is detailed in Appendix A. Depending on the further simplifying assumptions made, these equations can be solved using any of several techniques. These techniques form the candidate solution methods that were evaluated in Task I. A discussion of each follows.

COMPILATION OF DATA ON EXISTING MODELS

The injector modeling techniques which have been employed in existing models are described in the following paragraphs. The basic techniques for modeling multidimensional wave motion in the constituent portions of the injector are (1) lumped parameter approach, (2) continuous parameter approach, and (3) generalized wave equations. These techniques were reviewed. The extent of the use of these techniques, along with simplifying approximations employed, in existing injector models were also examined. Many injector models were developed for a "one-shot" analysis of a particular injector.

Lumped Parameter Technique

The lumped parameter description consists of dividing any given hydraulic system into a number of pressure nodes with flows calculated between those nodes. The allowable maximum length between each pressure node is determined by the acoustic velocity of the fluid, and the acoustic frequency of interest. This length can be explicitly given by the relation

$$L \leq \frac{a}{8\nu} = \lambda/8 \qquad (1)$$

where

- L = length between pressure nodes
- a = acoustic velocity of the hydraulic fluid
- ν = acoustic frequency
- λ = acoustic wavelength

Equation (1) states that there must be at least eight pressure nodes per acoustic wavelength.

Figure 5. shows how a given line segment of flow would be broken into lumps using the lumped parameter description. Each line segment consists of a series of pressure nodes, P_i, separated by a length L. Between these pressure nodes are mass flows, $\dot{w}_i$, which also must be included in the lumped description.

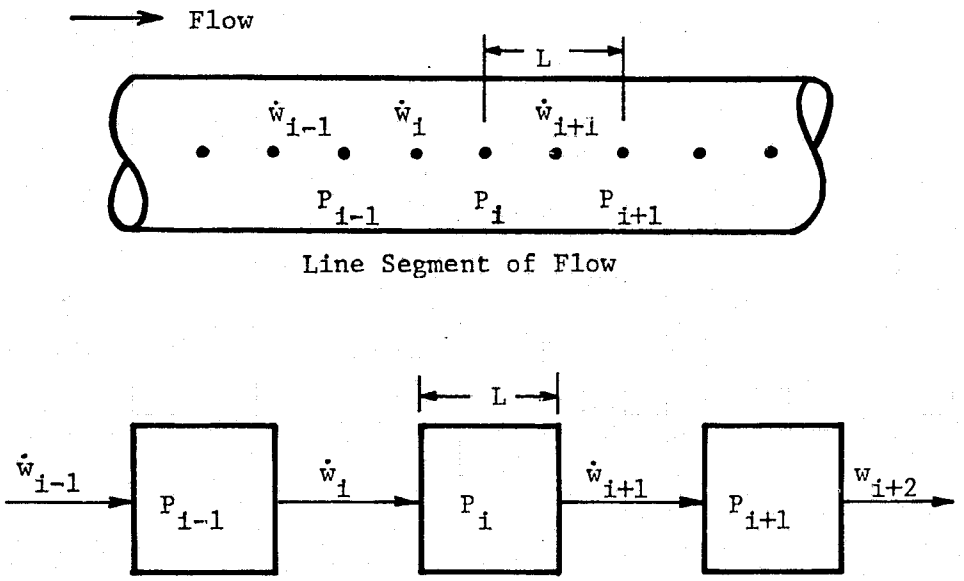

Figure 5. Lumped Parameter Technique

The mathematical development of the lumped parameter technique begins from the viscous one-dimensional equations for perturbed flow as shown in Appendix A. Taking the finite difference of the spatial derivative in Eq. (A-25), in Appendix A, the change in pressure of each pressure node in Fig.5 can be expressed as

$$C \frac{d\tilde{P}_i}{dt} = \tilde{w}_i - \tilde{w}_{i+1} \tag{2a}$$

such that

$$C \equiv \frac{Vg_c}{a^2} \tag{2b}$$

$$\tilde{w} \equiv \bar{\rho} A \tilde{v}_x \tag{2c}$$

where

C is the capacitance of the pressure node

$\tilde{w}$ is the perturbed mass flowrate

A is the cross-sectional area of the line segment

$\tilde{v}_x$ is the perturbed axial fluid velocity

V is the volume of the pressure node (L times A)

$\bar{\rho}$ is the time averaged fluid density (which is constant)

$\tilde{P}$ is the perturbed pressure

t is the time

and g_c is a units conversion factor between mass and force when Engineering units are used (386 in.-lbm/lbf-sec^2)

Finally, taking the finite difference of the spatial derivative in Eq. (A-26) in Appendix A, the perturbed mass flowrate between each pressure node in Fig 5 is determined by

$$I \frac{d\tilde{w}_i}{dt} = \tilde{P}_{i-1} - \tilde{P}_i - R_L \tilde{w}_i \tag{3a}$$

such that

$$I \equiv \frac{L}{Ag_c} \tag{3b}$$

$$R_L \equiv \frac{2|\Delta\bar{P}|}{|\bar{\dot{w}}|} \tag{3c}$$

where

| | denotes absolute value

I is the inertance of the fluid element

R_L is the linearized flow resistance based on time-averaged steady-state values

$\Delta\bar{P}$ is the time-averaged pressure drop across a pressure node of length L

$\bar{w}$ is the time-averaged mass flowrate

Equations (2) and (3) above are the governing equations for perturbed steady hydraulic systems, represented by the lumped parameter technique. They form a system of linear ordinary differential equations which is often solved on an analog computer in real time.

The lumped parameter technique can, however, be used in either the time domain or the frequency domain.* A frequency domain solution is indeed most appropriate when an oscillatory pressure at the injector face is used as input to the injector model. In this instance, a Laplace transform of Eqs. (2a) and (3a) are taken with the result being

$$S\,\tilde{P}_i = C(\tilde{w}_i - \tilde{w}_{i+1}) \tag{4}$$

and

$$S\,\tilde{w}_i = \frac{1}{I}\left[\tilde{P}_{i-1} - \tilde{P}_i - R_L\,\dot{w}_i\right] \tag{5}$$

* In the time domain, the ordinary differential equations are solved by integration as a function of time. In the frequency domain, a Laplace transformation is made which converts the differential operator to a Laplace operator. This is then replaced by $j\omega$ and solutions are obtained as a function of frequency. Frequency response gains and phases are the direct output of the frequency domain solution while the output form in the time domain solution are individual variables as a function of time. Therefore, to get gains, the amplitude and phase of each variable with respect to the input need to be determined from the time transients.

Now replacing "S" by "Jω", where ω is the frequency and $j = \sqrt{-1}$, a frequency response solution (Ref. 3) for the perturbed pressure and mass flowrate at any node can be determined by solving the matrix of equations given by Eqs. (4) and (5) above.

The lumped parameter description has previously been used with excellent results at Rocketdyne in analyzing several complex injector systems. These include the XRL booster, XRL sustainer, and the LE-3 injectors (Refs. 4 and 5). For these cases, a specific injector and a specific mode and frequency were analyzed. When analyzing a system at only one frequency, computer cost is generally small. Computer cost for a given number of equations is directly proportional to the number of frequencies to be analyzed.

Continuous Parameter Techniques

The continuous parameter approach is a method of solution which allows gradients of pressure and velocity to exist within the finite segments of fluid flow. Thus, the conservation equations describing this situation are partial differential equations, where pressure and velocity are functions of time and position. This contrasts with the lumped parameter technique which is characterized by ordinary differential equations where only time is the independent variables, Eqs. (2a) and (3a).

The continuous parameter technique has had previous usage at Rocketdyne especially on the OME feed system coupled stability investigation (Ref. 1), and has been shown to have a distinct potential gain in computer core storage and accuracy over the lumped parameter technique. This is due to the fact that by allowing for gradients to exist in a flow segment less nodes are needed to describe the overall flow. This means less equations which implies less core storage and less computing time.

As shown in Appendix A, the development of the continuous parameter technique begins from the one-dimensional wave equation for inviscid perturbed flow. This representation is found from Eqs. (A-23) and (A-24) of Appendix A which give,

$$\frac{1}{a^2}\frac{\partial^2 \tilde{P}}{\partial t^2} = \frac{\partial^2 \tilde{P}}{\partial x^2} \tag{6}$$

and

$$\bar{\rho}\frac{\partial \tilde{v}_x}{\partial t} = -\frac{\partial \tilde{P}}{\partial x} \tag{7}$$

where

x = axial direction

The technique used in the OME feed-system coupled stability investigation (Ref. 1) to solve the above system of equations, employed a D'Alembert solution (Ref. 6). The general form of the solution which satisfied Eq. (6) is

$$\tilde{P} = F_1 (t + x/a) + F_2 (t - x/a) \tag{8}$$

where F_1 and F_2 are arbitrary functions. Now, Eq. (7) and (8) can be shown to yield

$$\tilde{v}_x = \frac{1}{\bar{\rho}a}\left[- F_1 (t + x/a) + F_2 (t - x/a)\right] \tag{9}$$

Figure 6 shows how a long linear flow passage would be broken up into segments using a continuous parameter representation. Such segments may represent, for example, passages of various cross sections or passages connecting flow junctions.

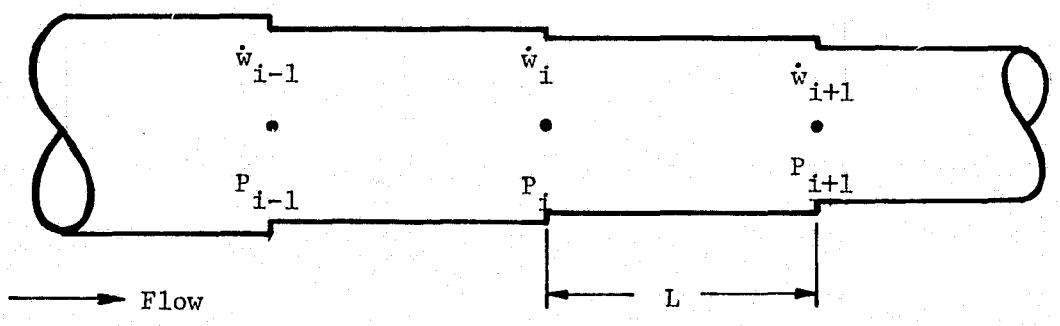

Continuous Parameter Description of Linear Flow Passage

Figure 6. Continuous Parameter Technique

Using the nodal representation of Fig. 6 above, Eqs. (8) and (9) can be combined to eliminate the functions, F_1 and F_2 and show that

$$\left[\tilde{P}_{i+1} - \frac{a}{Ag_c}\tilde{w}_{i+1}\right]_{(t-\tau_i)} = \left[\tilde{P}_i - \frac{a}{Ag_c}\tilde{w}_i\right]_t \tag{10}$$

and

$$\left[\tilde{P}_i + \frac{a}{Ag_c}\tilde{w}_i\right]_{(t-\tau_i)} = \left[\tilde{P}_{i+1} + \frac{a}{Ag_c}\tilde{w}_{i+1}\right]_t \tag{11}$$

where

$\tau_n = L/a$ the signal propagation time between modes

The subscripts, $(t - \tau_i)$ and (t) denote the time values at which the terms in brackets are to be evaluated.

Equations (10) and (11) are for inviscid one-dimensional flow. However, a viscous one-dimensional flow representation can be included by putting in the viscous momentum head loss terms at each node. This is done by simply replacing $\tilde{P}_{i+1}$ by $(\tilde{P}_{i+1} + R_L \tilde{w}_{i+1})$. Now, taking the Laplace Transform of Eqs. (10) and (11), and again replacing "S" by "$j\omega$", a frequency response solution to the matrix of equations can be obtained as in the lumped parameter techniques.

Multi-dimensional Wave Technique

This technique allows for a three-dimensional variation of axial perturbed flow. Using Eqs.(A-23) and (A-24) of Appendix A will give for the cylindrical coordinates of a pipe

$$\frac{1}{a^2}\frac{\partial^2 \tilde{P}}{\partial t^2} = \frac{\partial^2 \tilde{P}}{\partial r^2} + \frac{1}{r}\frac{\partial \tilde{P}}{\partial r} + \frac{1}{r^2}\frac{\partial^2 \tilde{P}}{\partial \theta^2} + \frac{\partial^2 \tilde{P}}{\partial z^2} \tag{12}$$

and

$$\frac{\partial \tilde{w}}{\partial t} = -A\frac{\partial \tilde{P}}{\partial z} \tag{13}$$

where

r = radial direction

θ = tangential direction

z = axial diration

Other cavity geometries may of course be chosen to describe parts of the feed system, however, this representation will allow the complexities of this method to be seen.

The simplest solution to the wave equation is obtained when the following uniform boundary conditions are given:

$$\tilde{P}(r = 0) = \text{finite} \tag{14a}$$

$$\left.\frac{\partial \tilde{P}}{\partial r}\right|_{r=r_w} = 0 \tag{14b}$$

where r_w = radius of pipe

$$\left.\frac{\partial \tilde{P}}{\partial \theta}\right|_{\theta=0} = 0 \tag{14c}$$

and

$$\tilde{P}\ (\theta = 0) = \text{continuous} \tag{14d}$$

Now taking the Laplace Transform of Eqs. (12) and (13) , replacing "S" with "jω", and separating variables in Eq. (12) yields

$$\tilde{P} = \sum_{m=0}^{\infty} \sum_{k_m} (A \cos k_m z + B \sin k_m z) \cos(m\theta) \quad J_m\left(\frac{\alpha_{mn} r}{r_w}\right) \tag{15}$$

and

$$\tilde{w} = \sum_{m=0}^{\infty} \sum_{k_m} -j \frac{A k_m}{\omega} (A \sin k_m z - B \cos k_m z) \cos (m\theta) J_m\left(\frac{\alpha_{mn} r}{r_w}\right) \tag{16}$$

where

$$k_m^2 = (\omega/a)^2 - \left(\frac{\alpha_{mn}}{r_w}\right)^2$$

$m = 0, 1, 2, 3, \ldots .$

J_m = Bessel Function of the first kind, order m

and the eigenvalues of α_{mn} are given by the transcendental equation

$$\left.\frac{d\left[J_m(\alpha_{mn})\right]}{dr}\right|_{r=r_w} = 0.$$

The above constants A and B must still be determined from the boundary conditions for the perturbed pressures at the pipe inlet and exit. This is a very complex solution and still no account for viscous momentum head losses has been included.

When non-uniform boundary conditions are given, the solution becomes even more complex and requires the use of Green's functions. Some analyses using Green's functions were used at Rocketdyne to investigate the potential for feed system coupling in the Rocketdyne OME (Ref. 7). In that case, for frequencies of 2300 to 2800 Hz, simple resonance phenomena were sought and only frequencies corresponding to $\tilde{P} = 0$ at the injector face were calculated.

The complexity of this approach is indeed such that it is way beyond the scope of this project.

EVALUATION OF EXISTING TECHNIQUES

The configurations of three injectors which have experienced stability problems possibly resulting from hydraulic coupling with the combustion process were documented in detail. This was done in order to ascertain the difficulty or complexity involved in the application of the various modeling techniques to describe multi-dimensional wave motion in a "typical" injector. Based upon the test evaluation range of variables such as thrust

(25 to 5000 lb_f), pressure (100 to 1000 psia) and frequency (100 to 3000 Hz) as enumerated in the Statement of Work (see Ref. 8), the maximum injector diameter of interest was calculated as shown below.

$$D_{ch} = \sqrt{\frac{4(F)(CR)}{\pi P_c C_F}} \sim \sqrt{\frac{4(5\times10^4)(2.5)}{\pi(10^3)(1.6)}} = 10 \text{ in.}$$

This 10-inch diameter corresponds to the diameter of a cylindrical chamber having a first tangential acoustic frequency of approximately 3000 Hz.

Typical Injector Design

Rocketdyne Lance XRL Booster Injector. Manifold and face pattern details of the Rocketdyne Lance XRL booster injector are shown in Figs. 7 through 9. This injector comprises an annular area around the central sustainer engine. The outer diameter of the annular booster injector is 13.2 inches while the inner diameter is 6.65 inches. An unlike doublet orifice pattern is utilized (Fig. 7). Orifice diameters are 0.0515 inch for the fuel and 0.073 inch for the oxidizer. The XRL injector contains three oxidizer ring grooves and two fuel ring grooves. EAch ring groove is fed in four locations from a supply manifold whose shape is shown in Figs. 8 and 9.

Rocketdyne Space Shuttle OME Technology Injector. Details of the Rocketdyne OME technology injector are shown in Figs. 10 through 14. The like-doublet orifice pattern is shown in Figs. 10 and 11. Orifice diameters are 0.028 inch to 0.033 inch for the fuel and 0.032 inch to 0.038 inch for the oxidizer. The injection orifices are fed by a total of 10 ring grooves (5 ox and 5 fuel) behind the 8.2-inch-diameter injector face (see Figs. 10 and 12). The oxidizer ring grooves are fed through slanted feeder passages from a central oxidizer manifold as shown in Figs. 13 and 14. The fuel ring grooves are fed through slanted feeder passages from an annular fuel manifold (see Figs. 13 and 14).

Aerojet Space Shuttle OME Technology Injector. Details of the Aerojet OME technology injector (Ref. 9) are shown in Figs. 15 and 16. The hydraulic diameters of the square injection orifices are 0.020 inch for the fuel and 0.024 inch for the oxidizer. An 867-element X-doublet platelet pattern on the 8.2-inch-diameter

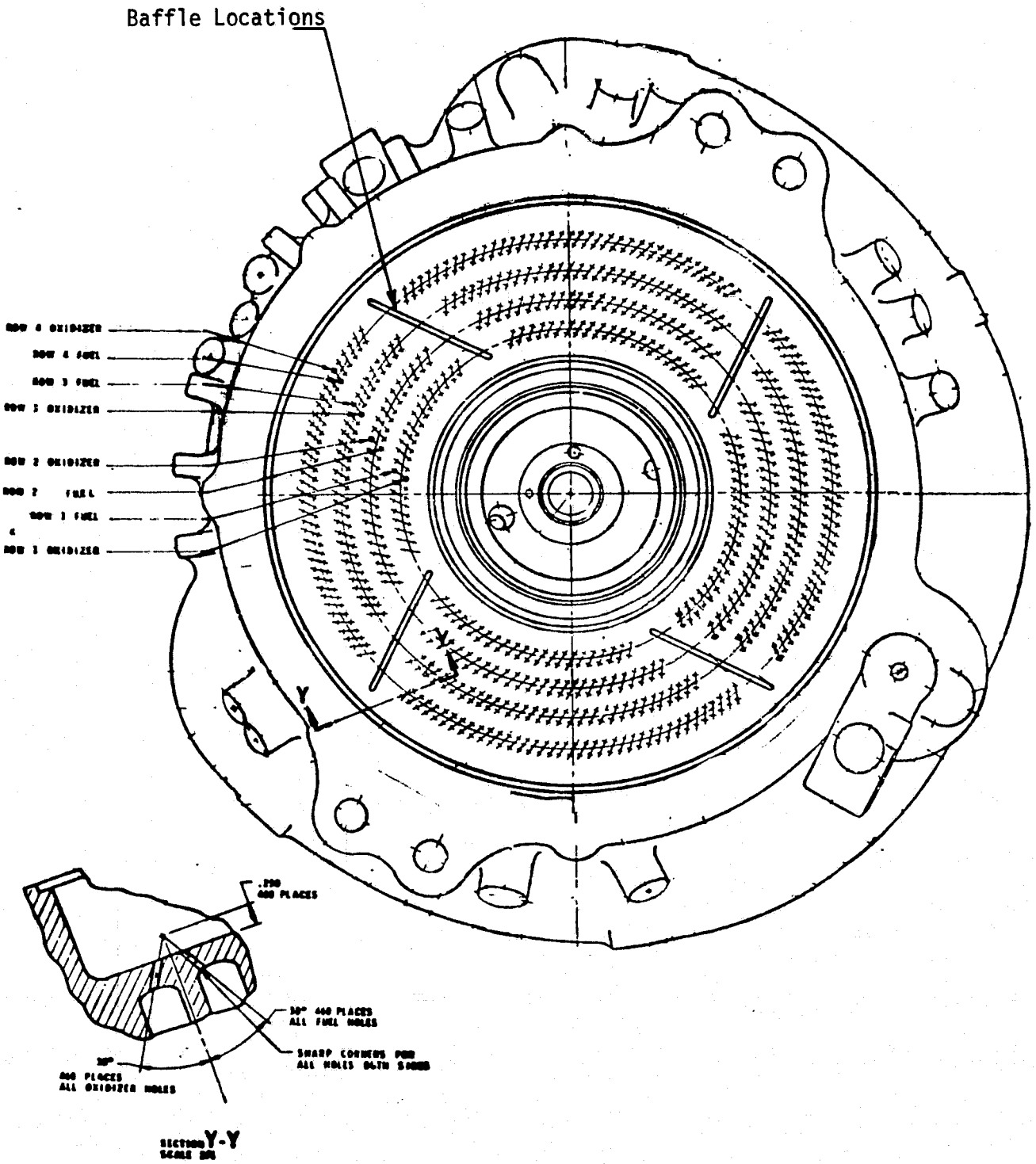

Figure 7. Frontside of XRL Injector Housing Showing Face Pattern

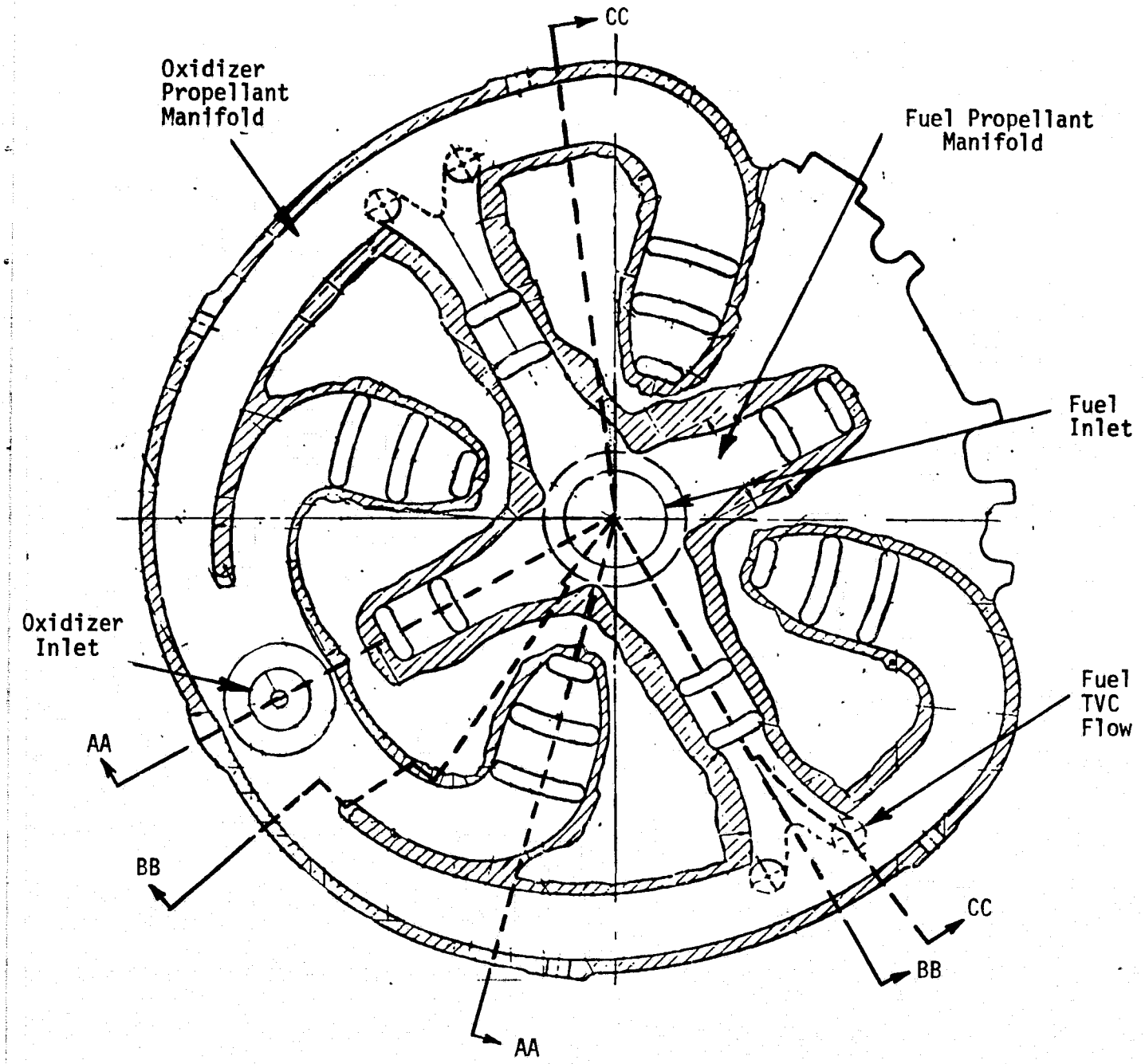

Figure 8. Cross-section of XRL Injector Housing
Showing Booster Oxidizer and Fuel Passages

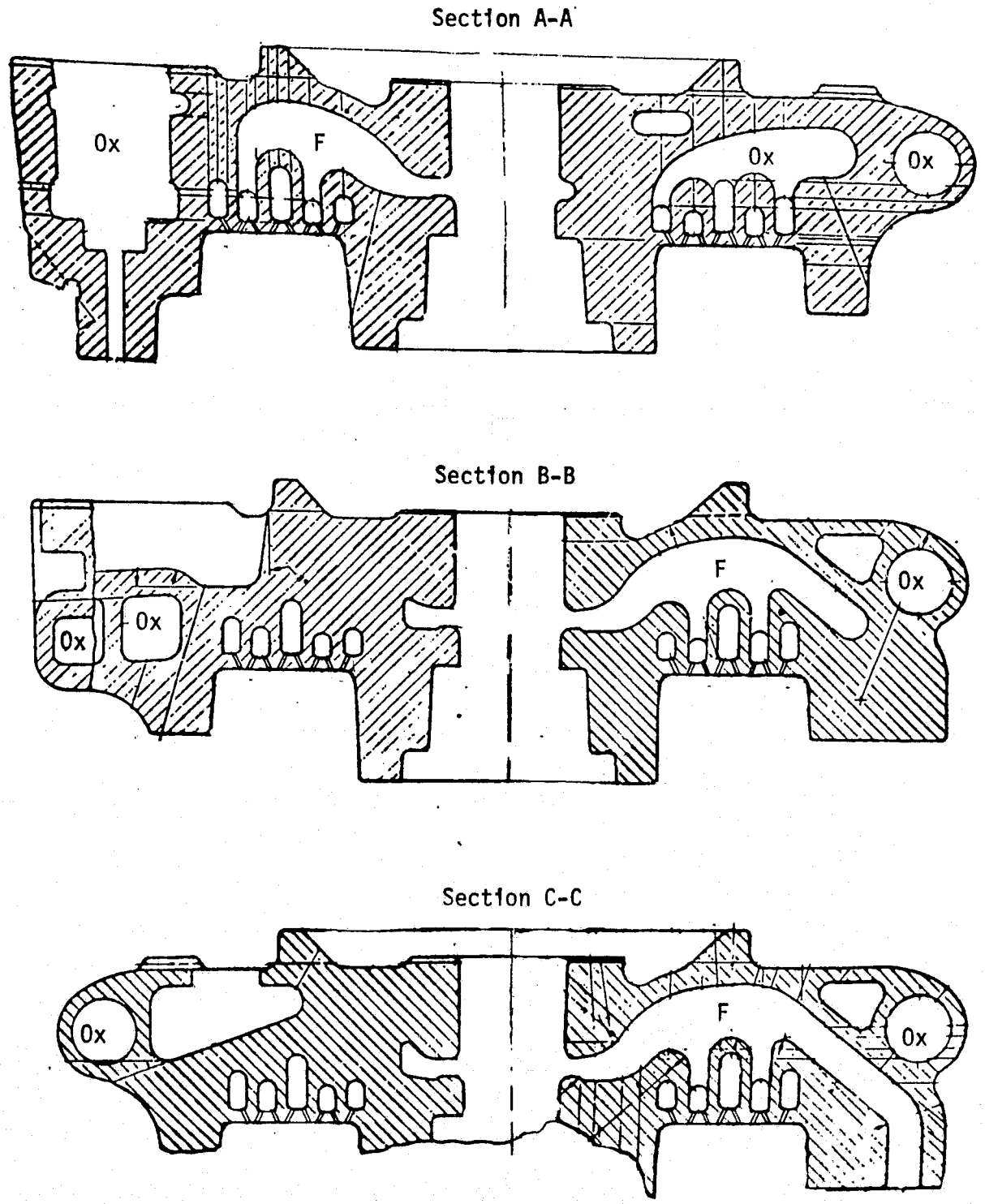

Figure 9. Axial Cross-sections Through XRL Injector Housing

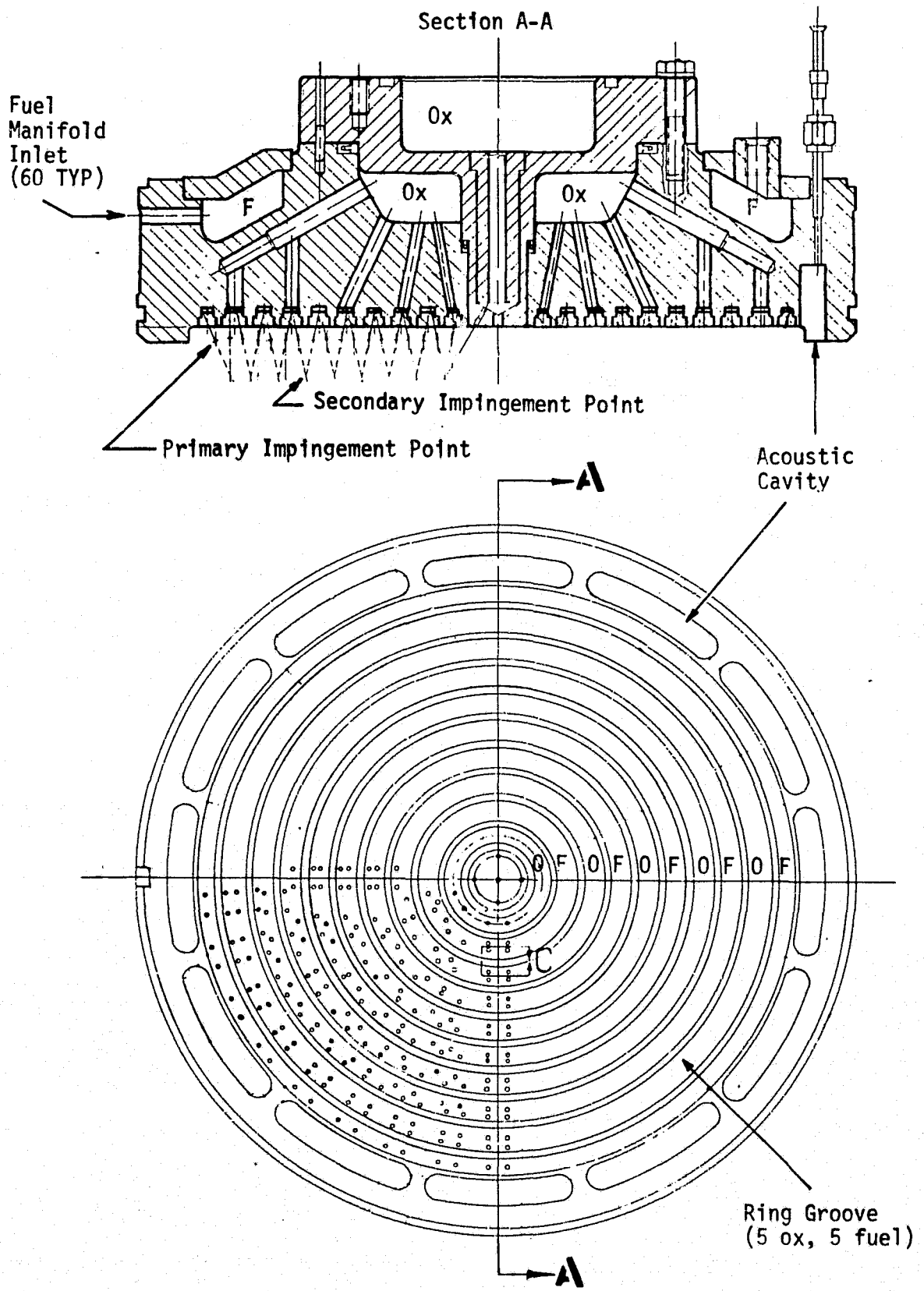

Figure 10. Face of Rocketdyne OME Technology Injector

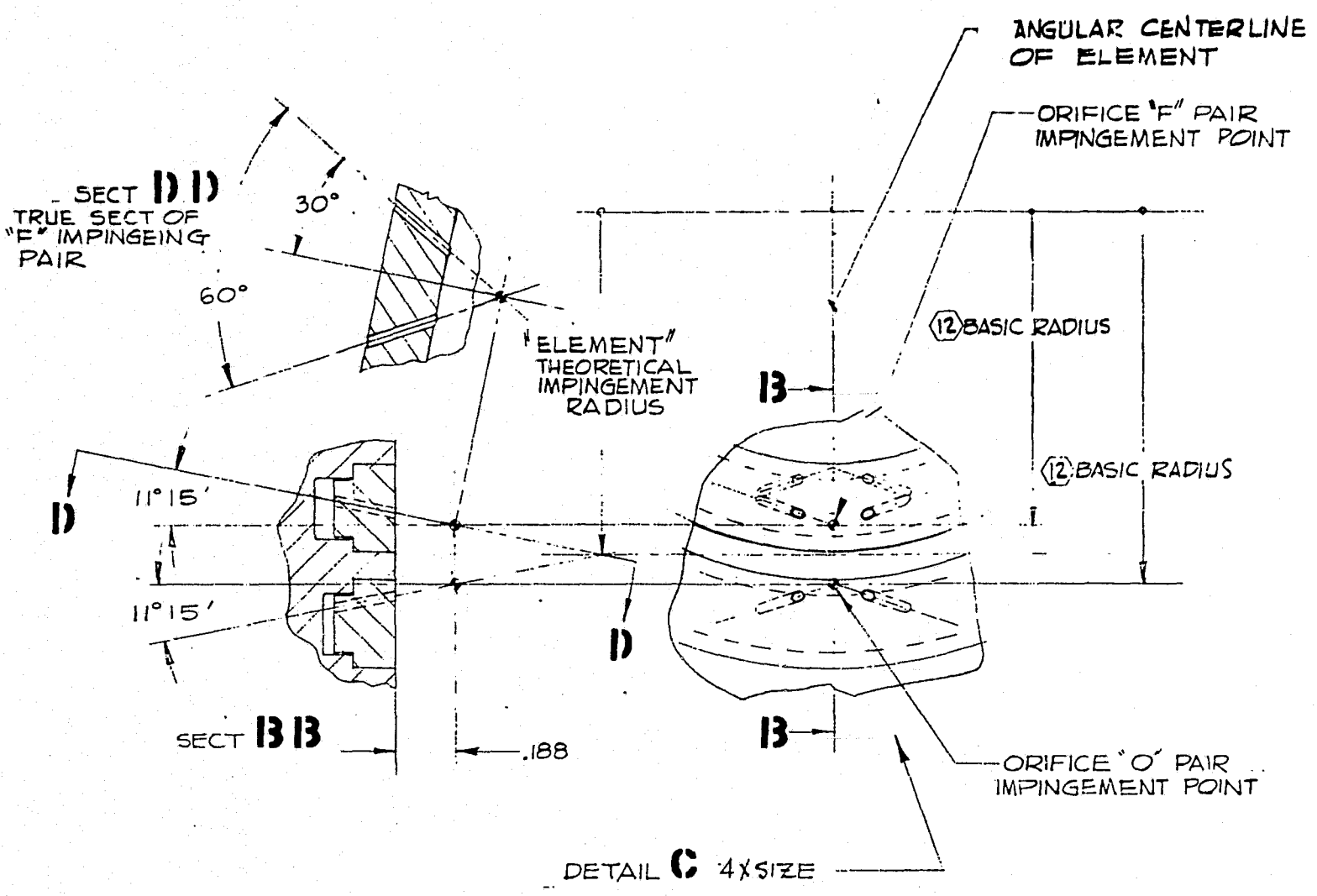

Figure 11. Typical Rocketdyne OME Technology Injector Element

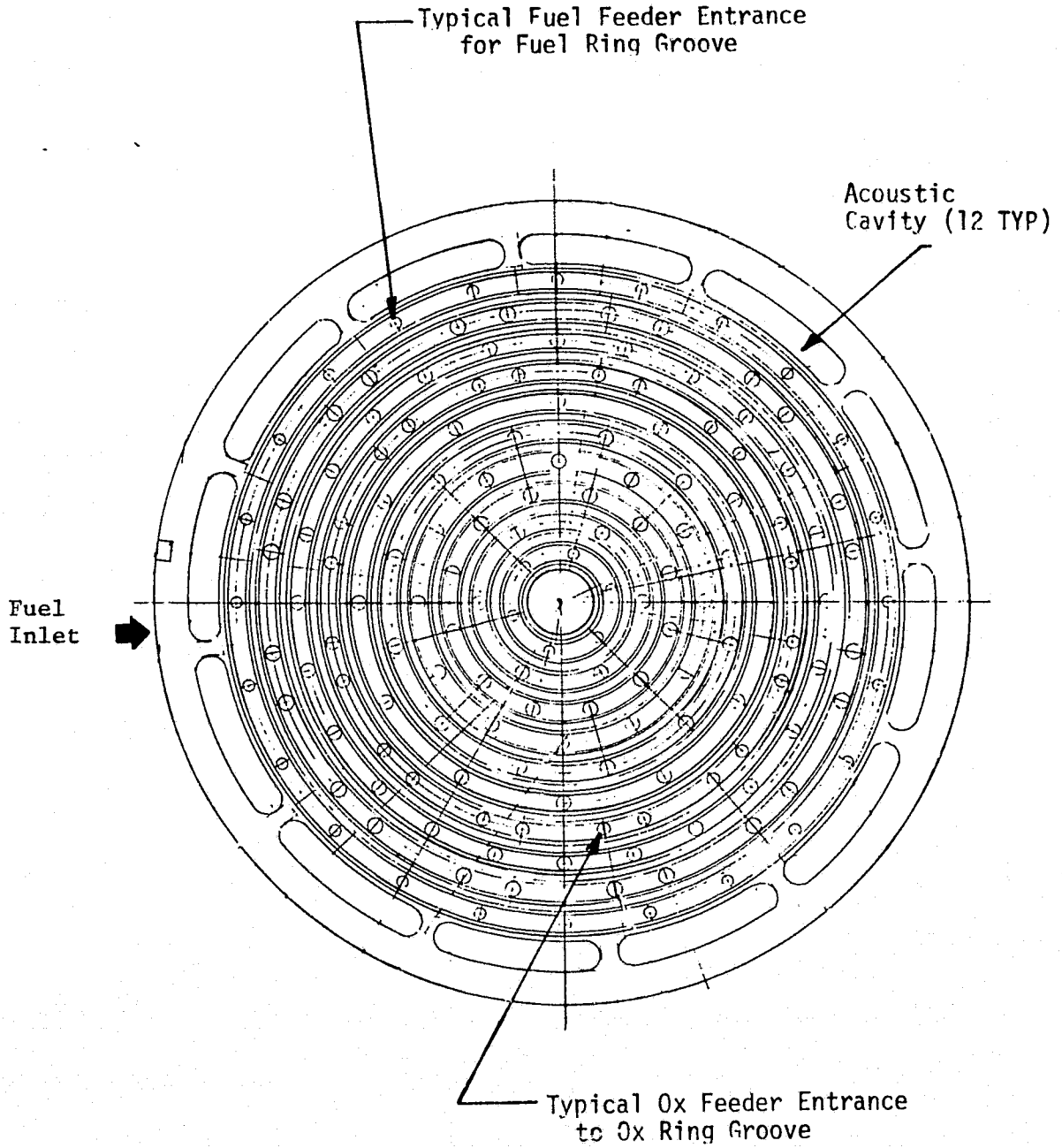

Figure 12. Injector-End View of Rocketdyne OME Technology Injector Housing Showing Ring Grooves and Feeder Entrances to Ring Grooves

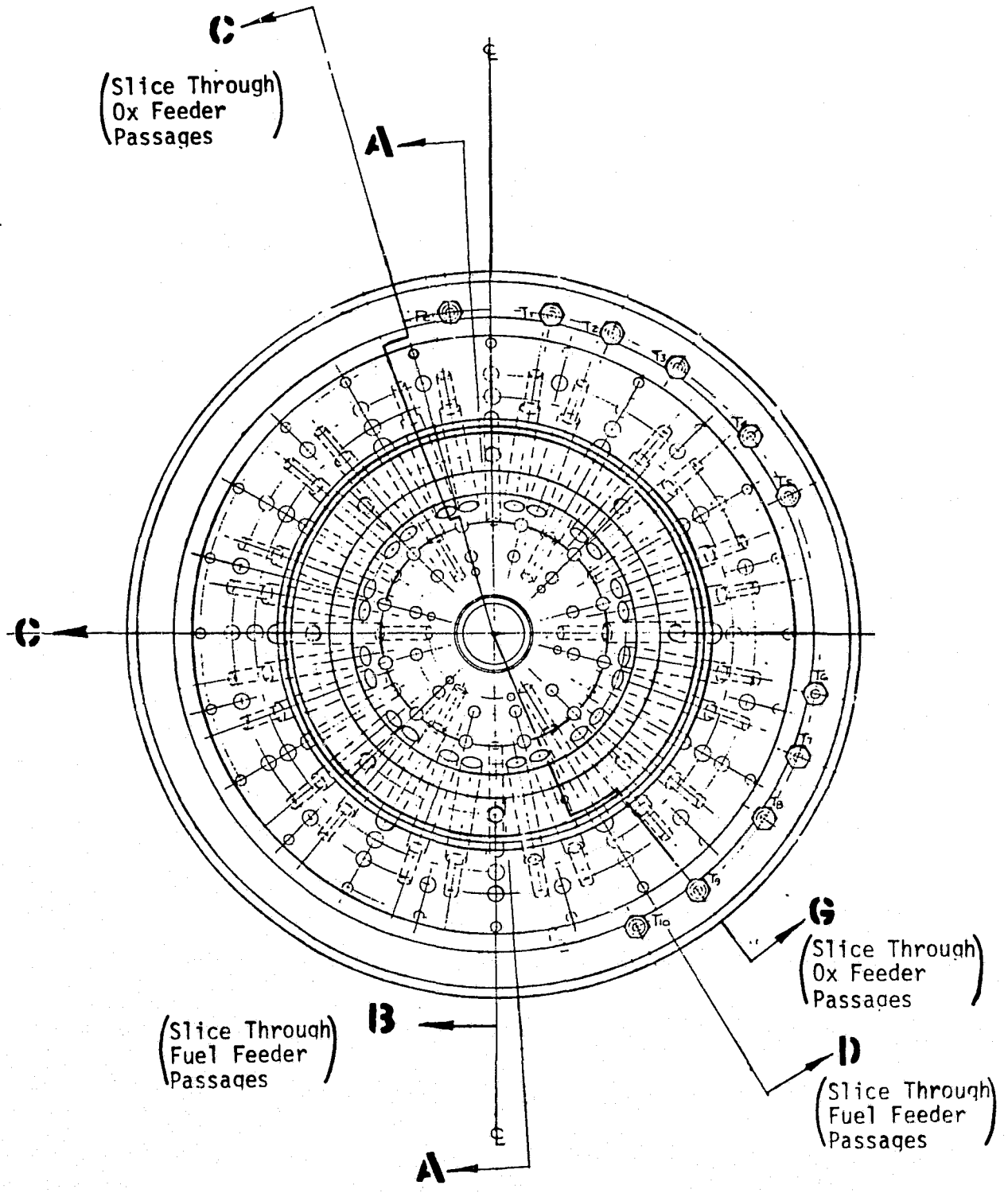

Figure 13. Top View of Rocketdyne OME Technology Injector Housing Showing Feeder Passages

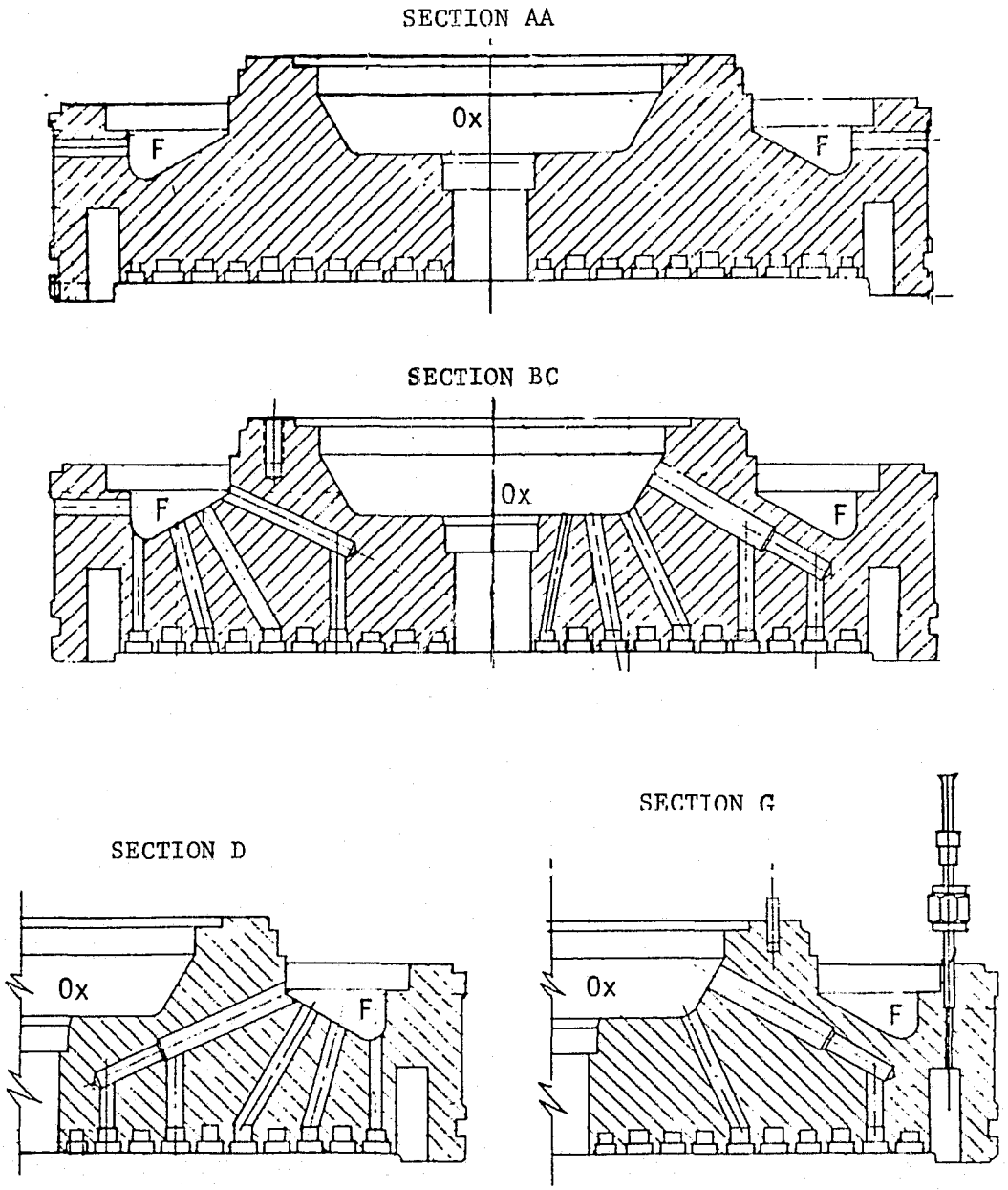

Figure 14. Axial Cross-Sections Through Rocketdyne OME Technology Injector Housing

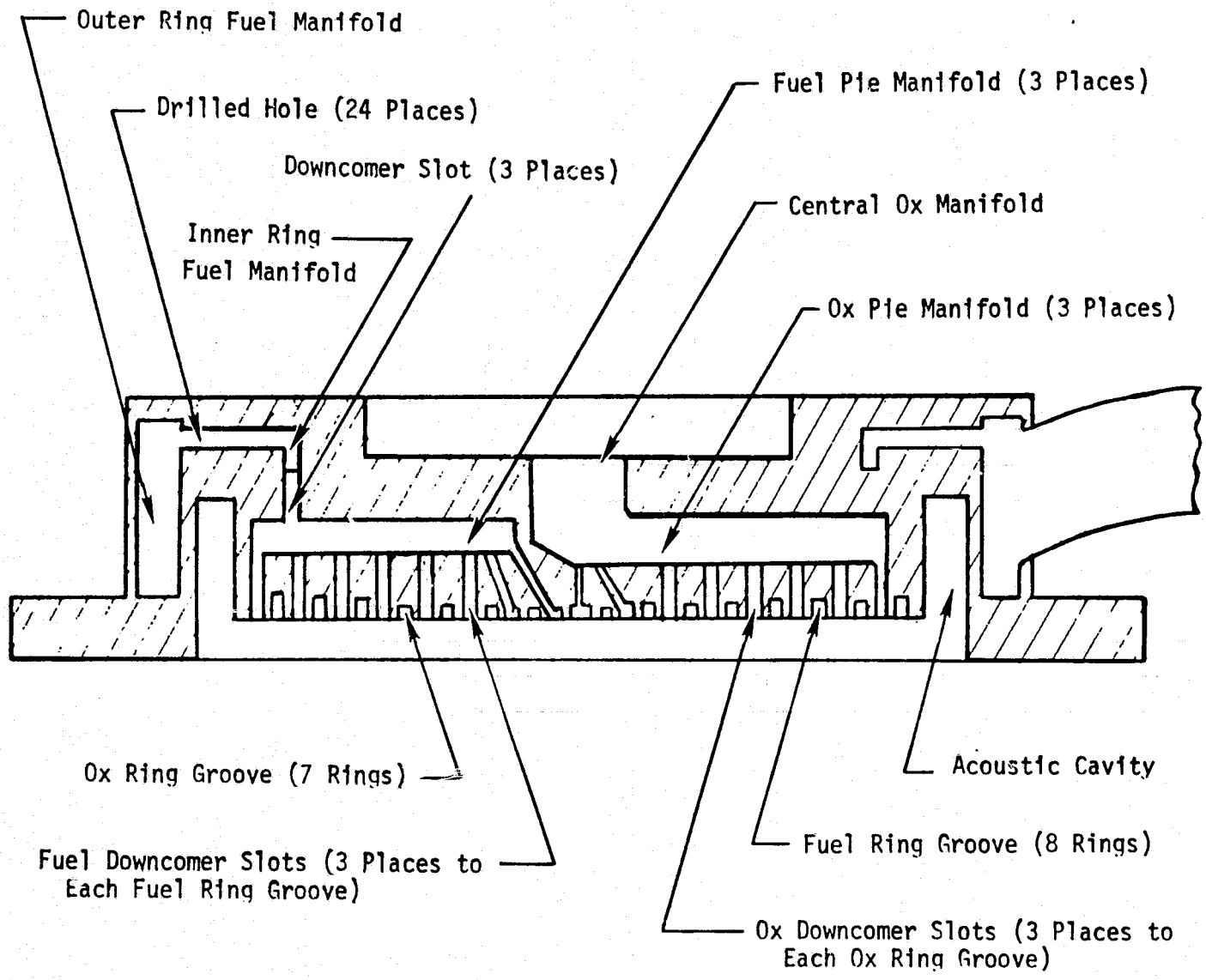

Figure 15. Cross-section of Aerojet OME Technology Injector

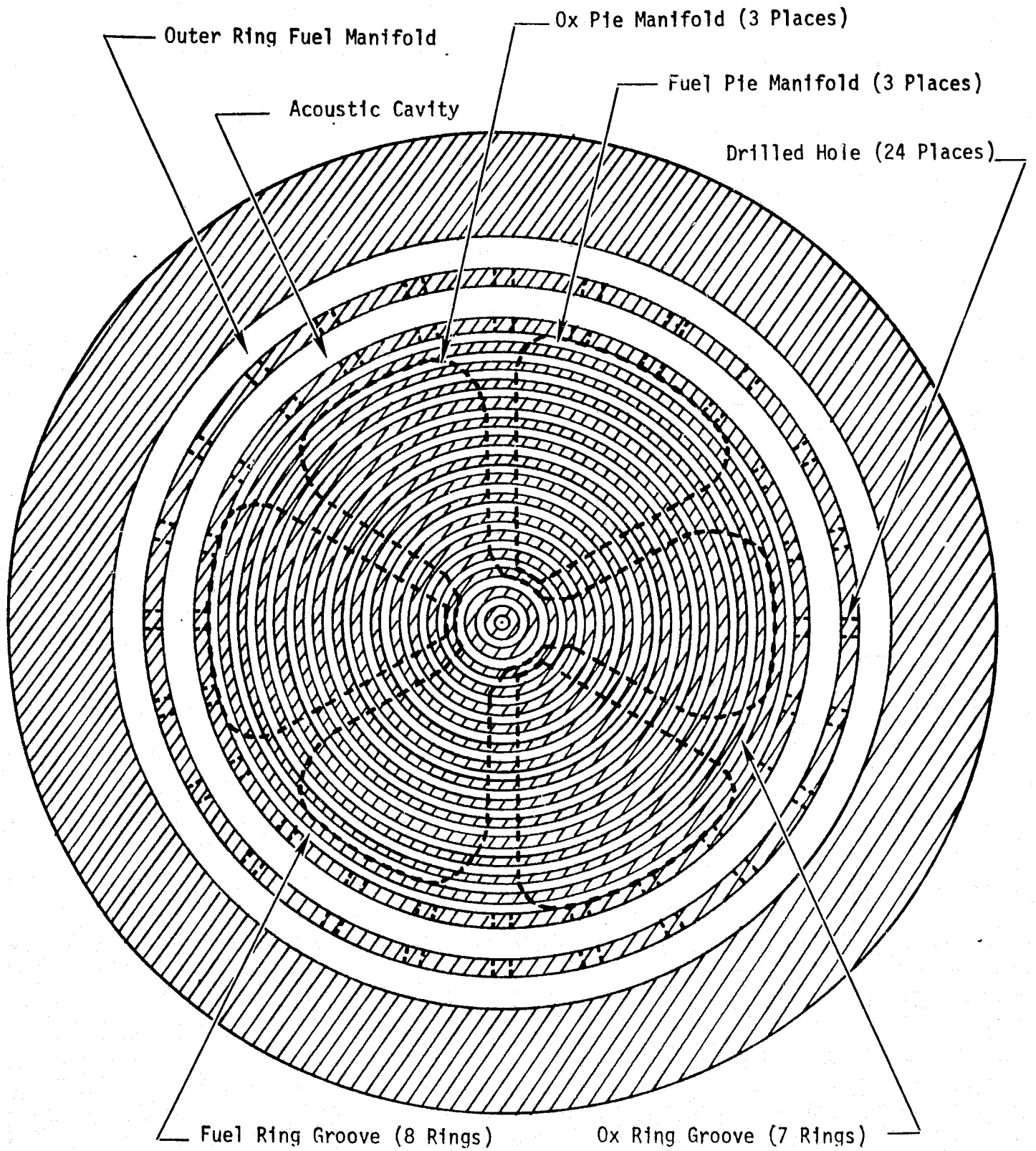

Figure 16. Bottom View of Aerojet OME Technology Injector

injector face is fed by a total of 15 ring grooves (8 fuel and 7 ox) as shown in Fig. 16. An outer ring circumferential fuel manifold feeds an inner ring fuel manifold through 24 drilled holes. Fuel flows from the inner fuel ring through three downcomer slots to three pie-shaped manifolds. Downcomer slots from the pie manifolds feed each fuel ring. The oxidizer is fed through a central manifold to three pie-shaped manifolds. As in the case of the fuel, downcomer slots from the ox pie manifold feed each ox ring.

The detail injector drawings show that injectors are, in general, comprised of constituent modules which may include (1) inlets, (2) domes, (3) torus or ring manifolds, (4) downcomers (holes or slots), (5) pie manifolds, (6) ring grooves, and (7) orifices. A myriad variety of geometric variations can exit for all of the constituent modules. Domes, for instance, may have either single or multiple inlets and often consist of a complex geometric shape with usually multiple outlets. A torus may also have either single or multiple inlets and outlets. Its geometry may be uniform but is often variable so as to result in constant velocity flow throughout the torus. Downcomers may consist of drilled cylindrical holes or slots. They may be directed radially, axially, or have both radial and axial components. Ring grooves may have either single or multiple inlets and always have multiple outlets (orifices). Their geometry may be either constant or variable (if constant velocity is desired in the ring groove). In addition, dams may be located in some or all of the ring grooves at particular angular locations. The number and size of the injection orifices can vary widely. The orifices themselves can compromise many distinctive types of injection elements.

It was of the utmost importance that the injector modeling technique selected for use in the model development task be sufficiently simple and flexible so that an injector model could be developed which is both general and yet capable of analyzing extremely complex injector geometries.

Advantages/Disadvantages of Various Techniques

Three injector modeling techniques (lumped parameter, continuous parameter, and multi-dimensional wave solution using Green's functions) were evaluated for possible utilization in the generalized injector model to be developed

in this program. While the three techniques utilize different approximations and methods of solution, the basic governing equations for each of these techniques is identical. This is shown in detail in Appendix A.

The advantages and disadvantages of the afore-mentioned injector modeling techniques which were initially apparent are summarized below.

Lumped Parameter Technique

- Advantages
  - State-of-the-art
  - Simplicity
  - Extensive previous usage
- Disadvantages
  - Core storage
  - Computer time
  - Potential limitation on injectors which can be described adequately with core storage limits
  - Potential accuracy due to possible description limitation

Continuous Parameter Technique

- Advantages
  - Previous usage
  - Potential gain in core storage and computer time accuracy
- Disadvantages
  - State-of-the-art does not exist for application to line segment which includes mass gains or losses along its length (i.e., a ring groove segment feeding injection orifices).

Multi-Dimensional Wave Solution (Green's Function)

- Advantages
  - Inherent high frequency capability
  - Computer core storage
- Disadvantages
  - Difficulty in handling complex boundaries
  - Difficulty in handling intermediate flow junctions
  - Mathematical instability of solution

Irrespective of the technique selected, the most appropriate output from the injector model should be gain and phase as a function of frequency relating injector flowrate as a function of the chamber pressure perturbation. Flow and pressure distribution throughout the injector is thus determined. In order to obtain the model output in this form, the governing injector model equations are linearized and subsequently arranged in matrix form. The coefficient matrix and input matrix serve as input data to the frequency response program, which then yields the required injector frequency response (see schematic representation below).

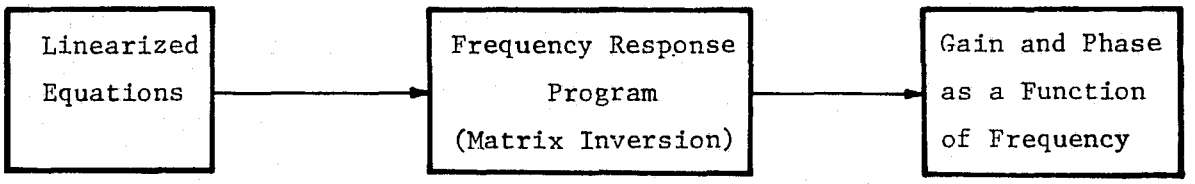

This approach was selected after careful consideration for use in the OME feed-system model (Ref. 1).*

Use of the frequency response program is cost effective since time transients are not included. Thus, a "steady-state" oscillatory determination of pressure and flowrate is obtained. The frequency response method is thus generally preferred over more lengthy (and costly) solutions in the time domain (Ref. 10).

Lumped Parameter Technique

The ability of the lumped parameter technique to adequately describe the complex injectors of interest within core storage and computation time limitations was deemed an item of urgent concern.

As stated earlier, the advantages of the lumped parameter description are that the technique is simple, flexible, and has extensive previous usage in analyzing the complex injector flow patterns. The disadvantages are the tendency to require larger core storage and computer time in order to have the injector adequately described. A promising technique was investigated

* Further, the statement of work called for an injector model whose structure and format is compatible with this existing generalized OME feed-system model.

to eliminate these disadvantages. An explanation of how the contemplated method would be used on a typical ring groove (Fig. 17) is discussed below.

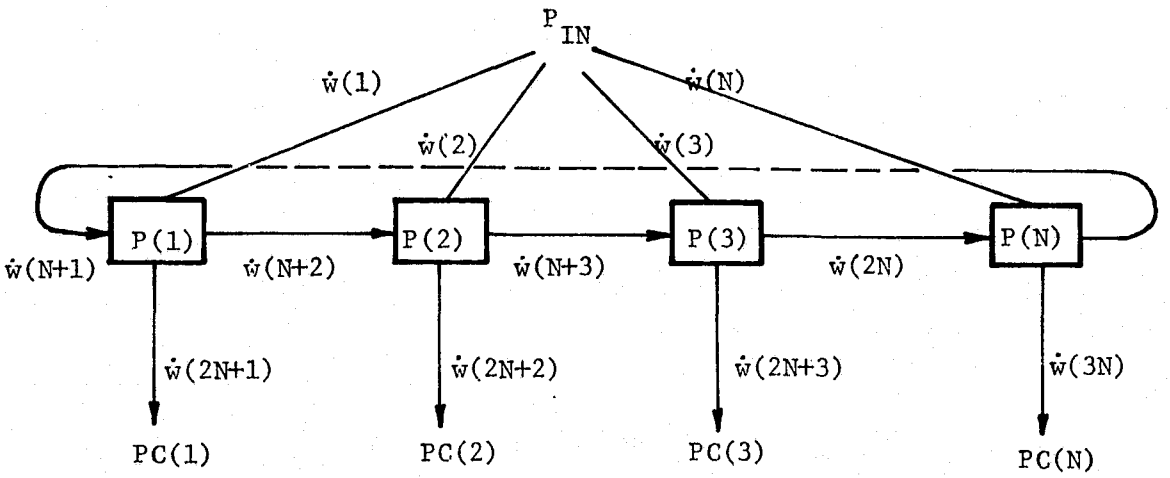

Figure 17. Typical Ring Groove for Evaluating Method

As shown in Fig. 17 , for a ring groove with N pressure nodes, N pressure equations and 3N flow equations are required. Therefore, for 12 pressure nodes, 48 equations are required. Since each variable and the input require a real and imaginary term, the matrix set up in the frequency response program would have to be a 48 by 98 matrix. For a complex injector with several ring grooves, the size of the matrix computer time for inversion would become very large. The method under evaluation involves the elimination of all the flows from the set of equations by substitution. As an example, the equations for $\tilde{P}(2)$ are:

$$S\tilde{P}(2) = \frac{a^2}{Vg_c}\left[\tilde{\dot{w}}(2) + \tilde{\dot{w}}(N+2) - \tilde{\dot{w}}(N+3) - \tilde{\dot{w}}(2N+2)\right]$$

where

$$S = d/dt$$

$$I(2)\ S\ \tilde{\dot{w}}(2) = \tilde{P}_{IN} - \tilde{P}(2) - R(2)\ \tilde{\dot{w}}(2)$$

$$I(N+2)\ S\ \tilde{\dot{w}}(N+2) = \tilde{P}(1) - \tilde{P}(2) - R(N+2)\ \tilde{\dot{w}}(N+2)$$

$$I(N+3)\ S\ \tilde{\dot{w}}(N+3) = \tilde{P}(2) - \tilde{P}(3) - R(N+3)\ \tilde{\dot{w}}(N+3)$$

$$I(2N+2)\ S\ \tilde{\dot{w}}(2N+2) = \tilde{P}(2) - \tilde{PC}(2) - R(2N+2)\ \tilde{\dot{w}}(2N+2)$$

where $I = \dfrac{L}{Ag_c}$

Each flow equation can be solved in the form

$$\tilde{\dot{w}}(2) = \frac{\tilde{P}_{IN} - \tilde{P}(2)}{R(2) + I(2)\ S}$$

The flow equations can then be substituted into the pressure equation to give:

$$S\ \tilde{P}(2) = \frac{a^2}{Vg_c}\left[\frac{\tilde{P}_{IN} - \tilde{P}(2)}{R(2) + I(2)\ S} + \frac{\tilde{P}(1) - \tilde{P}(2)}{R(N+2) + I(N+2)\ S} - \frac{\tilde{P}(2) - \tilde{P}(3)}{R(N+3) + I(N+3)\ S} - \frac{\tilde{P}(2) - \tilde{PC}(2)}{R(2N+2) + I(2N+2)\ S}\right]$$

By multiplying each term on the right hand side by R - IS, and substituting $j\omega$ for S, the equations will contain only pressure variables and be in the correct form for the frequency response technique. Thus, a system with 12 pressure nodes would be only 12 equations and the required matrix size would only be 12 by 26. This means that four times as many pressure nodes can be selected and require the same amount of computer time as the frequency response would require before substitution. It has been determined (by the comparison of results using single precision and double precision that single precision gives answers almost identical to those obtained using double precision, therefore, double precision is not required.

The above solution technique significantly reduces the core storage requirement for the lumped parameter technique. Thus, more pressure nodes can be selected (and the injector consequently more accurately described) without increasing computation time. While this improvement does much to eliminate

the lumped parameter technique disadvantages of a larger core storage requirement and increased computer time, it was felt absolutely necessary to demonstrate that a "typical" injector could indeed accurately be described by about 100 pressure nodes.*

Of the injector configurations presented in Figs. 7 through 16 , the Aerojet OME technology injector is believed to be the one that will require the largest number of pressure nodes to accurately define the system because of the large number of annular manifolds and ring grooves. A schematic of the lumped parameter distribution for the fuel side of the Aerojet OME injector is shown in Fig. 18 . The means in which the constituent modules are divided into pressure lumps (or nodes) is shown in Fig. 19.** Each box in Fig. 18 represents a pressure node and each line between pressure nodes represents a flowrate. This lumped parameter model thus represents all the constituent injector modules including the outer and inner manifold rings, the pie manifolds, the ring grooves, all the flow passages between the manifolds and ring grooves, and chamber pressures. This lumped parameter distribution has 99 individual pressure nodes and 223 individual flowrates. A frequency response model of this size will easily fit on the IBM or Univac computer.

The determination of this system of pressures and flowrates was based on the use of eight elements (nodes) per wavelength. At a frequency of 3000 Hz, each pressure node thus has a length equal to or less than approximately 2.25 inches. This criteria, while definitely adequate for accuracy (as shown later), may not be necessary. A discussion of the analysis of the results of using different numbers of lumps on a single ring groove is presented later in this section of the report.

In order to run the generalized injector computer model, a number of inputs need to be specified. The lumped parameter distribution which accurately

*It is believed that the core storage requirement on the Univac computer should allow at least 140 pressure nodes.

**The inner ring manifold is displaced from its actual location in Fig. 19 for clarity of understanding.

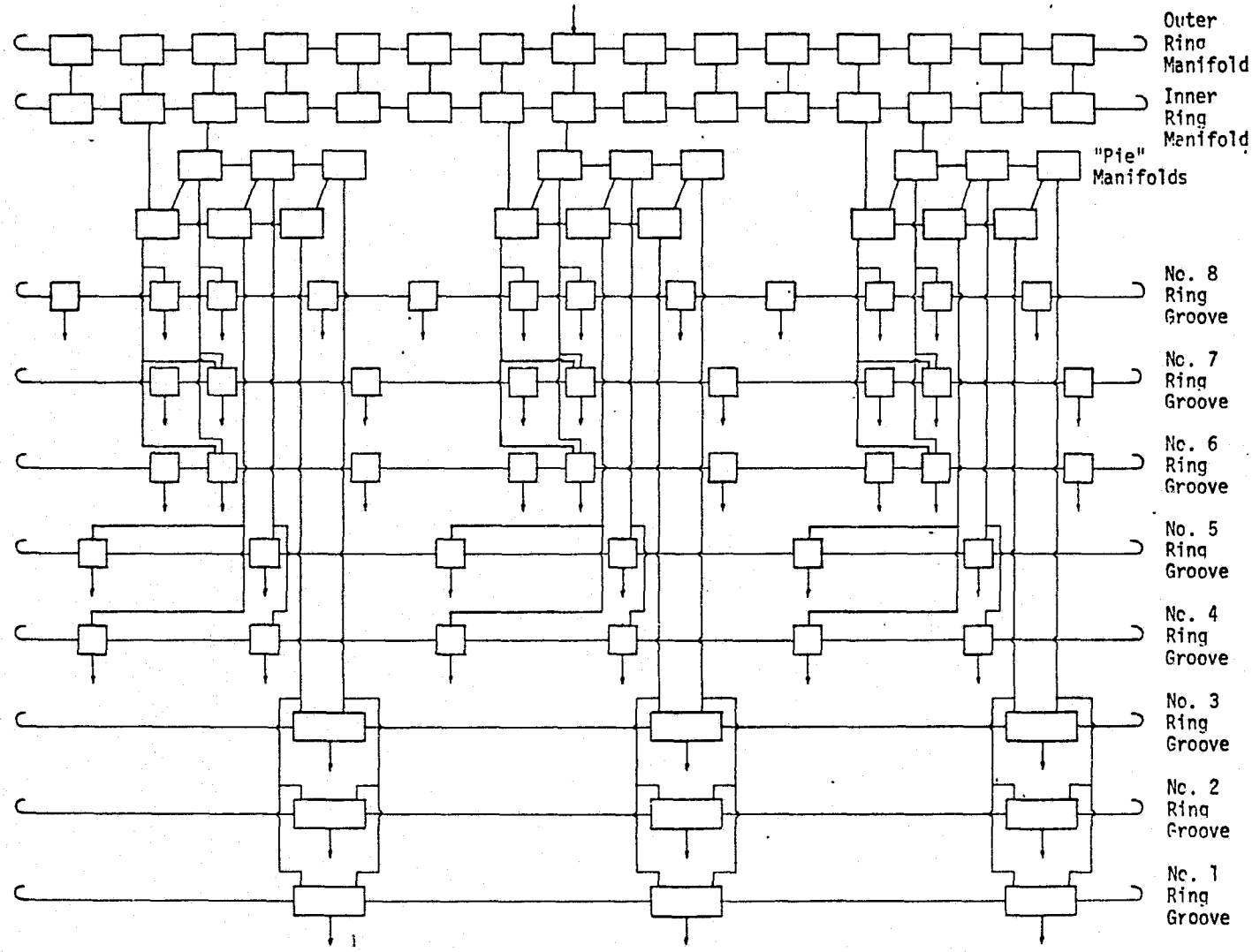

Figure 18. Lumped Parameter Representation of Fuel Side of Aerojet OME Technology Injector Showing Flows Between Pressure Nodes

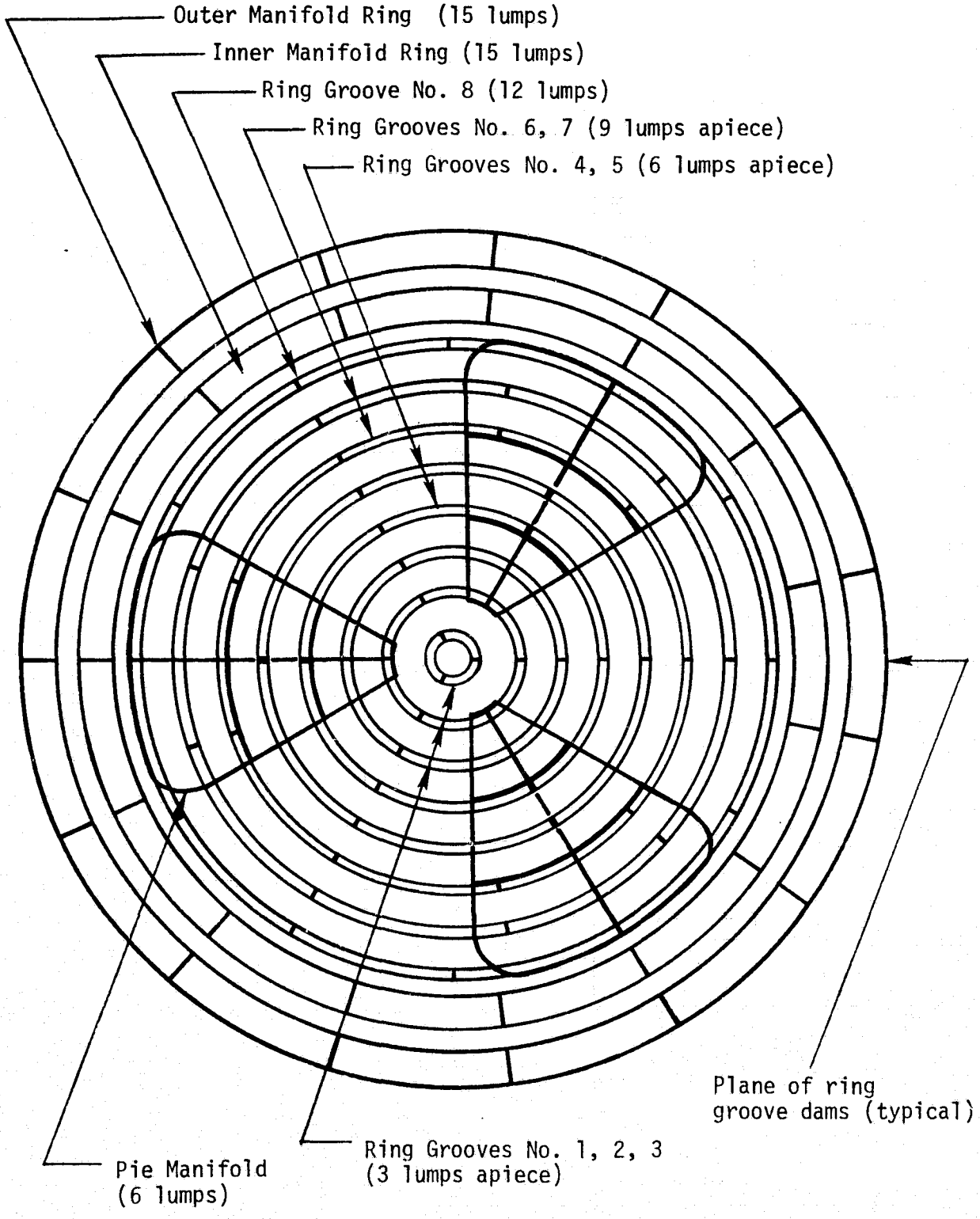

Figure 19. Distribution of Lumps for Fuel Side of Aerojet OME Technology Injector

describes the system (like Fig. 18) must be selected. Several options are available for generating the system of equations required to utilize the frequency response program. The system of equations consists of a pressure equation for each node and a flow equation for each flow between pressure nodes. Each linearized equation for pressure can be written (using Eq. (2a) as its source) as:

$$\tilde{P} = \frac{a^2}{S\,Vg_c} \left(\Sigma\, \tilde{\dot{w}}_{in} - \Sigma\, \tilde{\dot{w}}_{out}\right)$$

$\tilde{P}$ = peak-to-peak oscillatory pressure, psia,

$\tilde{\dot{w}}_{in}$ = oscillatory flow into element - lb/sec

$\tilde{\dot{w}}_{out}$ = oscillatory flow out of element - lb/sec

S = Laplace operator

V = fluid volume in pressure node - $in.^3$

g_c = 386 lb_m $in./lb_f$ sec^2

$\frac{Vg_c}{a^2}$ = capacitance of fluid element

Each linearized equation for flow can be written (using Eq.(3a) as its source) as:

$$w = \frac{Ag_c}{SL} \left(\tilde{P}_u - \tilde{P}_D - R\tilde{w}\right)$$

where

$\tilde{w}$ = peak-to-peak oscillatory flow - lb/sec

L = length of flow element - in.

S = Laplace operator

A = flow cross-sectional area - $in.^2$

g_c = 386 lb_m $in./lb_f$ sec^2

$\tilde{P}_u$ = peak-to-peak oscillatory upstream pressure, psia

$\tilde{P}_D$ = peak-to-peak oscillatory downstream pressure, psia

R = linearized flow resistance = $2\,\Delta\bar{P}/\bar{\dot{w}}$, $sec/in.^2$

L/Ag_c = fluid inertance, $lb_f\ sec^2/lb_m\ in.^2$

For these equations, the inputs consist of effective fluid acoustic velocity, volume of each pressure, node, fluid inertance and linearized resistance for each flow equation. In addition, the logic for coupling all the flow and pressure equations together with each chamber or upstream pressure input is required. For some typical injectors which fit a specific lumped parameter configuration, the logic for coupling the flows and pressures together may be contained in the program. For any configuration that does not fit a typical set of equations, the coupling must be included as part of the input. The flows entering and leaving each pressure node must be directionally specified as well as which flows terminate into each of the different input chamber pressures. As an example, take one of the ring groove pressure nodes that might have a flow distribution as follows:

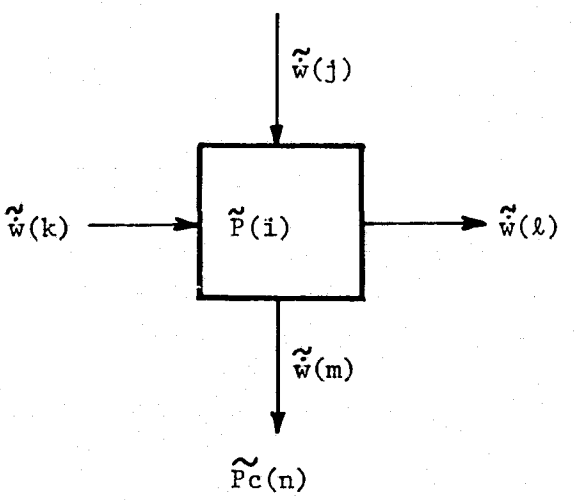

For this pressure node, the inputs would be the number of flows entering or leaving the pressure node (four in this case), and the subscript of each flow (+k and +j for flows entering and -ℓ and -m for flows leaving). In addition, the subscript of each flow terminating in each chamber pressure input must be specified. The amplitude and phase (0 or 180 degrees) of all the input pressures must be input referenced to one specific location. From this data, in addition to the inertias, resistances, and capacitances, the computer program could set up the equations, do the matrix manipulation, and print the output results.

The output of the model is gain and phase of each dependent variable (all the individual pressures and flowrates) with respect to the referenced inlet pressure. This provides the user with the complete flow and pressure distribution throughout the injector.

The lumped parameter technique could be solved in either the time or the frequency domain. The advantage of the time domain is that nonlinearities can be included. However, there are several disadvantages of the time domain. These include:

1. Computer time required
2. Insuring convergence of solution technique
3. Determination of when results have reached a constant oscillatory amplitude.

To calculate the injector operation in the time domain, all the equations are written, and the input amplitude and frequency are specified. Then the injector computer model is allowed to run for as many cycles as required to allow all the variables to reach a repeatable (constant) oscillatory amplitude and phase relationship. For a complex model, very small integration time intervals are generally required to keep the system of equations digitally stable. The net result is usually a large expenditure for computer time. This large cost is one of the main reasons that the frequency response technique was originally developed. Another reason is that the frequency

response solves the equations directly with no iteration or step type calculations required. Therefore, for linear systems analysis, the frequency response technique should be used.

The lumped parameter technique, using a frequency response method of solution, was used to analyze a typical ring groove as described in Fig. 17 . This method of solution (described earlier) was verified by comparison to a standard frequency response method* and then used to evaluate the effect of various number of pressure nodes in the ring groove. The ring groove analyzed had a total length of about 30 inches. Based on the criteria of eight elements per wavelength, this system could be accurately described by about 14 pressure nodes. The input chamber pressure profile corresponded to a chamber first tangential mode. Table I shows a comparison of the response of the ring groove

TABLE I

GAIN OF RING GROOVE PRESSURE TO CHAMBER REFERENCE PRESSURE

Frequency / Number of Lumps	0 Hz	2500 Hz	8000 Hz
6	0.0869	1.382	0.1977
12	0.08304	1.35	0.1984
24	0.08209	1.341	0.1986
48	0.08185	1.3394	0.1986
96	0.08183	1.3392	0.1986

*The standard frequency response method solves the full set of pressures and flowrate equations without doing any manipulation to eliminate variables. This method has extensive use and verification at Rocketdyne. The method of eliminating variables prior to the matrix inversion reduces the computer time and storage requirements. The test case run was compared to the standard frequency response to verify that the accuracy of the matrix solution process was not affected by the alteration of the equations.

pressure directly above the reference pressure for various numbers of pressure nodes selected. (Naturally, at zero frequency it would not be possible to have a first tangential chamber mode, but results are included for comparison purposes.) These results show that even using only six lumps gives results that are within 6.2% of the actual frequency response* at zero Hz, 3.1% at 2500 Hz, and only 0.5% at 8000 Hz. Two significant conclusions may be drawn from these results. First, the use of the crtieria of eight lumps per wavelength will definitely provide good results since any frequency response within 6% is generally satisfactory. Second, the technique gives accurate results for frequencies higher than 3000 Hz as long as the first tangential mode is being considered. This is probably due to (1) a reduced amount of response in the feed system at higher frequencies, or (2) a reduction of the distance into the feed system into which the input can propagate at higher frequency. It may be concluded that this lumped parameter frequency response technique is not limited to 3000 Hz, but may be accurately applied to higher frequencies as well.

Continuous Parameter and Multi-Dimensional Wave Solution Techniques

The continuous parameter and multi-dimensional wave solution (Green's function) techniques initially appeared attractive because the division of the injector into a nodal network (as is used in the lumped parameter technique) is not required. (The injector still may be divided into flow segments but the further division of these flow segments into nodes or lumps is unnecessary.) This possesses a potential advantage in terms of core storage and computation time. The extremely complex and nonuniform boundaries existing between the constituent modules of a "typical" injector present, perhaps, an even greater obstacle.

Examination of the continuous parameter technique led to the conclusion that the state of the art at this time does not exist for the application of this technique to line segments which allow for mass gains and/or losses along its length (i.e., a ring groove segment feeding injection orifices). An attempt was made to modify the continuous parameter technique such that it would be capable of describing flow segments having mass loss or gain.

---

* The actual frequency response is assumed to be that obtained using 96 lumps.

The conservative equations of mass and momentum were written for cylindrical control volume (considered to represent one line segment in a ring groove). While partial differential equations were developed and appropriate initial and boundary conditions established for describing flow segments having mass gain and/or loss with the continuous parameter technique, the resulting system of equations were not adapted to a frequency response type of solution. The progress made, therefore, was not sufficient to bring the continuous parameter technique to the point where a "side-by-side" computer comparison with the lumped parameter model could be made.

For feed lines to the ring grooves, waterhammer (continuous parameter) equations could be used, if this would be of value, even if the ring grooves were described by a finite difference network. The current Rocketdyne frequency response program (used in the hydrodynamics section of the OME Feed System Coupled Stability Investigation, NAS9-14315 (Ref. 1)) routinely handles combinations of waterhammer equations and finite difference equations. However, for "typical" injector designs such feed lines are usually short enough (less than 1/8 wavelength) to not require this type of presentation. Indeed, the combination of the continuous parameter and lumped parameter techniques to describe a single injector may increase the amount the core storage required.

The possible application of the Green's function technique to this program was discussed with Dr. Carl Oberg (who was responsible for all previous application of this technique at Rocketdyne). It was agreed that, based on current knowledge, the application of this technique to the injector model possesses little likelihood of success within a reasonable amount of time and dollars.

Finally, the three candidate modeling techniques were evaluated against a number of criteria as shown in Table II. This evaluation was done (for each technique) in respect to a "typical" injector configuration whose characteristics have been discussed earlier in this report.

TABLE II. EVALUATION OF CANDIDATE TECHNIQUES

CRITERIA \ TECHNIQUE	LUMPED PARAMETER	CONTINUOUS PARAMETER	GREEN'S FUNCTIONS
State-of-art	Within state-of-art	Not within state-of-art	Not within state-of-art
Previous Usage	Extensive	Limited	None
Accuracy	Sufficient	Sufficient	Sufficient
Complexity	Complex	More complex	Most complex
Computer storage	Acceptable storage required	Acceptable storage required	Least storage required
Computation time	Acceptable (1 min.)	Acceptable	Longer
Type of input	Physical geometric parameters	Physical geometric parameters	Physical geometric parameters
Ease of input	Laborious	Laborious	Impractical
Type/usability of output	Numeric/good	Numeric/good	Numeric/good
Number & obtainability of characterization parameters	Gain and phase/ adequate	Gain and phase/ adequate	Gain and phase/ adequate
Numerical stability of solutions	Not a factor	Not a factor	Definite problem
Applicability to digital solutions	Good	Good	Good
Limitations	Detail of input specification	Detail of input specification	Detail of input specification

SELECTION OF MODEL TECHNIQUE

In evaluating how the various candidate techniques could be applied to "typical" injector configurations (see Table II), it becomes apparent that the flexibility and versatility of the lumped parameter technique offers a great advantage.

This technique is extremely well suited to adequately describing even the most complicated injector configurations. Injectors having a lack of symmetry do not present a problem. The presence of ring groove or manifold dams can easily be handled by assigning a very large resistance to the particular flow branch thereby effectively eliminating its presence in the injector system (Ref. 1). Disadvantages previously believed associated with this technique (i.e., core storage, computer time, adequate injector description, high frequency capability) are believed to have been resolved.

In contrast, the other candidate techniques have been shown to require considerable advancement of the state-of-the-art before the feasibility of utilizing these techniques to model a "typical" injector could be satisfactorily determined.

The selection of the lumped parameter technique for utilization in the model development task thus appears to be the only reasonable, cost-conscious choice.

SECTION III

MODEL DEVELOPMENT

A digital computer model of the injector manifolding which describes the coupling of the injector hydraulics with the combustion process was formulated. This model was designed to be compatible with an overall generalized engine system dynamics model, developed by Rocketdyne for NASA/JSC under contract NAS9-14315 (Ref. 1), which includes propellant feed system hydrodynamics, combustion dynamics, and chamber dynamics. Compatibility is derived from the use of the complex matrix solution technique in both models. This technique can use either lumped parameter or continuous (distributed) parameter equations. The two models could be coupled by properly setting up the complex matrix with no changes in the equation types from either model. The generalized engine system dynamics model uses a single lump to describe the injector, while the engine hydraulic stability model employs a multi-lump (multi-dimensional) injector description. The engine hydraulic stability model cannot be coupled into the generalized system dynamics model at the present time because the latter model does not employ a multi-dimensional description of the combustor and combustion process.

FORMAT AND STRUCTURE

Generalized criteria which were employed to develop a format and structure for the injector model are as follows:

a. Input and output formats shall be appropriate to allow incorporation of the newly developed injector/manifold model in the generalized system dynamics model developed under contract NAS9-14315.

b. The model shall be structured to quantitatively evaluate the influence of injector design variables and geometry in terms of resistance, capacitance, and inertance on the ability to hydraulically couple with the combustion process.

c. The model shall be capable of analyzing a single portion of the injector, such as an orifice, propellant channel, downcomer, etc., independent of the remainder of the injector as well as be capable of analyzing the entire injector.

d. As a minimum the model shall accept an input pressure profile from either the chamber or the injector inlet. Profiles selected are as follows: For the inlet, a uniform pressure at any frequency for 100 to 3000 Hz. for the chamber, either a uniform profile or an acoustic profile corresponding to a particular chamber mode with nodal diameter orientation and frequency ranging from 100 to 3000 Hz.

e. The model output shall include a single-value gain to simplify model utilization and interpretation.

f. The model shall be formulated as simply as possible consistent with the quantitative sensitivity and shall require a minimum of engineering judgement factors.

The engine hydraulic stability computer model uses a frequency response program to solve a matrix of simultaneous linear equations. Since this is the same basic program used in the generalized engine system dynamics model, developed under contract NAS9-14315, the input and output formats would allow incorporation of this model into the generalized model.

As an example of showing how the model format and structure is developed, consider the fuel side of the Aerojet OME technology injector as described in Section II. Each of the pressure nodes, flow paths, and input pressures are numbered sequentially as shown in Fig. 20. This system has 99 dependent pressure variables (denoted by rectangles), 52 input pressures (circles) and 223 flowrates (arrows).

This feed system description provides the format for the introduction of the input parameters and solution technique. The following discussions show how the input parameters to the model are determined and how they are fed as input into the model.

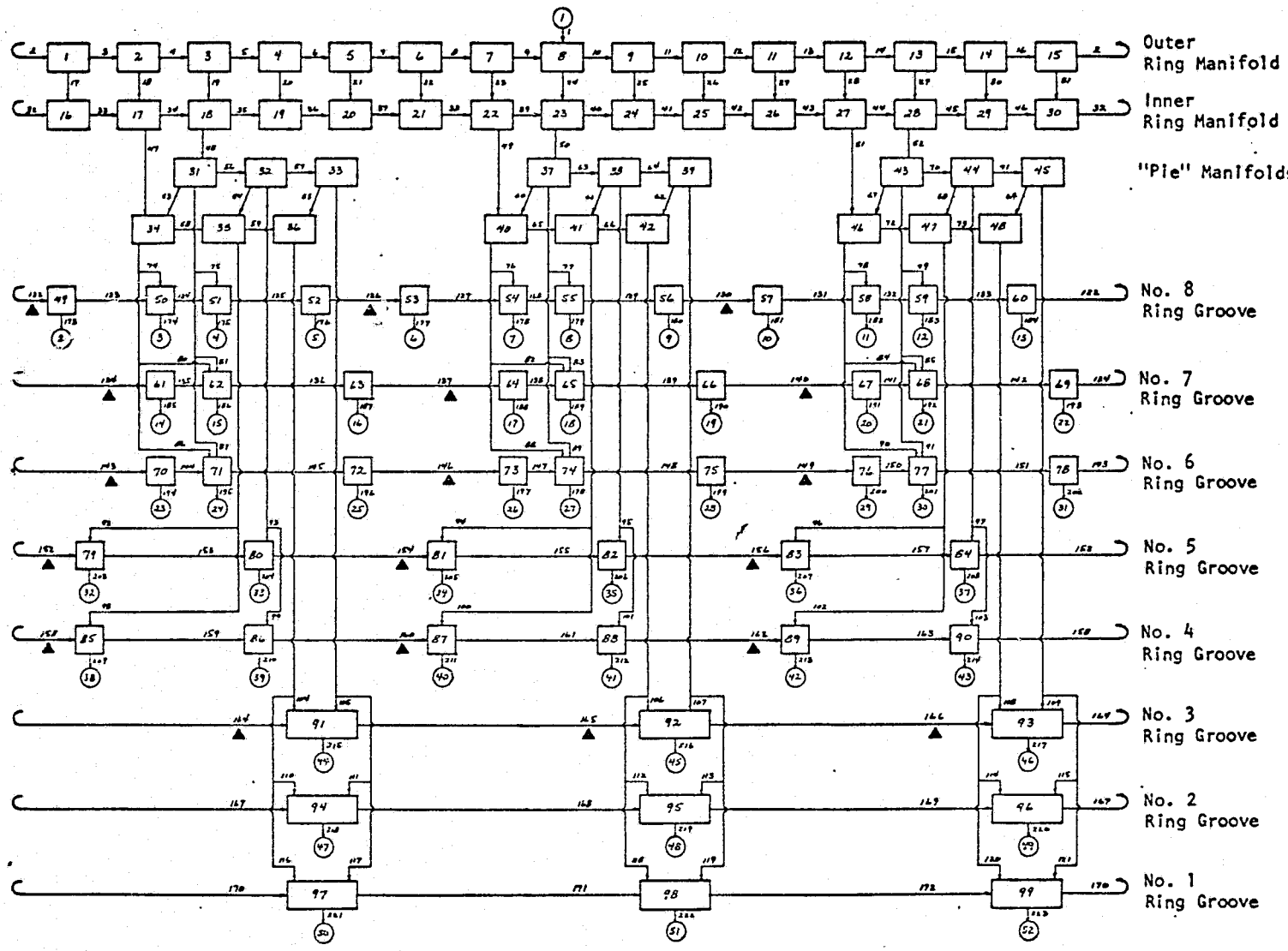

Figure 20. Lumped Parameter Representation of Fuel Side of Aerojet OME Technology Injector Showing Flows Between Pressure Nodes

MECHANIZATION OF DETAILS

As discussed previously, an injector is described in terms of which flow segments enter and leave each pressure node. For each flow segment, a resistance and an inertance are required as model inputs (line lengths and areas are used in determining inertance). For each pressure node, volume and acoustic velocity are required as model inputs (volume and acoustic velocity determine capacitance). The following paragraphs describe the methods used to calculate specific values for these model inputs.

The model input parameters which need to be determined when using the lumped parameter technique are capacitances, inertances, resistances, and input pressures (amplitude and phase). The criteria for calculating these model input parameters are given in the following discussion.

Capacitance

The fluid capacitance term is developed in Section II and given by Eq. (2b) as

$$C_i \equiv \frac{V_i \, g_c}{a^2} \tag{2b}$$

where C_i is the capacitance of the i^{th} pressure

V_i is the volume of the i^{th} pressure node

g_c is a units conversion factor between mass and force when engineering units are used (386 in-lbm/lbf-sec^2)

a is the acoustic velocity of the hydraulic fluid

In calculating the volume of a pressure node, its volume must also include half the volume of each flow segment connected to that particular pressure node. Thus, the summation of all nodal volumes must equal the total volume of the injector.

Inertance

The fluid inertance term is also developed in Section II and given by Eq. (3b). However, when flow segments of multiple cross-sectional areas are used Eq. (3b) must be changed to

$$I_i = \frac{1}{g_c} \left[\sum_{j=1}^{n} \frac{L_j}{A_j} \right]_i \tag{17}$$

where I_i is the inertance of the i^{th} flow segment

L_j is the length of the j^{th} flow passage within the i^{th} flow segment

A_j = cross-sectional area of the j^{th} flow passage within the i^{th} flow segment.

The inertance equation shown above takes into account that each flow segment may be composed of line lengths which have different cross-sectional areas. The overall length of one flow segment is determined by the actual distance between one pressure node center and another where the flow can be entirely characterized as one-dimensional.

Resistance

The linearized flow resistance is developed in Section II and given by Eq. (3c) as

$$R_{L_i} = \frac{2|\Delta\bar{P}_i|}{|\bar{w}_i|}$$

Where

R_{L_i} is the linearized flow resistance of the i^{th} flow segment based on time-averaged steady-state values

$\Delta\bar{P}_i$ is the time averaged steady-state pressure drop across the i^{th} flow segment

$\bar{\dot{w}}_i$ is the time-averaged mass flowrate through the i^{th} flow segment

If pressure drop and flowrate data were known for each flow segment, calculation of the linearized flow resistances, R_{L_i}'s becomes an easy task. However, when such data is not known the time averaged steady-state values of ΔP_i and $\dot{w}_i$ must be calculated analytically. The procedure used for analytically finding the pressure drops and flowrates is discussed below.

$$\Delta \bar{P}_i = \left\{ \left[K_f + \sum_{m=1}^{n} K_{t_m} \right] \frac{\bar{\rho}\,\bar{v}^2}{2\,g_c} \right\}_i \tag{18}$$

where

K_f is the pipe friction head losses (4f L/D)

K_t is the minor friction head losses due to entrance, exit, elbows, orifices, etc., within the line flow segment

$\bar{v}$ is the time-averaged steady-state fluid velocity within the i^{th} flow segment

It should be noted here that if the i^{th} flow segment consists of various cross-sectional areas all head losses must be referenced to the flow through one part of the flow segment. For example, consider Fig. 21 below which consists of a flow segment with line lengths of cross-section A_1, A_2, ... A_j respectively, and velocities, v_1, v_2, ... v_j respectively.

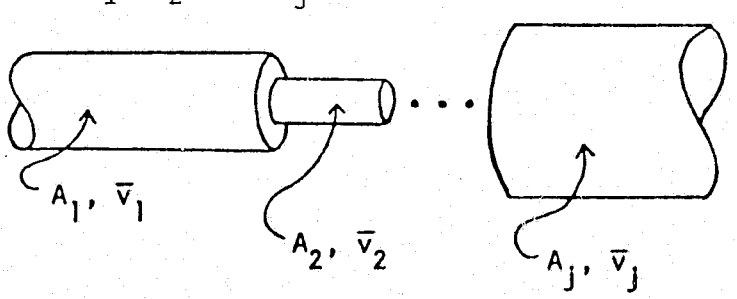

Figure 21. The i^{th} Flow Segment

Some of the K's will be referenced to line 1, others to line 2, and still others to line j. Therefore, $\Delta\bar{P}_i$ is written as

$$\Delta\bar{P}_i = \frac{\bar{\rho}}{2\,g_c}\left[(K_f + \Sigma K_{t_m})_1\ \bar{v}_1^{\,2} + (K_f + \Sigma K_{t_m})_2\ \bar{v}_2^{\,2} + \ldots + (K_f + \Sigma K_{t_m})_j\ \bar{v}_j^{\,2}\right]_i \tag{19}$$

However, using continuity, it is known that

$$\bar{\dot{w}}_i = (\bar{\rho}\,A_1\,\bar{v}_1)_i = (\bar{\rho}\,A_2\,\bar{v}_2)_i = (\bar{\rho}\,A_j\,\bar{v}_j)_i \tag{20}$$

Referencing all head losses to lire j by substituting Eq. (20) into Eq. (19) yields

$$\Delta\bar{P}_i = R_i\,\bar{\dot{w}}_i^{\,2} \tag{21a}$$

where

$$R_i = \frac{(K_f + \Sigma K_{t_m})_1\ \frac{A_j^{\,2}}{A_1^{\,2}} + (K_f + \Sigma K_{t_m})_2\ \frac{A_j^{\,2}}{A_2^{\,2}} + \ldots + (K_f + \Sigma K_{t_m})_j}{2\bar{\rho}\,A_j^{\,2}\,g_c} \tag{21b}$$

Any injector can be described by its R_i's regardless of total pressure drops and flowrates, since R_i is determined by geometry only. Therefore if an injectors R_i's can be combined and reduced to one overall injector resistance, R_T, then Eq. (21a) shows that total injector pressure drop, $\Delta\bar{P}_T$, can be determined directly from total injector mass flow, $\bar{\dot{w}}_T$, by the relation

$$\Delta\bar{P}_T = R_T\,\bar{\dot{w}}_T^{\,2} \tag{22}$$

Usually total injector mass flowrate is known so that once R_T has been found from the individual R_i's, then the total pressure drop can be determined directly. Once $\Delta\bar{P}_T$ has been found from $\bar{\dot{w}}_T$, all individual $\Delta\bar{P}_i$'s and $\bar{\dot{w}}_i$'s can be determined by separating R_T back into its individual components analogous to electric circuit resistance reductions. These circuit reductions for fluid flow have been developed for series and parallel flows and are described below.

First consider i flow segments in series with each other as shown in Fig. 22.

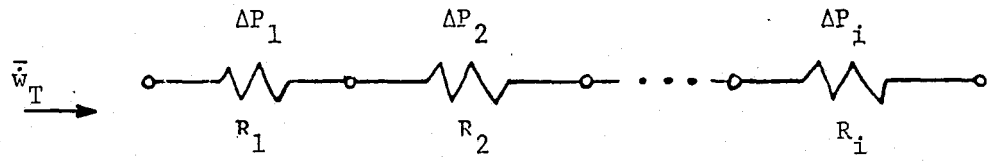

Figure 22. Series Flow

It is known that the total pressure loss through all i flow segments $\Delta\bar{P}_{TS}$, is given by

$$\Delta\bar{P}_{TS} = \Delta\bar{P}_1 + \Delta\bar{P}_2 + \ldots \Delta\bar{P}_i \tag{23}$$

or

$$\Delta\bar{P}_{TS} = R_1 \bar{\dot{w}}_1^2 + R_2 \bar{\dot{w}}_2^2 + \ldots R_i \bar{\dot{w}}_i^2 \tag{24}$$

From continuity it is known that

$$\bar{\dot{w}}_1 = \bar{\dot{w}}_2 = \bar{\dot{w}}_i = \bar{\dot{w}}_{TS} \tag{25}$$

where

$\bar{\dot{w}}_{TS}$ is the total flow through the series flow segments.

Therefore the total pressure loss across the series flow circuit is found from Eqs. (24) and (25)

$$\Delta\bar{P}_{TS} = (R_1 + R_2 + \ldots R_i)\, \bar{\dot{w}}_{TS}^2 \tag{26}$$

Now consider i flow segments in parallel with each other as shown in Fig. 23

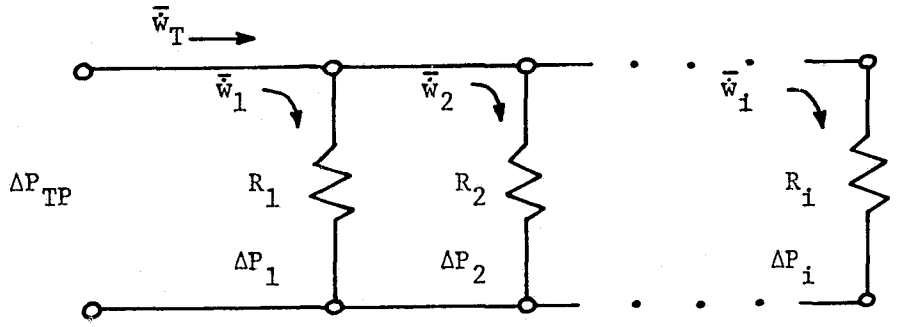

Figure 23. Parallel Flow

It is known that

$$\bar{\dot{w}}_{TP} = \bar{\dot{w}}_1 + \bar{\dot{w}}_2 + \ldots \bar{\dot{w}}_i. \tag{27}$$

Also the pressure drop across each flow segment is equal, thus

$$\Delta\bar{P}_{TP} = \Delta\bar{P}_1 = \Delta\bar{P}_2 = \Delta\bar{P}_i \tag{28}$$

where $\Delta\bar{P}_{TP}$ is the pressure drop across a parallel flow circuit.

Finally, using Eqs. (21a), (27), and (28), it can be shown that for flow segments in parallel,

$$\Delta P_{TP} = \left[\frac{1}{\frac{1}{\sqrt{R_1}} + \frac{1}{\sqrt{R_2}} + \ldots + \frac{1}{\sqrt{R_i}}} \right]^2 \bar{\dot{w}}_{TP}^{\,2} \tag{29}$$

Therefore, if an injector can be reduced to a simple network of flow resistances in series and parallel with one another, then Eqs. (21) - (29) can be used to analytically solve for the $\Delta\bar{P}_i$'s and $\bar{w}_i$'s. This in turn allows for the solution of the R_{L_i}'s which are then inputted into the computer model.

The fuel side of the Aerojet OME technology injector, completely diagrammed in Fig. 20, was reduced to a simple network of series and parallel flows as illustrated in Fig. 24. This network reduction was obtained by assuming negligible pressure drops in flow segments 2-16, 32-46, 53-73, and 122-172 of the OME fuel side manifolding. The network resistances used in Fig. 24 were obtained from Eq. (21b) using typical criteria for the K_f's and K_t's as found in the SAE Aero-space Applied Thermodynamic Manual (Ref. 11). Using the exact geometry of the injector (as reported by Aerojet in Ref. 9), a total injector pressure drop of 54.8 psid was analytically calculated for a fuel mass flowrate through the injector of 7.19 lbm/sec. This compares very well to the 57 psi pressure drop reported by Aerojet.

Input Pressure

For any feed system coupled instability above a frequency of 1000 hz, the combustion chamber response comes either from a combustion chamber resonance or from response of pressure in the cup of a recessed post injector. To analyze the case of a chamber resonant mode with the injector stability model, the relative amplitude and phase of the chamber pressure oscillations across the injector face must be input to the model.

An analytical formulation describing the perturbed flow in the combustion chamber was developed for the types of chamber instability modes commonly experienced during hot firing. This was especially needed in knowing how to input a standing tangential combustion chamber mode as opposed to a spinning tangential mode.

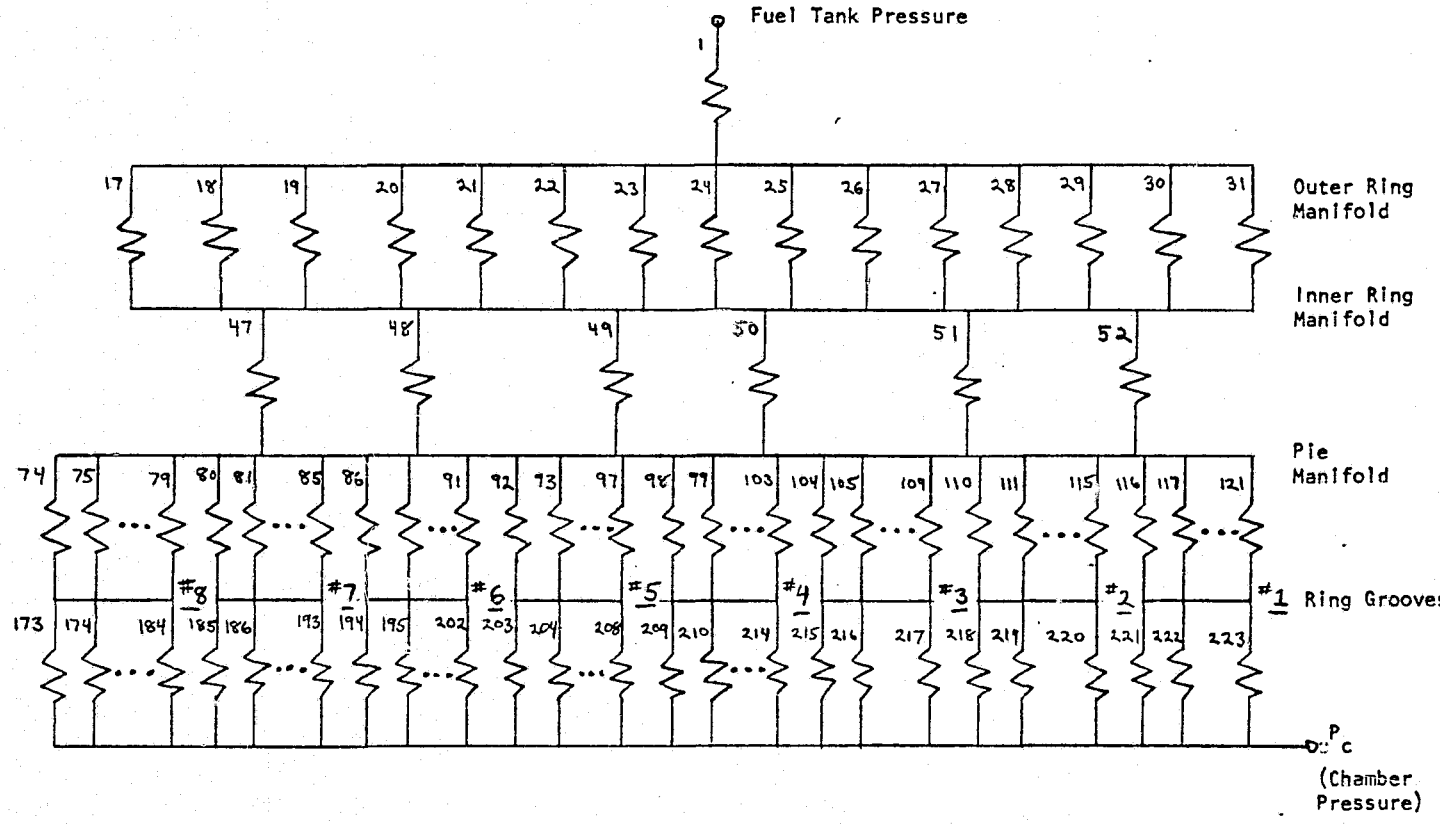

Figure 24. Simplified Resistance Network for Fuel Side of Aerojet OME Technology Injector

This analytical formulation, in the time domain, is shown in Appendix B. However, since the engine hydraulic stability computer model employs a frequency response solution, pressure inputs must be expressed in terms of gains and phases. For tangential pressure modes it is convenient to reference all pressures to the pressure at the combustion chamber location of $r = r_w$, and $\theta = 0$ (where r, r_w, and θ are defined as in Appendix B). The standard procedure in Frequency Response Theory (Ref. 12) is to define a new variable $\beta_{m,n}$ such that

$$\beta_{m,n} \equiv \frac{\mathcal{L}\left\{\tilde{P}_{m,n}\right\}}{\mathcal{L}\left\{\tilde{P}_{m,n}\Big|_{ref}\right\}} \tag{30}$$

where $\tilde{P}_{m,n}\Big|_{ref}$ is the perturbed pressure at $r = r_w$, and $\theta = 0$, and $\mathcal{L}$ is the Laplace transform defined as

$$\mathcal{L}\left\{\tilde{P}_{m,n}\right\} = \int_0^\infty e^{-S_{m,n}\,t}\,\tilde{P}_{m,n}\,dt$$

where t = time

Thus using Eq. (30) above, the time dependency can be removed from Eqs. (B-12) and (B-18) of Appendix B. By replacing "$S_{m,n}$" with "$j\omega_{m,n}$" (where $j = \sqrt{-1}$ and $\omega_{m,n}$ = frequency of oscillation in radians/sec) the frequency input for a standing tangential wave is

$$\beta_{m,n} = \frac{J_m\left(\frac{\omega_{m,n}\,r}{a_c}\right)\cos m\,\theta}{J_m\left(\frac{\omega_{m,n}\,r_w}{a_c}\right)} \tag{31}$$

and for a spinning tangential wave

$$\beta_{m,n} = \frac{J_m\left(\frac{\omega_{m,n}\,r}{a_c}\right)}{J_m\left(\frac{\omega_{m,n}\,r_w}{a_c}\right)}\left[\cos m\,\theta + j \sin m\,\theta\right] \tag{32}$$

where m = 0, 1, 2, 3, ...

n = 1, 2, 3, ...

a_c = sonic speed in chamber

J_m = Bessel function of the first kind order m.

Equations (31) and (32) above then give the needed information for expressing the chamber pressure input in terms of gains and phases. This is because $\beta_{m,n}$ is a complex vector on the $S_{m,n}$-plane. The magnitude of this vector is known as the gain, and the angle it makes with the positive real axis is known as the phase. Graphically this is shown in Fig. 25 below.

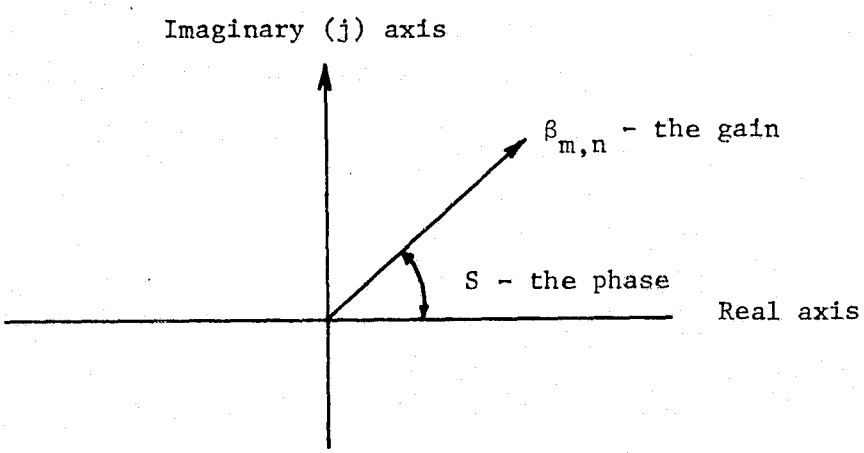

Figure 25. The $S_{m,n}$-plane

From Eq. (31) and Fig. 25 it can be seen that standing waves have only phase shifts of 0 and 180 degrees depending upon whether the expression on the right-hand side of Eq. (31) is positive or negative. On the other hand Eq. (32) shows that spinning waves will have phase shifts over the entire range of 0 to 360 degrees.

Figure B-3 of Appendix B shows the normalized maximum amplitudes for the first and second tangential modes and for the first radial chamber mode as a function of the non-dimensionalized radius. To simplify the input to the model (the fuel side of the injector has 51 separate chamber pressure inputs), curve fits were made for these three modes. The curve fits used are:

1T Mode - standing

$$\text{Amp} = (1.5056\ R + .0641\ R^2 - .5697\ R^3)\ \cos(\theta)$$

1T Mode - spinning

$$\text{Amp} = (1.5056\ R + .0641\ R^2 - .5697\ R^3)$$

2T Mode - standing

$$\text{Amp} = (-.17\ R + 3.583\ R^2 - 2.413\ R^3)\ \cos(2\theta)$$

2T Mode - spinning

$$\text{Amp} = (-.17R + 3.583\ R^2 - 2.413\ R^3)$$

1R Mode -

$$\text{Amp} = 1 + .15R - 4.87\ R^2 + 3.315\ R^3$$

where θ is the selected injector tangential location and R is the normalized radius. The location where $\theta = 0$ is defined as that location where the phase is zero degrees and the amplitude of a tangential input is maximum. The required model inputs to input one of these chamber modes are the radius and angle for the location of each chamber pressure input, and whether the mode is standing or spinning.* The model then calculates the amplitude and phase inputs for the selected chamber pressure mode. The model also has the option for any general input matrix. That is, the programmer can specify the amplitude and phase at each chamber pressure input.

INPUT AND OUTPUT ROUTINES

The input and output formats used in the model are compatible with those employed in the feed system coupled model developed by Rocketdyne for NASA/JSC under contract NAS9-14315 in the event that incorporation of the injector model into the latter model be desired at some later date.

Input routines were written which allowed the selection of either an imposed feed system pressure profile or an imposed chamber pressure profile (either uniform or characteristic of a particular chamber acoustic mode) with an arbitrarily selected attendant oscillation frequency. Output routines consist basically of the determination of flowrate and pressure variations

* A discussion of standing and spinning waves is found in Appendix B.

throughout the injector as a function of frequency for each imposed input pressure profile.

To provide a simple way to evaluate any specific injection configuration, output routines were included which allow printout of various summations of the oscillatory injector flow (for a unit pressure perturbation). These summations include (1) a summation of all the absolute values of injector flowrate, (2) a vector summation of all injector flowrates (attempt to include phase angle), and (3) and (4) the previous two cases except that each injector flow is multiplied by the relative amplitude of the chamber pressure that it feeds before making the summations. These summations are given in both lb/sec/psi and percent chamber pressure.

The first summation simply adds all the gains for all the injector flows. This provides a measure of the total injector flow response with no consideration as to how the flow could couple with the combustion process. The second summation considers the phase relationship between each injector flow and the chamber pressure flow that it feeds. If, for example, two flows that were 180 degrees out of phase both fed chamber pressures that had the same phase, it is unlikely that both flows could cause coupling since one or the other would have the wrong phase relationship. Therefore, the second flow summation was made where the flows were vectorially added. The phase assigned to each flow is based on the difference between the phase of the flow and the phase of the pressure that it was feeding.

Another characteristic that can affect the amount of coupling is the phase of the combustion chamber response. A flow that is feeding a location in the chamber that is a pressure node cannot cause coupling, whereas a flow feeding a pressure anti-node location would have maximum coupling potential. Therefore, the third and fourth summations were made where the amplitudes of each flow was multiplied by the respective chamber pressure amplitudes before

summing the values. All four summations are printed out so that the user can evaluate each of them.*

In addition to printout of the summation of injector flows (both absolute and vector), the ease of interpreting the output of the engine hydraulic stability computer model was also enhanced by an optional graphical display of the amplitudes of ring groove flows, ring groove pressures, injector flows, and chamber pressure inputs around each ring groove.

MODEL CHECKOUT

In order to first model the system the computer program must be told how many dependent and input pressure nodes there are. Also, the program must be told what flows are associated with each pressure node and what pressure nodes are input nodes. This tabular computer input is shown in Fig. C-1 of Appendix C. Flows assumed to enter the node are denoted by a plus sign and each flow assumed to leave a node by a minus sign. Each pressure node can have up to 12 flow terminations (6 entering flows and 6 leaving flows). If the node has less than the maximum number of flow terminations, the additional flows are read in as zero. For pressure node 1, for example, flow 2 enters, and flows 3 and 17 leave.

The model was run for the fuel side of the Aerojet OME technology injector using the resistances, capacitances, and inertias previously calculated, and using a spinning first tangential mode input at 2600 Hz (frequency of observed instability). The method for determining these resistances, capacitances, inertias, and pressure inputs was the same as that outlined in the "Mechanization of Details" portion of this section of this report.

---

* Generally, on the model simulations made so far in this program, all four summations tend to change in the same direction for any specific injector modification so that no one summation has to be considered the correct one to use. If one did have to be picked, the best one would probably be summation number four that is the vector sum times the chamber amplitudes. However, in a case where a modification had different effects on the different summations, any conclusions made should be considered questionable.

Appendix C gives a tabulation of the model input and output data for the fuel side of the Aerojet injector. A list of the input data deck used for this run is shown in Fig. C-1. Fig. C-2 shows the amplitude and phase inputs calculated in the program. For each flow, the printout shows the upstream and downstream pressures, the input resistance and inertia, and the calculated outputs of gain and phase (Fig. C-3). The upstream and downstream pressures, as well as the resistances and inertances, are tabulated in this manner for each flow to simplify checking for proper input of the data. For each pressure mode, the printout shows the flows in and out, the volume and acoustic velocity, and the calculated outputs of gain and phase (Fig. C-4). Again, this format simplifies model checkout.

Also shown in Fig. C-3 are the four model summations of the injector flowrates in both lb/sec/psi and percent flow per percent chamber pressure.

The output of magnitude and phase gives information on the amount of response throughout the system. For example, nodes 49 through 60 represent the pressures in the outer ring groove. For this case, the amplitude of pressure node 51 is 0.9399 at a phase angle of 335.3 degrees which is nearly the same as the maximum chamber pressure input. Therefore, the volumes in the injector manifolds are not so large as to filter out the pressure oscillations in the ring grooves. This means that the injector flow oscillations can be affected by changes upstream of the injector face. If there had been little or no pressure response in the ring groove, the only feed system modifications that could alter the system would be changes to the injector orifices. Another comparison that lends insight into the system response is the amount of injector flow to ring groove flow. The maximum amplitude for flow through the injector for the outer ring groove is 4.716×10^{-4} lb/sec per psi while the maximum ring groove flow is 3.396×10^{-4}. Since the ring groove flow is significant compared to the injector flow, dams in the ring groove could significantly affect the ring groove pressure response, and therefore the injector flow oscillations. This type of analysis for a specific injector has to be performed for each of the ring grooves, and throughout the rest of the injector flow passages.

Before any conclusions can be reached concerning injector hydraulic coupling in a specific injector, both the oxidizer and fuel feed systems must be analyzed. The relative injector flow oscillations between the oxidizer and fuel sides may indicate the likelihood of one side being the controlling side, or indicate if both sides are important. Injector modifications could then be analyzed for possible beneficial effects.

SECTION IV

MODEL CORRELATION

Utilizing the model whose development is documented in Section III, three different test cases (injectors) for which test data exists and for which coupling between the injector hydraulics was known to occur were analyzed. The test cases selected were those cases for which solutions to the coupling problems were obtained and whose solutions could be analyzed using the developed computer model to post-predict the influence of the solution relative to the potential for coupling. These test cases were: the Rocketdyne Space Shuttle OME Technology Injector, the Rocketdyne Lance XRL Booster injector, and the Aerojet Space Shuttle OME Technology injector.

REVIEW OF TEST CASES

Compilation of test histories for the three above mentioned injectors are summarized below. These injectors most clearly exhibit a "high-frequency" coupling between the injector hydraulics and the chamber dynamics. Injector manifolding details for these injectors have been previously discussed in Section II of this report and reference is frequently made to figures presented earlier in Section II.

Rocketdyne Space Shuttle OME Technology Injector

The Rocketdyne SS/OME technology engine produces 6000 pounds thrust at a chamber pressure of 125 psia using N_2O_4/MMH propellants. Chamber diameter and contraction ratio are 8.2 inches and 2.0, respectively. A like-doublet injection element pattern is utilized. The injector has a total of 186 primary elements (744 orifices) having orifice sizes of 0.032 to 0.038-inch diameter (ox) and 0.028 to 0.033-inch diameter (fuel). Injector ΔP's are 56 psid (ox) and 62 psid (fuel).

Details of the Rocketdyne OME technology injector were shown earlier in Figs. 10-14. The injection orifices are fed by a total of 10 ring grooves (5 ox and 5 fuel) behind the 8.2-inch-diameter injector face. The oxidizer ring grooves

are fed through slanted feeder passages from a central oxidizer manifold. The fuel ring grooves are fed through slanted feeder passages from an annular fuel manifold.

A dual mode quarter-wave absorber with a contoured entrance (see Fig. 10, Acoustic Cavity) was included in the original OME technology injector design. The annular slot was partitioned radially by 12 dams. Eight of the twelve individual slots were "tuned" to damp the 1T acoustic mode of the chamber having a 1.60-inch effective slot depth and 0.5-inch slot width (14.8 percent open area). The remaining 4 slots were tuned to damp the 3T, 1R acoustic modes of the chamber and had a 0.78-inch effective slot depth and 0.5-inch slot width (7.4 percent open area). With this absorber configuration, the OME combustor was stable until the combustion was perturbed by an explosive bomb. A 25-percent occurrence of dynamic instability was obtained, a 2600 Hz mode of instability being recorded. Analysis of this instability mode* indicated a coupling between the injector hydraulics and the combustion process (Ref. 13). The addition of three radial dams in the annular fuel manifold succeeded in achieving a dynamically stable combustor.

A slight alteration in slot width to obtain open areas of 12 percent (1T) and 6 percent (3T, 1R), however, resulted again in a 12-percent occurrence of dynamic instability. The 2800 Hz instability mode was again believed indicative of hydraulic coupling and the addition of dams in the injector ring grooves was considered. No further testing of this injector was done, however.

*The mode appeared to have the angular pressure distribution of a first tangential mode with the nodal position influenced by location of the fuel inlet.

Rocketdyne Lance XRL Booster Injector

The Lance XRL booster engine produces 42,000-lb-thrust at a chamber pressure of 950 psia using IRFNA/UDMH propellants. The annular combustor has a 12.5 inch O.D. and a 7.0-inch I.D. Contraction ratio is 2.8. The injector pattern consists of four concentric rows of unlike doublets that impinge 0.250-inch from the injector face. The orifice hole sizes are 0.073-inch diameter for the oxidizer and 0.0515 inch for the fuel. Injector ΔP's are 184 psid (ox) and 140 psid (fuel). Figure 7 shows the frontside view of this injector face. Top and side views of the overall injector are provided by Figs. 8 and 9.

During development of the flightweight engine system, oscillations with frequencies from 1000 to 9000 Hz were incurred. Theoretical and empirical studies were conducted which culminated in the successful stabilization of this engine (Refs. 4 and 14).

A four-vane, 5.75-inch-long injector face baffle (chordal alignment) was included in the injector design to preclude occurrences of tangential instability. A combination of "L" shaped Helmholtz resonators was included in the injector design as shown in Fig. 26 to preclude oscillatory frequencies believed associated with second-baffle compartment modes (4400 Hz), the fourth tangential model (4800 Hz), the sixth and eighth tangential mode, and the first radial mode, and thus provide dynamic stability of the flightweight engine. The entrance to the modified Helmholtz cavity is located at the injector face and the cavity volume is located in the ablative thrust chamber body. The XRL booster engine incorporates 16 modified Helmholtz resonators (four per baffle compartment) tuned to 6120 Hz. Each resonator has an aperture area of 0.238 $in.^2$, an aperture length of 0.100 inch, and a cavity volume of 0.552 $in.^3$. The absorber open area is thus 6.5 percent of the total injector area. The acoustic absorbers are designed to provide strong attenuation over a wide band on either side of the tuned frequency. The absorbers proved completely successful in damping the modes of instability for which they were designed.

Despite the presence of both baffles and acoustic absorbers, the engine repeatedly exhibited a unique 1300 Hz, sinusoidal, linear instability. The

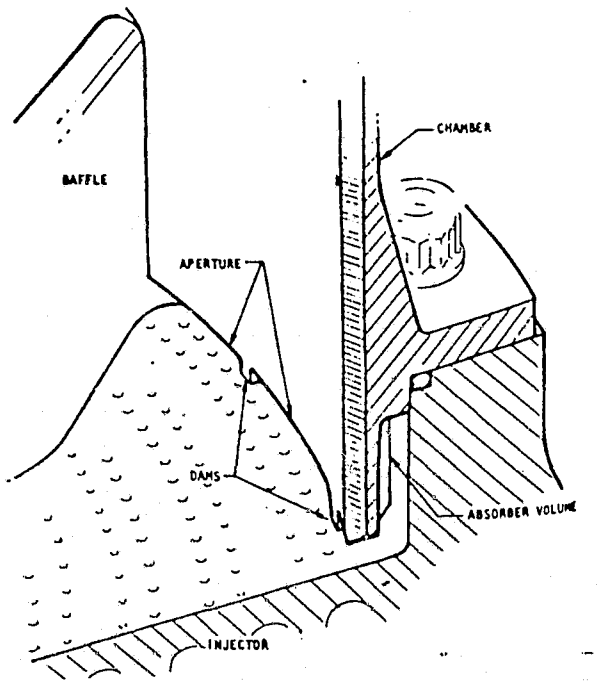

Figure 26. Injector End Absorber

observed instability was determined from test data and model simulation to be a chamber resonant mode with flow under the baffles combined with hydraulic coupling of the injector (Fig. 27). For this mode, pressures in adjacent baffle compartments were 180 degrees out of phase (observed from pressure measurements in the various compartments). This resonant chamber mode is a slight variation of the second tangential mode in that, at the injector face, there is no flow but near the chamber throat the flow is tangential. This mode has a frequency lower than the second tangential (2490 Hz) due to the additional flow path length to get under the baffles.

The oxidizer and fuel injector feed systems had four individual feeder arms that distributed propellants to ring grooves. From the ring groove, the propellant flowed through the injector orifices into the combustion chamber. A "lumped parameter" injector model was made for each of the propellant manifolds in the Lance XRL booster (Fig. 28) to analyze the unique 1300 Hz mode of instability. The model employed a numerical method of solution of the

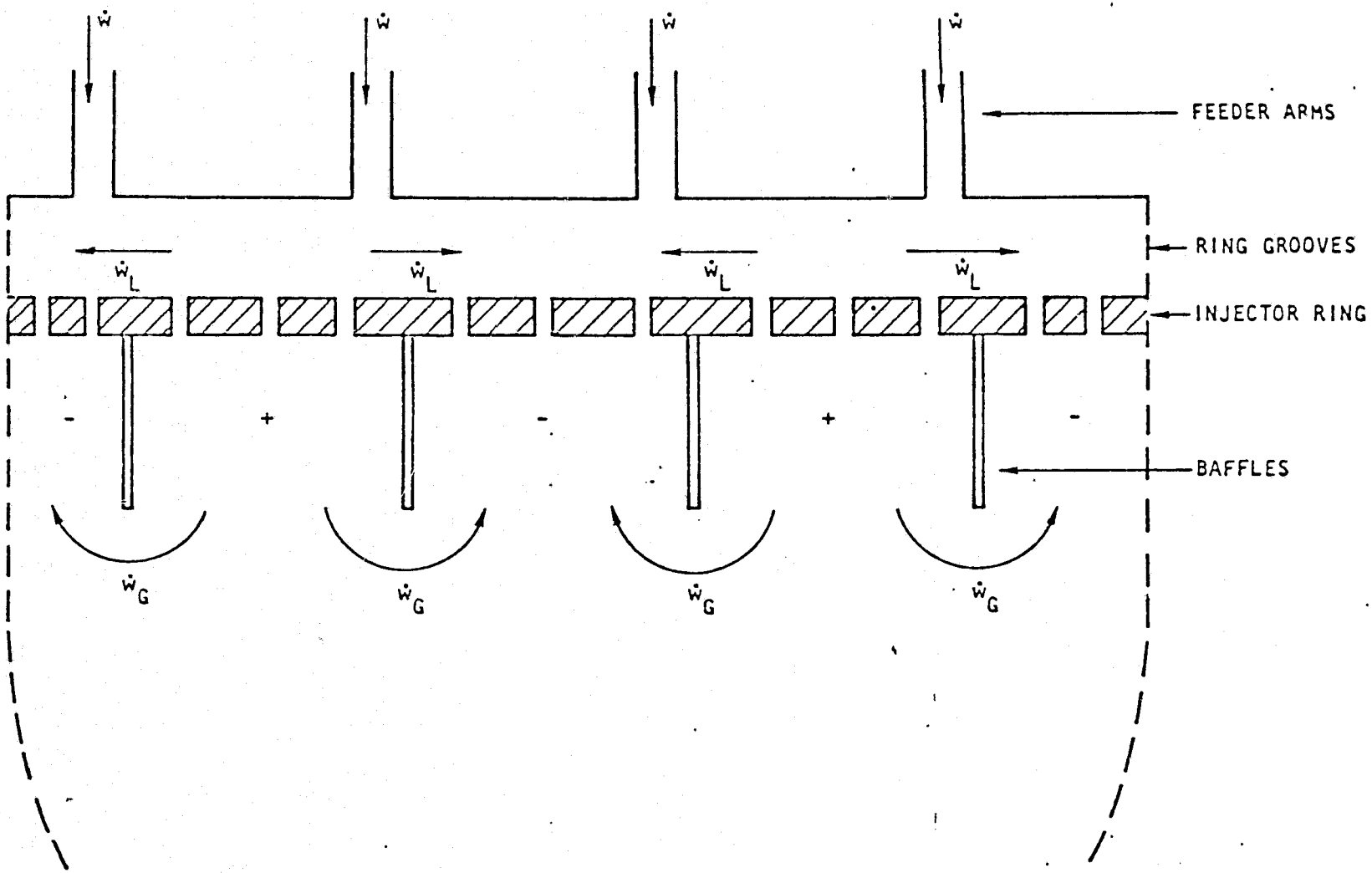

Figure 27. Schematic of XRL Booster Injector Without Dams Showing Ring Groove Crossflow Model Causing Coupling With 1300 Hz Anomalous Second Tangential Mode

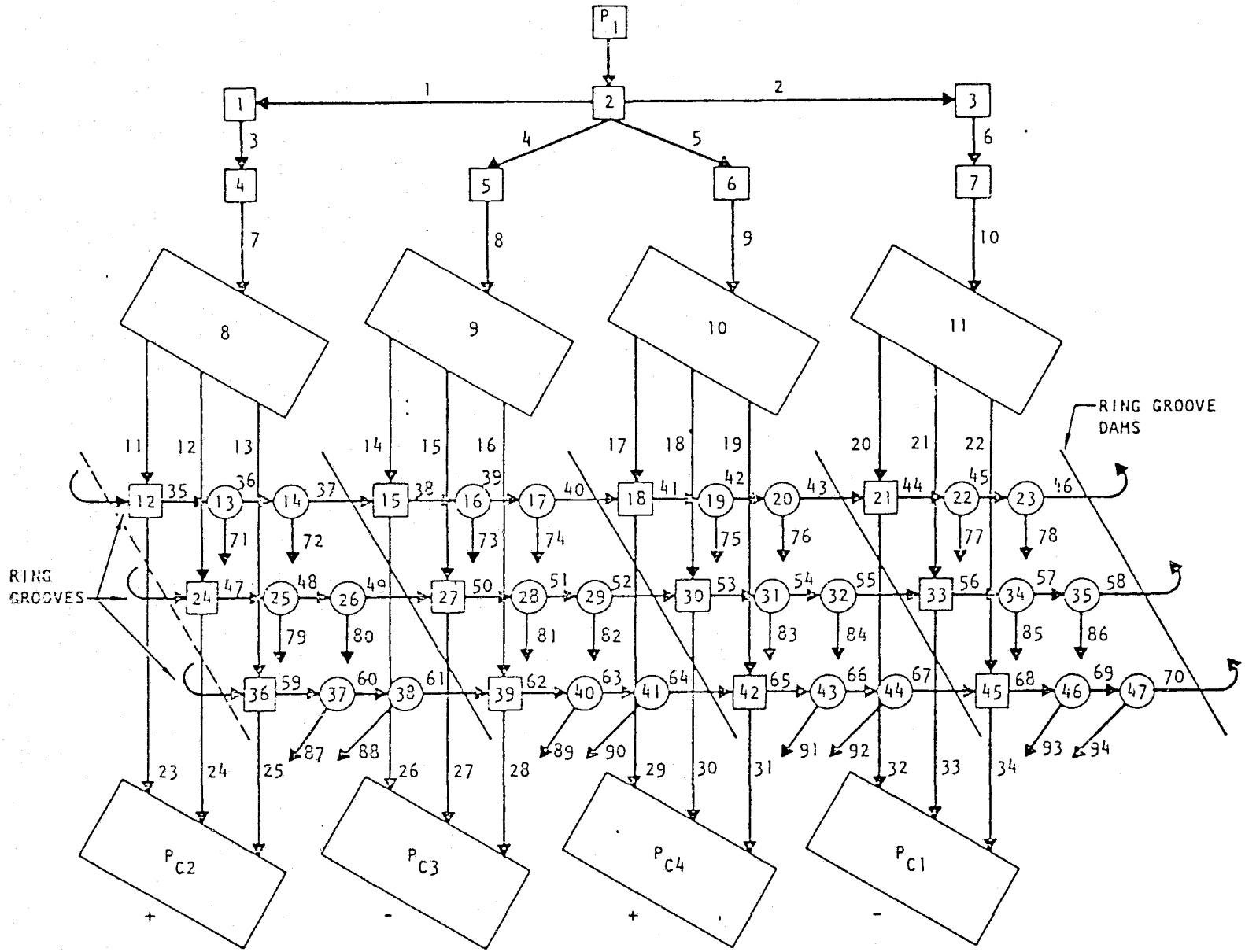

Figure 28. Injector Model Schematic

continuity and momentum equations to obtain a predicted injector response to a pressure oscillation mode imposed at the injector face.

Thus, the response of the various elements was affected by tangential flow in the ring grooves. The ring groove pressures tended to follow the oscillations in chamber pressure. Therefore, in the ring grooves just above a baffle, the pressures tended to be out of phase which produced tangential ring groove flow. The net effect was to produce the pressure distribution shown in Fig. 29 . The shaded area then represents the oscillatory injector pressure drop which produced injector flow oscillations. By putting in ring groove dams just above the location of the baffles (location of dams above the baffles is very important), the pressure distribution shown in Fig. 30 was predicted by the model.

The shaded area representing the oscillation in injector pressure drop was drastically reduced which made injector flow nearly constant. Incorporation of the ring groove dams in the XRL engine completely eliminated the 1300 Hz mode of instability with no change in injector pressure drops or other engine operating parameters. The Lance XRL booster engine is in production today and over 1000 have been produced, operating stably with ring groove dams, acoustic absorbers, and baffles.

Aerojet Space Shuttle OME Technology Injector

The Aerojet engine produces 6000 lbf thrust at a chamber pressure of 125 psia, using nitrogen tetroxide, N_2O_4, and monomethyl/hydrazine, MMH propellants. Details of the Aerojet injector are shown in Figs. 15 and 16. An 867-element X-doublet platelet pattern (see Fig. 31) on the 8.2-inch-diameter injector face is fed by a total of 15 ring grooves (8 fuel and 7 ox). An outer ring circumferential fuel manifold feeds an inner ring fuel manifold through 24 drilled holes. Fuel flows from the inner fuel ring through 3 downcomer slots to 3 pie-shaped manifolds. Downcomer slots from the pie manifolds feed each fuel ring. The oxidizer is fed through a central manifold to 3 pie-shaped manifolds. As in the case of the fuel, downcomer slots from the ox pie manifold feed each ox ring. A baseline injector-acoustic cavity configuration was established, which

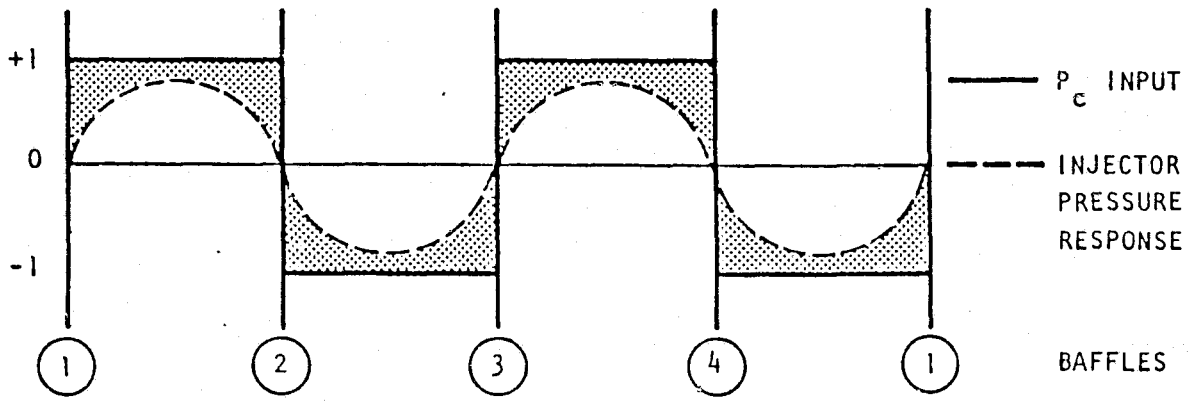

Figure 29. Pressure Response Characteristics

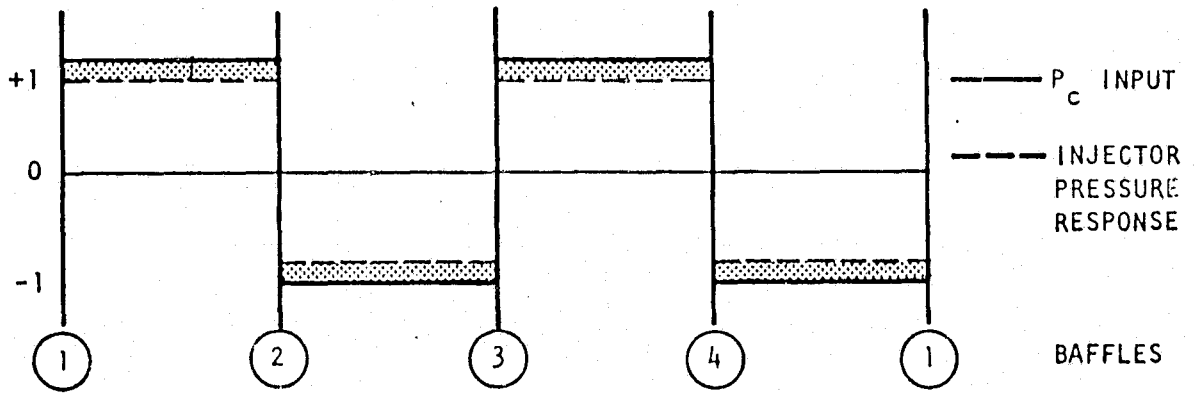

Figure 30. Response With Ring Groove Dams

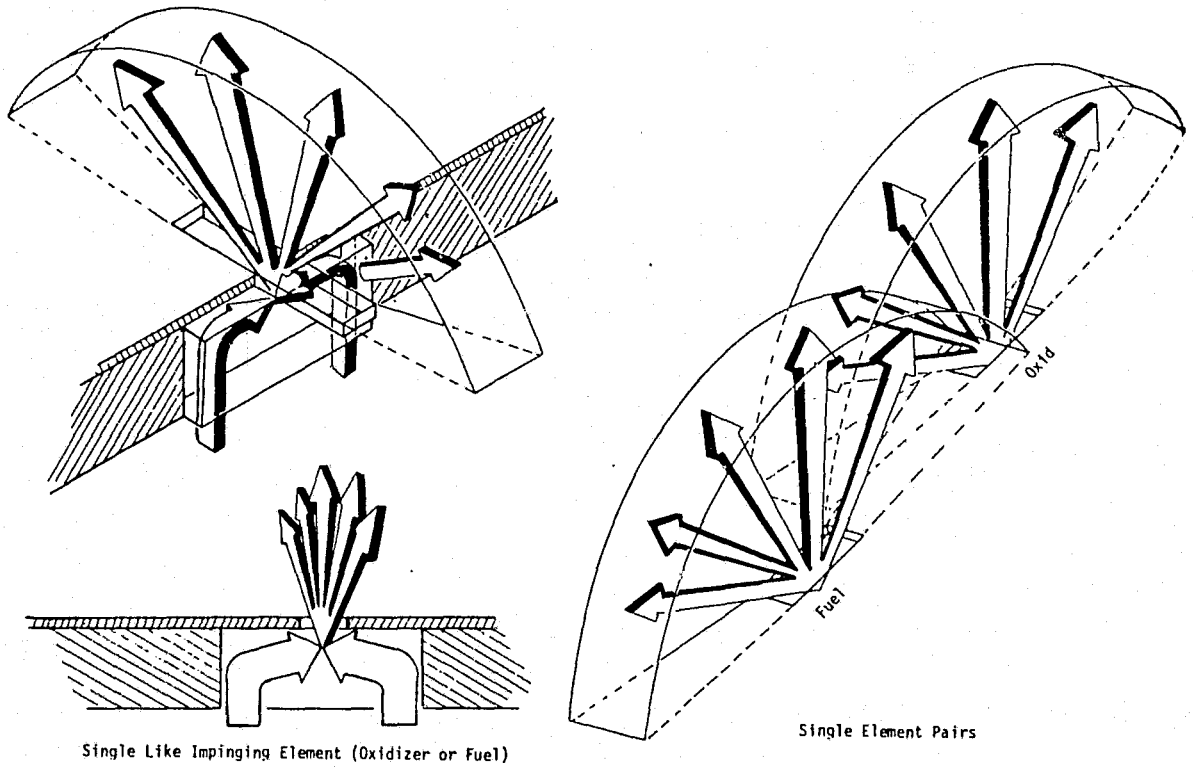

Figure 31. Aerojet X-Doublet Platelet Injector Element

consisted of an X-doublet platelet injector, in conjunction with a circumferential cavity housing. The cavity housing holds eight 1-T (nominal 18% open area) and four 3-T acoustic cavities (nominal 9% open area). Cavities were of the quarterwave slot type.

The primary mode of instability with the X-doublet pattern was resurging, which consists of periodic burst of a spinning 1-T mode at about 2600 Hz. The frequency of these bursts is about 400 Hz. Three changes to the OME engine were tested to determine their effect on eliminating resurging. Two of these changes dealt with the OME injector, while the other dealt with the combustion chamber acoustic cavities.

The most successful of the three changes was found to be the installation of ring groove dams. These dams were installed at the three null points in each of the outer 12 ring grooves. The insertion of a ring in the fuel circuit torus as shown in Fig. 32 to increase the injector pressure drop was another change incorporated in the injector to eliminate resurging. However, this had no demonstrated effect in changing resurge behavior. Finally, acoustic cavity geometry was altered considerably as the last of these changes. Both cavity inlet area and overlap (see Fig. 33) were altered. The results showed that decreasing inlet area tended to give more acoustic mode instabilities with less resurging, but that increasing overlap improves stability. For more detail on the Aerojet OME injector, see Ref. 8.

Thus, like the Rocketdyne OME technology injector, the Aerojet injector also exhibited a 2600 Hz instability whose mode was feed system coupled. Instability was highly resistant to suppression with acoustic cavities alone, but was influenced by the cavity entrance configuration. As in the Rocketdyne case, instability suppression was most successfully achieved through the use of dams.

PREPARATION OF MODEL INPUT DATA

Model input data was prepared for the three chosen test cases. This included computing the capacitances, inertances, and linearized flow

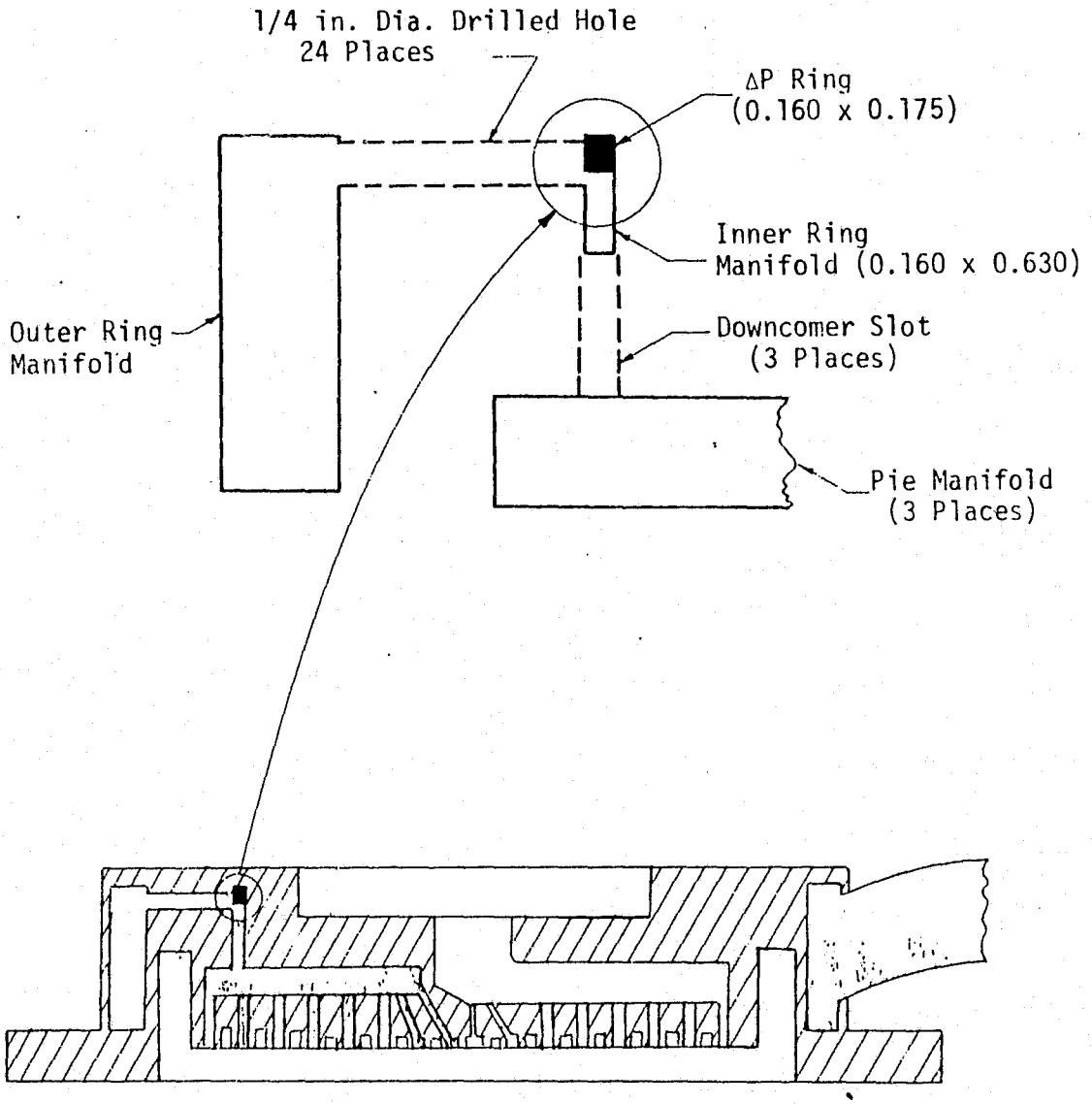

Figure 32. Fuel Circuit Pressure Drop Ring

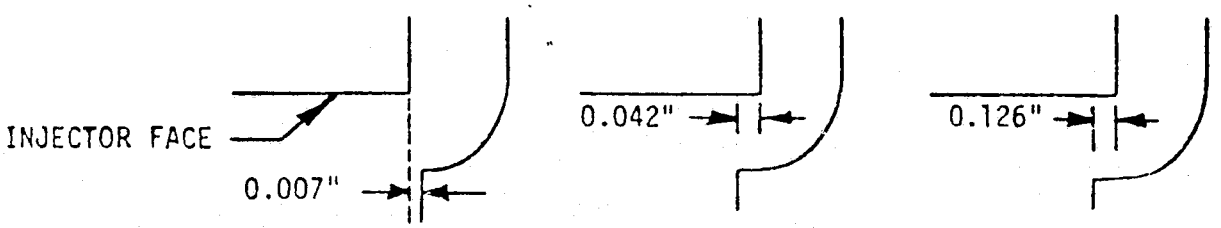

NO. TESTS	19	4	32
INSTABILITIES	9	0	0
TESTS WITH POST BOMB RESURGES (MARGINAL)	0	4	0

Figure 33. Cavity Overlap Results

resistances for the "lumped" fuel and oxidizer sides of each injector test case as described in the previous section. Schematics of these lumped injectors are shown in the discussions to follow.

Rocketdyne Space Shuttle OME Technology Injector

Modeling of this injector was concentrated on the analysis of the fuel side due to the fact that all injector fixes were associated with this side.

The fuel side of this injector was "lumped out" as schematically shown in Fig. 34 , with 78 pressure nodes (shown by rectangles), 168 flow segments (shown by lines) and 39 pressure input locations (shown by circles). The black triangles in this figure and all further injector schematics denote the locations of injector dams which were later incorporated into the injector design after unstable operation occurred. The angular locations of these pressure nodes, flow segments, and dams can be determined from Fig. 35. By assuming negligible pressure drops in flow segments 100-138 for the non-dammed case, the fuel side was reduced to a simple network of series and parallel flows as shown in Fig. 36 . This assumption is made from the fact that the time-averaged steady-state flow is very small in these segments giving a time-averaged pressure drop of zero. Based on a total flowrate of 7.27 lbm/sec an overall injector pressure drop of 51 psid was calculated. This compares to a reported pressure drop of 62 psid which gives a 17% error.

The oxidizer side of the Rocketdyne OME technology injector was described as shown in Figs.37 and 38 . The oxidizer side consists of 69 pressure nodes, 129 flow segments, and 31 pressure input locations. By assuming negligible pressure drops in flow segments 70-99 the oxidizer side was reduced to a simple network of series and parallel flows as illusrated in Fig. 39 . Based on a total oxidizer flowrate of 12 lbm/sec, an overall injector pressure drop of 47 psid was calculated. This compares to a reported pressure drop of 56 psid for a 17% error.

Rocketdyne Lance XRL Booster Injector

The fuel side, schematically shown in Fig. 40, consists of 53 pressure nodes, 88 flow segments, and 28 pressure input locations. The angular

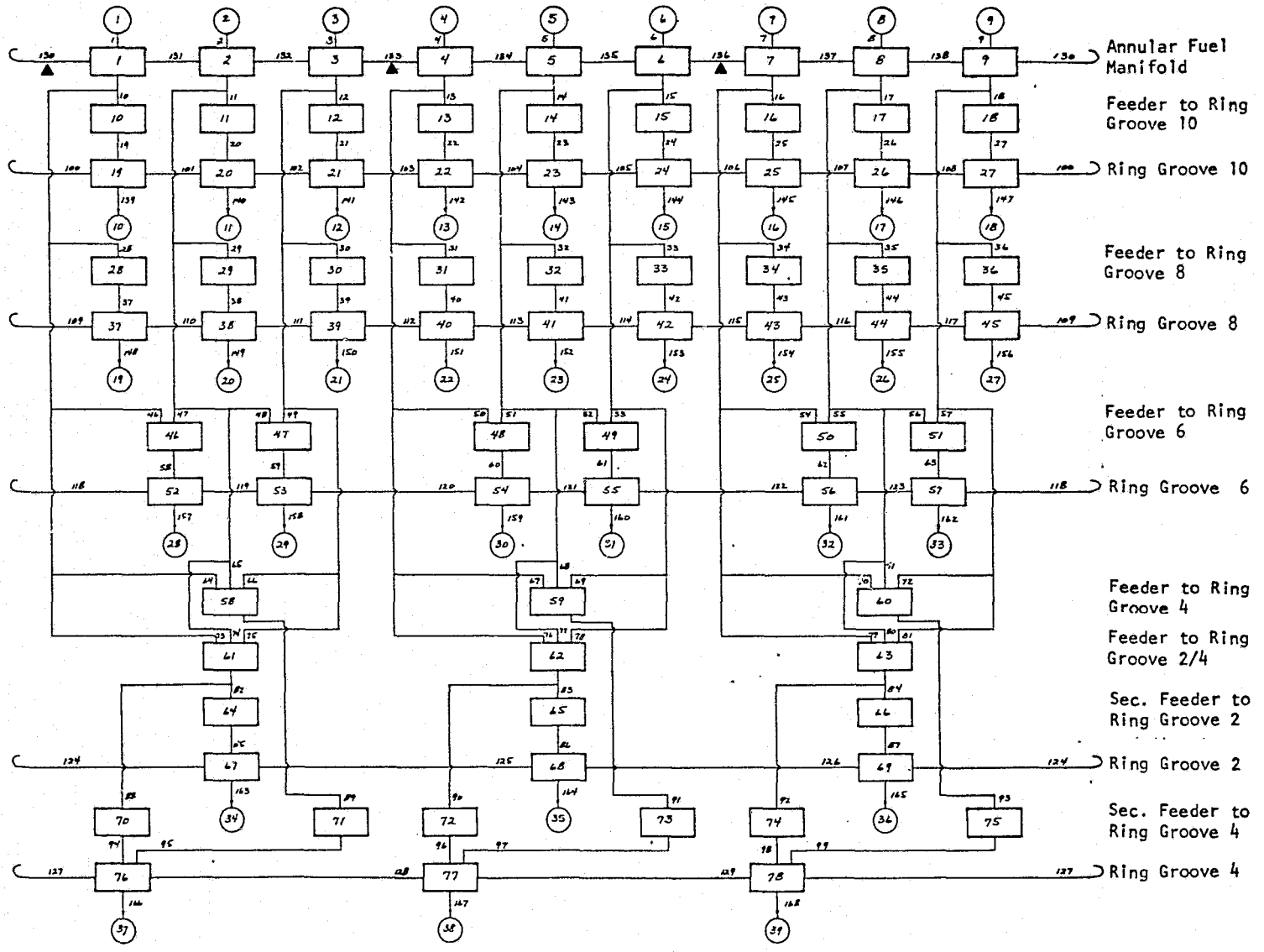

Figure 34. Lumped Parameter Representation of Fuel Side of Rocketdyne OME Technology Injector Showing Flows Between Pressure Nodes

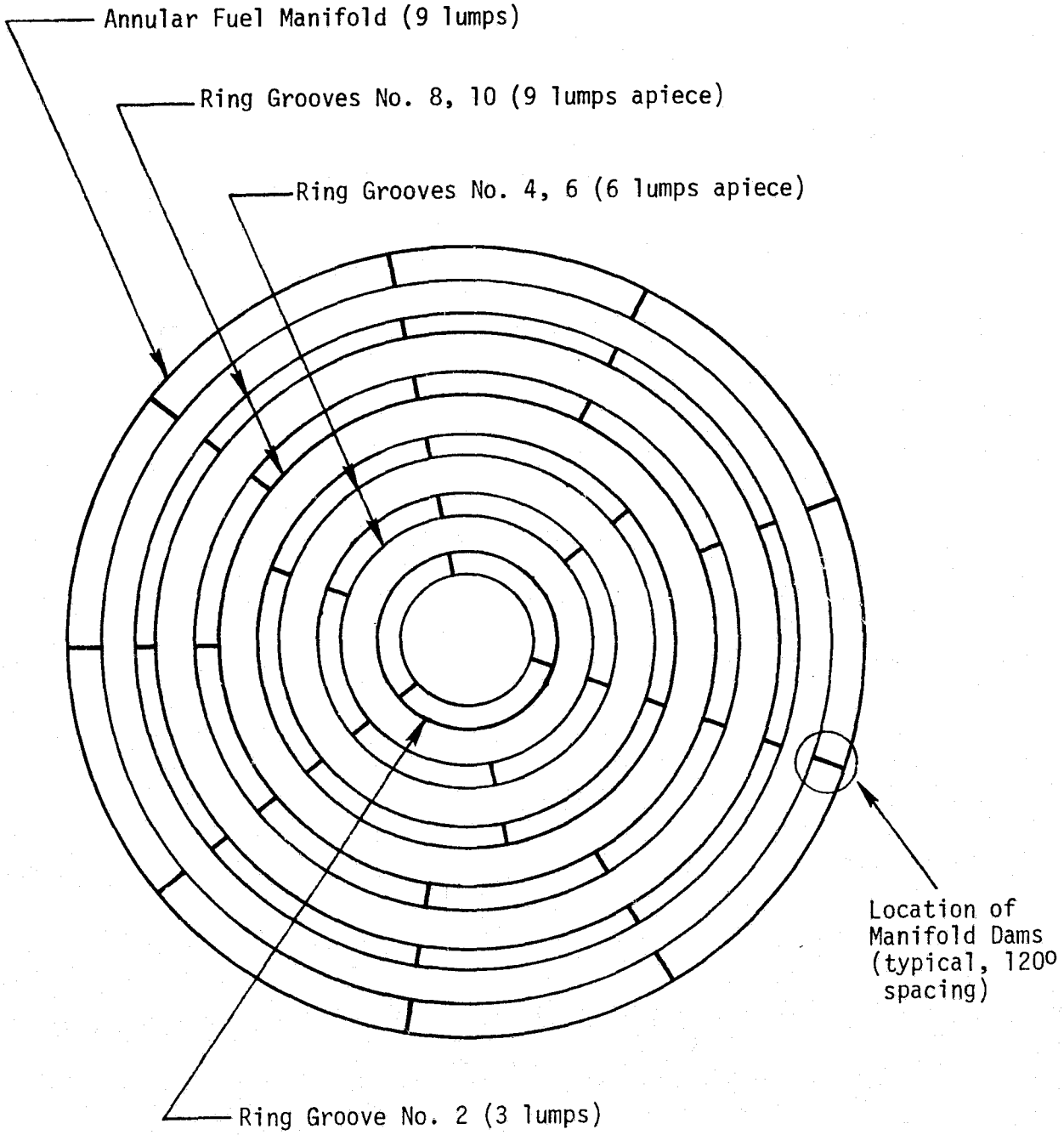

Figure 35. Distribution of Lumps for Fuel Side of Rocketdyne OME Technology Injector

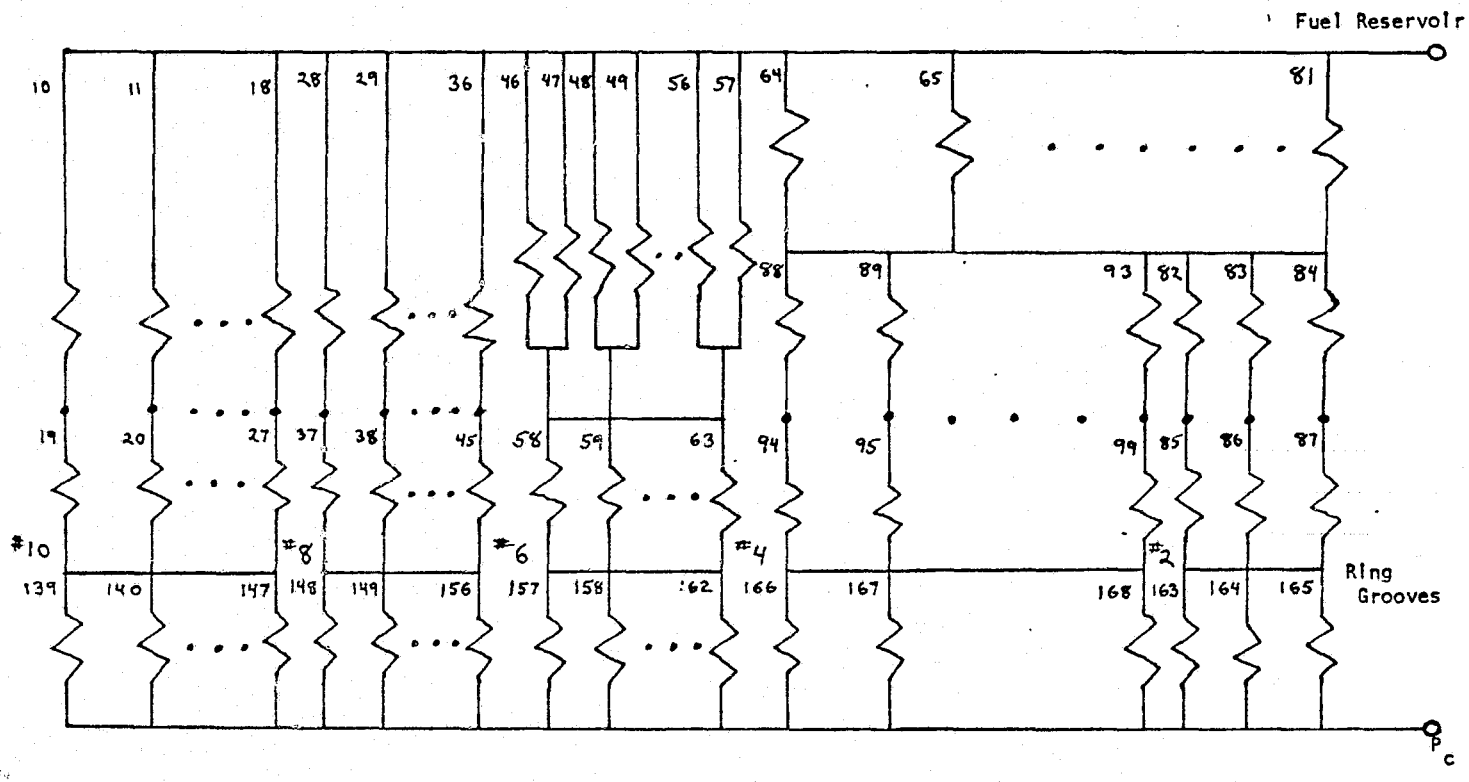

Figure 36. Simplified Resistance Network for Fuel Side of Rocketdyne OME Technology Injector

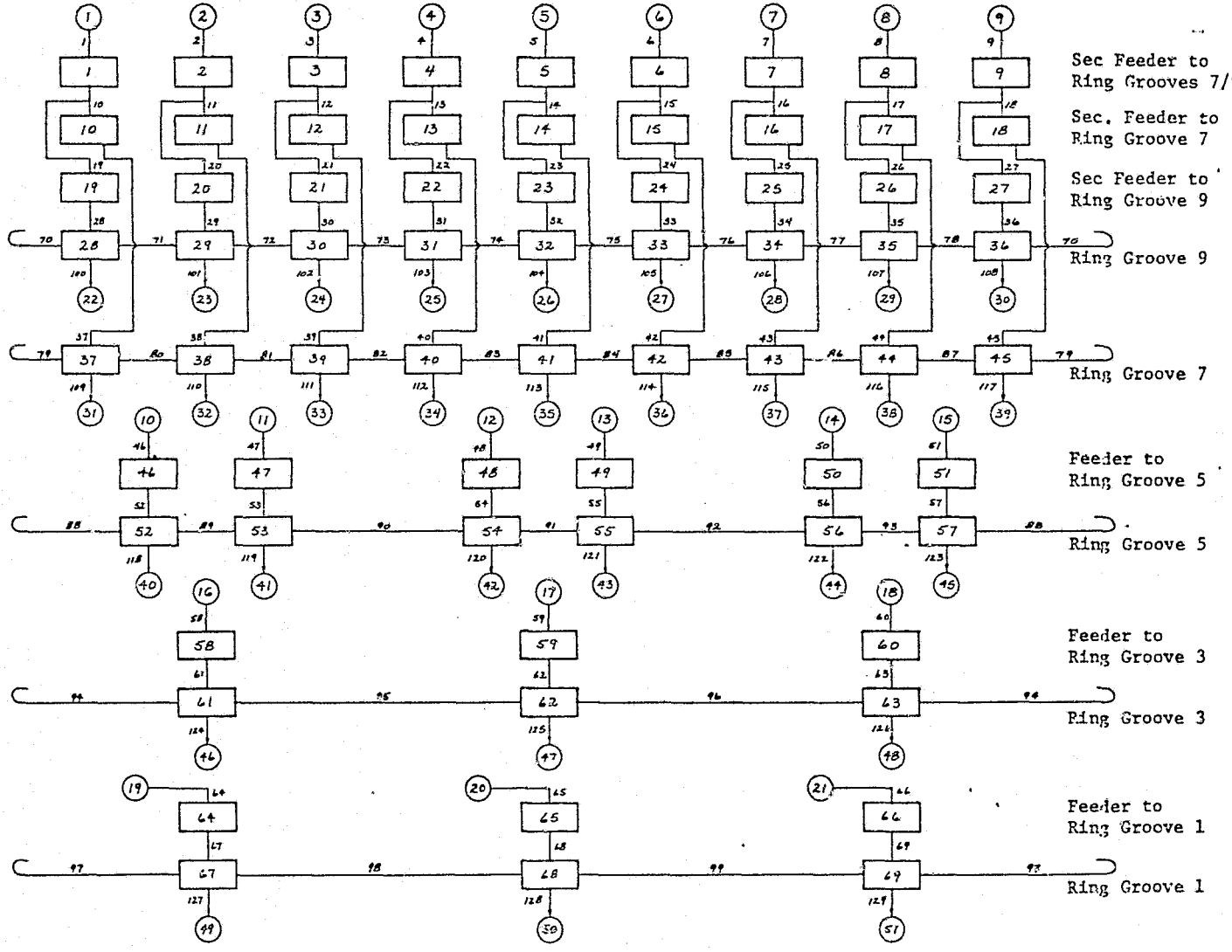

Figure 37. Lumped Parameter Representation of Oxidizer Side of Rocketdyne OME Injector Showing Flows Between Pressure Nodes

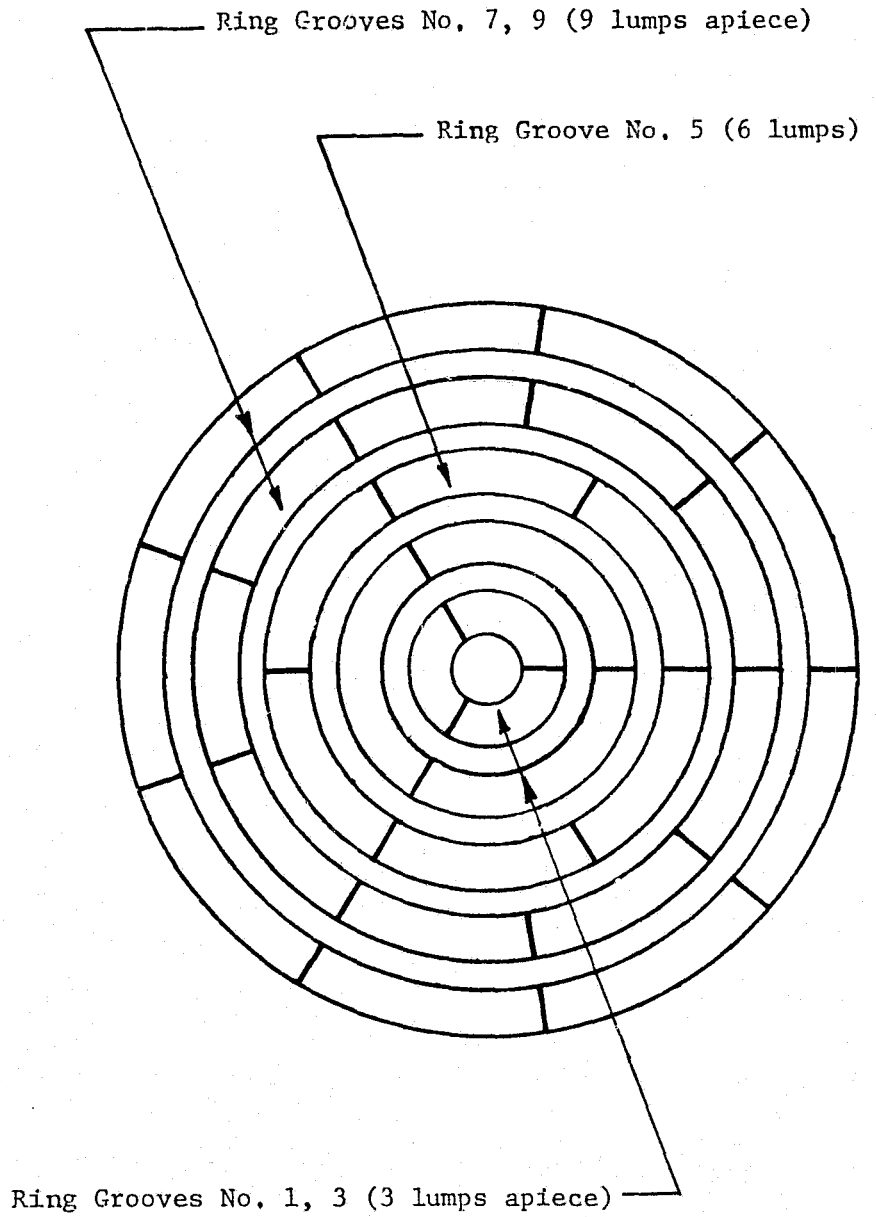

Figure 38. Distribution of Lumps for Ox Side of Rocketdyne OME Technology Injector

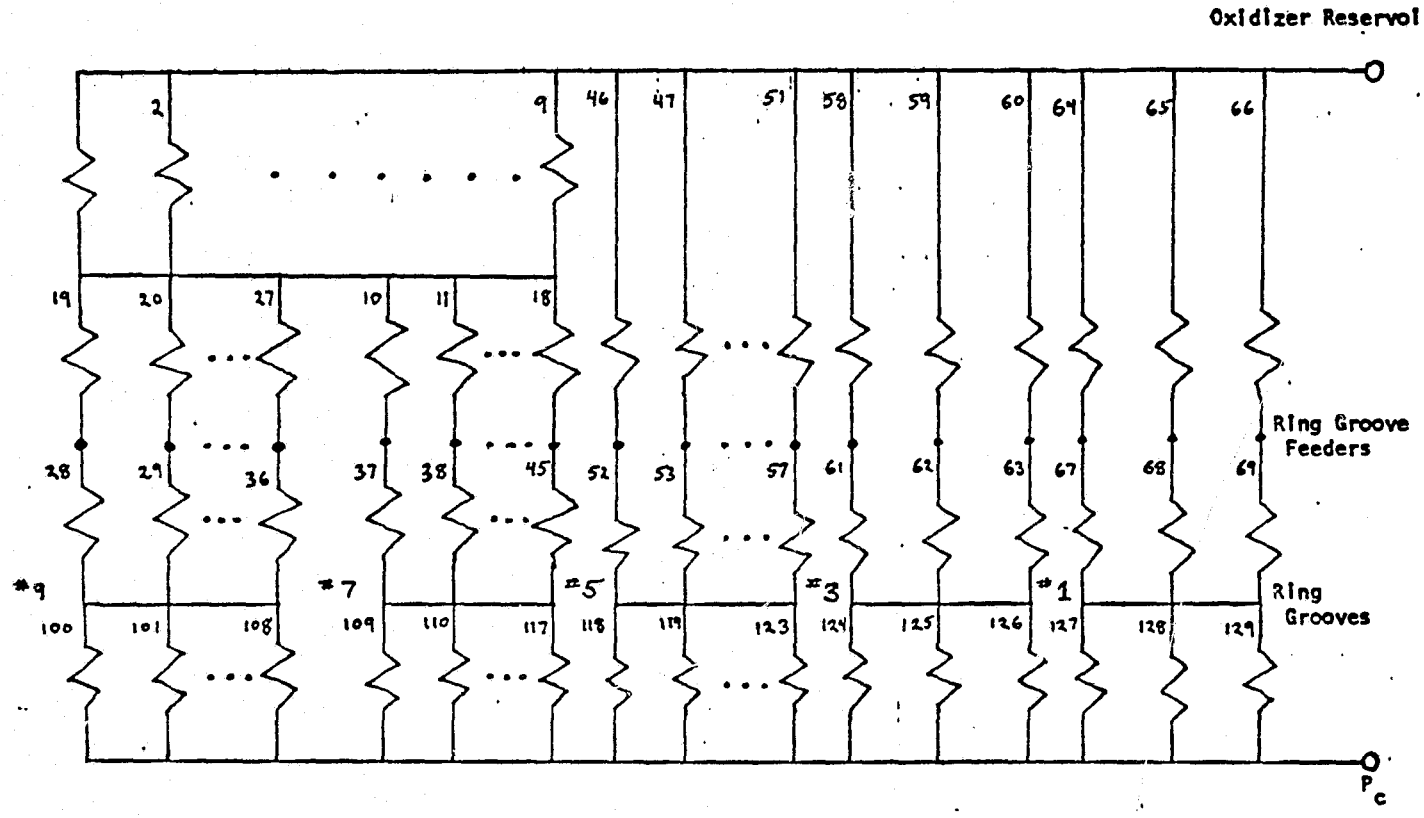

Figure 39. Simplified Resistance Network for Oxidizer Side of Rocketdyne OME Technology Injector

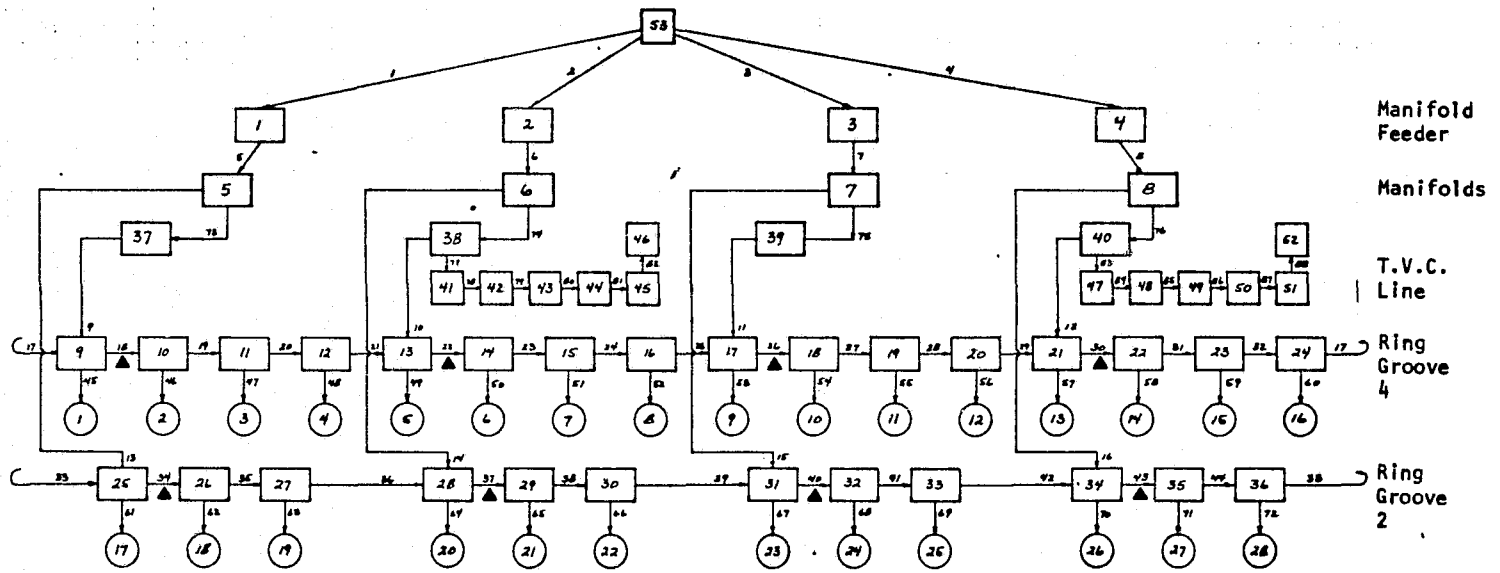

Figure 40. Lumped Parameter Representation of Fuel Side of Rocketdyne XRL Injector Showing Flows Between Pressure Nodes

locations of these lumped constituents can be determined from Fig. 41. By assuming negligible pressure drops in flow segments 17-44 and 77-88 the fuel side was reduced to the simple network as shown in Fig. 42 . Based on a total fuel flowrate of 33.3 lbm/sec an overall injector pressure drop of 129 psid was calculated. This compares quite well to a reported pressure drop of 140 psid which yields an error of 8%.

The oxidizer side, schematically shown in Fig. 43 , consists of 61 pressure nodes, 108 flow segments, and 36 pressure input locations. The angular placement of these constituents can be determined from Fig. 44 . By assuming negligible pressure drops in flow segments 37-72 the oxidizer side was reduced to a simple network of series and parallel flows as illustrated in Fig. 45. Based on a total oxidizer flowrate of 133 lbm/sec, an overall injector pressure drop of 211psid was calculated. This compares to a reported pressure drop of 184 psid which gives a 15% error.

Aerojet Space Shuttle OME Technology Injector

The fuel side, schematically shown in Fig. 20 , consists of 99 pressure nodes, 223 flowrates, and 52 pressure input locations. The angular locations of these lumped constituents can be determined from Fig. 19. By assuming negligible pressure drops in flow segments 2-16, 32-46, 53-73, and 122-172, the fuel side was reduced to the simplified network shown in Fig. 24. An overall fuel side pressure drop of 58 psid was calculated based on a total fuel flowrate of 7.19 lbm/sec. This compared very well with a 57 psid pressure drop reported by Aerojet which gives an error of 2% between the two values.

The oxidizer side of the Aerojet OME technology injector was schematically described as shown in Fig. 46. The oxidizer side consists of 71 pressure nodes, 171 flow segments, and 50 pressure input locations. The angular position of these components can be determined from Fig. 47. By assuming negligible pressure drops in flow segments 11-31 and 75-122, the oxidizer side was reduced to a simple network of series and parallel flows as illustrated in Fig. 48. Based on a total oxidizer flowrate of 11.86 lbm/sec an overall injector pressure drop of 56 psid was calculated. This compares to a reported pressure drop by Aerojet of 44 psid for a 27% error.

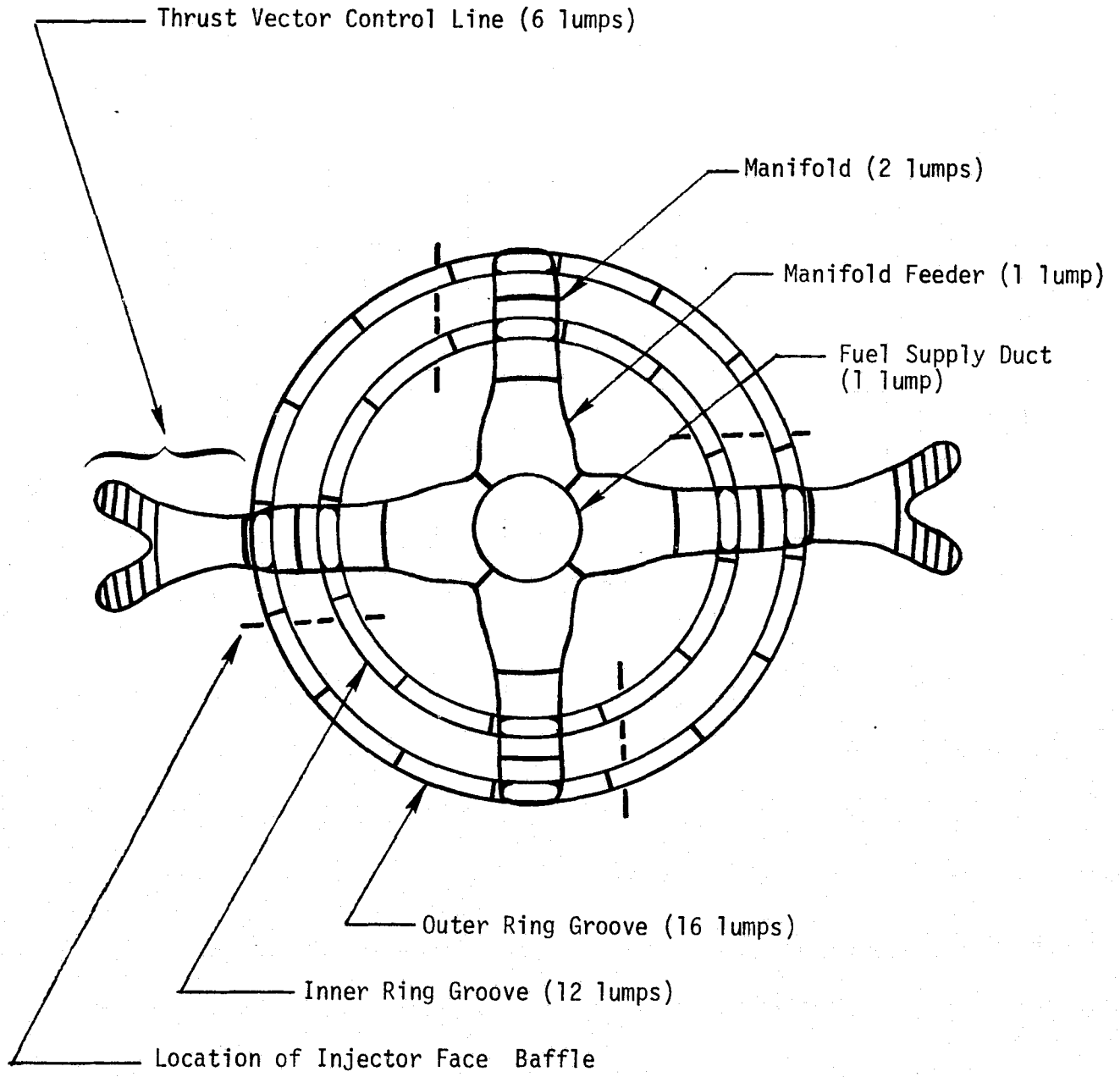

Figure 41. Distribution of Lumps for Fuel Side of Rocketdyne Lance XRL Booster Injector

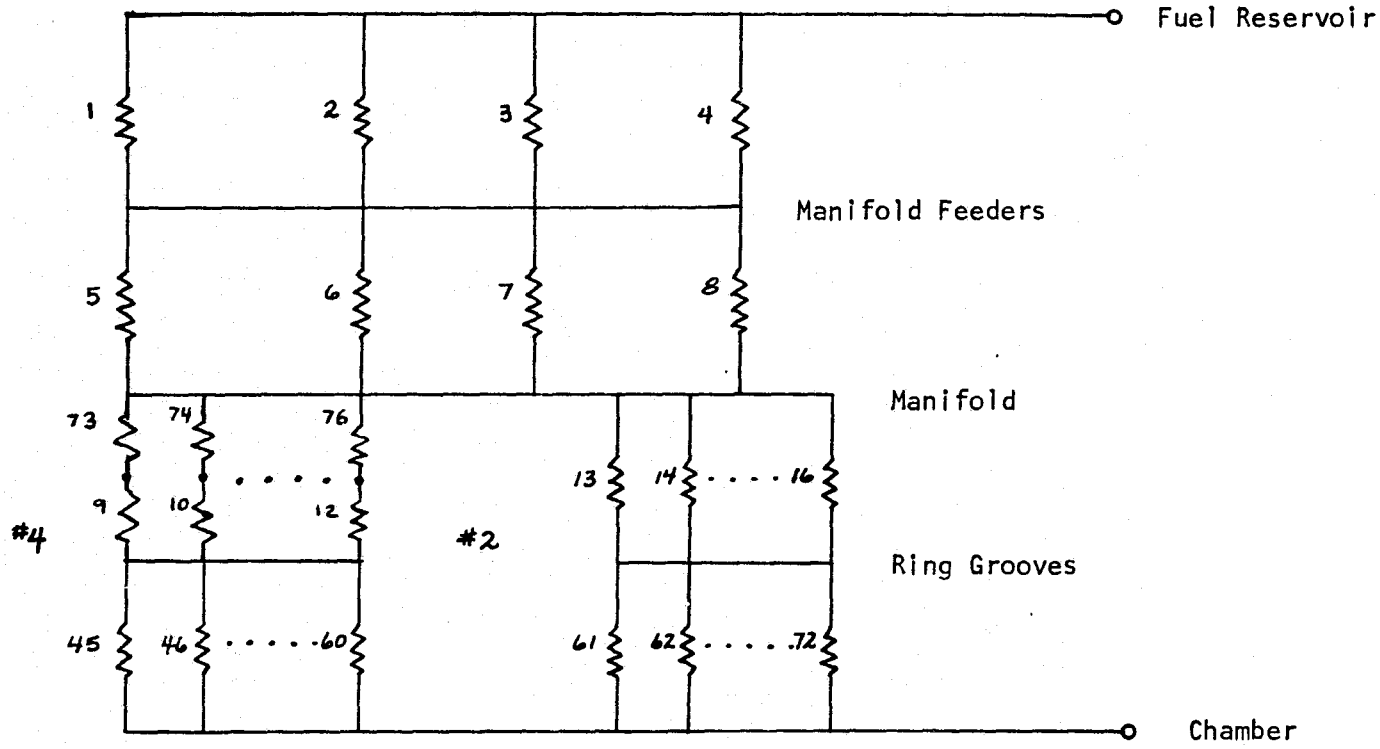

Figure 42. Simplified Fuel Side
Rocketdyne XRL Injector

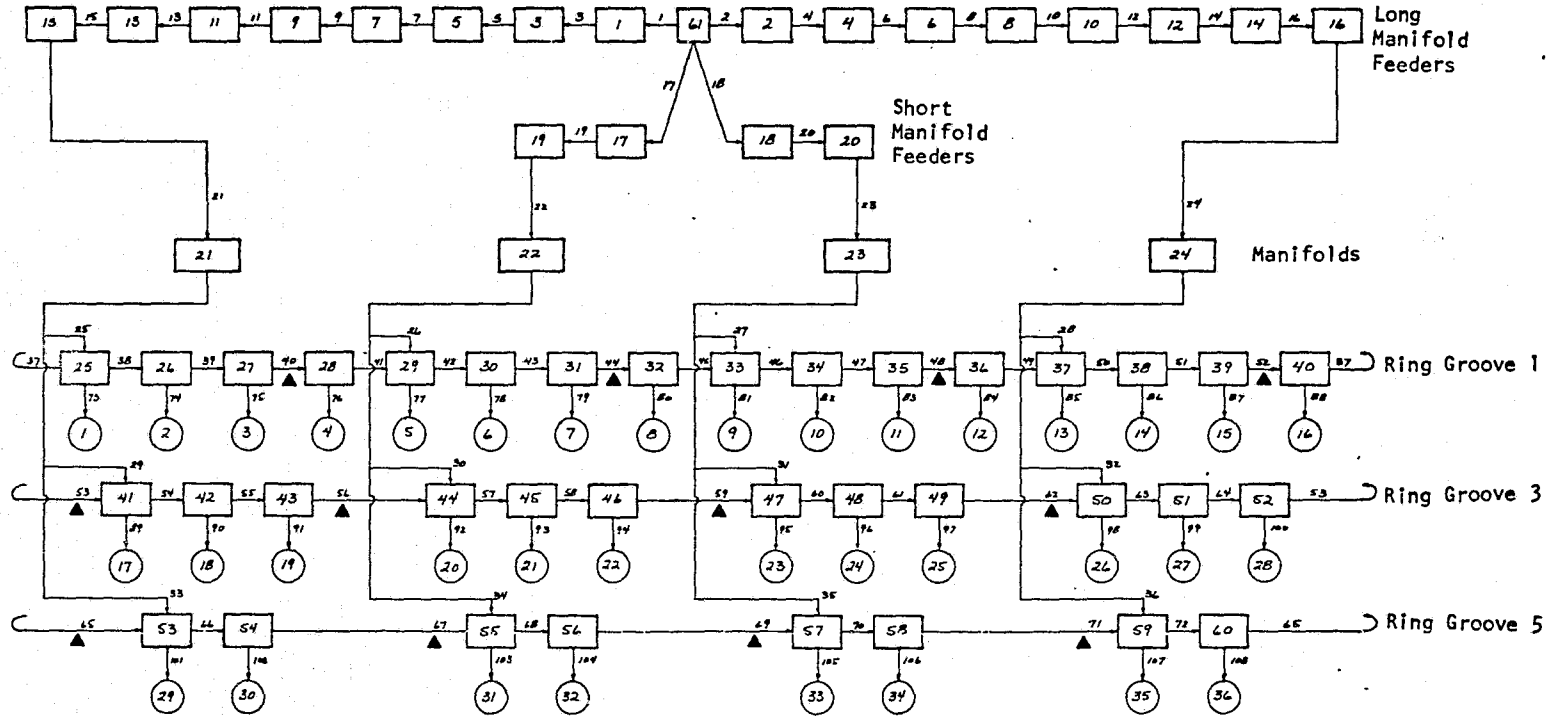

Figure 43. Lumped Parameter Representation of Oxidizer Side of Rocketdyne XRL Injector Showing Flows Between Pressure Nodes

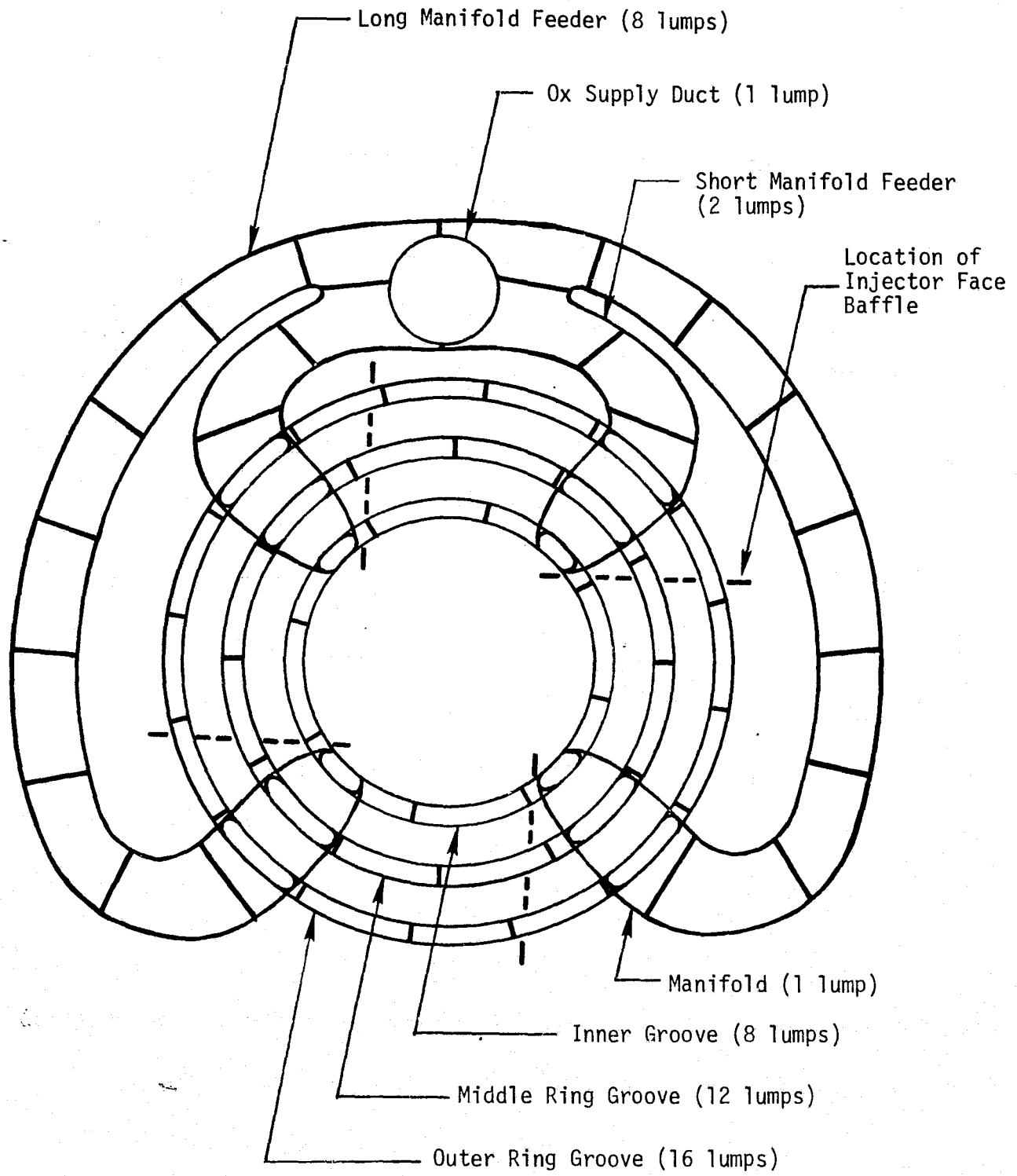

Figure 44. Distribution of Lumps for Oxidizer Side of Rocketdyne Lance XRL Booster Injector

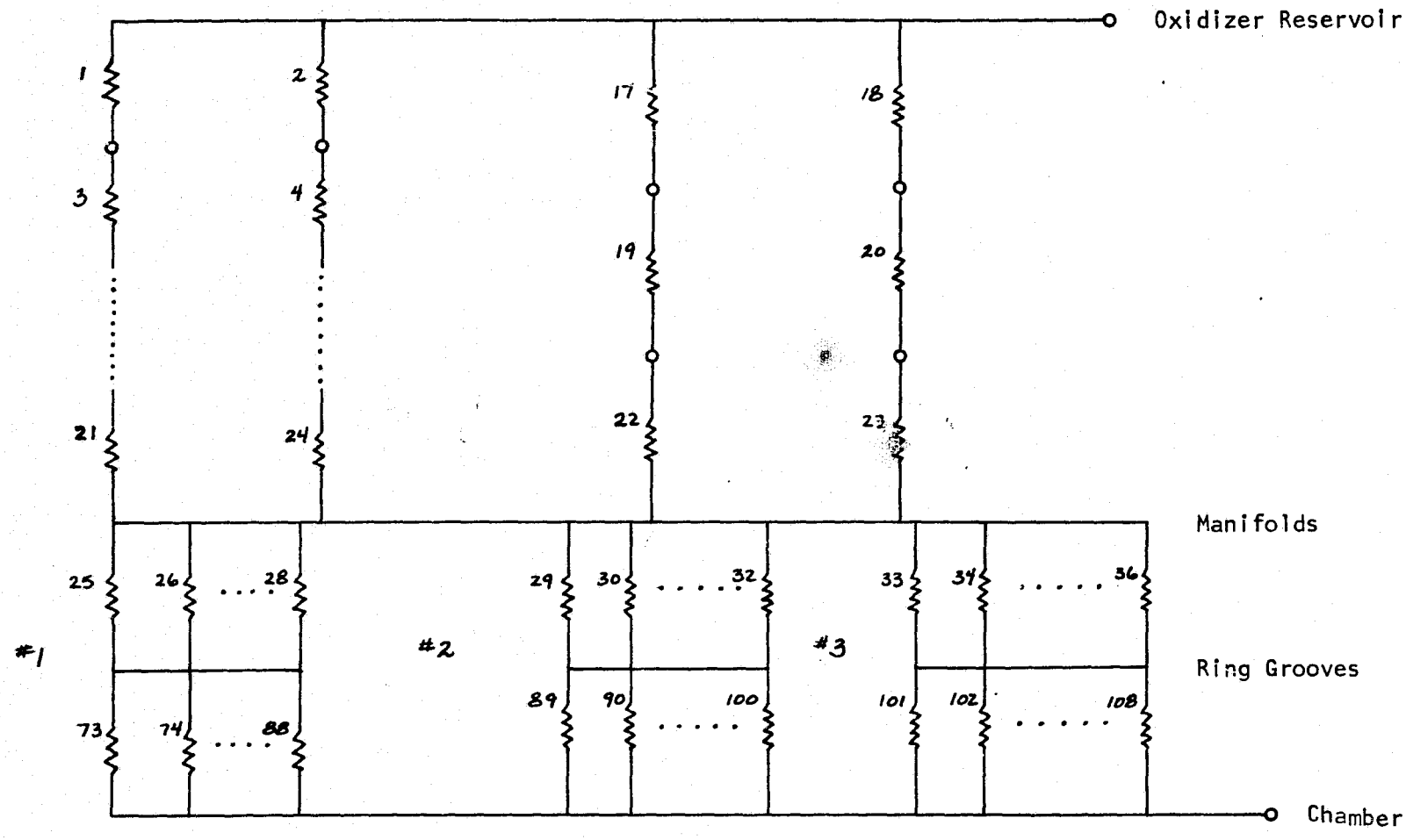

Figure 45, Simplified Oxidizer Side Rocketdyne XRL Injector

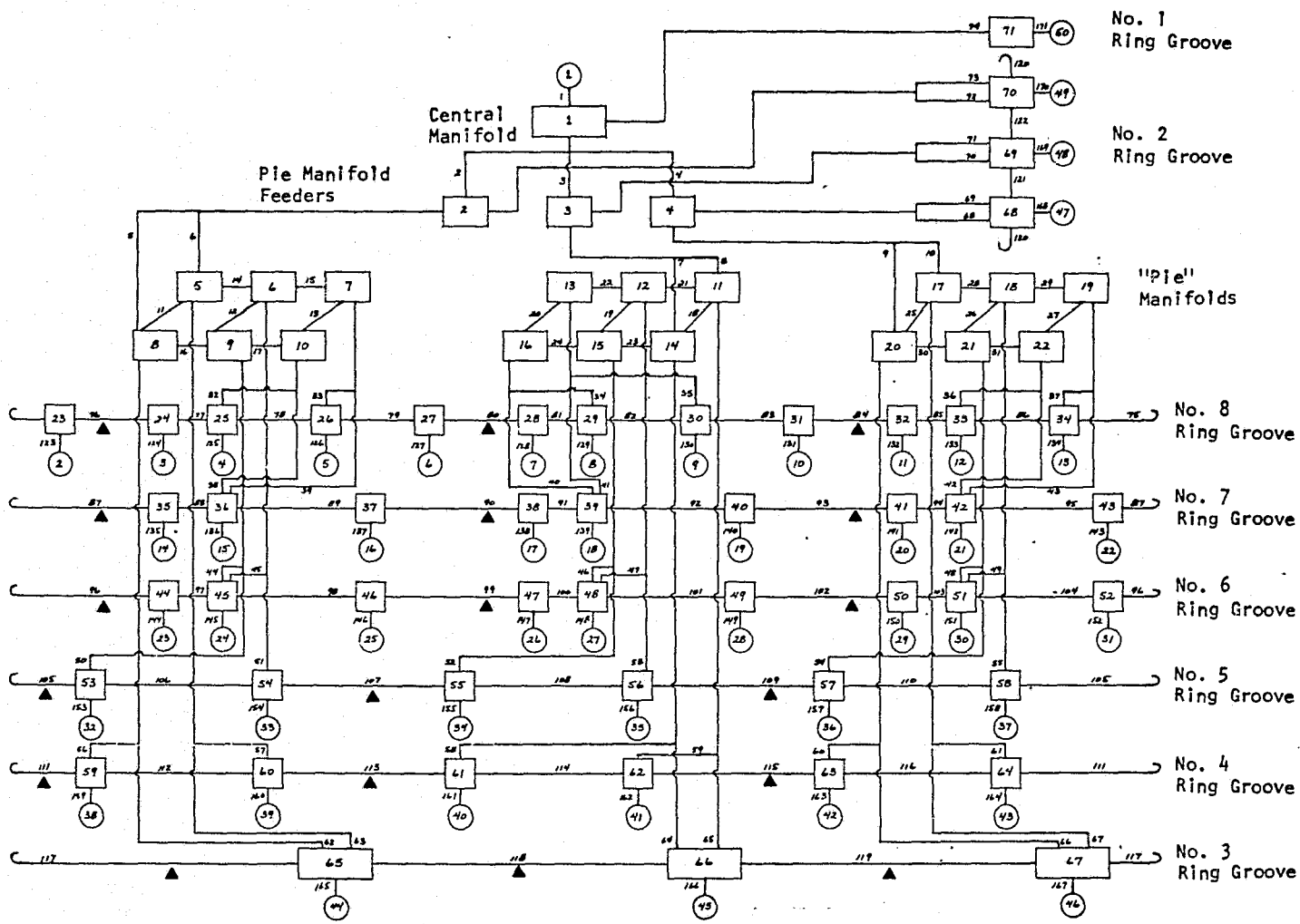

Figure 46. Lumped Parameter Representation of Oxidizer Side of Aerojet OME Technology Injector Showing Flows Between Pressure Nodes

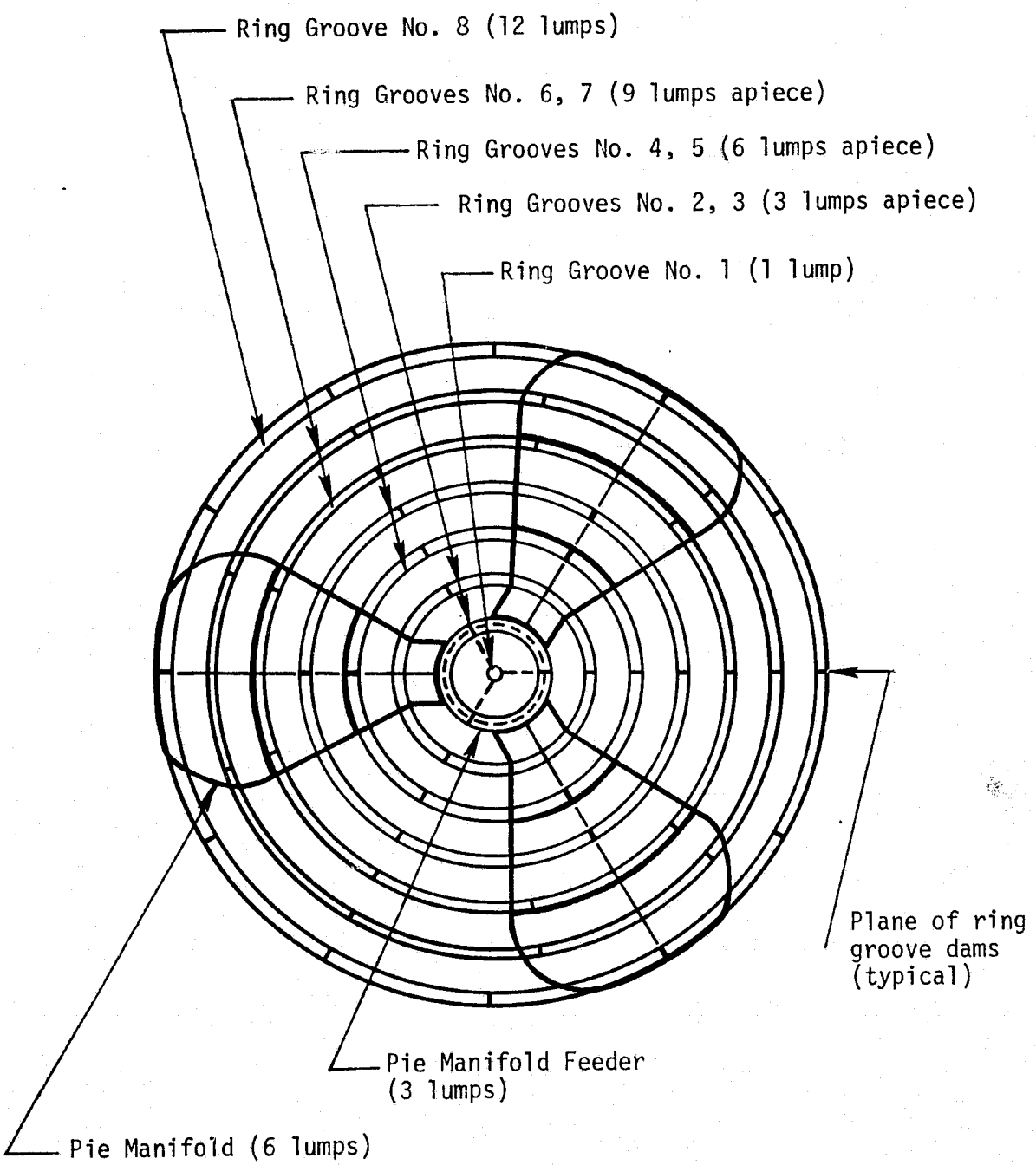

Figure 47. Distribution of Lumps for Oxidizer Side of Aerojet OME Technology Injector

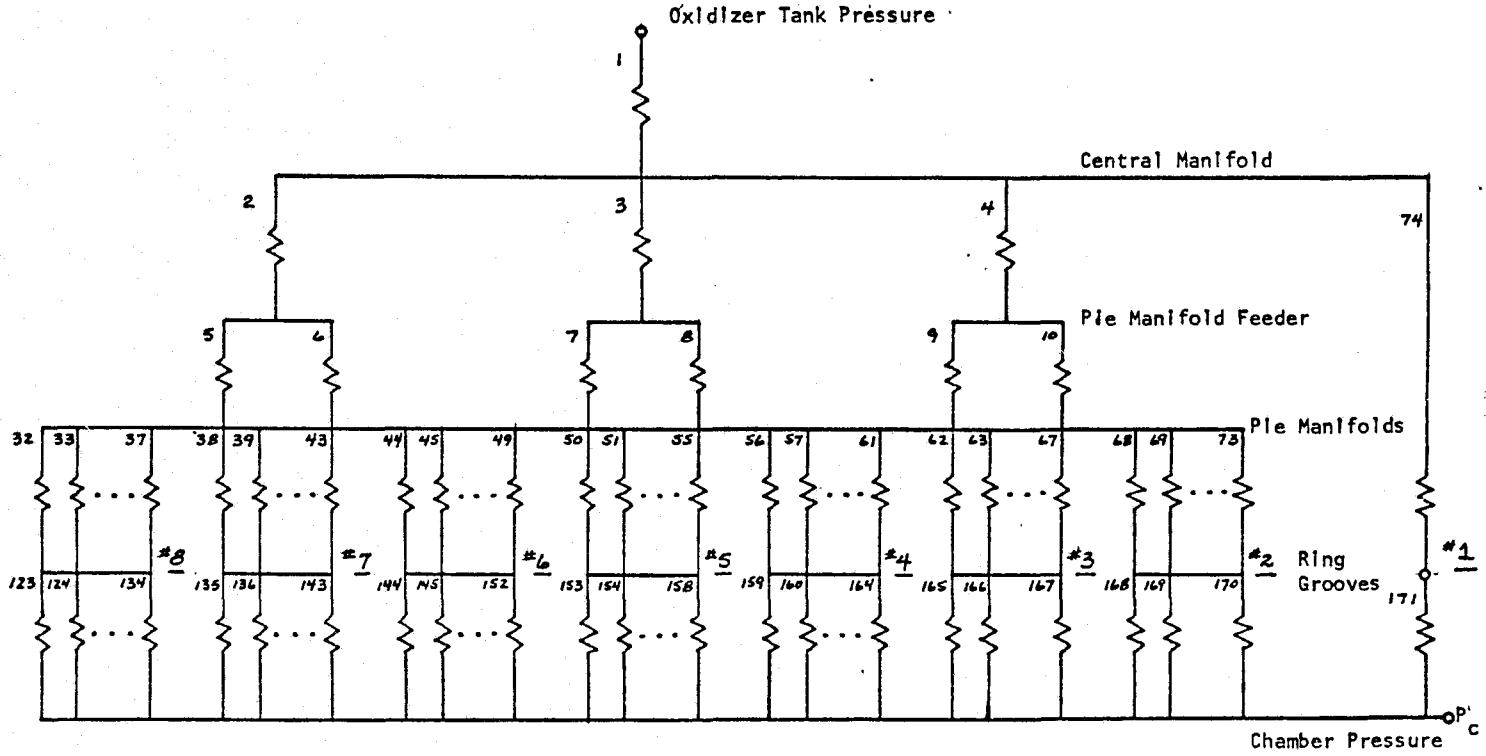

Figure 48. Simplified Oxidizer Side, Aerojet OME Technology Injector

CORRELATION OF MODEL

The engine hydraulic stability model was run for the Rocketdyne OME technology and XRL engines and for the Aerojet OME technology engine. Complete sets of input and output data are shown for each side of the three correlation injectors in Appendices C through H.*

Rocketdyne Space Shuttle OME Technology Injector

The Rocketdyne OME technology injector exhibited a 1T mode of instability on 25% of the tests where bombs were detonated in the chamber. By adding three radial dams in the annular fuel manifold, the instability was eliminated. The same injector with the dams and a different acoustic cavity design had a 12% incidence of instability when bombed. This means that the incorporation of dams did reduce the loop gain, but the reduction was probably not a big reduction or the modification of the acoustic cavities would not have caused the instability to reappear.

The lumped parameter representations for the fuel and oxidizer sides of the Rocketdyne OME technology injector are shown in Figs. 34 and 37. Input for the fuel side without the dams is shown in Appendix E. The resistance values for flows 130, 133, and 136 (see lumped parameter description shown in Fig. 34) were set equal to 10^{10} when simulating the addition of manifold dams to the fuel side of the injector. A standing first tangential mode (ν = 2600 Hz) in the combustor was input to the injector face. A summary of the injector flow results is shown in Table III. This table has the four different total injector flow summations with the output in both lb/sec/psi and % flow/% P_c. The results presented in Table III show about a 17% reduction in fuel flow with the radial dams. Plots for the outer fuel ring groove with and without dams are shown in Figs. 49 and 50. Therefore, it is concluded that adding the annular dams reduces the hydraulic coupling with the combustion chamber thus increasing, to a limited extent, the stability of the combustor.

---

* These appendices show results for the injectors of interest without the inclusion of dams or any other injector "fix."

TABLE III. ROCKETDYNE OME TECHNOLOGY INJECTOR RESULTS

	Total Injector Flow		Total Vector Injector Flow		Total Injector Flow Proportioned by PC Amplitudes		Total Vector Injector Flow Proportioned by PC Amplitudes	
	Lb/Sec / Psi	% Flow / % P_c	Lb/Sec / Psi	% Flow / % P_c	Lb/Sec / Psi	% Flow / % P_c	Lb/Sec / Psi	% Flow / % P_c
Fuel Side No Dams	.00633	.109	.00632	.109	.00442	.0760	.00441	.0758
Fuel Side With Dams	.00521	.0896	.00508	.0873	.00371	.0638	.00367	.0631
Ox Side No Dams	.00551	.0574	.00550	.0573	.00370	.0385	.00370	.0385

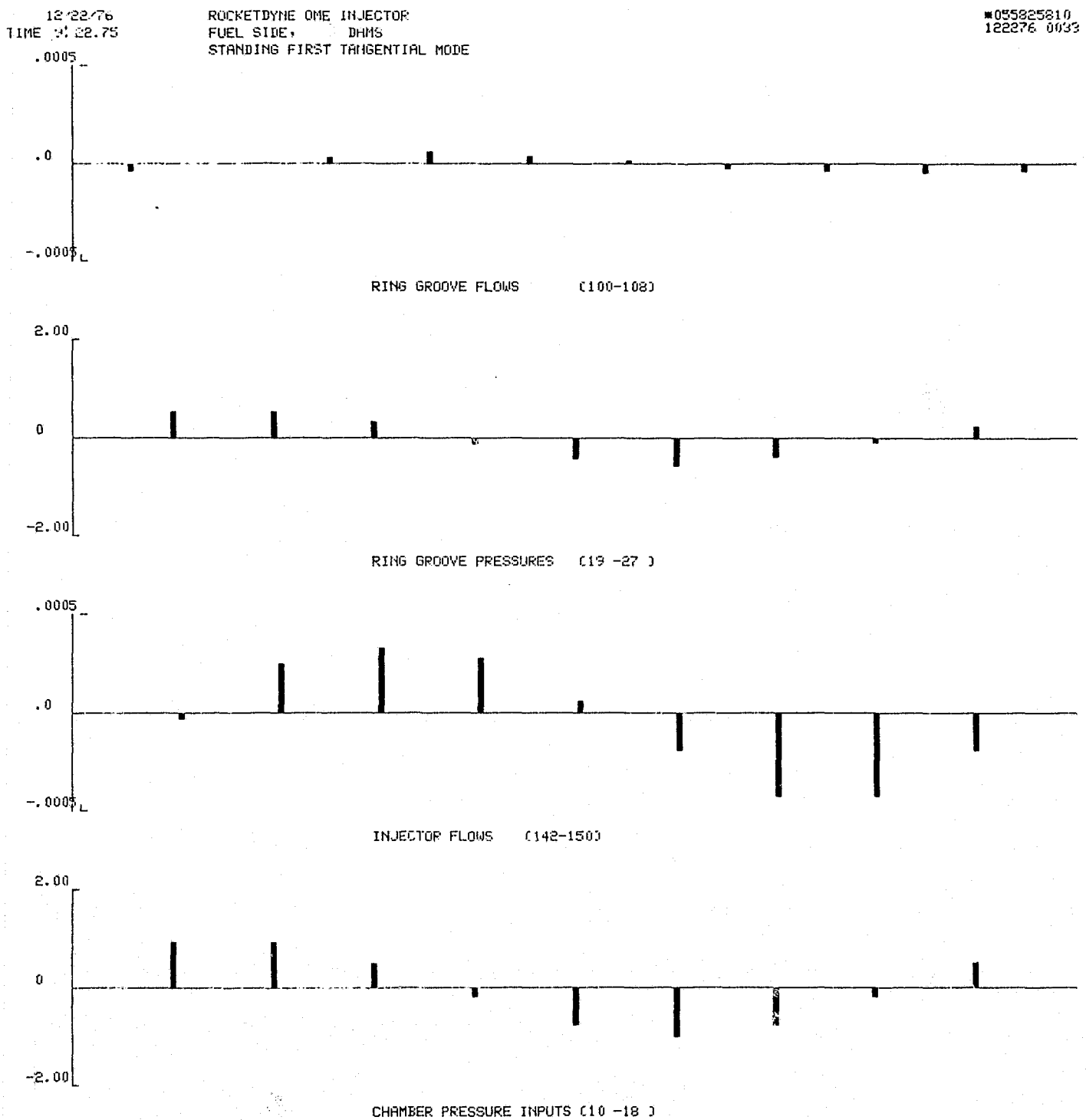

Figure 49. Results for Outer Fuel Ring Groove of Rocketdyne OME Technology Injector - Dams

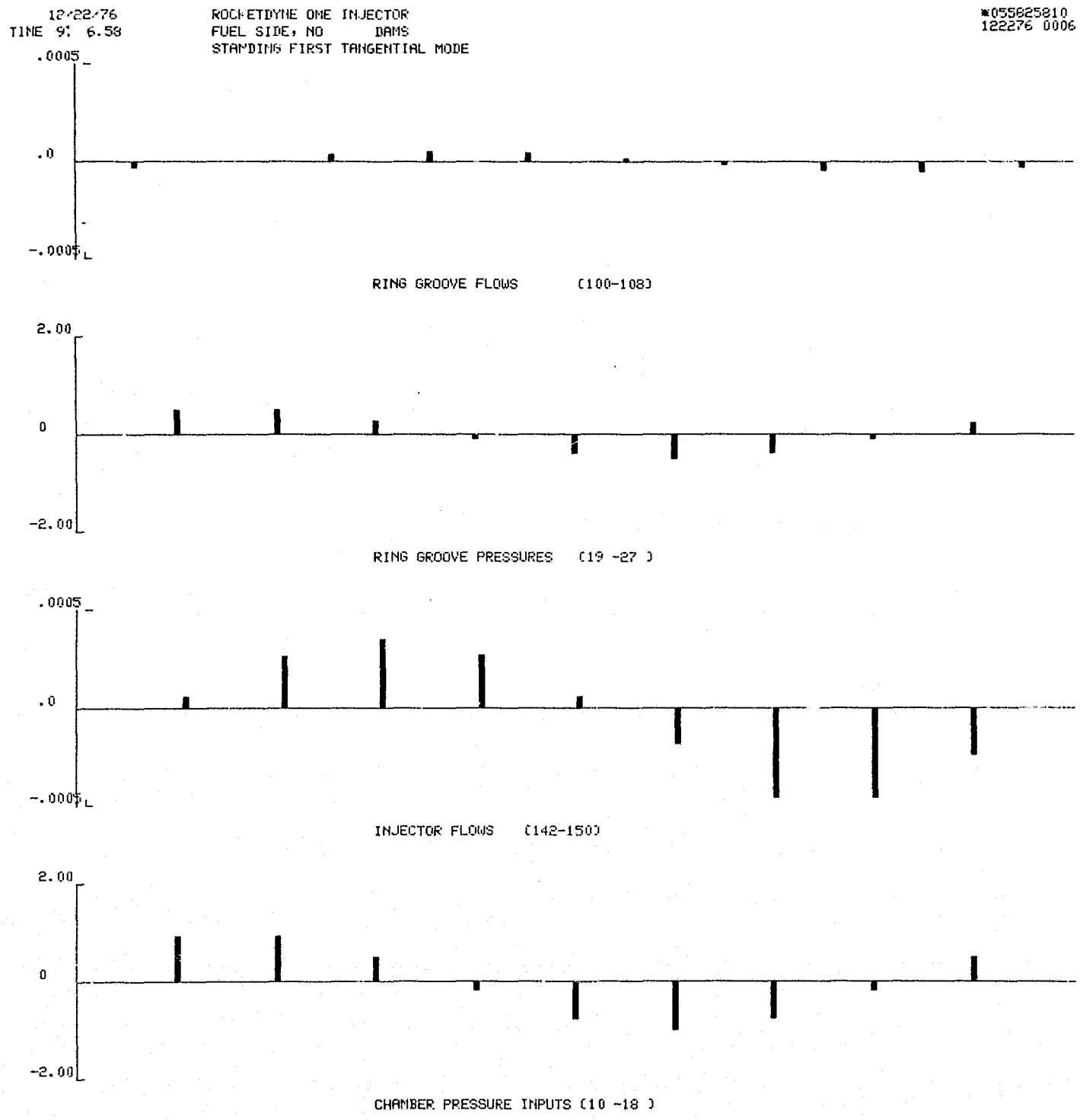

Figure 50. Results for Outer Fuel Ring Groove of Rocketdyne OME Technology Injector - No Dams

Rocketdyne Lance XRL Booster Injector

The lumped parameter representations for the fuel and oxidizer sides of the XRL are shown in Figs. 40 and 43. The XRL had a 1300 Hz mode with chamber pressure amplitudes of 200 to 300 psi peak-to-peak on every test. Incorporation of ring groove dams at four locations in each ring groove (directly above chamber baffle locations) eliminated the 1300 Hz mode. A summary of the results for the oxidizer and fuel sides are shown in Table IV. The oxidizer side amplitude was reduced to less than one-third of the original value while the fuel side was reduced to about 70 percent of its original value. Typical plots for the oxidizer and fuel side with and without dams are shown in Figs. 51 through 54. The model shows a substantial reduction in hydraulic coupling which is consistent with the observed results.

Aerojet OME Technology Injector

The lumped parameter representations for the fuel and oxidizer sides of the Aerojet injector are shown in Figs. 20 and 46. The Aerojet injector had a spinning 1T mode at about 2600 Hz with resurging at about 400 Hz. Installation of dams at the three null points in each of the outer 12 ring grooves was most successful in eliminating the instability.

Results of the model for the fuel and oxidizer side with and without dams is shown in Table V. These results show that the inclusion of dams on the oxidizer side had very little effect on the injector flowrates. However, inclusion of dams on the fuel side increased the injector oscillatory flow by a factor of 1.4.

Initially, this seemed inconsistent with the observed results. However, a re-examination of the resurging type of instability experienced by Aerojet was made to determine whether the model prediction of increased injector coupling with a spinning 1T chamber mode did indeed correlate with the experimental results. The resurging instability is reported to manifest itself as periodic low frequency (~400 Hz) burst of high frequency (>2000 Hz)

TABLE IV. XRL INJECTOR RESULTS

	Total Injector Flow		Total Vector Injector Flow		Total Injector Flow Proportioned by PC Amplitudes		Total Vector Injector Flow Proportioned by PC Amplitudes	
	Lb/Sec / Psi	% Flow / % P_c	Lb/Sec / Psi	% Flow / % P_c	Lb/Sec / Psi	% Flow / % P	Lb/Sec / Psi	% Flow / % P_c
XRL Fuel Side No Dams	.0551	1.34	.0544	1.32	.0551	1.34	.0544	1.32
XRL Fuel Side With Dams	.0397	.966	.0394	.958	.0397	.966	.0394	.958
XRL Ox Side No Dams	.1246	.911	.1242	.907	.1246	.911	.1242	.907
XRL Ox Side With Dams	.0386	.282	.0270	.198	.0386	.282	.0270	.198

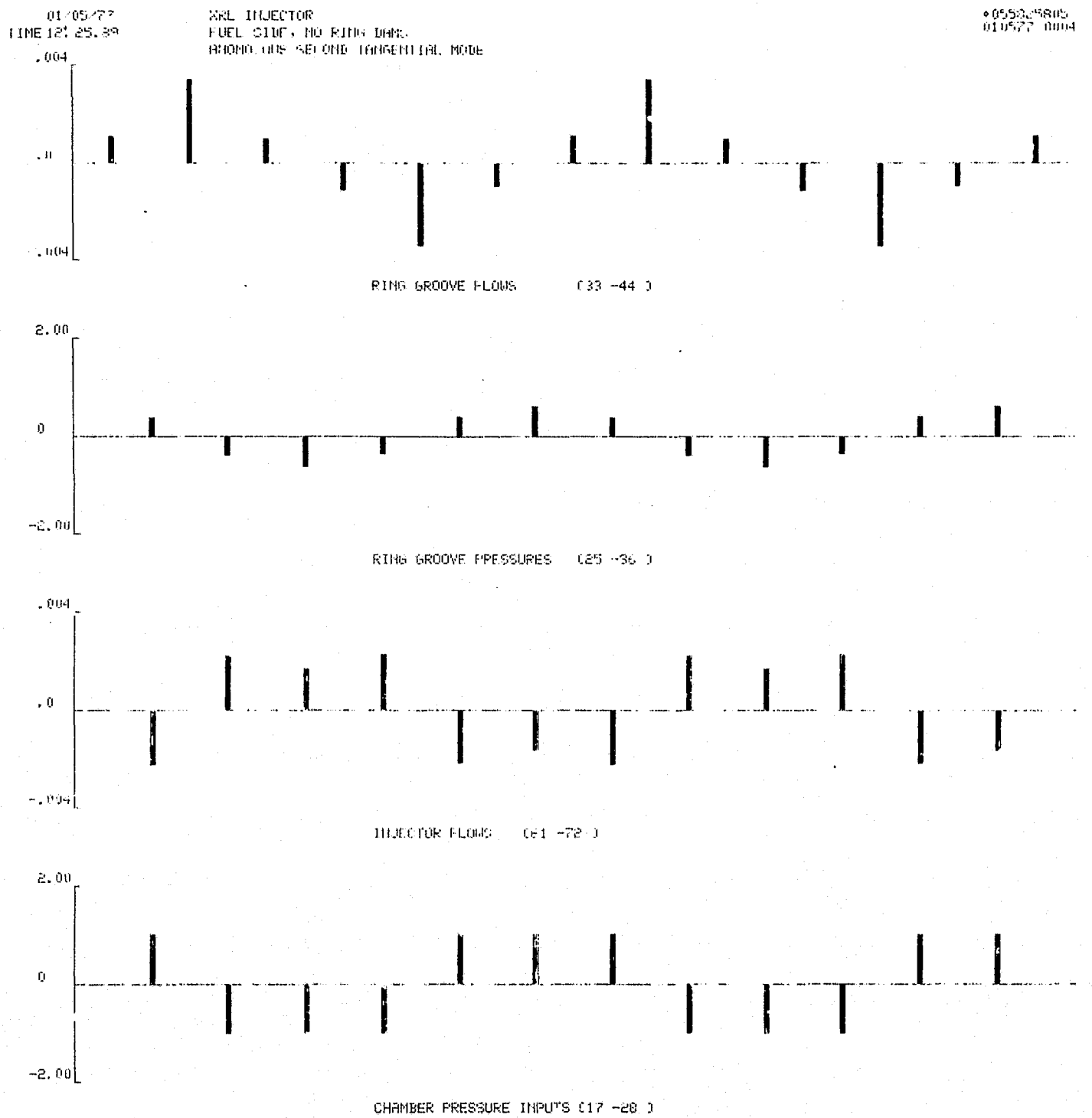

Figure 51. Results for Fuel Ring of XRL Injector - No Dams

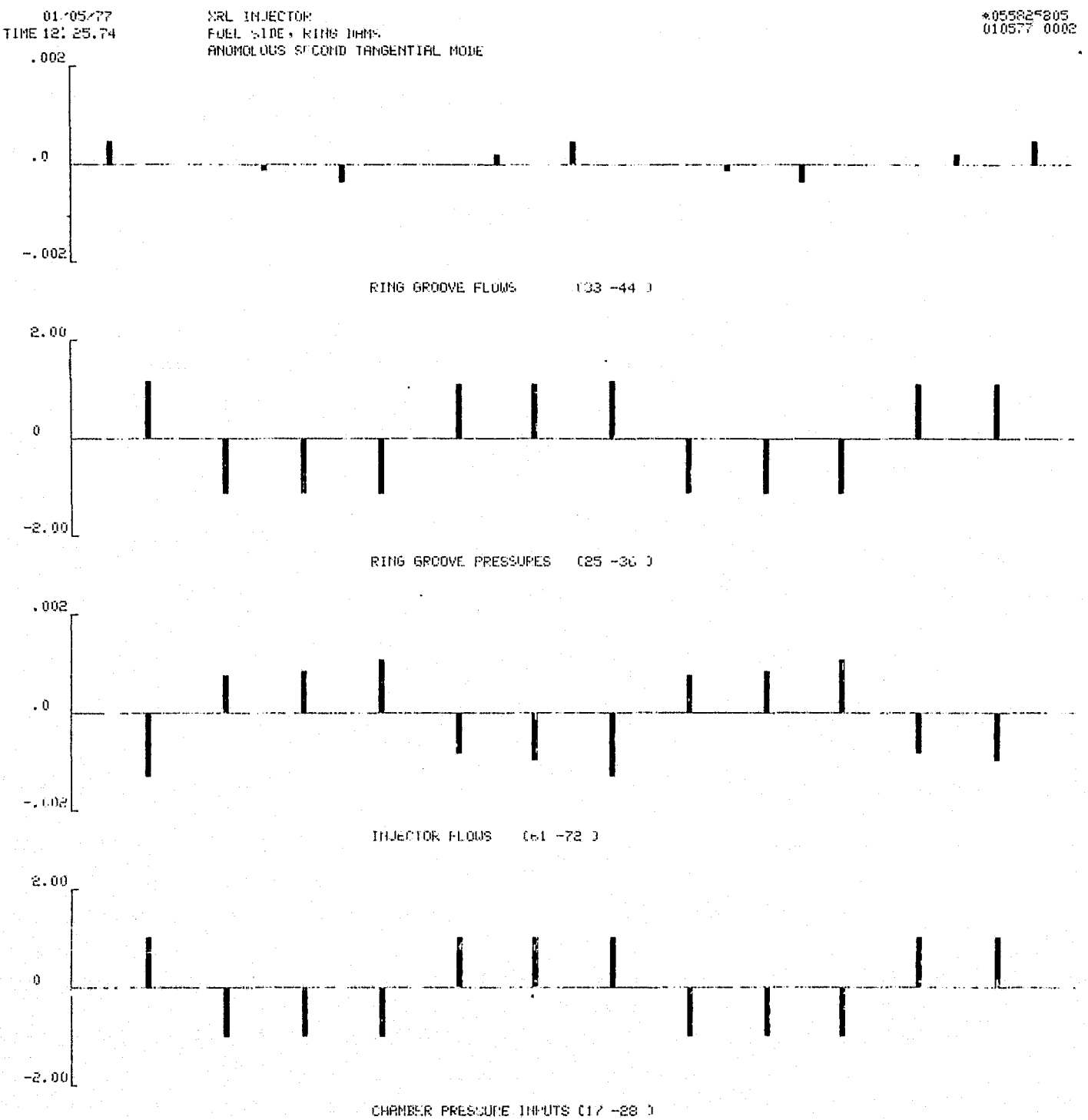

Figure 52. Results for Fuel Ring of XRL Injector - Dams

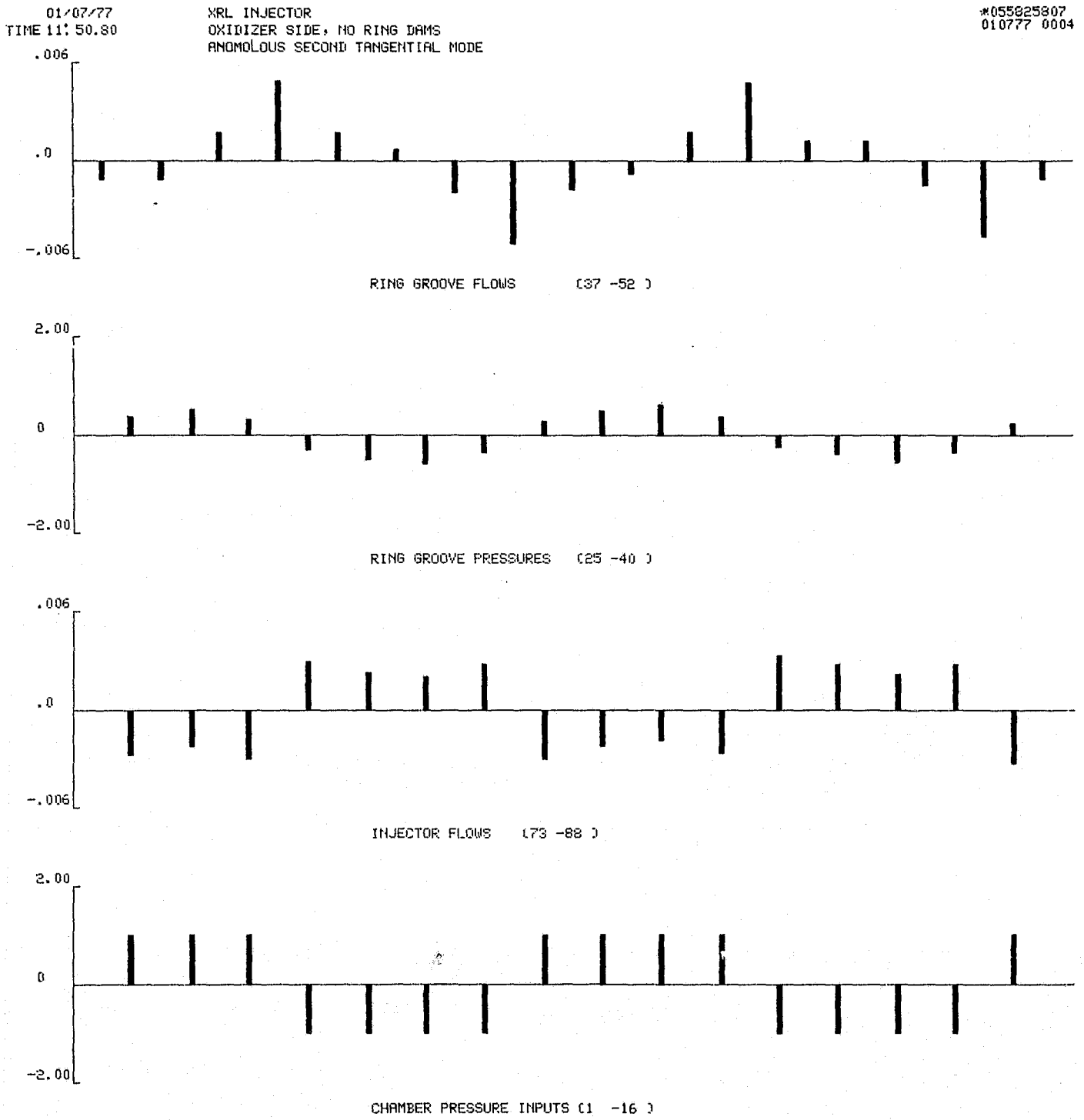

Figure 53. Results for Ox Ring of XRL Injector - No Dams

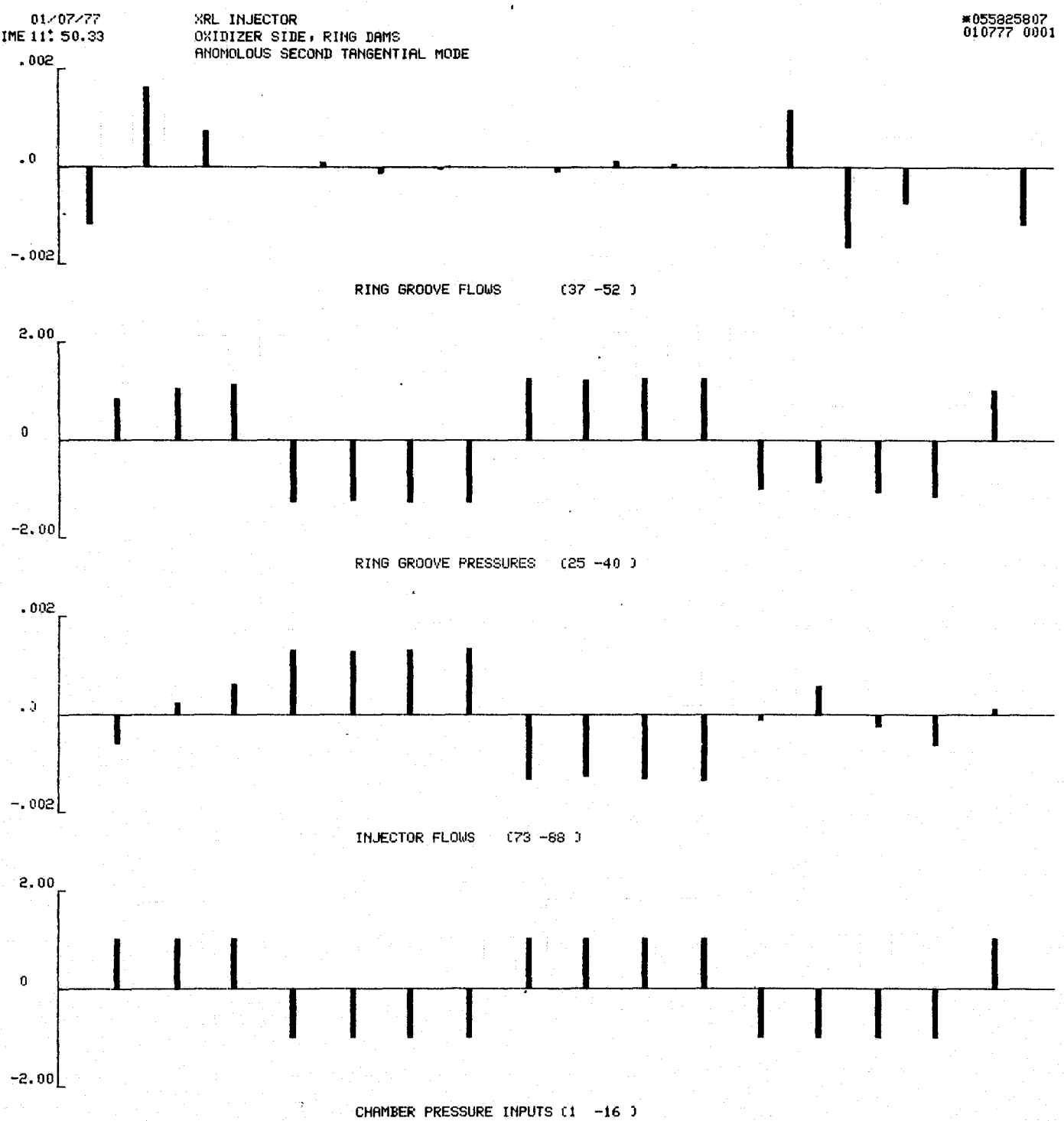

Figure 54. Results for Ox Ring of XRL Injector - Dams

TABLE V. AEROJET OME TECHNOLOGY INJECTOR RESULTS

	Total Injector Flow		Total Vector Injector Flow		Total Injector Flow Proportioned by PC Amplitudes		Total Vector Injector Flow Proportioned by PC Amplitudes	
	Lb/Sec / Psi	% Flow / % P_c	Lb/Sec / Psi	% Flow / % P_c	Lb/Sec / Psi	% Flow / % P_c	Lb/Sec / Psi	% Flow / % P_c
Fuel Side No Dams Spinning 1T	.0194	.337	.0167	.290	.0149	.259	.0130	.226
Fuel Side With Dams Spinning 1T	.0267	.464	.0228	.396	.0211	.367	.0179	.311
Ox Side No Dams Spinning 1T	.0636	.670	.0587	.619	.0545	.574	.0504	.531
Ox Side With Dams Spinning 1T	.0629	.663	.0584	.616	.0532	.561	.0496	.522

instability. The resurge is reported in Ref. 9 to originate with a low amplitude spinning 1T wave which grows rapidly in amplitude and frequency until it becomes a detonation wave. The detonation wave is made possible because of an accumulation of unburned propellant (due to poor mixing inherent with the x-doublet injector pattern) within the chamber near the injector face. The detonation wave makes one circuit of the chamber wiping out all propellant in its path. Pressure then decays (with acoustic ringing) and steady-state flow is re-established. Acoustic cavities were found to be unable to damp out the resurge and, in fact, were believed to foster the resurge by virtue of damping the high frequency modes which would normally promote mixing and combustion of the unburned propellant. Indeed, it is reported that when 1T damping was removed from the system*, the resurging disappeared to be replaced by a normal (standing) 1T or 2T acoustic mode. According to the engine hydraulic stability model, the addition of ring groove dams increases (not decreases) injector coupling with the spinning 1T chamber mode. This is interpreted as decreasing the 1T damping and promoting the mixing and combustion of the unburned propellant which otherwise would accumulate near the injector face and ultimately contribute to the resurging instability.** Therefore, it is concluded that the model does correlate with the observed test data.

Typical plots for the outer ring grooves with and without dams are shown in Figs. 55 through 58.

As described above, the engine hydraulic stability computer model was run for each of the "correlation" injectors with both pre-fix and post-fix injector model input. Examination and analysis of the model output reveals that the computer model successfully predicted that the fixes applied to each correlation injector would increase combustor stability with respect to the instability mode actually observed.

*By virtue of changes in the acoustic cavity.
**Sustainment of the 1T or 2T mode is precluded by the presence of the acoustic cavities.

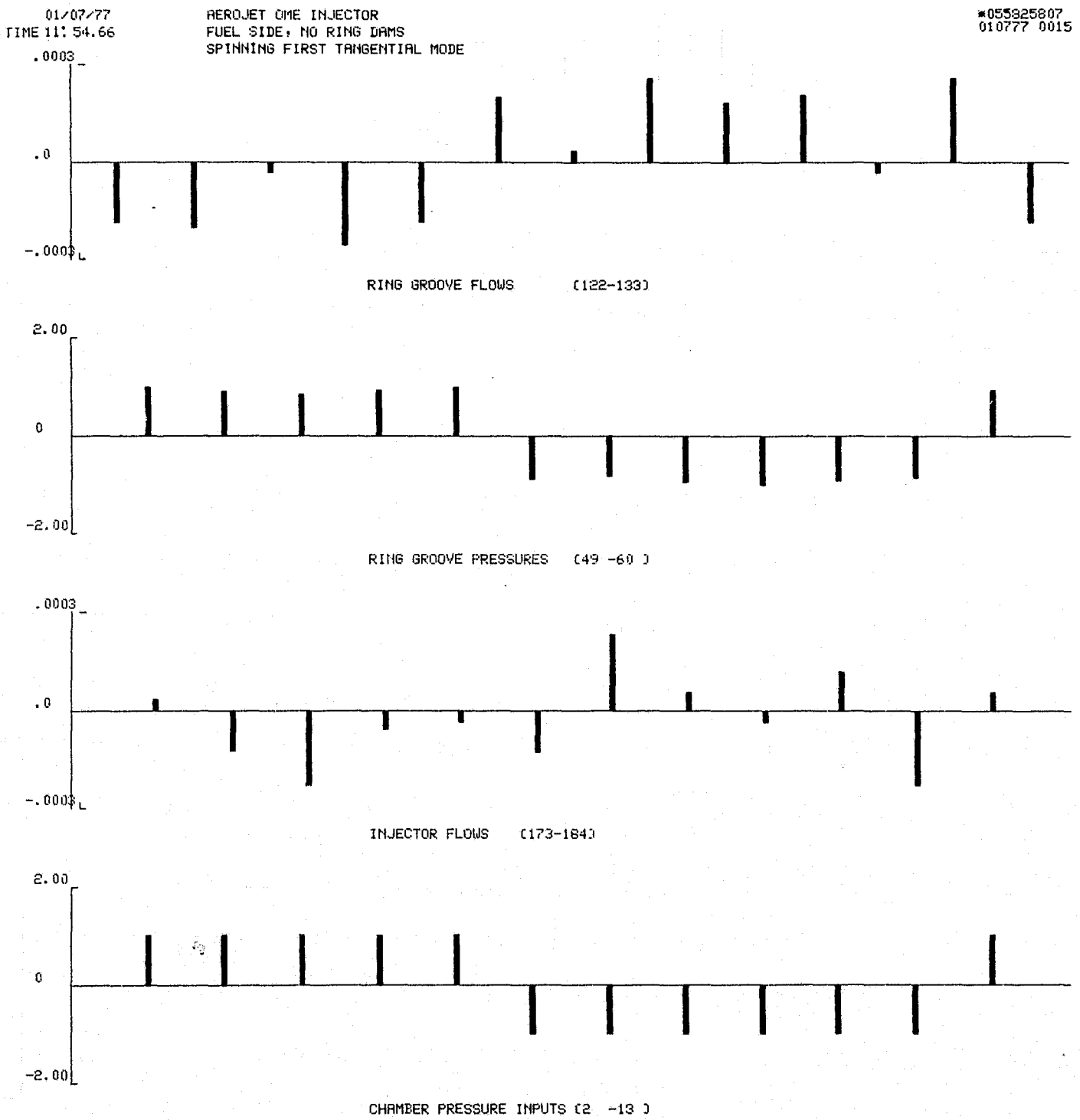

Figure 55. Results for Outer Fuel Ring Groove of Aerojet Injector - No Dams

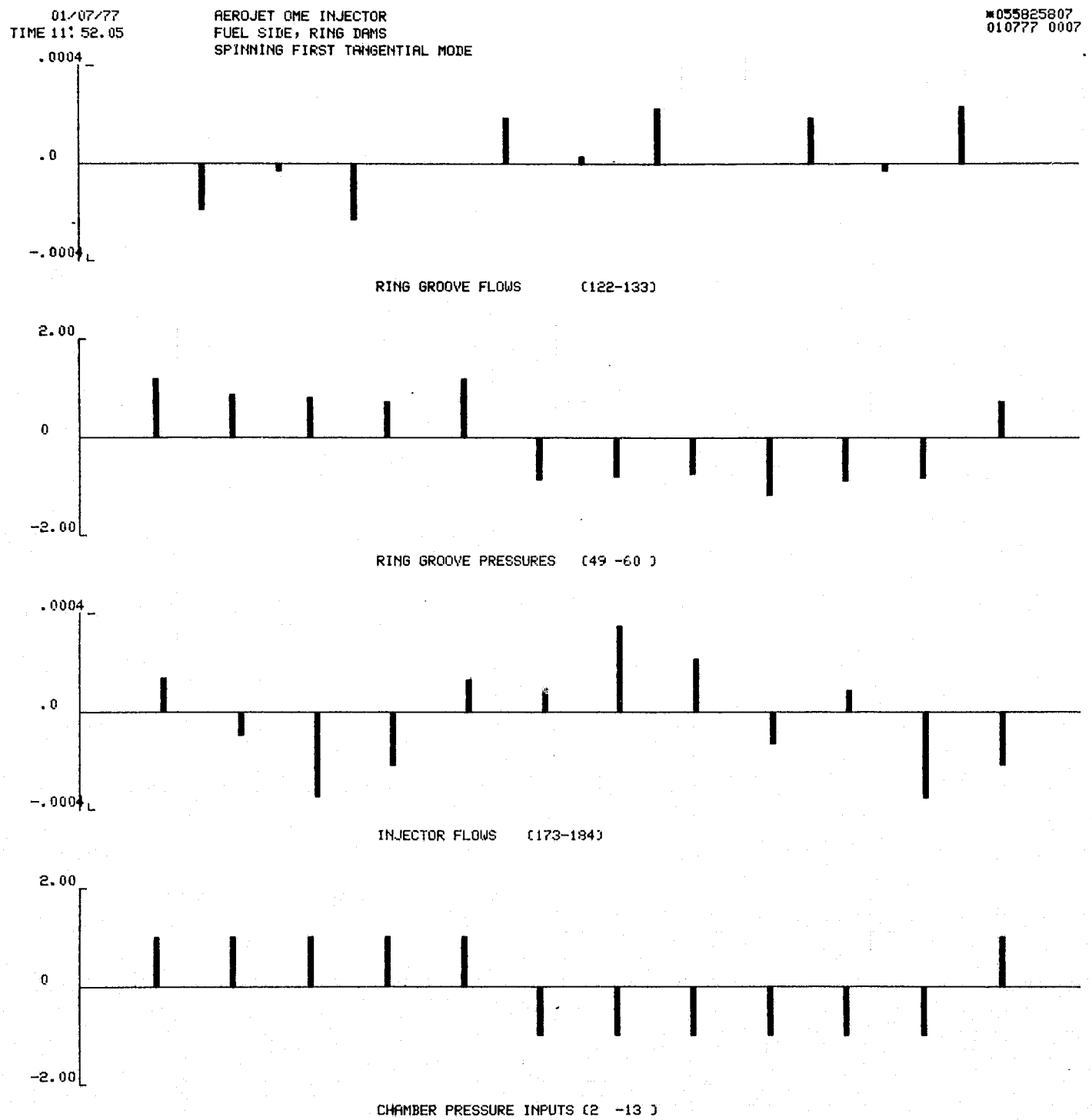

Figure 56. Results for Outer Fuel Ring Groove of Aerojet Injector - Dams

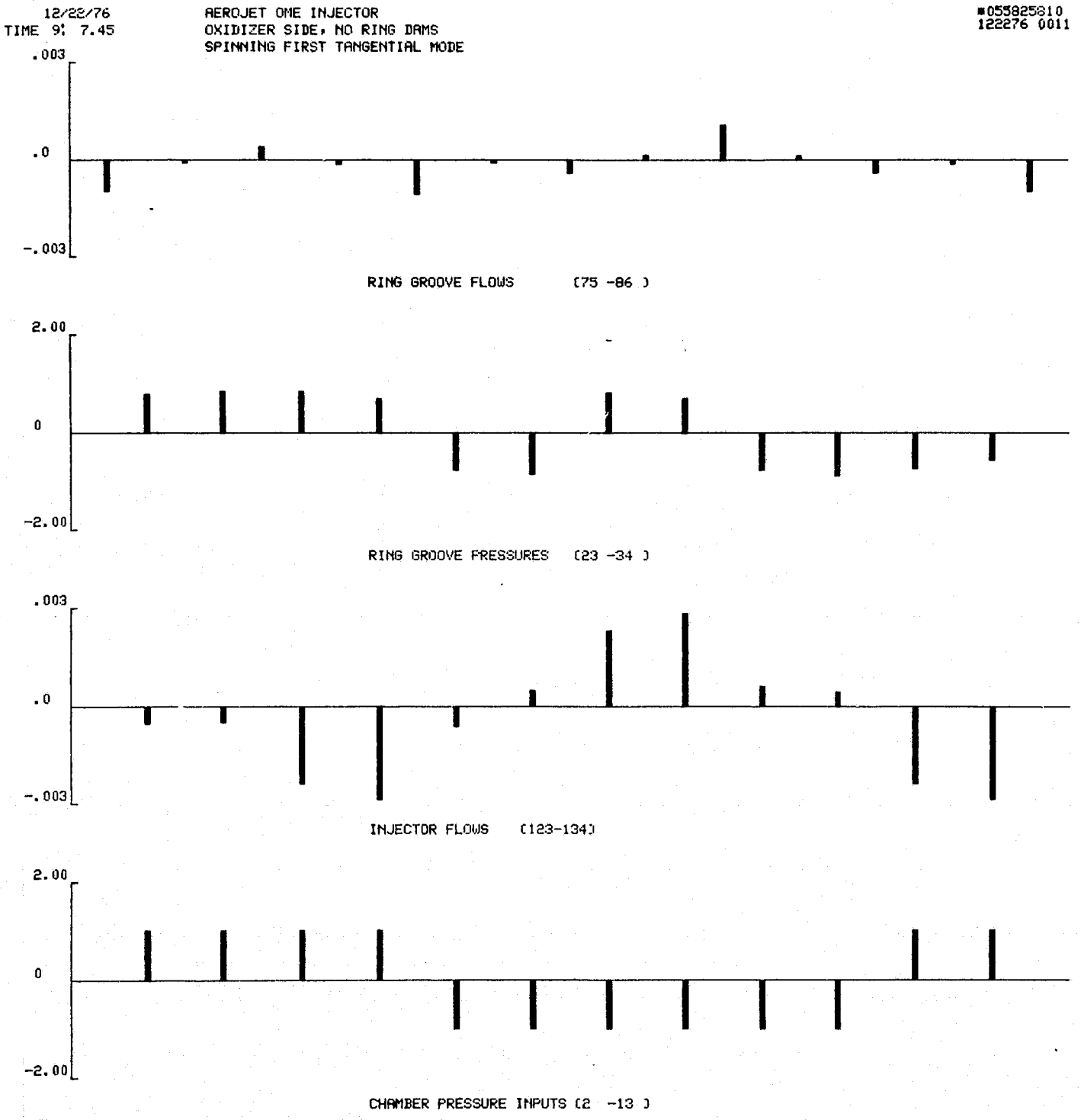

Figure 57. Results for Outer Ox Ring Groove of Aerojet Injector - No Dams

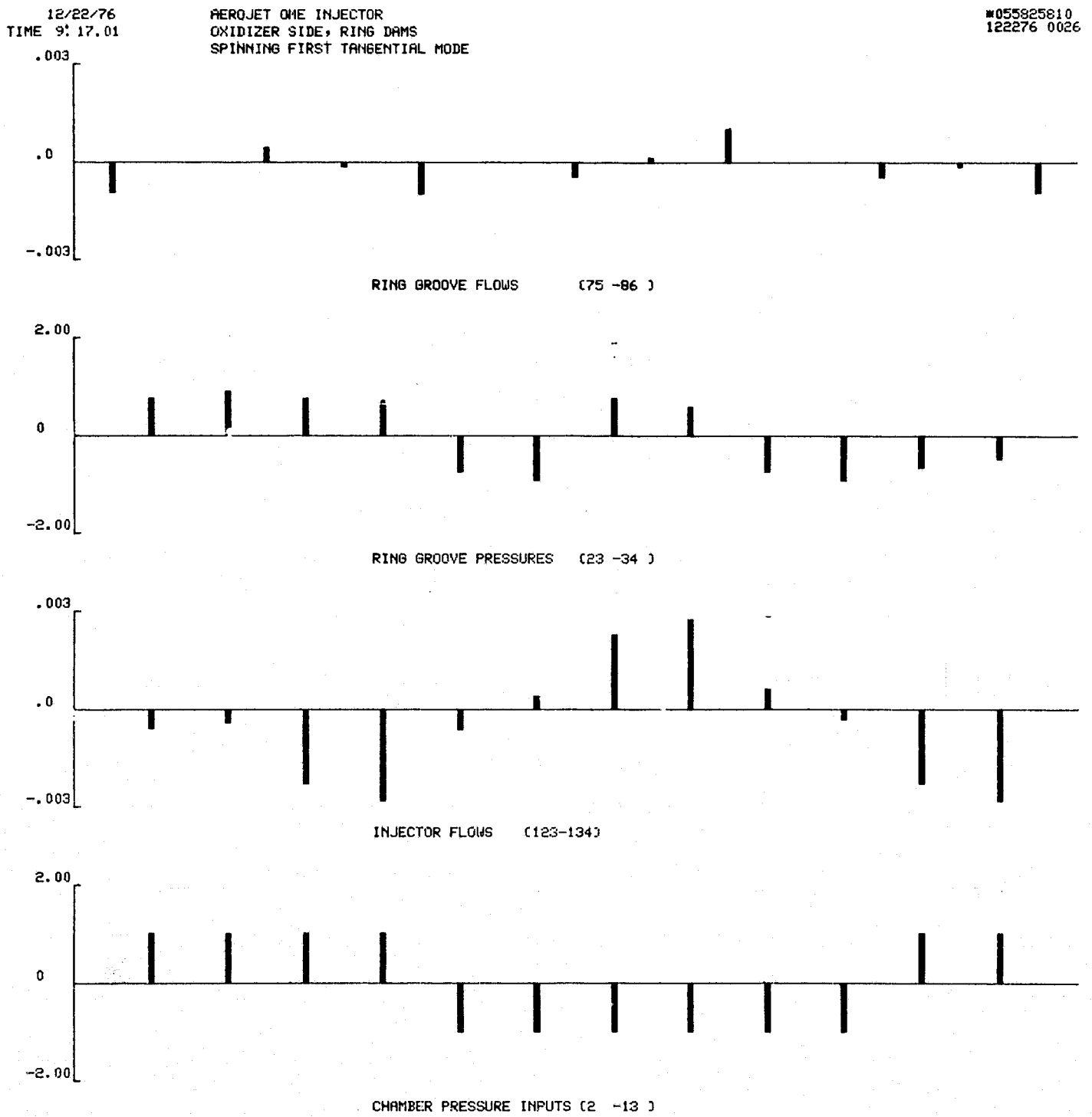

Figure 58. Results for Outer Ox Ring Groove of Aerojet Injector - Dams

SECTION V

SENSITIVITY ANALYSIS

A systematic parametric variation of some major injector design variables was made to gauge the effect of the individual parameters on injector gain and to identify the most sensitive variables. The objective of this task was to develop, to the maximum extent possible, generalized design criteria to preclude coupling between the injector hydraulics and the combustion process.

The "sensitive variables" whose effect was investigated (using the computer model) included:

1. Propellant temperature
2. Frequench of a particular mode
3. Resistance values of the injector orifices
4. Inertance values of the injector orifices
5. Ring groove area (i.e., capacitance and inertance of the ring groove nodes)
6. Chamber instability mode
7. Presence of dams

The effect of these variables was computed for the fuel and oxidizer sides of both the Aerojet and Rocketdyne OME technology injectors. Model predictions are summarized in Tables VI through IX. These same predictions are also displayed graphically in Figs. 59 through 67 where the gain plotted is based on the total vector injector flow proportioned by P_c amplitude.

It is evident from Tables VI through IX and Figs. 60, 62, 64, and 66 that any error in linearized resistance input to the model due to disagreement between calculated and experimental injector ΔP^* is unimportant from a

---

* See Section IV.

TABLE VI. MODEL PREDICTION OF AEROJET FUEL SIDE GAIN*

Off Nominal Condition**		Ring Groove Dams							
Variable	Input Value	No	No	No	No	Yes	Yes	Yes	Yes
		Tot. Inj. Flow	Tot. Vec. Inj. Flow	Tot. α P_c Amp.	Tot. Vec. α P_c Amp.	Tot. Inj. Flow	Tot. Vec. Inj. Flow	Tot. α P_c Amp.	Tot. Vec. α P_c Amp.
Nominal**		.0194	.0167	.0149	.0130	.0267	.0228	.0211	.0179
Inj. temp.	70°F	.0129	.00637	.0104	.00637	.0160	.00414	.0127	.00424
Inj. temp.	200°F	.0151	.0113	.0112	.00863	.0231	.0183	.0181	.0143
Inj. temp.	300°F	.0265	.0242	.0210	.0192	.0308	.0278	.0246	.0221
Frequency	2200 Hz	.0117	.00304	.00866	.00315	.0190	.0113	.0149	.00895
Frequency	3000 Hz	.0283	.0261	.0224	.0207	.0325	.0293	.0259	.0233
Resistance	0.75 R nom	.0207	.0167	.0156	.0127	.0296	.0238	.0232	.0185
Resistance	1.25 R nom	.0184	.0164	.0143	.0129	.0243	.0214	.0193	.0169
Orifice inertance	0.75 I nom	.0188	.0161	.0144	.0126	.0256	.0218	.0202	.0171
Orifice inertance	1.25 I nom	.0200	.0173	.0154	.0135	.0280	.0239	.0221	.0188
Orifice inertance	2.0 I nom	.0224	.0197	.0173	.0153	.0324	.0281	.0257	.0222
Orifice inertance	3.0 I nom	.0267	.0241	.0208	.0189	.0392	.0348	.0312	.0276
Ring groove area	-25% nom***	.0196	.0169	.0150	.0131	.0249	.0214	.0195	.0167
Ring groove area	+25% nom****	.0190	.0164	.0147	.0128	.0284	.0241	.0227	.0191
Mode	Standing 1T	.0145	.00938	.00736	.00654	.0196	.0124	.0101	.00900
Mode	Standing 2T	.0185	.0148	.00958	.00810	.0181	.0142	.00984	.00785

*Gain, (lb/sec)/psi, is shown for each of the four single value summations.

**Nominal conditions include T_{inj} = 230°F, f = 2600 Hz, spinning 1T mode

***0.75 C_{nom}, 1.333 I_{nom}

****1.25 C_{nom}, 0.8 I_{nom}

TABLE VII. MODEL PREDICTION OF AEROJET OX SIDE GAIN*

Off Nominal Condition**		Ring Groove Dams							
Variable	Input Value	No	No	No	No	Yes	Yes	Yes	Yes
		Tot. Inj. Flow	Tot. Vec. Inj. Flow	Tot. α P_c Amp.	Tot. Vec. α P_c Amp.	Tot. Inj. Flow	Tot. Vec. Inj. Flow	Tot. α P_c Amp.	Tot. Vec. α P_c Amp.
Nominal		.0636	.0587	.0545	.0504	.0629	.0584	.0532	.0496
Frequency	2200 Hz	.0580	.0512	.0495	.0441	.0618	.0542	.0521	.0462
Frequency	3000 Hz	.0560	.0522	.0479	.0446	.0543	.0516	.0459	.0438
Resistance	0.75 R nom	.0829	.0762	.0710	.0656	.0827	.0759	.0701	.0647
Resistance	1.25 R nom	.0521	.0481	.0446	.0411	.0514	.0481	.0434	.0407
Orifice inertance	0.75 I nom	.0627	.0574	.0536	.0492	.0622	.0574	.0526	.0487
Orifice inertance	1.25 I nom	.0629	.0585	.0539	.0501	.0618	.0577	.0524	.0491
Orifice inertance	2.0 I nom	.0533	.0504	.0457	.0432	.0518	.0492	.0440	.0418
Orifice inertance	3.0 I nom	.0390	.0374	.0334	.0320	.0378	.0364	.0321	.0310
Ring groove area	-25% nom	.0609	.0563	.0519	.0481	.0598	.0560	.0509	.0477
Ring groove area	+25% nom	.0661	.0610	.0568	.0524	.0653	.0603	.0559	.0517
Mode	Standing 1T	.0432	.0388	.0269	.0256	.0429	.0389	.0264	.0253
Mode	Standing 2T	.0219	.0164	.0127	.00970	.0218	.0134	.0140	.00844

*Gain (lb/sec)/psi, is shown for each of the four single value summations.

**Nominal conditions include f = 2600 Hz, spinning 1T mode.

TABLE VIII. MODEL PREDICTION OF ROCKETDYNE FUEL SIDE GAIN*

Off Nominal Condition**		Annular Manifold Dams							
Variable	Input Value	No	No	No	No	Yes	Yes	Yes	Yes
		Tot. Inj. Flow	Tot. Vec. Inj Flow	Tot. α P_c Amp.	Tot. Vec. α P_c Amp.	Tot. Inj. Flow	Tot. Vec. Inj. Flow	Tot. α P_c Amp.	Tot. Vec. α P_c Amp.
Nominal		.00633	.00632	.00442	.00441	.00521	.00508	.00371	.00367
Frequency	2200 Hz	.00818	.00817	.00567	.00566	.00734	.00731	.00517	.00516
Frequency	3000 Hz	.00460	.00457	.00325	.00324	.00331	.00224	.00212	.00185
Resistance	0.75 R nom	.00637	.00636	.00445	.00445	.00523	.00511	.00373	.00370
Resistance	1.25 R nom	.00627	.00626	.00437	.00437	.00518	.00504	.00368	.00364
Orifice inertance	0.333 I nom	.00856	.00849	.00601	.00598	.00715	.00648	.00497	.00480
Orifice inertance	0.50 I nom	.00786	.00782	.00551	.00550	.00652	.00606	.00457	.00445
Orifice inertance	0.75 I nom	.00701	.00699	.00490	.00490	.00578	.00552	.00409	.00402
Orifice inertance	1.25 I nom	.00577	.00576	.00402	.00401	.00477	.00470	.00340	.00338
Ring groove area	-25% nom	.00623	.00622	.00437	.00437	.00512	.00494	.00366	.00361
Ring groove area	+25% nom	.00661	.00659	.00463	.00463	.00520	.00375	.00375	.00373
Mode	Spinning 1T	.00988	.00986	.00863	.00882	.00827	.00805	.00750	.00735
Ring groove dams	—	.00524	.00510	.00382	.00378	.00468	.00318	.00310	.00266

*Gain (lb/sec)/psi, is shown for each of the four single value summations.

**Nominal conditions include T_{inj} = 200°F, f = 2600 Hz, standing 1T mode.

TABLE IX. MODEL PREDICTION OF ROCKETDYNE OX SIDE GAIN*

Off Nominal Condition**		Ring Groove Dams							
Variable	Input Value	No	No	No	No	Yes	Yes	Yes	Yes
		Tot. Inj. Flow	Tot. Vec. Inj Flow	Tot. α P_c Amp.	Tot. α P_c Amp.	Tot. Vec. α P_c Amp.	Tot. Vec. Inj. Flow	Tot. α P_c Amp.	Tot. Vec. α P_c Amp.
Nominal		.00551	.00550	.00370	.00370	.00535	.00535	.00346	.00346
Frequency	2200 Hz	.00738	.00737	.00503	.00503	.00721	.00721	.00478	.00477
Frequency	3000 Hz	.00386	.00386	.00251	.00251	.00371	.00371	.00228	.00228
Resistance	0.75 R nom	.00552	.00552	.00371	.00371	.00537	.00536	.00347	.00347
Resistance	1.25 R nom	.00529	.00548	.00369	.00368	.00534	.00533	.00345	.00345
Orifice inertance	0.333 I nom	.00712	.00710	.00468	.00467	.00686	.00684	.00432	.00431
Orifice inertance	0.50 I nom	.00661	.00660	.00438	.00437	.00639	.00638	.00406	.00405
Orifice inertance	0.75 I nom	.00600	.00599	.00400	.00400	.00582	.00581	.00373	.00373
Orifice inertance	1.25 I nom	.00510	.00509	.00344	.00344	.00497	.00496	.00323	.00323
Ring groove area	-25% nom	.00558	.00558	.00376	.00376	.00499	.00498	.00322	.00322
Ring groove area	+25% nom	.00543	.00542	.00363	.00361	.00523	.00523	.00333	.00332
Mode	Spinning 1T	.00880	.00880	.00739	.00739	.00830	.00820	.00701	.00691

*Gain (lb/sec)/psi, is shown for each of the four single value summations.

**Nominal conditions include f = 2600 Hz, standing 1T mode.

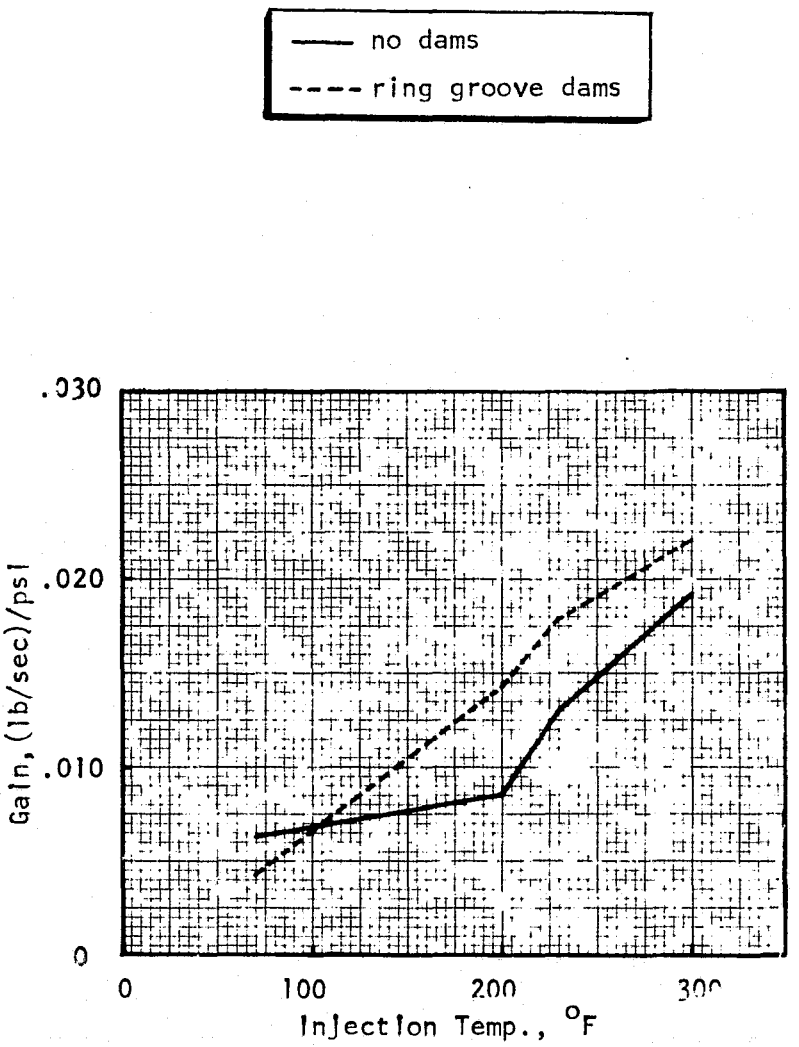

Figure 59. Effect of Injection Temperature on Gain for Fuel Side of Aerojet OME Technology Injector

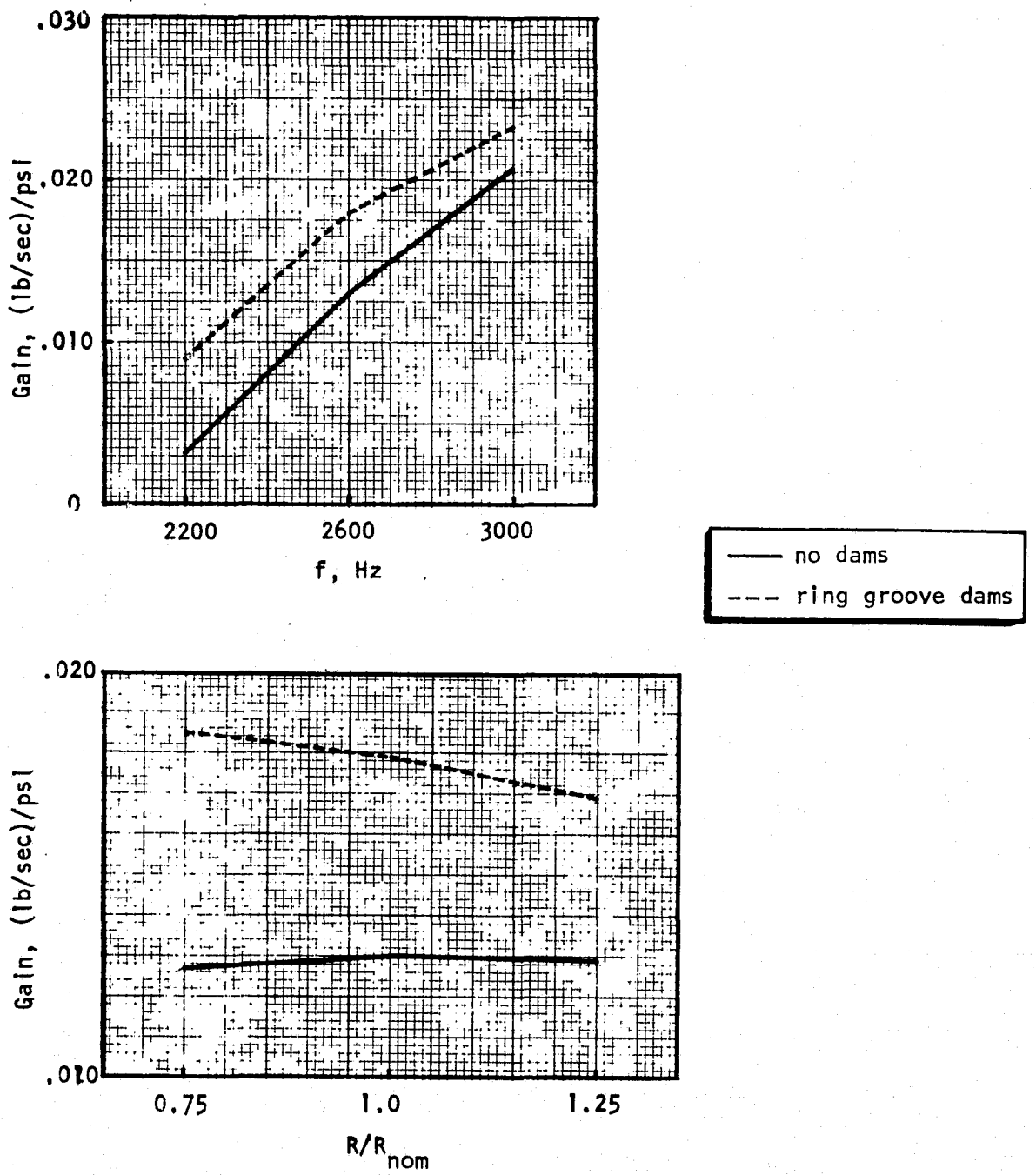

Figure 60 . Effect of Frequency and Resistance on Gain for Fuel Side of Aerojet OME Technology Injector

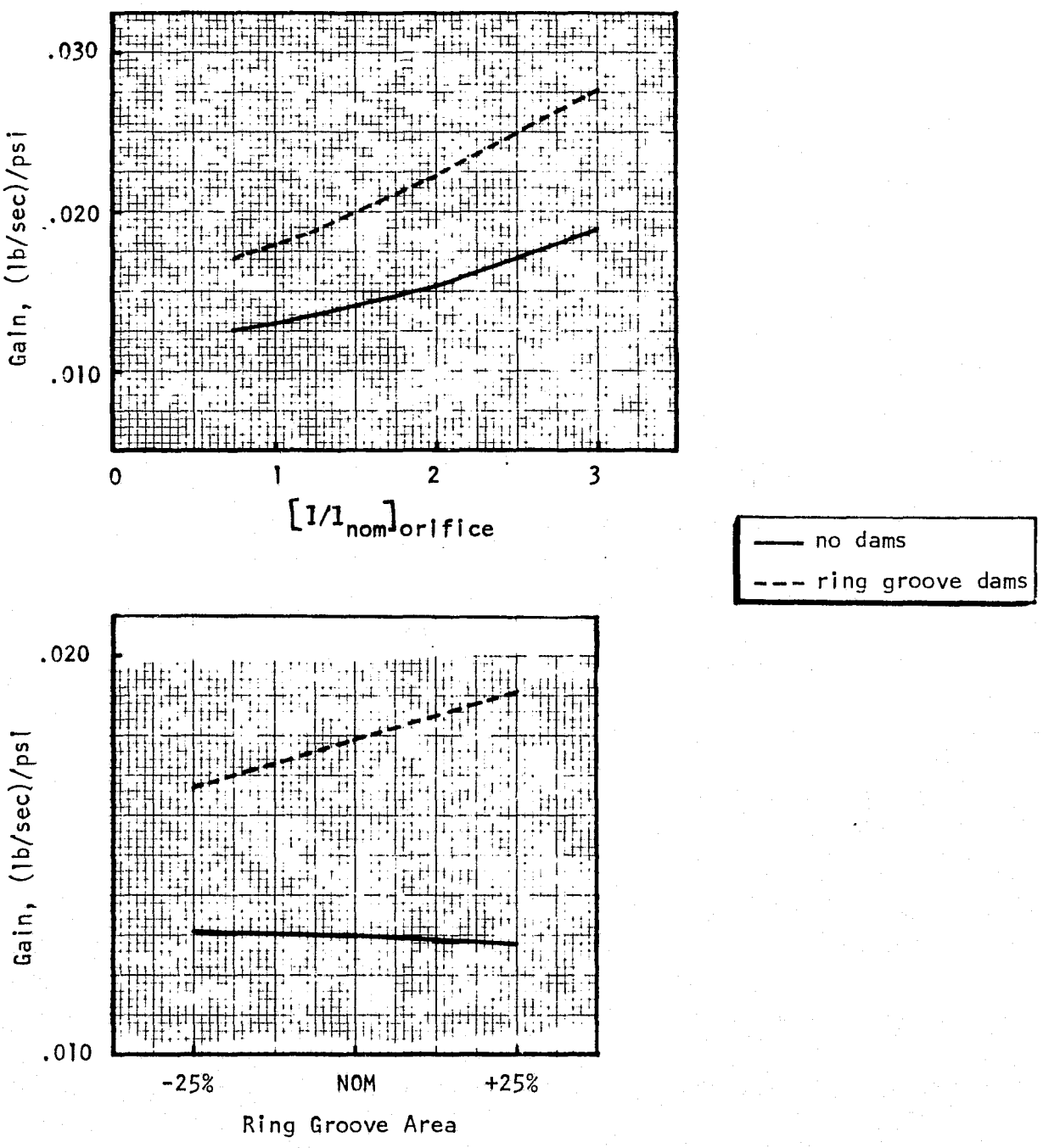

Figure 61. Effect of Orifice Inertance and Ring Groove Area on Gain for Fuel Side of Aerojet OME Technology Injector

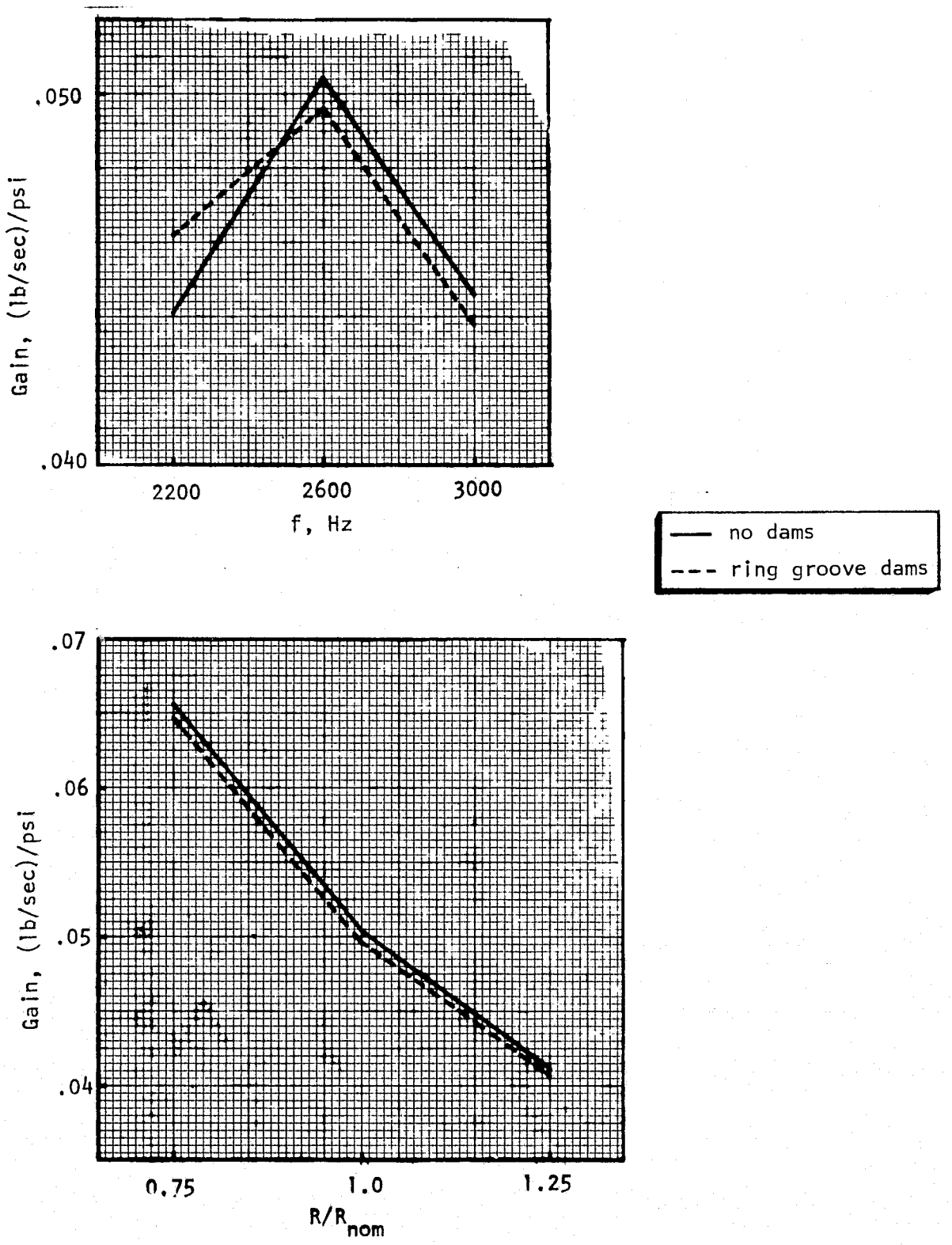

Figure 62. Effect of Frequency and Resistance on Gain for Oxidizer Side of Aerojet OME Technology Injector

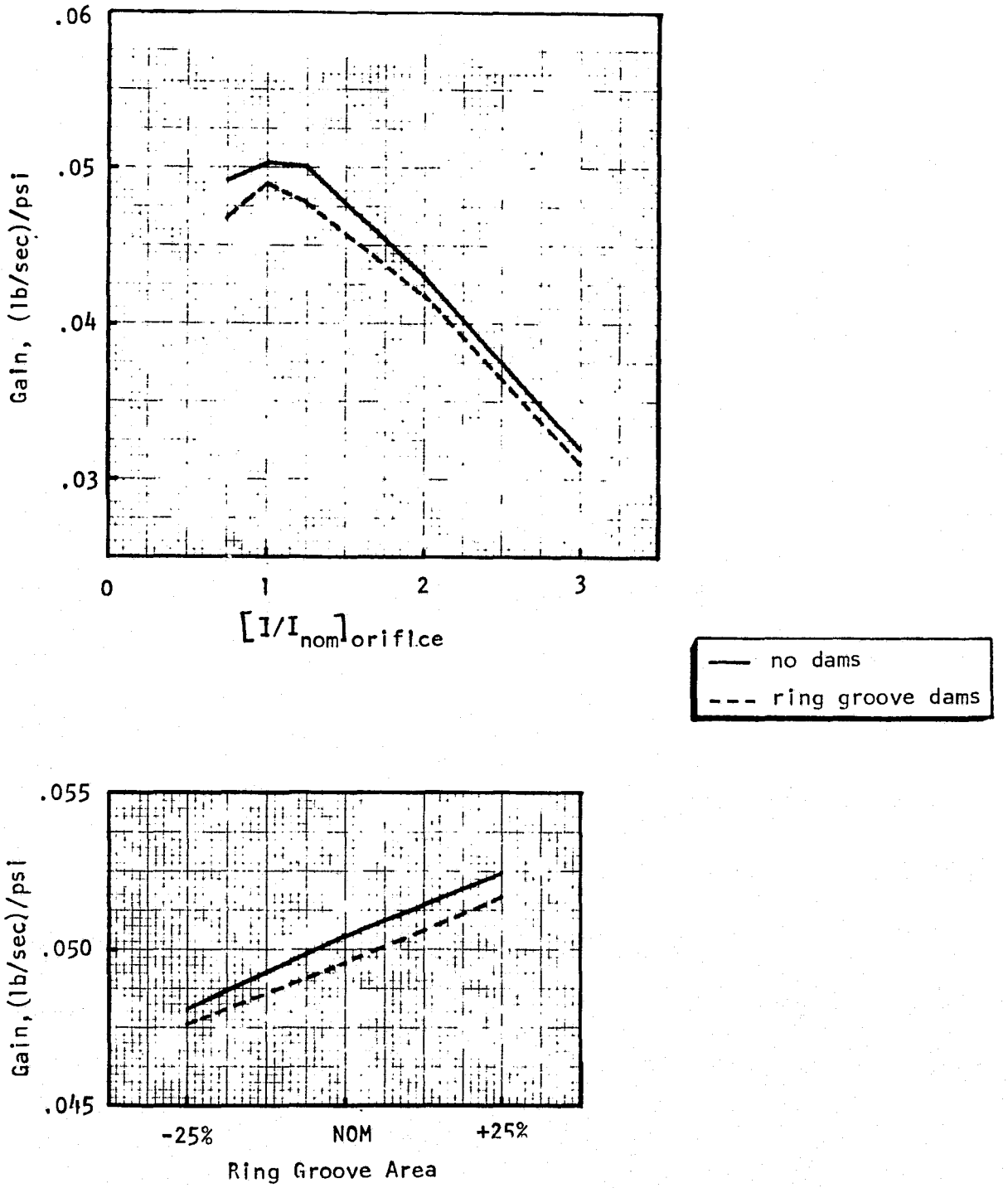

Figure 63 . Effect of Orifice Inertance and Ring Groove Area on Gain for Oxidizer Side of Aerojet OME Technology Injector

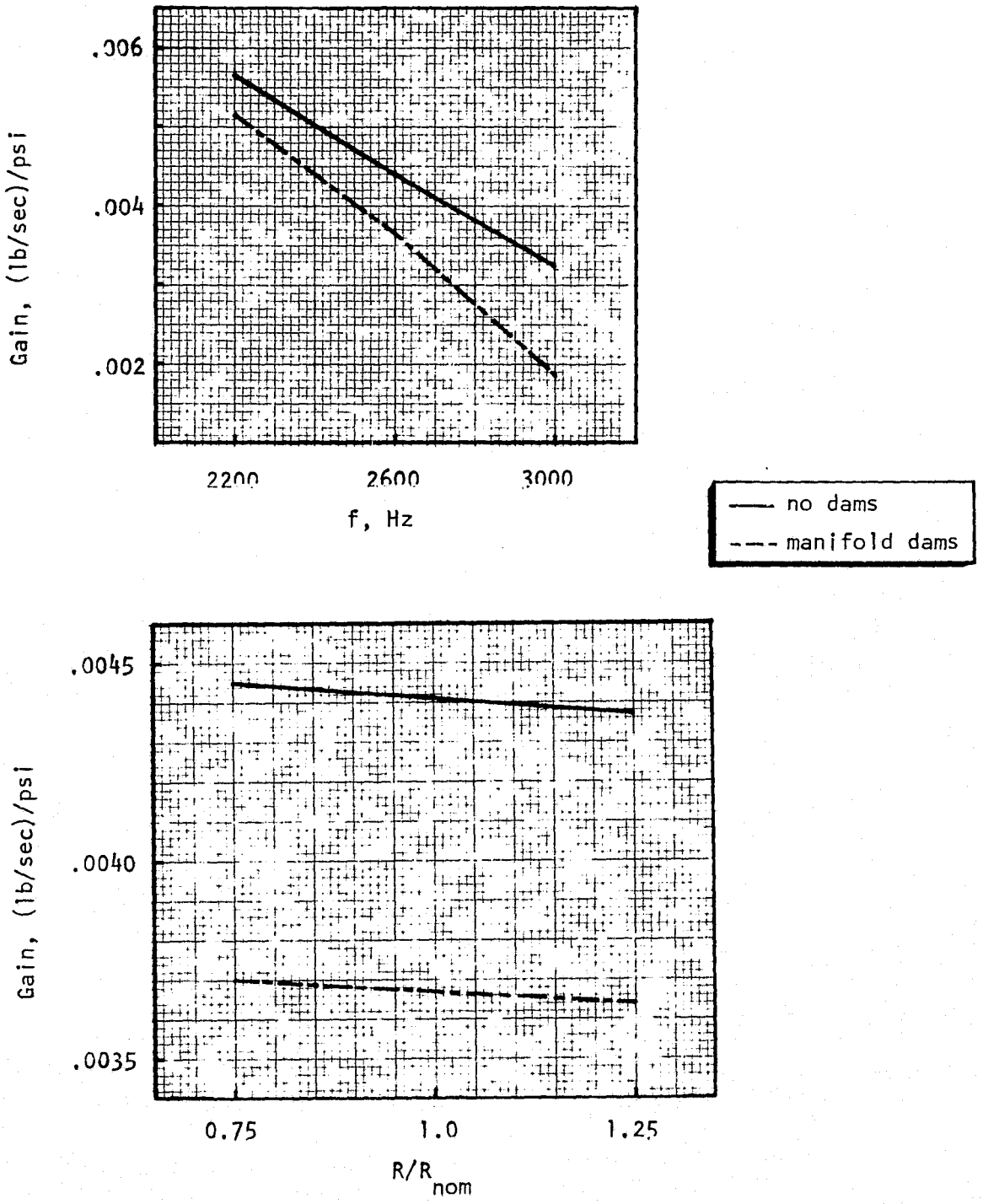

Figure 64. Effect of Frequency and Resistance on Gain for Fuel Side of Rocketdyne OME Technology Injector

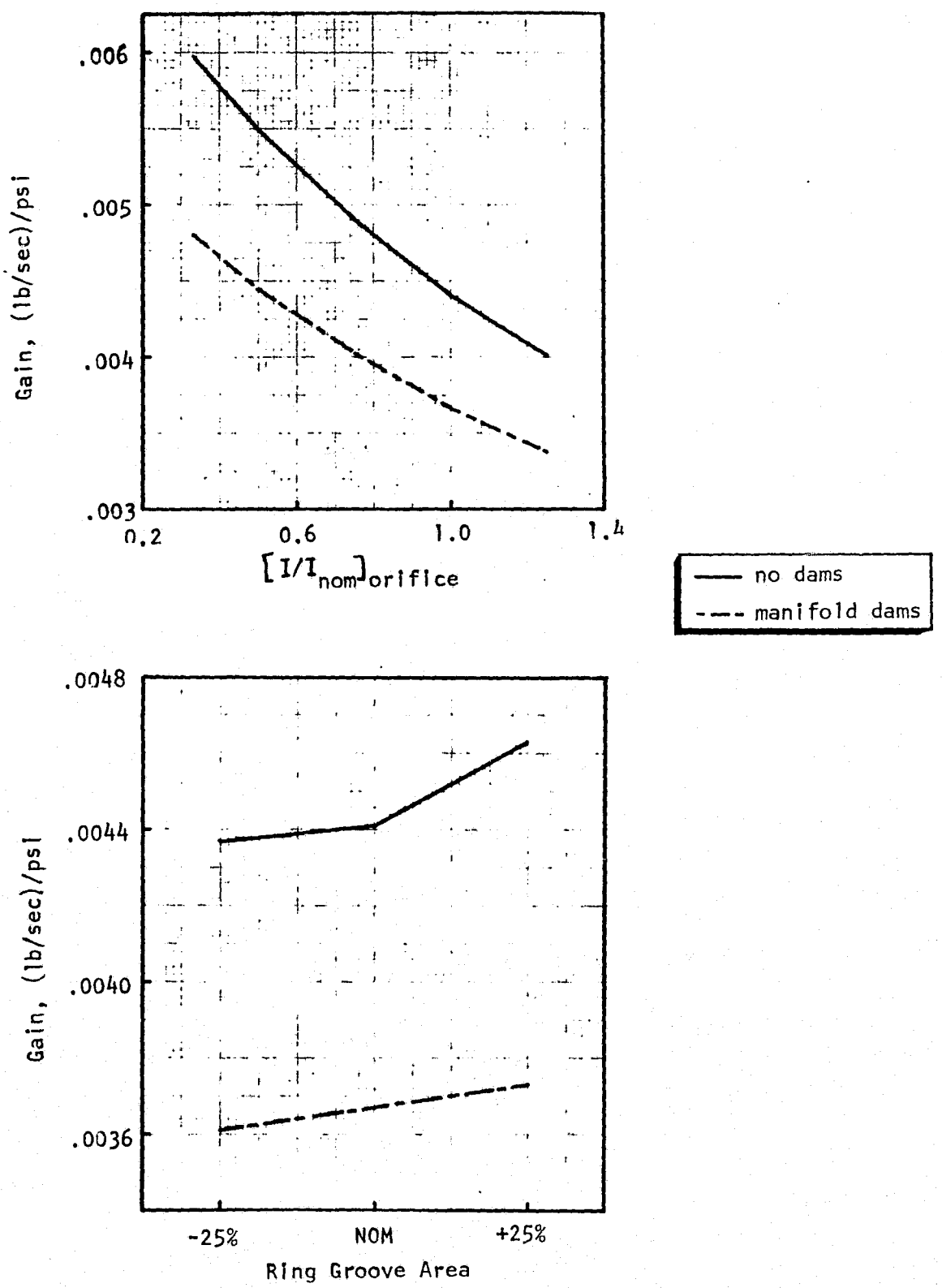

Figure 65. Effect of Orifice Inertance and Ring Groove Area on Gain for Fuel Side of Rocketdyne OME Technology Injector

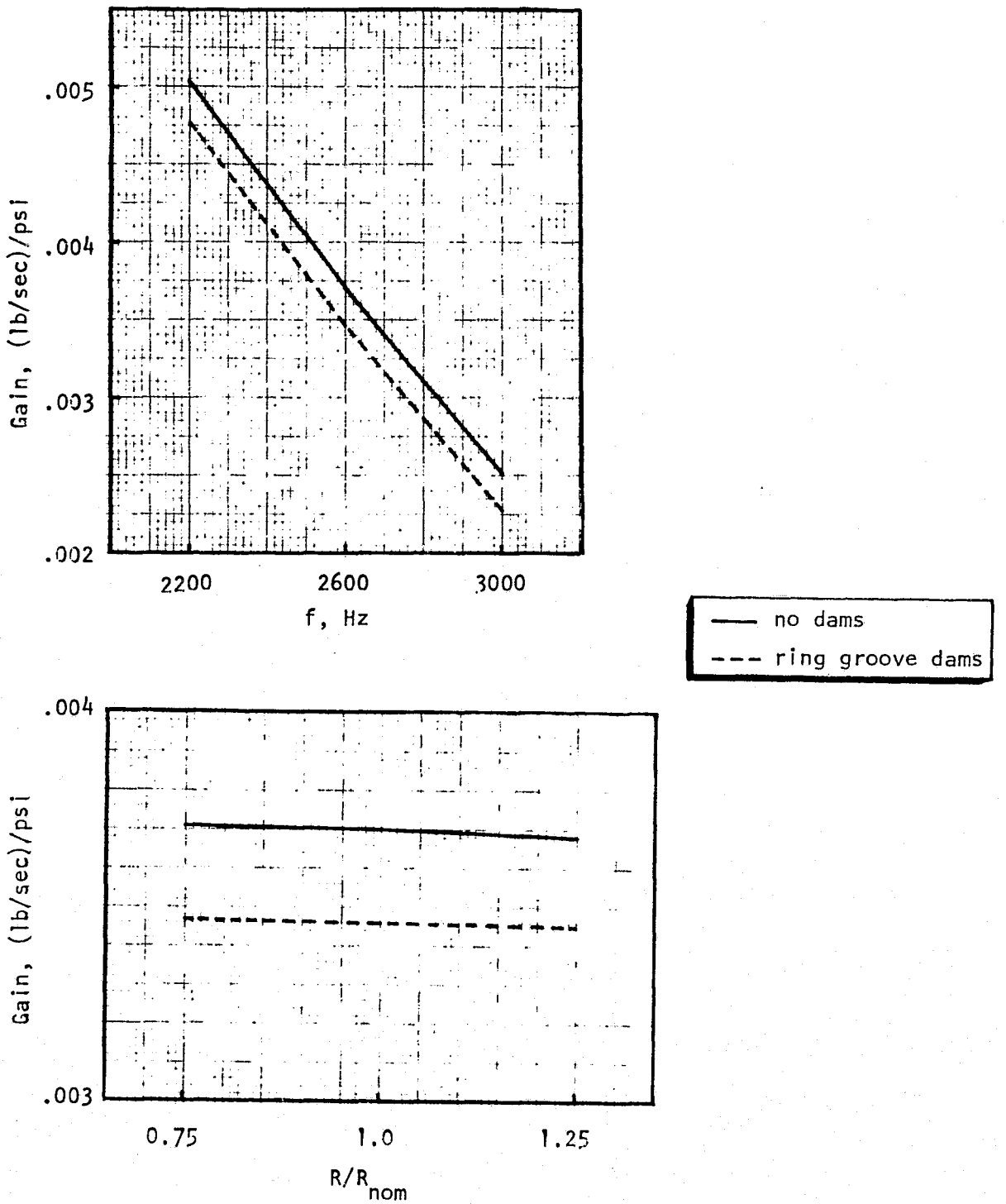

Figure 66. Effect of Frequency and Resistance on Gain for Oxidizer Side of Rocketdyne OME Technology Injector

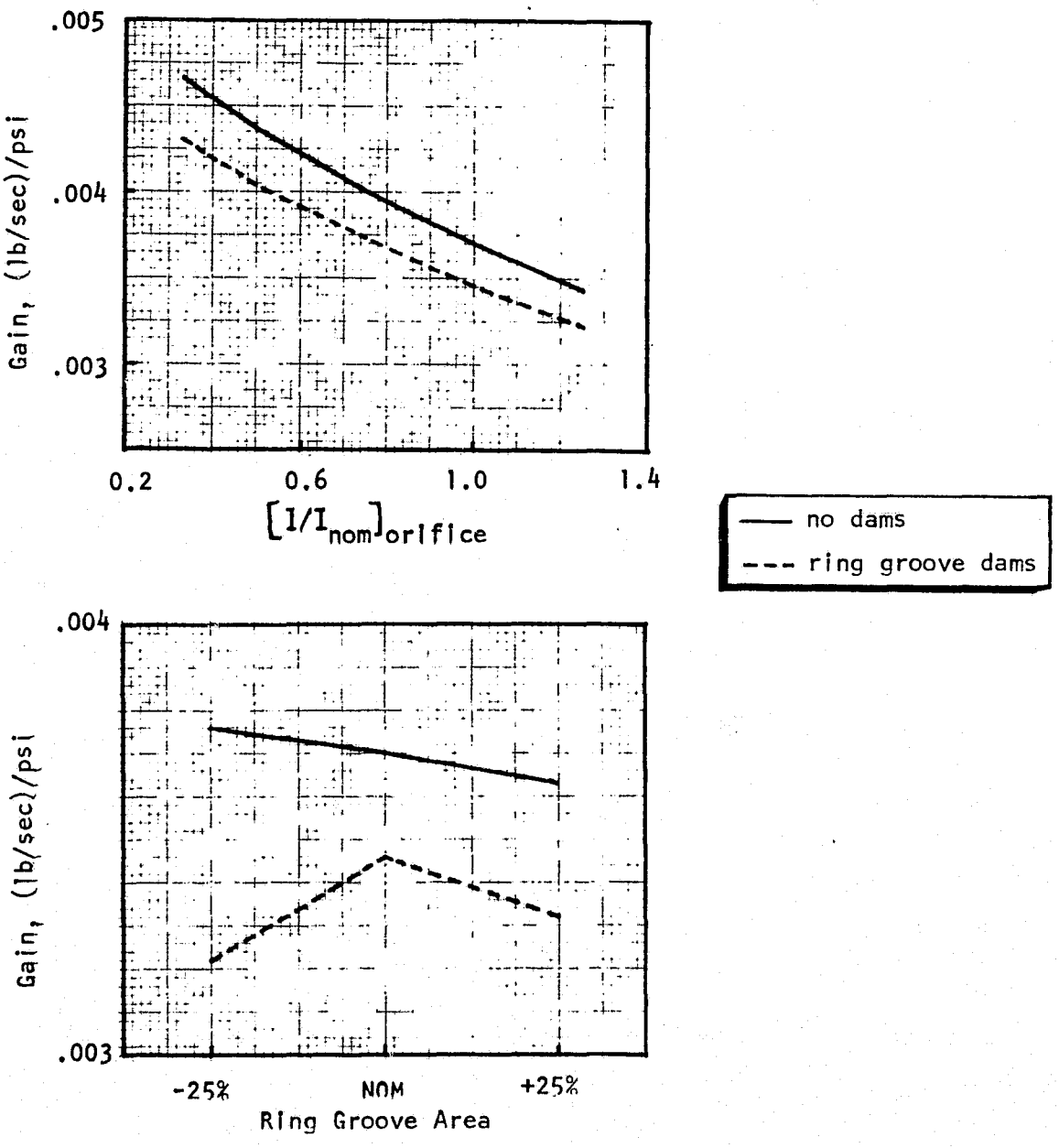

Figure 67. Effect of Orifice Inertance and Ring Groove Area on Gain for Oxidizer Side of Rocketdyne OME Technology Injector

model correlation standpoint. That is, the difference in gain between the base case and the base case with injector fix is not a function of the linearized resistance over the range of uncertainty in injector ΔP.

It is observed in Figs. 59 through 67 that the general effect a specific parameter has on the gain varies between the Aerojet and Rocketdyne injectors and, indeed, between the fuel and oxidizer side of the Aerojet injector itself. In order to gain an understanding of why the predicted gain varies in a particular manner for various changes, an evaluation of the expected system responses was made. It is recalled that the linearized equation for flowrate across a segment is:

$$\tilde{\dot{w}} = \frac{\tilde{P}_u - \tilde{P}_d}{R + IS} \tag{33}$$

where $\tilde{P}_u$ is the oscillatory upstream pressure

$\tilde{P}_d$ is the oscillatory downstream pressure

R is the linearized resistance

I is the inertance

Assuming that the flow segment is just upstream of the combustion chamber (the orifice) $\tilde{P}_d = \tilde{P}_c$, and setting $S = j\omega$, Equation (33) may also be written as

$$\frac{\tilde{\dot{w}}}{\tilde{P}_u - \tilde{P}_c} = \frac{1/R}{1 + (I/R)\, j\omega} = \frac{1/R}{1 + j\omega/\omega_b} \tag{34}$$

where

ω is frequency in radians/sec

ω_b is termed the break frequency = R/I

Figure 68 shows a plot of log gain* versus log frequency. At low frequencies, i.e., ω much less than ω_b, the gain $\tilde{\dot{w}}/(\tilde{P}_u - \tilde{P}_c)$ becomes simply 1/R since

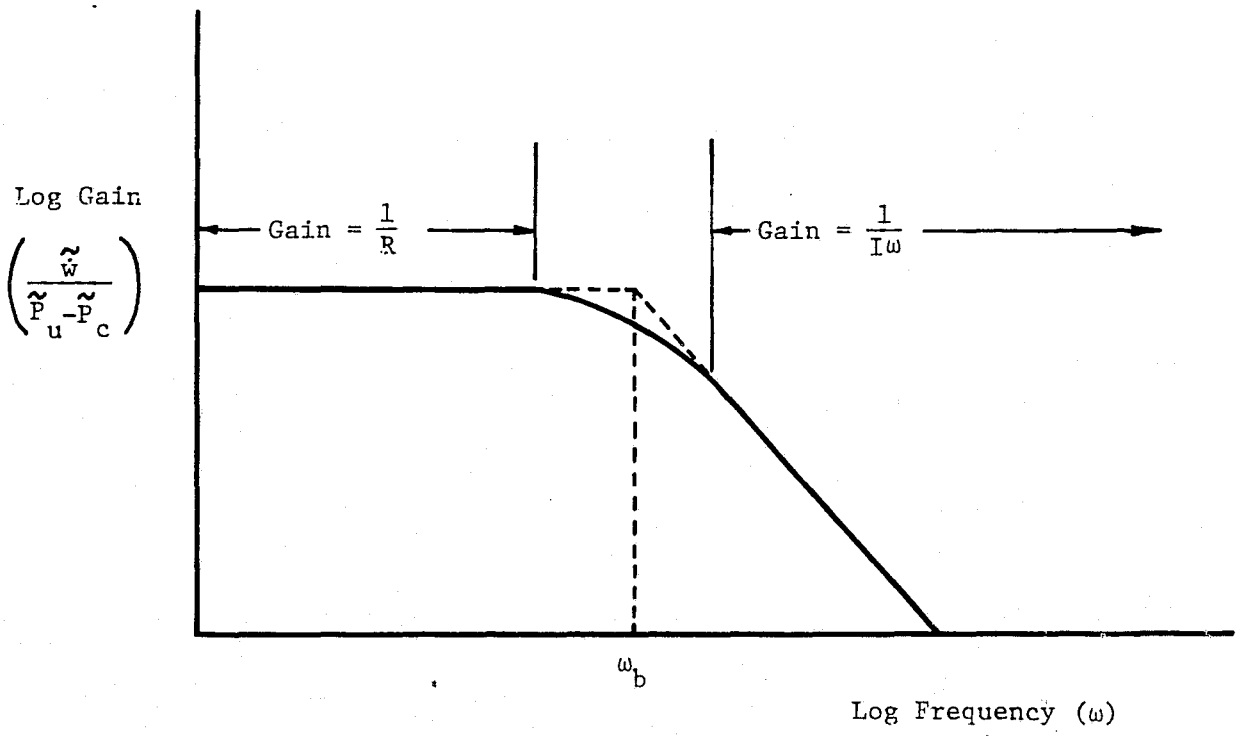

Figure 68. Gain versus Frequency

*In Fig. 68 gain is denoted by the expression $\tilde{\dot{w}}/(\tilde{P}_u - \tilde{P}_c)$ whereas in the computer model output (see Tables VI through IX) gain is denoted by $\tilde{\dot{w}}/\tilde{P}_c$. The latter term is employed in the model since it most effectively represents that quantity by which an injectors sensitivity to coupled instability is expressed. The term $\tilde{P}_u$ in the gain shown in Fig. 68 is, of course, an additional variable whose value (for fixed $\tilde{P}_c$) is dependent upon R, I, and ω.

the $j\omega/\omega_b$ term in the denominator of Eq. (34) becomes small compared to unity. At high frequencies, i.e., ω much greater than ω_b, the gain becomes a function of both the inertance and the frequency ($1/I\omega$) since $j\omega/\omega_b$ becomes large compared to unity. For frequencies near the break frequency, resistance, inertance, and frequency all affect the gain.

The break frequencies for the fuel and oxidizer sides of both the Aerojet and Rocketdyne OME technology injectors (calculated from injector orifice resistances and inertances) are:

OME Technology Injector	Break Frequency	
	Radians/sec	Hz
Aerojet fuel side	38,696	6,159
Aerojet Ox side	23,500	3,740
Rocketdyne fuel side	7,581	1,206
Rocketdyne Ox side	4,727	752

Looking at the sensitivity analysis results for the Rocketdyne injector shown in Tables XIII and IX, it is observed that gain is independent of orifice resistance, but a function of both orifice inertance and frequency. Since the results shown in Tables XIII and IX were obtained for a 1T mode frequency of 2600 Hz, these observed model results are consistent with the anticipated results based on the consideration of the break frequency. That is, since the break frequencies for the Rocketdyne injector (1206 Hz-fuel and 752 Hz-ox) are significantly less than the model input frequency (2600 Hz), the flowrate gain should be primarily affected by inertance and frequency (higher inertance or frequency should reduce the gain) and not affected by resistance changes. Figures 64 - 67 show these trends.

For the Aerojet injector, the break frequencies (6159 Hz-fuel and 3740 Hz-ox) are higher than the input frequency (2600 Hz). Therefore, for a fixed input $(\tilde{P}_u - \tilde{P}_c)$ amplitude at 2600 Hz, it is expected that resistance increases will decrease the flow gain while inertance and frequency variations should have

little or no effect. The actual model results shown in Tables VI and VII do not agree well with these expectations. Thus, a closer examination of the model results was made. The model results showed that the injector pressure ($\tilde{P}_u$) was changing substantially, therefore overcoming the effect on flow gain due to resistance variation alone.* The model results also show (see Figs. 60-63) that orifice inertance (I) and frequency (ω) affect the flow gain as well. These observed results indicate that some other mechanism is affecting the model output for the Aerojet injector.

Prior to proceeding with the identification of the mechanism believed responsible for the unexpected trends in the gain of the Aerojet injector, an expedient effort was undertaken to clarify the difference in gain between the Aerojet and Rocketdyne OME technology injectors. A total of seven additional computer runs were made. These are summarized in Table X. Base runs for the above two injectors were made using identical input modes (spinning 1T) and frequency (2600 Hz). Also, a common fuel injection temperature (230^{o}F) was employed. Results from these four runs are shown in the first four lines of Table X.

Table X shows that fuel side gains for the Aerojet injector are approximately two times as high as gains for the Rocketdyne injector. Oxidizer side gains for the Aerojet injector are approximately seven times as high as gains for the Rocketdyne injector.

One possible explanation for these differences in gain is the difference between the ring groove volumes and orifice inertances/resistances for the two injectors as summarized below in Table XI.

*From Eq. (34), for $\omega << \omega_b$, $\tilde{\dot{w}}/(\tilde{P}_u - \tilde{P}_c) = 1/R$. Therefore, $\tilde{\dot{w}}/\tilde{P}_c = \phi(\tilde{P}_u, 1/R)$.

TABLE X. COMPARISON BETWEEN MODEL OUTPUT FOR AEROJET AND ROCKETDYNE OME TECHNOLOGY INJECTORS

Injector	Fuel or Ox Side	Freq. Hz	Mode	Mod.	Total Inj. Flow (lb/sec)/psi	Total Vector Inj. Flow (lb/sec)/psi	Tot. Inj. Flow Proportioned by P_c Ampl. (lb/sec)/psi	Tot. Vector Inj. Flow Proportioned by P_c Ampl. (lb/sec)/psi
Aerojet	Fuel	2600	Spin IT		.0194	.0167	.0149	.0130
Aerojet	Ox				.0636	.0587	.0545	.0504
Rocketdyne	Fuel				.00941	.00938	.00844	.00843
Rocketdyne	Ox				.00880	.00880	.00739	.00739
Rocketdyne	Fuel			Aerojet Ring Grooves & Orifices	.0102	.00963	.00912	.00888
Rocketdyne	Ox				.00970	.00181	.00813	.00272
Aerojet	Ox	↓	↓	Decreased Volume of Pie Manifold by Factor of 10	.0146	.00305	.0118	.00287

TABLE XI. INJECTOR COMPARISONS

	Aerojet Injector	Rocketdyne Injector
Fuel Ring Groove Volume, $in.^3$	4.182	1.80
Oxidizer Ring Groove Volume, $in.^3$	5.39	0.78
Average Fuel Orifice Inertance	2.3×10^{-2}	6.2×10^{-2}
Average Oxidizer Orifice Inertance	2.0×10^{-2}	5.5×10^{-2}
Average Fuel Orifice Resistance	8.9×10^{2}	4.7×10^{2}
Average Oxidizer Orifice Resistance	4.7×10^{2}	2.6×10^{2}

Two additional runs were therefore made for the Rocketdyne injector in which inputs representing the ring grooves and orifices were modified to simulate the substitution of the Aerojet injector ring grooves and orifices in the Rocketdyne injector. In general, this resulted in fuel and oxidizer side gains which fell in between the gains reported for the Aerojet and Rocketdyne injectors (see Table X). Although, this input modification shifted the results in the right direction (i.e., towards the Aerojet injector) the extent of the shift was not nearly as great as was expected (especially in the case of the oxidizer side). Consequently, the difference in predicted gain between the Aerojet and Rocketdyne injectors could not be explained totally from the standpoint of ring groove volume and orifice inertance/resistance differences.

It was thus postulated that whatever mechanism was responsible for the unexpected trends of the Aerojet injector was also responsible for the qualitative difference in gain between the Aerojet and Rocketdyne injectors.

In order to determine what this mechanism was, a detailed evaluation of the injector inertances and volumes upstream of the orifices was made. Schematically, the oxidizer and fuel sides of the Aerojet injector are as shown in Fig.69. The pie manifold feeders have a high enough inertance that they have little oscillatory flow in the frequency range of interest. The ring groove volumes

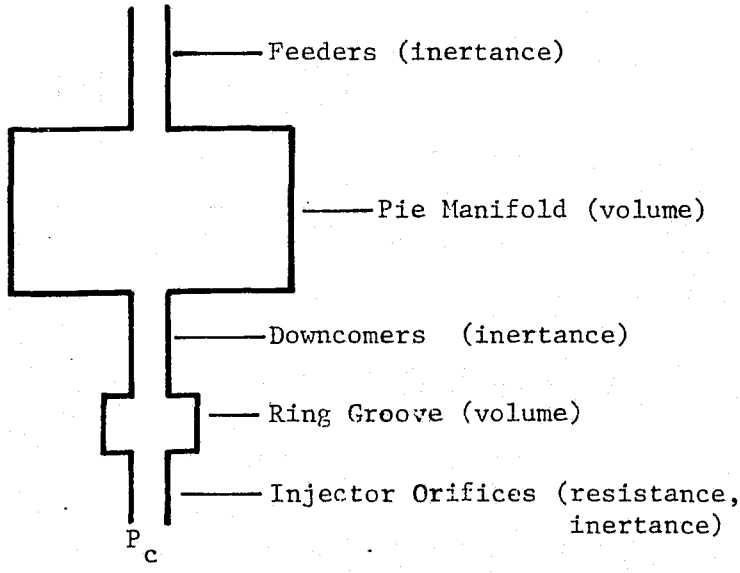

Figure 69. Aerojet Injector System Schematic

are small compared to the pie manifold volumes. Therefore, this system can be closely approximated by a simplification (Fig. 70) that is essentially a

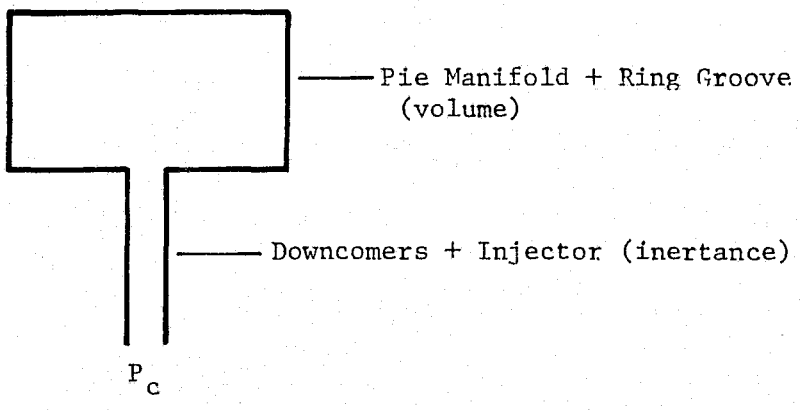

Figure 70. Aerojet Injector Simplified System Schematic

Helmholtz resonator. The resonant frequency of a Helmholtz resonator is:

$$f = \frac{a}{2\pi}\sqrt{\frac{1}{V\,g\,I}}$$

where f = resonant frequency, Hz

a = acoustic velocity - in./sec

V = volume, $in.^3$

g = 386.4 lb_m in./lb_f sec^2

I = inertance, lb_f sec^2/lb_m $in.^2$

Therefore, the calculated Helmholtz resonant frequencies for the Aerojet oxidizer and fuel sides are 2460 Hz and 4290 Hz, respectively. This means that peaks in the flow gain would be expected at these frequencies. Figure 62 shows a peak in the oxidizer side at 2600 Hz which is quite close. On the fuel side (Fig. 60) the gain is increasing for increasing frequencies below the resonant frequency, which is also expected. The plots of gain versus inertance for both the oxidizer and fuel sides (Fig. 61 and 63) are also consistent. On the fuel side, increasing inertance lowers the Helmholtz frequency and therefore, causes an increase in gain (Fig. 61). On the oxidizer side, the actual resonant frequency was very near the input frequency (2600 Hz). Therefore, either an increase or decrease in inertia would move the resonant frequency away from the input frequency causing a reduction in gain (Fig. 63).

To further verify the hypothesis that the Aerojet pie manifolds (especially the oxidizer manifold) were acting like Helmholtz resonators in resonance with the imposed pressure oscillation frequency and, thus, contributing to the relatively high gains associated with that injector, a final computer run was made in which the volume of the oxidizer pie manifold was decreased by a factor of 10. Since this would increase the Helmholtz resonant frequency by over a factor of three, a significant reduction in flow gain would be expected. The results (see Table X) showed that the gain dropped to 0.12 - 0.24 of the value with the correct pie manifold volumes, depending on which

of the four flow summations were used. Therefore, the hypothesis that an effective Helmholtz resonance occurs involving the pie manifolds is analytically predicted.

The results of this run (see Table X) were also in very good agreement with results obtained for the Rocketdyne injector with modified ring grooves and orifices. Thus, it was concluded that the differences in gain between the Aerojet and Rocketdyne injectors are attributable to (1) the presence of the pie manifolds in the Aerojet injector (primary), and (2) differences in the ring groove areas and orifice inertances/resistances (secondary).

Another model result observed in Tables VI through IX is that a higher gain results from a spinning 1T mode than for a standing 1T mode. A spinning 1T mode chamber pressure input for any ring groove is the same amplitude with various phases. The phase of a standing 1T mode is either at zero or 180 degrees, but the amplitude varies with the sine of location of the input. Therefore, since the average value of a sine function is 0.64 times the maximum value, the average input magnitude for a standing mode is 0.64 times the average input for a spinning mode (the reference pressure in both cases is the pressure at the maximum amplitude). This difference in flow gains for a 1T standing mode versus a 1T spinning is close to the same ratio.

As previously mentioned, the objective of the sensitivity analysis was to determine generalized injector design criteria to preclude hydraulic coupling. It is obvious from the preceding discussion concerning the Rocketdyne and Aerojet injectors that the sensitivity analyses were not successful in establishing generalized injector design criteria. This is due to the complex interactions which may exist between the constituent portions of an injector. The analyses did result in a number of observations, however:

1. Any uncertainty in the linearized orifice resistance due to uncertainties in the analytical calculation of injector ΔP should not appreciably alter the effect observed by the addition of dams to the injector.

2. If the ring groove flow calculated by the model is significant compared to the injector flow, dams in the ring groove could significantly affect the ring groove pressure response, and therefore the injector flow oscillations.

3. For injectors in which complex interactions are absent, the injector gain can be simply related to linearized orifice resistance (R), orifice inertance (I), and instability frequency (ω) through a term called the break frequency (ω_b) which is simply the linearized orifice resistance divided by the orifice inertance. These simple relationships are:

   gain is proportional to $1/R$ for $\omega < \omega_b$

   gain is proportional to $1/I\omega$ for $\omega > \omega_b$

4. The presence of large manifold volumes in critical locations may introduce complicating mechanisms by acting as Helmholtz resonators in resonance with the imposed pressure oscillation. Such action can greatly increase the injector gain and nullify completely the simple gain relationships presented above. The engine hydraulic stability model can be used to show the effect of such large manifold volumes and suggest design changes to avoid adverse effects.

Therefore, the engine hydraulic stability model must be utilized in order to obtain a quantitative, and in many cases even a qualitative, evaluation of geometric injector design options, or operating condition changes, on stability.

To illustrate the use of the model for such purposes mentioned above, reference can be made to the results shown in Tables VI through IX. Figure 59, for example, appears to indicate that a reduction in fuel injection temperature (for the Aerojet injector) from 230°F to 70°F would decrease the flow gain, thus providing less stabilization against the spinning 1T mode and more stabilization against the resurge mode. Caution must be exercised in making such a prognostication, however, since Fig. 59 considers only the effect of fuel injection temperature on the injector side of the coupling.

The effect the fuel injection temperature has on the combustion side of the coupling is, of course, not predicted by the model, and could be overwhelming.

Of particular interest to the injector designer are the model predictions for the Rocketdyne injector. It is recalled that this technology injector had only annular fuel manifold dams. No ring groove dams were ever tested on either the fuel or oxidizer sides of the injector. According to Table VIII, the fuel side gain* is decreased from 0.00441 (lb/sec)/psi to 0.00367 (lb/sec)/psi when the annular fuel manifold dams are added. This corresponds to a percentage reduction in gain of 16.8 percent. If three symmetrical ring groove dams were added to each fuel ring** instead of the three symmetrical manifold dams, results from the model show (see Table VIII) that the fuel side gain* would be 0.00378 (lb/sec)/psi or a reduction of 14.3 percent from the nominal gain with no injector fix. Thus, for the fuel side of the Rocketdyne OME technology injector, the addition of manifold dams is predicted to be a bit more effective than the addition of ring groove dams in preventing coupled instability. However, as shown in Table VIII, simultaneous employment of both manifold and ring groove dams would reduce the gain from 0.00441 (lb/sec)/psi to 0.00266 (lb/sec)/psi. This corresponds to a reduction in gain of 39.7 percent.

The advisability of adding ring groove dams to the oxidizer side of the Rocketdyne injector was also explored using the model. These results are shown in Table IX. The addition of three symmetrical dams to each ox ring (at common theta planes***) is shown in Table IX to reduce the ox side gain from 0.00370 (lb/sec)/psi to 0.00346 (lb/sec)/psi. This 6.5% reduction in ox-side gain is less than half the percentage reduction predicted for the fuel side.

---

* Using the total vector injector flow proportioned by P_c amplitude.

** Dams positioned in each fuel ring at same theta planes as manifold dams (see Fig. 35).

*** See Fig. 38.

No effort was made in this program to investigate the effect of ring groove dam location on the predicted gain. Such effect may be of considerable importance*, however, and can be easily studied using the engine hydraulic stability computer model.

* For instance, the location of the ring groove dams in the XRL injector was analytically shown to be most critical (Ref. 4).

SECTION VI

CONCLUSIONS AND RECOMMENDATIONS

The engine hydraulic stability computer model developed during this program is deemed to be of sufficient worth to be included among those models commonly used to investigate combustion instability in rocket engines. The range of model applicability is summarized in Table XII. The engine hydraulic stability model is designed to specifically investigate coupling between the combustion chamber and the injector hydraulics. It may, however, be input in such a fashion to permit the open-loop analysis of feed system hydraulics as well.

The engine hydraulic stability computer model was successful in predicting that injector hardware fixes applied to each of three correlation injectors would increase combustor stability with respect to the instability mode actually observed.

The model is extremely well suited to:

1. Quantitatively evaluate the effect of proposed injector fixes on stability
2. Quantitatively evaluate (from a stability standpoint) geometric design options or operating condition changes relative to each other
3. Determine potential optimum locations for injector fixes or modifications such as dams
4. Determine the depth of penetration of injector face oscillations into the feed system or manifold

The open-loop model is unable to predict stability per se. However, the model can be used to look at the injector design detail and indicate what changes to make to reduce a high value of injector gain at expected instability frequencies.

TABLE XII. RANGE OF MODEL APPLICABILITY

Parameter	Evaluation Range of Interest	Range of Correlation Test Cases	Model Limitation
Propellants	acid/amine LOX/amine acid/ hydrocarbon LOX/ hydrocarbon	IRFNA/UDMH N_2O_4/MMH	Liquid propellants only
Thrust	25 to 50,000 lbf	6,000 to 42,000 lbf	None
Chamber Pressure	100 to 1000 psia	125 to 950 psia	None
Mixture Ratio	Maximum permance ±20%	3.99 (IRFNA/UDMH) 1.65 (N_2O_4/MMH)	None
Fuel Temperature	40°F to 0° subcooling at injected conditions	200°F (MMH) 65°F (UDMH)	Liquid propellants (no two-phase injector flow)
Acid Temperature	40°F to 0° subcooling at injected conditions	65°F (N_2O_4) 65°F (IRFNA)	Liquid propellants (no two-phase injector flow)
LOX Temperature	-298°F to 0° subcooling at injected conditions		Liquid propellants (no two-phase injector flow)
Orifice Size	0.020 to 0.040 0.040-in.dia	0.020- to 0.073-in. dia	None
Orifice ΔP	25 to 50 psid (or 15% P_c)	44 to 184 psid (15 to 50% P_c)	None (no local cavitation)
Frequency range of coupling problem	100 to 3000 Hz	1300 to 2600 Hz	Injector description limited to 8 lumps per wavelength for optimum accuracy

It is not recommended that the model be used in an attempt to predict such things as a preferred mode or the effect of propellant injection temperature since these quantities affect both the combustion side as well as the injector hydraulics. The combustion-side response is, of course, input like a boundary condition in the model in order to calculate the injector response. The effect of variables on the combustion side response is, therefore, not calculated in any manner whatsoever and must be assumed.

The sensitivity analyses were not successful in establishing generalized injector design criteria to preclude hydraulic coupling. This is because of the complex interactions which may exist between the constituent portions of the injector. The analyses were most informative, however. For injectors in which complex interactions are absent, the injector gain can be simply related to orifice resistance, orifice inertance, and instability frequency through a term called the break frequency which is simply the orifice resistance divided by the orifice inertance. These simple relationships are:

gain is proportional to $1/R$ for $\omega < \omega_b$

gain is proportional to $1/I\omega$ for $\omega > \omega_b$

The presence of large manifold volumes in critical locations may introduce complicating mechanisms by acting as Helmholtz resonators in resonance with the imposed pressure oscillation. Such action can greatly increase the injector gain and nullify completely the simple gain relationships presented above. The engine hydraulic stability model can be used to predict the effect of such large manifold volumes and suggest design changes to avoid adverse effects.

The attainment of additional experimental data with which the model can be correlated is deemed to be of most urgent concern. In particular, the attainment of data for which such injector parameters as manifold volume, ring groove volume, feed passage inertance, and dam location have been varied is considered necessary. Such experimental effort would best be conducted in conjunction with parametric studies of the experimental variables using

the engine hydraulic stability model. Results from the model could then be used to help guide the experimental effort.

Therefore, it is highly recommended that an experimental evaluation of injector/combustion-coupled instability be conducted* in conjunction with additional sensitivity analyses and parameter variation studies. Such effort would include the design and fabrication of a versatile injector, testing of that injector to determine the most effective means of preventing injector hydraulic-coupled instabilities, and attendant analysis and evaluation to improve the analytical computer model and develop design criteria and recommended procedures. The injector should have sufficient flexibility to permit configurational changes (such as the capability for readily installing or removing ring groove dams, manifold baffles, orifices in injector feed passages, resonators, and the inlet configurations) which are predicted to substantially effect the oscillatory flow behavior of the injector but, nevertheless, be representative of good injector design practice and fabrication techniques.

* Such an effort was originally proposed as Phase II of the Engine Hydraulic Stability Contract (NAS9-14801) and is detailed in Ref. 15.

REFERENCES

1. Kahn, D. R., M. D. Schuman, J. K. Hunting, and K. W. Fertig, "Orbital Maneuvering Engine Feed System Coupled Stability Investigation," Final Report for NASA Contract NAS9-14315, Report No. T-1067, (R-9807), Rocketdyne Division, Rockwell International, Canoga Park, CA, 1 Sept. 1975.

2. Nelson, R. L., R. C. Kesselring, and K. M. Sprouse, "Engine Hydraulic Stability Model Computer Manual," Final Documentation for NASA Contract NAS9-14801, Report No. , Rocketdyne Div., Rockwell International, Canoga Park, CA, July 1977.

3. Harrison, H. L., Bollinger, J. G., Introduction to Automatic Controls, Second Edition, International Textbook Co., Scranton, Pennsylvania, 1969, Chapter 9.

4. Extended Range Lance, Final Report, Contract MD-M-46, Rocketdyne Report No. R-8417, Rocketdyne Division, Rockwell International, Canoga Park, CA, March 1971.

5. Nestlerode, J. A., and F. R. Linow, "Phase Stabilization of an Intermediate Frequency Instability Through Propellant Flight Time Adjustment," CPIA Publ, 261, Dec. 1974.

6. Kreyszig, Erwin, Advanced Engineering Mathematics, John Wiley and Sons, New York, 1965, pp 536-540.

7. Oberg, C. L., "Space Shuttle Maneuvering Engine Reusable Thrust Chamber Program - Task XI, Stability Analysis and Acoustic Model Testing Data Dump," CT-74-13, NASA Contract NAS9-12802, Rocketdyne Division, Rockwell International, Canoga Park, CA, Dec. 1974.

8. Program Plan, Engine Hydraulic Stability, Rocketdyne Memo Number CT 75-14, Rocketdyne Division, Rockwell International, Canoga Park, CA, December 1975.

9. Space Shuttle Orbital Maneuvering Engine Platelet Injector Program, Final Report on Contract NAS9-13133, Report No. 13133-F-1, Aerojet Liquid Rocket Co., Sacramento, CA, 1 Dec. 1975.

10. Liquid Propellant Rocket Combustion Instability, D. Harrje, editor, NASA SP-194, NASA, Washington, D.C., 1972, p. 258.

11. Society of Automotive Engineers, SAE Aero-Space Applied Thermodynamics Manual.

12. D'Azzo, J. J., and Houpis, C.H., Feedback Control System Analysis and Synthesis, Second Edition, McGraw-Hill, New York, 1966.

13. Space Shuttle OME Reusable Thrust Chamber, Final Report on Contract NAS9-12802, Rocketdyne Report R-9686, Rocketdyne a Division of Rockwell International, Canoga Park, CA, 29 August 1975.

14. Nestlerode, J. A., and C. L. Oberg, Combustion Instability in an Annular Engine, 6th ICRPG Combustion Conference CPIA publication No. 192, Vol. 1, December 1969.

15. Engine Hydraulic Stability, R-9792P-1, Vol. 1 - Technical Proposal, Rocketdyne, a Division of Rockwell International, Canoga Park, CA, 8 Aug. 1975.

APPENDIX A

DEVELOPMENT OF GOVERNING EQUATIONS FOR LIQUID ROCKET FEED SYSTEMS

GENERAL FUNDAMENTAL EQUATIONS OF CONTINUITY AND MOMENTUM

The following discussion relates to the development of the differential equations governing viscous fluid flow as applied to the analysis of liquid rocket feed system stability. Using tensor notation, the continuity equation describing general fluid motion is (Ref. A-1):

$$\frac{\partial \rho}{\partial t} + \nabla \cdot (\rho \underset{\rightarrow}{v}) = 0 \quad . \tag{A-1}$$

where

ρ is density (mass/volume)

$\underset{\rightarrow}{v}$ is the velocity vector (distance/time)

t is time.

From isentropic relations, for compression and expansion

$$\frac{\partial P}{\partial \rho} = a^2 \tag{A-2}$$

where

P is pressure (force/area)

a is the sonic speed of the hydraulic fluid (distance/time).

Thus substituting Eq. (A-2) into Eq. (A-1) will yield a continuity equation of

$$\frac{1}{a^2} \frac{\partial P}{\partial t} + \nabla \cdot (\rho \underset{\rightarrow}{v}) = 0 \tag{A-3}$$

Again, using tensor notation, and ignoring body forces, the equation governing momentum conservation can be written as (Ref. A-1)

$$\rho \left[\frac{\partial \underrightarrow{v}}{\partial t} + \underrightarrow{v} \cdot \nabla \underrightarrow{v} \right] = - \nabla P + \underrightarrow{h} \qquad \text{(A-4)}$$

where

$\underrightarrow{h}$ is the momentum head loss vector due to viscous surface forces (force/volume)

Equations (A-3) and (A-4) above are the generalized equations describing viscous fluid flow. A few assumptions are introduced to allow the use of present mathematical techniques in the solution of the set of equations.

These assumptions are:

a. Assume that the system undergoes an initial transient period followed by steady state. Thus, only the steady-state solution will be sought.

b. Assume that the steady-state solution can be characterized as being composed of time average values with small perturbed values superimposed on top. This is the perturbation assumption. Thus let

$$P = \bar{P} + \tilde{P} \qquad \text{(A-5a)}$$

$$\underrightarrow{v} = \underrightarrow{\bar{v}} + \underrightarrow{\tilde{v}} \qquad \text{(A-5b)}$$

$$\rho = \bar{\rho} + \tilde{\rho} \qquad \text{(A-5c)}$$

and

$$\underrightarrow{h} = \underrightarrow{\bar{h}} + \underrightarrow{\tilde{h}} \qquad \text{(A-5d)}$$

where $(-)$ denotes time averaged values

$(\sim)$ denotes small perturbed values which approximately equal zero.

Additionally assume that:

c. The time averaged velocity vector is also small, although $\underrightarrow{\bar{v}}$ is greater than $\underrightarrow{\tilde{v}}$, and

d. That the fluid is incompressible, that is the time averaged density, $\bar{\rho}$, is constant.

Assumptions a, b, c, and d above, reduce Equations (A-3) and (A-4) to a time averaged steady-state form for continuity

$$\nabla \cdot \bar{\underline{v}} = 0 \tag{A-6}$$

and for momentum conservation

$$\nabla \bar{P} = \bar{\underline{h}} \tag{A-7}$$

and, finally, a perturbed steady-state form for continuity

$$\frac{1}{a^2} \frac{\partial \tilde{P}}{\partial t} + \bar{\rho} \nabla \cdot \tilde{\underline{v}} = 0 \tag{A-8}$$

and for momentum conservation

$$\bar{\rho} \frac{\partial \tilde{\underline{v}}}{\partial t} = -\nabla \tilde{P} + \tilde{\underline{h}} \tag{A-9}$$

It should be pointed out that $\bar{\rho}$ and a are the only constants in Eqs. (A-6) - (A-9) and their values are known for most liquids.

DEVELOPMENT OF THE VISCOUS MOMENTUM HEAD LOSS VECTOR

Until now no attempt has been made to quantify the viscous momentum head loss vector, $\underline{h}$. The following discussion will begin this development for both general multi-dimensional flow and one-dimensional axial flow in pipes.

General Multi-dimensional Flow

It has been shown in Bird (Ref. A-1) that the viscous momentum vector for laminar flow can be represented in tensor form as

$$\underline{h} = -\left[\nabla \cdot \tau\right] \tag{A-10}$$

where τ is the viscous surface force tensor.

The expressions for τ as developed in Schlichting (Ref. A-2) for Newtonian fluids are:

$$\tau_{xx} = -2\mu \frac{\partial v_x}{\partial x} + \frac{2}{3}\mu (\nabla \cdot \underline{v}) \tag{A-11a}$$

$$\tau_{yy} = -2\mu \frac{\partial v_h}{\partial y} + \frac{2}{3}\mu (\nabla \cdot \underline{v}) \tag{A-11b}$$

$$\tau_{zz} = -2\mu \frac{\partial v_z}{\partial z} + \frac{2}{3}\mu (\nabla \cdot \underline{v}) \tag{A-11c}$$

$$\tau_{xy} = \tau_{yx} = -\mu \left(\frac{\partial v_x}{\partial y} + \frac{\partial v_y}{\partial x} \right) \tag{A-11d}$$

$$\tau_{yz} = \tau_{zy} = -\mu \left(\frac{\partial v_y}{\partial z} + \frac{\partial v_z}{\partial y} \right) \tag{A-11e}$$

$$\tau_{zx} = \tau_{xz} = -\mu \left(\frac{\partial v_z}{\partial x} + \frac{\partial v_x}{\partial z} \right) \tag{A-11f}$$

where μ is the dynamic viscosity (mass/time-distance)
and x, y, and z denote direction

Using Eq. (A-10) and assumptions (a), (b), and (c), a steady-state time-averaged-representation and a steady-state perturbed representation of h can be obtained. However, this will not be done here since Eqs. (A-10) and (A-11) would add too great a complexity in the solution of Eqs. (A-3) and (A-4) to be treated in this discussion.

One-dimensional Axial Flow in a Pipe

For steady-state incompressible isothermal flow in pipes of constant cross-sectional area, the Fanning or Darcy equation (Ref. A-3) has shown that the pressure changes according to

$$\frac{\Delta P}{\rho} = -4f \frac{L}{D} \frac{|v_x| v_x}{2} \tag{A-12}$$

where

| | denotes absolute value

ΔP is the pressure change across the length of pipe section in the positive axial direction

f is the fanning friction factor

D is the hydraulic diameter

L is the length of pipe section (always positive)

v_x is the axial fluid velocity in the positive x-direction

The Fanning equation above has been written in such a fashion as to show that in the positive x-direction, the pressure will decrease for positive axial fluid velocities, and increase for negative axial fluid velocities.

Using assumptions (a), (b), and (c), it can be shown that Eq. (A-4) will be reduced to the one-dimensional non-perturbed form of

$$\frac{\partial P}{\partial x} = h_x \tag{A-13}$$

Since these assumptions state that transient terms can be ignored along with the non-linear velocity term. Substituting Eq. (A-12) into Eq. (A-13) yields an expression for the momentum head loss of

$$h_x = \frac{-2f\rho \ |v_x| v_x}{D} \tag{A-14}$$

Now substituting Eqs. (A-5b), (A-5c), and (A-5d) from assumption (b) into Eq. (A-14) gives for a time averaged head loss term,

$$\bar{h}_x = \frac{-2f\bar{\rho} \ |\bar{v}_x| \bar{v}_x}{D} \tag{A-15}$$

and for a perturbed head loss term,

$$\tilde{h}_x = \frac{-4f\bar{\rho}\ |\bar{v}_x|\tilde{v}_x}{D} \qquad \text{(A-16)}$$

Finally, using Eq. (A-15), the one-dimensional representation of Eq. (A-7), and remembering that $\Delta\bar{P}$ is opposite in sign from $\bar{v}_x$ will show that the perturbed head loss term can also be expressed as,

$$\tilde{h}_x = \frac{-2|\Delta\bar{P}|}{L|\bar{v}_x|}\ \tilde{v}_x \qquad \text{(A-17)}$$

BOUNDARY CONDITIONS FOR FUNDAMENTAL EQUATION

This discussion relates to the boundary equations needed to solve Eqs. (A-6) through (A-9). The spatial flow parameters of pressure and velocity on a boundary can be characterized as consisting of the sum of two functions; one time dependent, the other time independent. Mathematically, this can be represented as

$$B_{Bc} = B_{Bc}(x,y,z) + B_{Bc}(x,y,z,t) \qquad \text{(A-18)}$$

where

B_{Bc} is the pressure or velocity boundary condition at a surface

$B_{Bc}(x,y,z)$ is some time independent function

$B_{Bc}(x,y,z,t)$ is some time dependent function

No boundary conditions are needed for the viscous momentum head loss vector, $\underline{h}$, since it is a function of velocity (see Eqs. (A-10), (A-11), and (A-14).

Then from Eq. (A-18) the time averaged boundary conditions used in Eqs. (A-6) and (A-7) can be expressed as

$$\bar{B}_{Bc} = B_{Bc}(x,y,z) \qquad \text{(A-19)}$$

and the perturbated boundary condition used in Eqs. (A-8) and (A-9) can be written as

$$\tilde{B}_{Bc} = B_{Bc}(x,y,z,t) \tag{A-20}$$

Finally, since assumption (a) states that the solution is a steady-state representation, the initial conditions given for Eqs. (A-8) and (A-9) at $t = 0$ can be taken as equal to zero. Mathematically this is expressed as

$$\tilde{B}_{Ic} \ (t = 0) = 0 \tag{A-21}$$

where

$\tilde{B}_{Ic}$ is the perturbed pressure or velocity initial condition

The importance of feed-system stability lies in the development of the perturbed steady-state equations. Therefore, continued development of the general time average steady-state equations, Eq. (A-6), (A-7), and (A-19), will be dismissed from further discussion.

MULTI-DIMENSIONAL INVISCID PERTURBED FLOW
(THE WAVE EQUATION)

In the previous sections, a complete multi-dimensional perturbed flow representation can be given by Eqs. (A-8) and (A-9), and the perturbated description of Eqs. (A-10) and (A-11). However, as was stated before, Eqs. (A-10) and (A-11) will add too great a complexity to the solution of Eqs. (A-8) and (A-9). Therefore, in the case of general multi-dimensional fluid flow, assume that any viscous effects are negligible on the perturbed flow, i.e.,

$$\underrightarrow{\tilde{h}} \approx 0 \tag{A-22}$$

Then, using Eq. (A-22), it can be shown that Eqs. (A-8) and (A-9) can be combined to yield,

$$\frac{1}{a^2} \frac{\partial^2 \tilde{P}}{\partial t^2} = \nabla^2 \tilde{P} \tag{A-23}$$

and that Eq. (A-9) alone reduces to

$$\bar{\rho}\,\frac{\partial \tilde{\vec{v}}}{\partial t} = -\nabla \tilde{P} \qquad \text{(A-24)}$$

Equation (A-23) above is a partial differential equation more commonly known as the "wave equation". It can be solved by the method of separation of variables, or by the use of Green's function. Once the solution to Eq.(A-23) is known, the time history of the perturbed velocity can be found directly from Eq. (A-24).

ONE-DIMENSIONAL VISCOUS PERTURBED FLOW

The perturbed one-dimensional axial flow momentum head loss vector, $\tilde{h}_x$, given by Eqs. (A-16) or (A-17) is of simple enough form that viscous effects can easily be included in one-dimensional flow representations. Expressing Eq. (A-8) in one-dimensional form yields for continuity

$$\frac{1}{a^2}\,\frac{\partial \tilde{P}}{\partial t} + \bar{\rho}\,\frac{\partial \tilde{v}_x}{\partial x} = 0 \qquad \text{(A-25)}$$

By substituting Eq. (A-17) into Eq. (A-9), the one-dimensional momentum equation becomes

$$\bar{\rho}\,\frac{\partial \tilde{v}_x}{\partial t} = \frac{-\partial \tilde{P}}{\partial x} - \frac{2|\Delta \bar{P}|}{L|\bar{v}_x|}\,\tilde{v}_x \qquad \text{(A-26)}$$

REFERENCES

A-1. Bird, R. B., Stewart, W.E. Lightfoot, E. H., Transport Phenomena, John Wiley and Sons, Inc., New York, 1960.

A-2. Schlichting, H., Boundary-Layer Theory, 6th Edition, McGraw-Hill, New York, 1968.

A-3. Perry, R. H., and Chilton, C. H., Chemical Engineer's Handbook, Fifth Edition, McGraw Hill, New York, 1973.

APPENDIX B

CLASSICAL CHAMBER ACOUSTICS OF CYLINDRICAL COMBUSTORS

INTRODUCTION

When studying liquid rocket feed system dynamics it is necessary to know the pressure profile at the injector face. This pressure profile is needed for use as a boundary condition on the hydrodynamic feed system differential equations. To know how the pressure profile varies across the injector face, means that the dynamics of the combustion chamber itself needs to be known. This by no means is an easy task since in many cases the dynamics of the combustion chamber are coupled with the dynamics of the feed system. But assuming that the combustion chamber and feed system are not dynamically coupled, a first approximation to the pressure profile on the injector face may be found. The discussion which now follows is the simplified or classical development of cylindrical combustion chamber acoustics. It will begin by first defining a chamber geometry and coordinate system. Once this is done, simplifying assumptions for the analytical derivation will be listed with the mathematical solution following.

GEOMETRY

As stated previously, the geometry of the combustion chamber is cylindrical with the spatial coordinates placed as shown in Fig. B-1. Every location within the combustor can be described by its radial direction (r), its tangential direction (θ), and its axial direction (x). The injector face is located at $x = 0$, and the radius of the combustor is given by r_w.

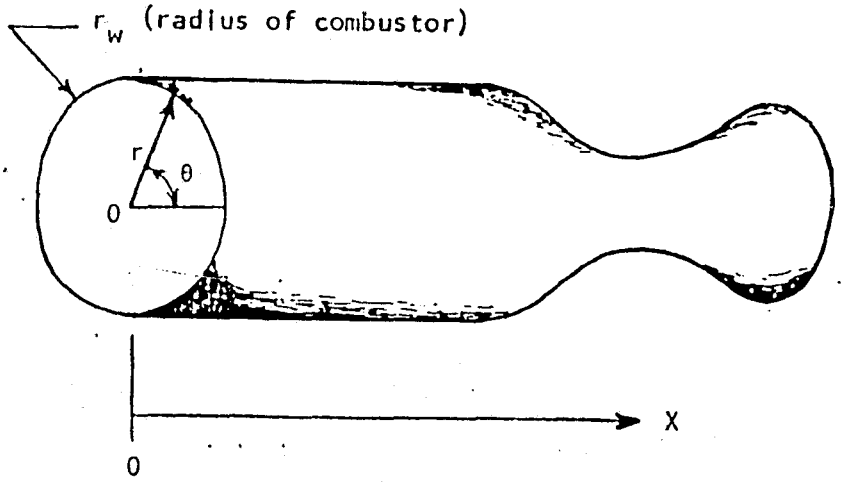

Figure B-1. Combustor Geometry

ANALYTICAL DEVELOPMENT

Before the equation governing fluid flow within the combustor is written, it is best to first list the assumptions which go into its formulation. These assumptions are given as follows:

a. Assume that the system reaches steady-state, so that only a steady-state solution will be sought.

b. Assume that this steady-state solution is a perturbed solution such that it is composed of small oscillatory perturbations of pressure, density, velocity, etc., superimposed on top of their time-averaged steady-state values.

c. The time-averaged steady-state velocity is small.

d. The fluid is considered incompressible. That is the time-averaged density is constant.

e. The fluid flow is inviscid.

f. The flow is homogeneously non-reacting. That is, the reaction kinetics are infinitely fast such that the reaction takes place and is completed at one axial, z location. This axial location will be considered at the injector face (x = 0).

and

g. Gradients in the axial direction are negligible.

Using assumptions (a) - (g), the continuity and momentum equations can be combined to yield a partial differential equation for the perturbed chamber pressure. This equation is developed in Chapter A and given by Eq. (A-23) as

$$\frac{1}{a_c^2}\frac{\partial^2 \tilde{P}}{\partial t^2} = \frac{\partial^2 \tilde{P}}{\partial r^2} + \frac{1}{r}\frac{\partial \tilde{P}}{\partial t} + \frac{1}{r^2}\frac{\partial^2 \tilde{P}}{\partial \theta^2} \qquad \text{(B-1)}$$

where

$\tilde{P}$ = perturbed pressure (force/area)

a_c = sonic speed of the gases in the combustion chamber (distance/time)

t = time

r, θ = spatial coordinates

The solution to Eq. (B-1) is easily obtained when the functional form of the dependent variable can be represented as a product solution of the independent variables.

It has been shown experimentally that two types of pressure waves exist in the tangential (θ) direction of cylindrical combustors. They are standing tangential waves and spinning tangential waves. Figure B-2 below graphically shows the difference between the two, for a given radial location and one period wave (the first tangential).

Figure B-2a shows that a standing wave is characterized by spatial oscillatory pressure nodes and anti-nodes, much like a vibrating string. However, Fig. B-2b clearly shows that spinning waves have no such spatial nodes. All θ locations experience the full amplitude of the tangential wave. It is because of this difference that Eq. (B-1) will need to be solved for both these modes.

THE STANDING TANGENTIAL WAVE

For the standing tangential wave it will be assumed that the solution to Eq. (B-1) can be represented as

$$P = R(r)\ \Theta(\theta)\ T(t) \qquad \text{(B-2)}$$

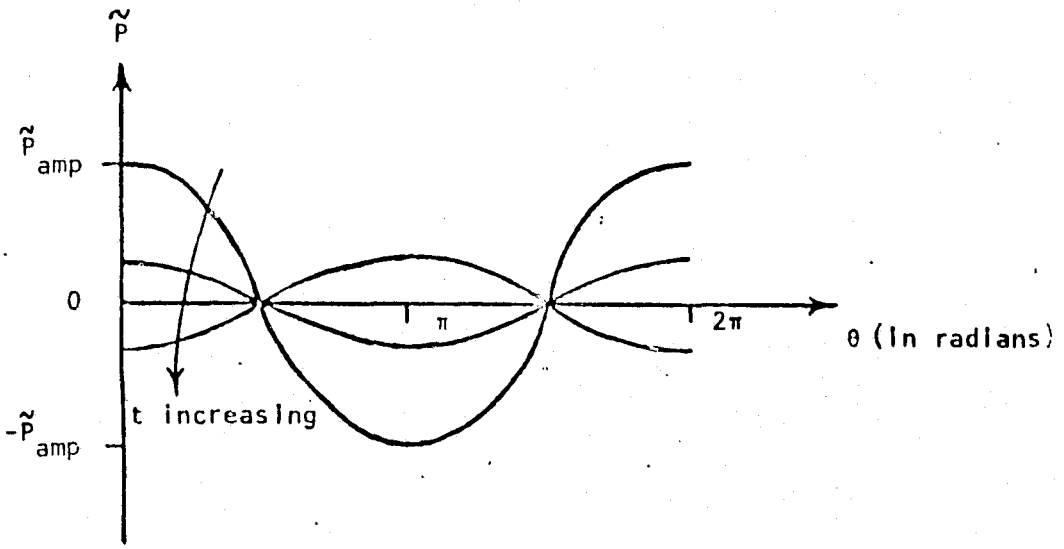

a) The Standing Tangential Wave

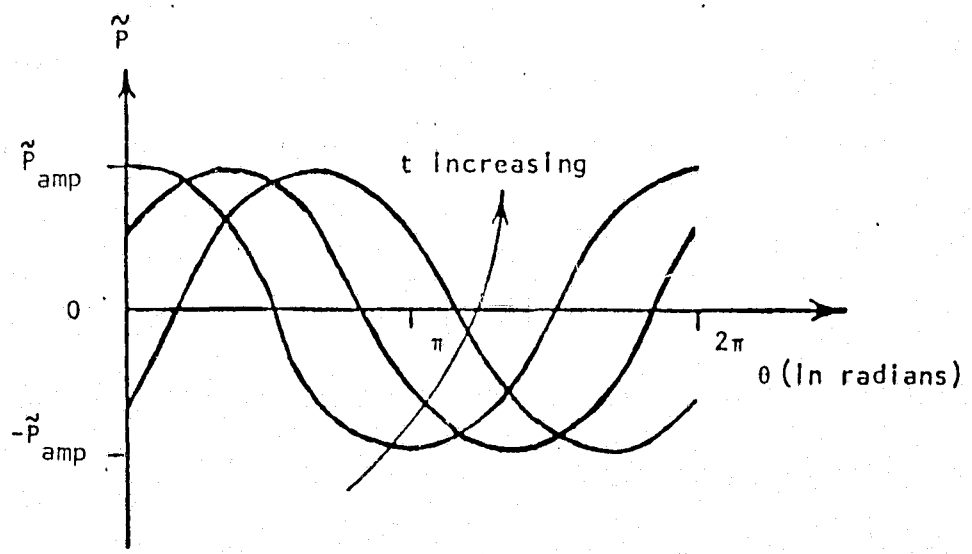

b) The Spinning Tangential Wave

Figure B-2. The First Tangential Standing and Spinning Wave (at a given radial location with amplitude, $\tilde{P}_{amp}$)

where R is some function in r

Θ is some function in θ

T is some function in t

Further, Fig. C-2a shows that the functional form of T can be given as

$$T = \sin \omega t$$

where

ω = angular frequency of oscillations (radians/time)

Substituting Eqs. (B-2) and (B-3) into Eq. (C-1) will yield

$$r^2 \frac{d^2R}{dr^2} + r \frac{dR}{dr} + \left[\frac{\omega^2}{a_c^2} r^2 - m^2 \right] R = 0 \qquad \text{(B-4a)}$$

and

$$\frac{d^2\Theta}{d\theta^2} + m^2\Theta = 0 \qquad \text{(B-4b)}$$

where m = separation constant.

Solving Eqs. (B-4a) and (B-4b) will then yield a solution to Eq. (B-2) of

$$P = \left[c_1 J_m \left(\frac{\omega r}{a_c} \right) + c_2 Y_m \left(\frac{\omega r}{a_c} \right) \right] \cdot \left[c_3 \cos m\theta + c_4 \sin m\theta \right] \sin \omega t \qquad \text{(B-5)}$$

where

J_m = Bessel function of the first kind, order m

Y_m = Bessel function of the second kind, order m

c_1, c_2, c_3, c_4 = arbitrary constants

The boundary conditions of a standing wave which are needed to solve for the constants in Eq. (B-5) are

$$\tilde{P}(r = 0) = \text{finite} \tag{B-6}$$

$$\left.\frac{\partial \tilde{P}}{\partial r}\right|_{r = r_w} = 0 \tag{B-7}$$

$$\tilde{P}(\theta = 0) = \tilde{P}\ (\theta = 2\pi) \tag{B-8}$$

and

$$\left.\frac{\partial \tilde{P}}{\partial \theta}\right|_{\theta = 0} = \left.\frac{\partial \tilde{P}}{\partial \theta}\right|_{\theta = 2\pi} = 0 \tag{B-9}$$

Applying Eqs. (B-6) and (B-9) to Eq. (B-5) shows that the constants c_2 and c_4 equal zero. For Eq. (B-8) to hold, the constant "m" must be an integer, so that

$$m = 0, 1, 2, 3, \ldots\ldots \tag{B-10}$$

Finally, applying Eq. (B-7) to Eq. (B-5) will show that the system must oscillate at discrete frequencies such that

$$\left.\frac{d\ J_m\left(\frac{\omega_{m,n}}{a_c}\, r\right)}{dr}\right|_{r = r_w} = 0 \tag{B-11a}$$

where

$$n = 1, 2, 3, \ldots\ldots \tag{B-11b}$$

Table B-1 below shows some of the solutions to Eq. (B-11), giving the eigenvalues of $\omega_{m,n}$ for the various transverse modes. Fig. B-3 then graphs out the Bessel function, J_m, versus the non-dimensional radius, (r/r_w), for the first and second tangentials, and the first radial acoustic modes.

TABLE B-1. TRANSVERSE ACOUSTIC MODES

m	n	$\left(\frac{\omega_{m,n} r_w}{a_c}\right)$	Transverse Mode
1	1	1.8413	First tangential
2	1	3.0543	Second tangential
0	2	3.8317	First radial
3	1	4.2012	Third tangential
0	3	7.0156	Second radial
1	2	5.3313	Combined first tangential and first radial
1	3	8.5263	Combined first tangential and second radial
2	2	6.7060	Combined second tangential and first radial

Thus, in light of the previous discussion, Eq. (B-5) finally reduces to

$$\tilde{P}_{m,n} = \tilde{P}_{rad} J_m\left(\frac{\omega_{m,n} r}{a_c}\right) \cos m\theta \sin \omega_{m,n} t \qquad \text{(B-12)}$$

Where $\tilde{P}_{rad} = c_1 c_3$ (the amplitude of the first radial mode at r = 0).

Equation (B-12) shows the complete functional form of all the oscillatory modes associated with standing tangential waves. The actual oscillatory pressure for a given "r", "θ", and "t" is made up of the sum of the contributing pressures of each mode so that

$$\tilde{P} = \sum_{m=0}^{\infty} \sum_{n-1}^{\infty} \tilde{P}_{m,n} \qquad \text{(B-13)}$$

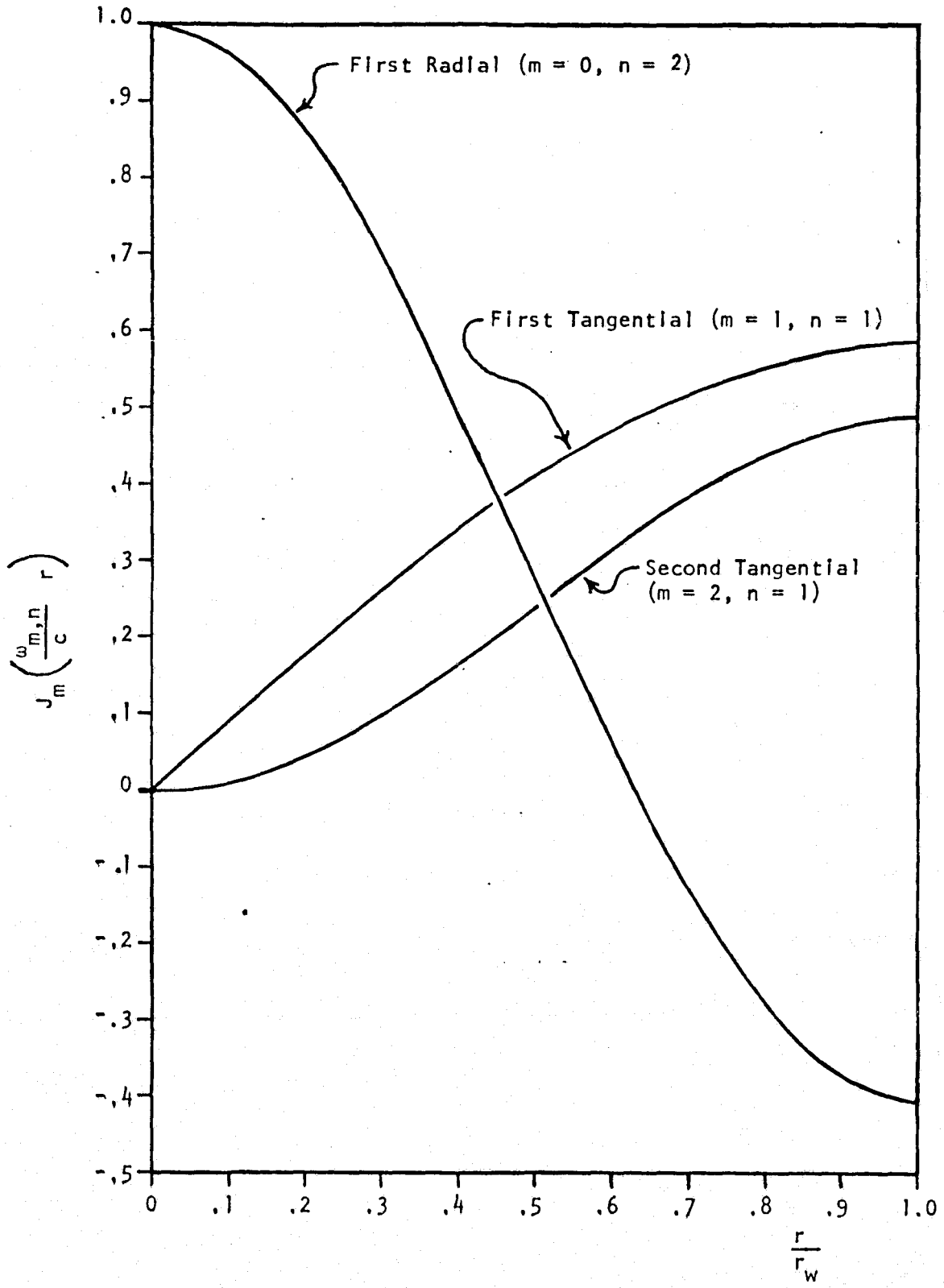

Figure B-3. Bessel Functions for the First Three Acoustic Modes Plotted Versus Non-Dimensional Radius

THE SPINNING TANGENTIAL WAVE

For the spinning tangential wave it will be assumed that the solution to Eq. (B-1) can be represented as

$$\tilde{P} = R(r)\, F(\theta,t) \tag{B-14}$$

where F is some function in θ and t.

Further, Fig. B-2b shows that the functional form of F is given by

$$F = \sin(\omega t + m\theta) \tag{B-15}$$

Substituting Eqs. (B-14) and (B-15) into Eq. (B-1) will yield

$$r^2 \frac{d^2 R}{dr^2} + r \frac{dr}{dr} + \left\{ \frac{\omega^2}{a_c^2} r^2 - m^2 \right\} R = 0. \tag{B-4a}$$

This is the same result for the radially dependent function that was obtained for the standing wave. Thus the solution to Eq. (B-14) is simply

$$\tilde{P} = \left[c_1 J_m \frac{\omega r}{a_c} + c_2 Y_m \frac{\omega r}{a_c} \right] \sin(\omega t + m\theta) \tag{B-16}$$

The boundary conditions of a spinning wave are the same as those for standing waves (Eqs. B-6) - (B-8)), with the exception being that Eq. (B-9) is given only as

$$\left.\frac{\partial \tilde{P}}{\partial \theta}\right|_{\theta = 0} = \left.\frac{\partial \tilde{P}}{\partial \theta}\right|_{\theta = 2\pi} \tag{B-17}$$

Therefore once again c_2 equals zero, "m" is given by Eq. (B-10), and the system will oscillate at the same frequencies given by Eq. (B-11).

Thus for a cylindrical combustor with spinning tangential waves the oscillatory pressure is given by

$$\tilde{P}_{m,n} = \tilde{P}_{rad} J_m \left(\frac{\omega_{m,n} r}{a_c} \right) \sin (\omega_{m,n} t + m\theta) \qquad \text{(B-18)}$$

where here $\tilde{P}_{rad} = c_1$ (again the amplitude of the first radial mode at $r = 0$).

As is easily seen, the only difference between Eq. (B-12) for standing waves and Eq. (B-18) for spinning waves is in replacing "cos mθ sin ωt" by "sin (ωt + mθ)". Therefore Table B-1 and Fig. B-3, which were generated from the radial function only, will still apply to both standing as well as spinning waves.

APPENDIX C

COMPUTER MODEL

DOCUMENTATION OF AEROJET

OME TECHNOLOGY INJECTOR

FUEL SYSTEM FREQUENCY RESPONSE

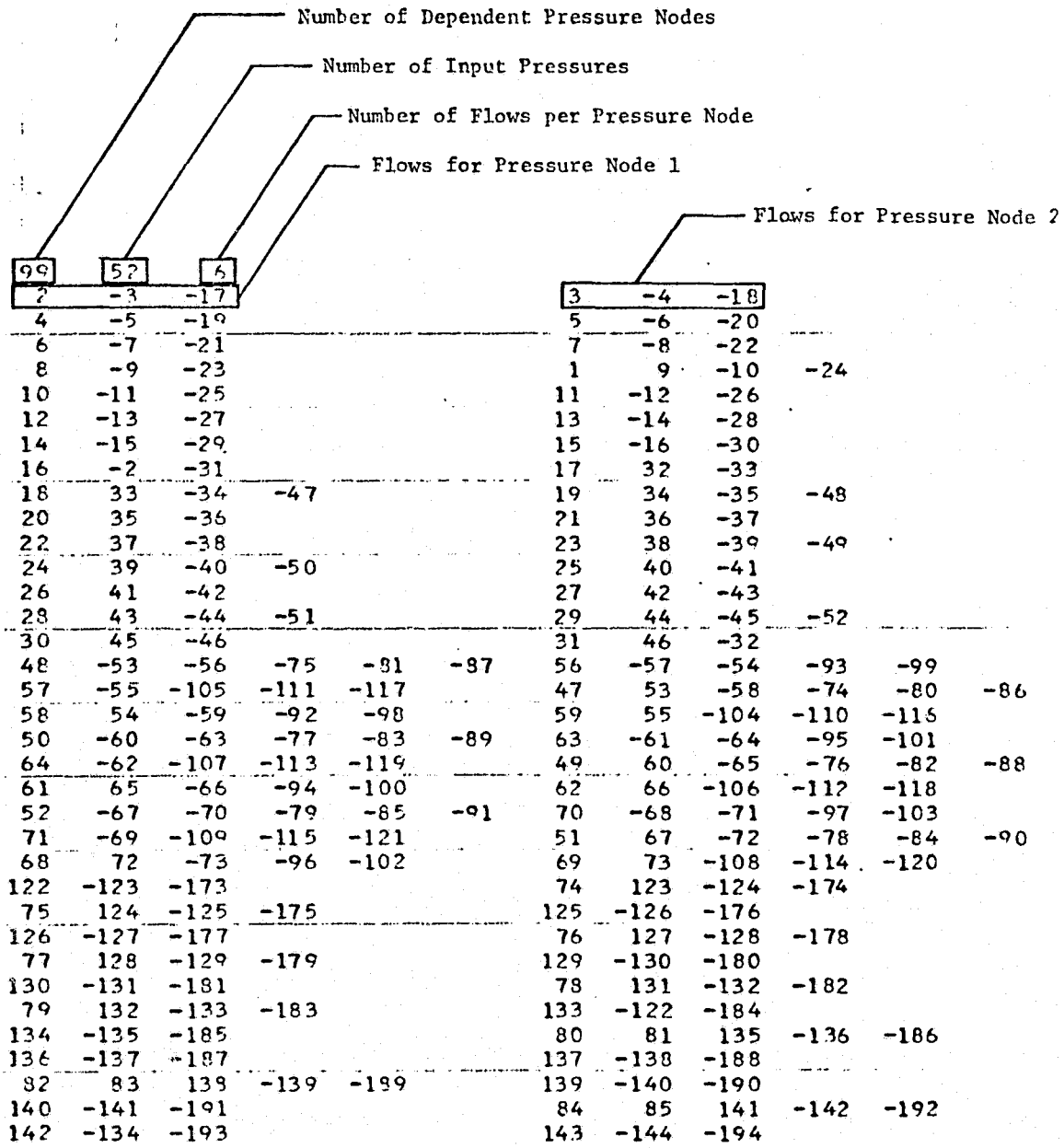

Figure C-1. Data Deck for Aerojet Injector Fuel Side

```
 86    87   144  -145  -195        145  -146  -196
146  -147  -197                    88   147    89  -148  -198
148  -149  -199                   149  -150  -200
 90    91   150  -151  -201        151  -143  -202
 92   152  -153  -203               93   153  -154  -204
 94   154  -155  -205               95   155  -156  -206
 96   156  -157  -207               97   157  -152  -208
 98   158  -159  -209               99   159  -160  -210
100   160  -161  -211              101   161  -162  -212
102   162  -163  -213              103   163  -158  -214
104   105   164  -165  -215        106   107   165  -166  -216
108   109   166  -164  -217        110   111   167  -168  -218
112   113   168  -169  -219        114   115   169  -167  -220
116   117   170  -171  -221        118   119   171  -172  -222
120   121   172  -170  -223
```

Flows Terminating in Input Pressures

```
  1  -173  -174  -175  -176  -177  -178  -179  -180  -181  -182  -183
-184  -185  -186  -187  -188  -189  -190  -191  -192  -193  -194  -195
-196  -197  -198  -199  -200  -201  -202  -203  -204  -205  -206  -207
-208  -209  -210  -211  -212  -213  -214  -215  -216  -217  -218  -219
-220  -221  -222  -223
```

(One Frequency at 2600 Hz)

```
1        2600
```

1 (1T Mode)		2		1 (Spinning)	
0.	3.838	315.	3.838	345.	3.838
15.	3.838	45.	3.838	75.	3.838
105.	3.838	135.	3.838	165.	3.838
195.	3.838	225.	3.838	255.	3.838
285.	3.312	320.	3.312	0.	3.312
40.	3.312	80.	3.312	120.	3.312
160.	3.312	200.	3.312	240.	3.312
280.	2.788	320.	2.788	0.	2.788
40.	2.788	80.	2.788	120.	2.788
160.	2.788	200.	2.788	240.	2.788
280.	2.262	330.	2.262	30.	2.262
90.	2.262	150.	2.262	210.	2.262
270.	1.738	330.	1.738	30.	1.738
90.	1.738	150.	1.738	210.	1.738

Angle and Radius for Each Chamber Pressure Input

Figure C-1. (Continued)

```
270.          1.212          0.          1.212          120.          1.212
240.          .688           0.          .688           120.          .688
240.          .162           0.          .162           120.          .162
240.
0.0
0.0
&D1 R=16*0.,15*23.3,15*0.,6*2.02,21*0.,6*.223,6*.287,6*.354,6*.5,
6*.761,6*1.33,6*7.,6*41.7,0.0,3*0.0,0.0,3*0.0,0.0,3*0.0,
0.0,2*0.,0.0,2*0.,0.0,2*0.,0.0,2*0.,0.0,2*0.,
0.0,2*0.,0.0,0.,0.0,0.,0.0,0.,0.0,0.,0.0,0.,
0.0,0.0,3*0.0,6*0.0,12*1294.,9*559.,9*663.,6*534.,6*648.,
3*474.,3*883.,3*2458.,
Z=16*.004604,15*.04407,15*.03782,
6*.006545,.008757,.005913,.002841,.005693,.009231,.005693,.009231,
.008757,.005913,.002841,.005693,.009231,.005693,.009231,.008757,
.005913,.002841,.005693,.009231,.005693,.009231,6*.006959,6*.005274,
6*.006788,6*.009161,6*.01342,6*.02233,6*.06481,6*.2637,12*.1742,
9*.1255,9*.1202,6*.1735,6*.1732,3*.3447,3*.21,3*.07531,12*.03307,
9*.01429,9*.01684,6*.01367,6*.01655,3*.01209,3*.02245,3*.06286,
V=15*2.756,.1813,2*.2383,3*.1813,2*.2383,3*.1813,2*.2383,2*.1813,1.195,
.5272,.1576,1.195,.5272,.1576,1.195,.5272,.1576,1.195,.5272,.1576,
1.195,.5272,.1576,1.195,.5272,.1576,.06416,.0642,.0642,.06416,
.06416,2*.0642,2*.06416,2*.0642,.06416,2*.1192,.1192,2*.1192,.1192,
2*.1192,.1192,2*.0894,.0894,2*.0894,.0894,2*.0894,.0894,.09369,
.0937,.09369,.0937,.09369,.0937,.05724,.0572,.05724,.0572,.05724,
.0572,3*.1172,3*.06414,3*.02318,
C=99*47880, &END
7.19          125.
```

Mainstage Flowrate and Chamber Pressure

```
  8     1
 49    61    70    79    85    91    94    97     2    14    23    32
 38    44    47    50   173   185   194   203   209   215   218   221
122   134   143   152   158   164   167   170    12     9     9     6
  6     3     3     3
```

Data for Plot Setup

```
AEROJET CME INJECTOR
FUEL SIDE, NO RING DAMS, TEMP=230 F
SPINNING FIRST TANGENTIAL MODE
```

Input for Labeling Plots and Printed Output

Figure C-1. (Continued)

REAL INPUT MATRIX AMPLITUDES - PSI

0.0	7.0711E-01	9.6593E-01	9.6593E-01	7.0711E-01	2.5882E-01
-2.5882E-01	-7.0711E-01	-9.6593E-01	-9.6593E-01	-7.0711E-01	-2.5882E-01
2.5882E-01	7.5140E-01	9.8089E-01	7.5140E-01	1.7033E-01	-4.9044E-01
-9.2173E-01	-9.2173E-01	-4.9044E-01	1.7033E-01	6.9644E-01	9.0914E-01
6.9644E-01	1.5787E-01	-4.5457E-01	-8.5432E-01	-8.5432E-01	-4.5457E-01
1.5787E-01	6.8675E-01	6.8675E-01	0.0	-6.8675E-01	-6.8675E-01
0.0	5.5602E-01	5.5602E-01	0.0	-5.5602E-01	-5.5602E-01
0.0	4.6390E-01	-2.3195E-01	-2.3195E-01	2.6867E-01	-1.3434E-01
-1.3434E-01	6.3622E-02	-3.1811E-02	-3.1811E-02		

IMAGINARY INPUT MATRIX AMPLITUDES - PSI

0.0	-7.0711E-01	-2.5882E-01	2.5882E-01	7.0711E-01	9.6593E-01
9.6593E-01	7.0711E-01	2.5882E-01	-2.5882E-01	-7.0711E-01	-9.6593E-01
-9.6593E-01	-6.3050E-01	0.0	6.3050E-01	9.6599E-01	8.4947E-01
3.3548E-01	-3.3548E-01	-8.4947E-01	-9.6599E-01	-5.8439E-01	0.0
5.8439E-01	8.9533E-01	7.8734E-01	3.1095E-01	-3.1095E-01	-7.8734E-01
-8.9533E-01	-3.9650E-01	3.9650E-01	7.9299E-01	3.9650E-01	-3.9650E-01
-7.9299E-01	-3.2102E-01	3.2102E-01	6.4204E-01	3.2102E-01	-3.2102E-01
-6.4204E-01	0.0	4.0175E-01	-4.0175E-01	0.0	2.3268E-01
-2.3268E-01	0.0	5.5098E-02	-5.5098E-02		

Figure C-2. Real and Imaginary Input Matrix Amplitudes

FLOW	UPSTREAM PRESSURE	DOWNSTREAM PRESSURE	RESISTANCE SEC/IN SQ	INERTANCE SEC SQ/IN SQ	AMPLITUDE LB/SEC/PSI	PHASE DEGREES
1	PIN(1)	P(8)	0.0	4.604E-03	1.021E-03	130.7
2	P(15)	P(1)	0.0	4.604E-03	1.891E-03	54.6
3	P(1)	P(2)	0.0	4.604E-03	2.694E-03	20.8
4	P(2)	P(3)	0.0	4.604E-03	2.447E-03	342.0
5	P(3)	P(4)	0.0	4.604E-03	2.315E-03	295.9
6	P(4)	P(5)	0.0	4.604E-03	1.813E-03	251.8
7	P(5)	P(6)	0.0	4.604E-03	1.600E-03	186.0
8	P(6)	P(7)	0.0	4.604E-03	2.128E-03	131.3
9	P(7)	P(8)	0.0	4.604E-03	2.575E-03	85.6
10	P(8)	P(9)	0.0	4.604E-03	3.216E-03	71.6
11	P(9)	P(10)	0.0	4.604E-03	1.689E-03	40.1
12	P(10)	P(11)	0.0	4.604E-03	1.468E-03	290.1
13	P(11)	P(12)	0.0	4.604E-03	2.974E-03	253.3
14	P(12)	P(13)	0.0	4.604E-03	3.109E-03	225.9
15	P(13)	P(14)	0.0	4.604E-03	2.466E-03	192.6
16	P(14)	P(15)	0.0	4.604E-03	1.346E-03	136.6
17	P(1)	P(16)	2.330E+01	4.407E-02	5.287E-04	43.9
18	P(2)	P(17)	2.330E+01	4.407E-02	1.100E-03	59.5
19	P(3)	P(18)	2.330E+01	4.407E-02	1.055E-03	70.5
20	P(4)	P(19)	2.330E+01	4.407E-02	4.980E-04	85.6
21	P(5)	P(20)	2.330E+01	4.407E-02	3.442E-04	123.9
22	P(6)	P(21)	2.330E+01	4.407E-02	5.234E-04	161.2
23	P(7)	P(22)	2.330E+01	4.407E-02	1.111E-03	177.2
24	P(8)	P(23)	2.330E+01	4.407E-02	1.114E-03	187.9
25	P(9)	P(24)	2.330E+01	4.407E-02	5.250E-04	204.6
26	P(10)	P(25)	2.330E+01	4.407E-02	3.695E-04	246.2
27	P(11)	P(26)	2.330E+01	4.407E-02	5.624E-04	283.6
28	P(12)	P(27)	2.330E+01	4.407E-02	1.161E-03	299.6
29	P(13)	P(28)	2.330E+01	4.407E-02	1.099E-03	312.3
30	P(14)	P(29)	2.330E+01	4.407E-02	5.191E-04	328.4
31	P(15)	P(30)	2.330E+01	4.407E-02	3.571E-04	7.2
32	P(30)	P(16)	0.0	3.782E-02	5.885E-04	72.5
33	P(16)	P(17)	0.0	3.782E-02	9.511E-04	55.8
34	P(17)	P(18)	0.0	3.782E-02	5.422E-05	326.8
35	P(18)	P(19)	0.0	3.782E-02	8.624E-04	252.3
36	P(19)	P(20)	0.0	3.782E-02	5.644E-04	232.3
37	P(20)	P(21)	0.0	3.782E-02	5.702E-04	194.7
38	P(21)	P(22)	0.0	3.782E-02	8.951E-04	174.6
39	P(22)	P(23)	0.0	3.782E-02	7.451E-05	72.1
40	P(23)	P(24)	0.0	3.782E-02	8.933E-04	17.6
41	P(24)	P(25)	0.0	3.782E-02	5.354E-04	358.0

Figure C-3. Input and Output Data for Flowrates

42	P(25)	P(26)	0.0	3.782E-02	5.687E-04	312.2
43	P(26)	P(27)	0.0	3.782E-02	9.843E-04	293.5
44	P(27)	P(28)	0.0	3.782E-02	7.858E-05	217.9
45	P(28)	P(29)	0.0	3.782E-02	8.456E-04	137.1
46	P(29)	P(30)	0.0	3.782E-02	5.284E-04	113.4
47	P(17)	P(34)	2.020E+00	6.545E-03	1.492E-03	57.5
48	P(18)	P(31)	2.020E+00	6.545E-03	1.352E-03	73.0
49	P(22)	P(40)	2.020E+00	6.545E-03	1.462E-03	175.5
50	P(23)	P(37)	2.020E+00	6.545E-03	1.416E-03	193.7
51	P(27)	P(46)	2.020E+00	6.545E-03	1.580E-03	296.6
52	P(28)	P(43)	2.020E+00	6.545E-03	1.392E-03	316.1
53	P(31)	P(34)	0.0	8.757E-03	1.444E-04	42.0
54	P(32)	P(35)	0.0	5.913E-03	5.673E-04	30.5
55	P(33)	P(36)	0.0	2.841E-03	1.472E-04	30.5
56	P(31)	P(32)	0.0	5.693E-03	1.073E-03	255.3
57	P(32)	P(33)	0.0	9.231E-03	5.059E-04	273.0
58	P(34)	P(35)	0.0	5.693E-03	8.907E-04	274.5
59	P(35)	P(36)	0.0	9.231E-03	9.111E-04	249.6
60	P(37)	P(40)	0.0	8.757E-03	1.566E-04	168.7
61	P(38)	P(41)	0.0	5.913E-03	5.700E-04	151.5
62	P(39)	P(42)	0.0	2.841E-03	1.479E-04	151.5
63	P(37)	P(38)	0.0	5.693E-03	1.067E-03	15.6
64	P(38)	P(39)	0.0	9.231E-03	5.061E-04	33.1
65	P(40)	P(41)	0.0	5.693E-03	9.081E-04	35.1
66	P(41)	P(42)	0.0	9.231E-03	7.157E-04	10.0
67	P(43)	P(46)	0.0	8.757E-03	1.282E-04	288.7
68	P(44)	P(47)	0.0	5.913E-03	5.576E-04	271.0
69	P(45)	P(48)	0.0	2.841E-03	1.447E-04	271.0
70	P(43)	P(44)	0.0	5.693E-03	1.044E-03	135.5
71	P(44)	P(45)	0.0	9.231E-03	5.012E-04	153.8
72	P(46)	P(47)	0.0	5.693E-03	8.671E-04	156.9
73	P(47)	P(48)	0.0	9.231E-03	7.016E-04	130.5
74	P(34)	P(50)	2.230E-01	6.959E-03	8.317E-05	312.8
75	P(31)	P(51)	2.230E-01	6.959E-03	5.770E-04	212.4
76	P(40)	P(54)	2.230E-01	6.959E-03	8.779E-05	74.4
77	P(37)	P(55)	2.230E-01	6.959E-03	5.748E-04	332.6
78	P(46)	P(58)	2.230E-01	6.959E-03	8.271E-05	201.4
79	P(43)	P(59)	2.230E-01	6.959E-03	5.686E-04	92.1
80	P(34)	P(62)	2.870E-01	5.274E-03	5.178E-04	218.4
81	P(31)	P(62)	2.870E-01	5.274E-03	2.791E-04	215.2
82	P(40)	P(65)	2.870E-01	5.274E-03	5.237E-04	340.6
83	P(37)	P(65)	2.870E-01	5.274E-03	2.691E-04	332.5
84	P(46)	P(68)	2.870E-01	5.274E-03	4.898E-04	99.6

Figure C-3. (Continued)

85	P(43)	P(68)	2.870E-01	5.274E-03	2.818E-04	92.6
86	P(34)	P(71)	3.540E-01	6.788E-03	4.828E-04	225.5
87	P(31)	P(71)	3.540E-01	6.788E-03	2.971E-04	227.6
88	P(40)	P(74)	3.540E-01	6.788E-03	4.893E-04	347.3
89	P(37)	P(74)	3.540E-01	6.788E-03	2.875E-04	346.1
90	P(46)	P(77)	3.540E-01	6.788E-03	4.698E-04	106.9
91	P(43)	P(77)	3.540E-01	6.788E-03	2.955E-04	105.8
92	P(35)	P(79)	5.000E-01	9.161E-03	4.932E-04	278.6
93	P(32)	P(80)	5.000E-01	9.161E-03	1.358E-03	232.4
94	P(41)	P(81)	5.000E-01	9.161E-03	4.979E-04	38.9
95	P(38)	P(82)	5.000E-01	9.161E-03	1.359E-03	352.7
96	P(47)	P(83)	5.000E-01	9.161E-03	4.869E-04	160.5
97	P(44)	P(84)	5.000E-01	9.161E-03	1.341E-03	112.7
98	P(35)	P(85)	7.610E-01	1.342E-02	6.383E-04	274.5
99	P(32)	P(86)	7.610E-01	1.342E-02	1.063E-03	237.4
100	P(41)	P(87)	7.610E-01	1.342E-02	6.424E-04	34.7
101	P(38)	P(88)	7.610E-01	1.342E-02	1.065E-03	357.7
102	P(47)	P(89)	7.610E-01	1.342E-02	6.336E-04	155.7
103	P(44)	P(90)	7.610E-01	1.342E-02	1.050E-03	117.8
104	P(36)	P(91)	1.330E+00	2.233E-02	4.631E-04	255.9
105	P(33)	P(91)	1.330E+00	2.233E-02	4.501E-04	257.6
106	P(42)	P(92)	1.330E+00	2.233E-02	4.648E-04	16.3
107	P(39)	P(92)	1.330E+00	2.233E-02	4.516E-04	17.9
108	P(48)	P(93)	1.330E+00	2.233E-02	4.579E-04	136.9
109	P(45)	P(93)	1.330E+00	2.233E-02	4.452E-04	138.6
110	P(36)	P(94)	7.000E+00	6.481E-02	3.321E-04	250.0
111	P(33)	P(94)	7.000E+00	6.481E-02	3.271E-04	250.7
112	P(42)	P(95)	7.000E+00	6.481E-02	3.336E-04	10.1
113	P(39)	P(95)	7.000E+00	6.481E-02	3.286E-04	10.8
114	P(48)	P(96)	7.000E+00	6.481E-02	3.304E-04	130.7
115	P(45)	P(96)	7.000E+00	6.481E-02	3.255E-04	131.4
116	P(36)	P(97)	4.170E+01	2.637E-01	1.650E-04	240.1
117	P(33)	P(97)	4.170E+01	2.637E-01	1.637E-04	240.4
118	P(42)	P(98)	4.170E+01	2.637E-01	1.660E-04	0.1
119	P(39)	P(98)	4.170E+01	2.637E-01	1.646E-04	0.4
120	P(48)	P(99)	4.170E+01	2.637E-01	1.648E-04	120.7
121	P(45)	P(99)	4.170E+01	2.637E-01	1.635E-04	120.9
122	P(60)	P(49)	0.0	1.742E-01	1.759E-04	96.7
123	P(49)	P(50)	0.0	1.742E-01	1.348E-04	141.0
124	P(50)	P(51)	0.0	1.742E-01	3.087E-05	208.5
125	P(51)	P(52)	0.0	1.742E-01	3.396E-04	193.1
126	P(52)	P(53)	0.0	1.742E-01	1.766E-04	216.3
127	P(53)	P(54)	0.0	1.742E-01	1.360E-04	260.7

Figure C-3. (Continued)

128	P(54)	P(55)	0.0	1.742E-01	3.126E-05	330.2
129	P(55)	P(56)	0.0	1.742E-01	3.396E-04	313.3
130	P(56)	P(57)	0.0	1.742E-01	1.773E-04	336.7
131	P(57)	P(58)	0.0	1.742E-01	1.373E-04	22.1
132	P(58)	P(59)	0.0	1.742E-01	3.001E-05	89.6
133	P(59)	P(60)	0.0	1.742E-01	3.362E-04	73.3
134	P(69)	P(61)	0.0	1.255E-01	2.800E-04	109.1
135	P(61)	P(62)	0.0	1.255E-01	1.714E-04	142.2
136	P(62)	P(63)	0.0	1.255E-01	4.825E-04	189.4
137	P(63)	P(64)	0.0	1.255E-01	2.801E-04	228.7
138	P(64)	P(65)	0.0	1.255E-01	1.729E-04	261.9
139	P(65)	P(66)	0.0	1.255E-01	4.821E-04	309.7
140	P(66)	P(67)	0.0	1.255E-01	2.815E-04	348.9
141	P(67)	P(68)	0.0	1.255E-01	1.754E-04	23.3
142	P(68)	P(69)	0.0	1.255E-01	4.770E-04	69.6
143	P(78)	P(70)	0.0	1.202E-01	2.686E-04	106.2
144	P(70)	P(71)	0.0	1.202E-01	1.634E-04	129.9
145	P(71)	P(72)	0.0	1.202E-01	4.808E-04	195.3
146	P(72)	P(73)	0.0	1.202E-01	2.692E-04	225.8
147	P(73)	P(74)	0.0	1.202E-01	1.649E-04	249.8
148	P(74)	P(75)	0.0	1.202E-01	4.807E-04	315.5
149	P(75)	P(76)	0.0	1.202E-01	2.705E-04	346.0
150	P(76)	P(77)	0.0	1.202E-01	1.665E-04	11.3
151	P(77)	P(78)	0.0	1.202E-01	4.754E-04	75.5
152	P(84)	P(79)	0.0	1.735E-01	4.655E-04	86.8
153	P(79)	P(80)	0.0	1.735E-01	7.621E-05	212.3
154	P(80)	P(81)	0.0	1.735E-01	4.686E-04	206.4
155	P(81)	P(82)	0.0	1.735E-01	7.625E-05	332.6
156	P(82)	P(83)	0.0	1.735E-01	4.695E-04	326.9
157	P(83)	P(84)	0.0	1.735E-01	7.578E-05	92.5
158	P(90)	P(85)	0.0	1.732E-01	4.370E-04	85.2
159	P(85)	P(86)	0.0	1.732E-01	7.152E-05	204.6
160	P(86)	P(87)	0.0	1.732E-01	4.400E-04	204.8
161	P(87)	P(88)	0.0	1.732E-01	7.149E-05	324.9
162	P(88)	P(89)	0.0	1.732E-01	4.408E-04	325.3
163	P(89)	P(90)	0.0	1.732E-01	7.104E-05	84.7
164	P(93)	P(91)	0.0	3.447E-01	2.085E-04	85.3
165	P(91)	P(92)	0.0	3.447E-01	2.096E-04	204.9
166	P(92)	P(93)	0.0	3.447E-01	2.104E-04	325.3
167	P(96)	P(94)	0.0	2.100E-01	2.508E-04	82.0
168	P(94)	P(95)	0.0	2.100E-01	2.522E-04	201.6
169	P(95)	P(96)	0.0	2.100E-01	2.531E-04	322.0
170	P(99)	P(97)	0.0	7.531E-02	1.802E-04	86.8

Figure C-3. (Continued)

171	P(97)	P(98)	0.0	7.531E-02	1.814E-04	206.5
172	P(98)	P(99)	0.0	7.531E-02	1.818E-04	327.0
173	P(49)	PIN(2)	1.294E+03	3.307E-02	5.760E-05	206.6
174	P(50)	PIN(3)	1.294E+03	3.307E-02	1.588E-04	229.0
175	P(51)	PIN(4)	1.294E+03	3.307E-02	4.716E-04	237.6
176	P(52)	PIN(5)	1.294E+03	3.307E-02	1.247E-04	222.8
177	P(53)	PIN(6)	1.294E+03	3.307E-02	5.644E-05	328.1
178	P(54)	PIN(7)	1.294E+03	3.307E-02	1.565E-04	350.4
179	P(55)	PIN(8)	1.294E+03	3.307E-02	4.704E-04	357.8
180	P(56)	PIN(9)	1.294E+03	3.307E-02	1.244E-04	342.7
181	P(57)	PIN(10)	1.294E+03	3.307E-02	5.343E-05	87.4
182	P(58)	PIN(11)	1.294E+03	3.307E-02	1.486E-04	108.6
183	P(59)	PIN(12)	1.294E+03	3.307E-02	4.634E-04	117.7
184	P(60)	PIN(13)	1.294E+03	3.307E-02	1.229E-04	103.5
185	P(61)	PIN(14)	5.590E+02	1.429E-02	1.964E-04	196.9
186	P(62)	PIN(15)	5.590E+02	1.429E-02	7.289E-04	233.5
187	P(63)	PIN(16)	5.590E+02	1.429E-02	1.516E-04	222.6
188	P(64)	PIN(17)	5.590E+02	1.429E-02	1.947E-04	317.4
189	P(65)	PIN(18)	5.590E+02	1.429E-02	7.250E-04	354.0
190	P(66)	PIN(19)	5.590E+02	1.429E-02	1.513E-04	343.0
191	P(67)	PIN(20)	5.590E+02	1.429E-02	1.903E-04	77.2
192	P(68)	PIN(21)	5.590E+02	1.429E-02	7.076E-04	113.4
193	P(69)	PIN(22)	5.590E+02	1.429E-02	1.482E-04	103.8
194	P(70)	PIN(23)	6.630E+02	1.684E-02	1.271E-04	188.8
195	P(71)	PIN(24)	6.630E+02	1.684E-02	5.968E-04	241.5
196	P(72)	PIN(25)	6.630E+02	1.684E-02	1.786E-04	208.6
197	P(73)	PIN(26)	6.630E+02	1.684E-02	1.250E-04	309.4
198	P(74)	PIN(27)	6.630E+02	1.684E-02	5.944E-04	2.1
199	P(75)	PIN(28)	6.630E+02	1.684E-02	1.781E-04	328.8
200	P(76)	PIN(29)	6.630E+02	1.684E-02	1.212E-04	68.6
201	P(77)	PIN(30)	6.630E+02	1.684E-02	5.792E-04	121.7
202	P(78)	PIN(31)	6.630E+02	1.684E-02	1.746E-04	89.2
203	P(79)	PIN(32)	5.340E+02	1.367E-02	1.795E-04	282.8
204	P(80)	PIN(33)	5.340E+02	1.367E-02	1.204E-03	242.8
205	P(81)	PIN(34)	5.340E+02	1.367E-02	1.830E-04	44.8
206	P(82)	PIN(35)	5.340E+02	1.367E-02	1.204E-03	3.0
207	P(83)	PIN(36)	5.340E+02	1.367E-02	1.728E-04	168.8
208	P(84)	PIN(37)	5.340E+02	1.367E-02	1.189E-03	123.2
209	P(85)	PIN(38)	6.480E+02	1.655E-02	2.886E-04	285.3
210	P(86)	PIN(39)	6.480E+02	1.655E-02	8.817E-04	251.1
211	P(87)	PIN(40)	6.480E+02	1.655E-02	2.914E-04	46.3
212	P(88)	PIN(41)	6.480E+02	1.655E-02	8.821E-04	11.4
213	P(89)	PIN(42)	6.480E+02	1.655E-02	2.839E-04	168.2

Figure C-3. (Continued)

214	P(90)	PIN(43)	6.480E+02	1.655E-02	8.714E-04	131.7
215	P(91)	PIN(44)	4.740E+02	1.209E-02	7.829E-04	260.6
216	P(92)	PIN(45)	4.740E+02	1.209E-02	7.842E-04	21.0
217	P(93)	PIN(46)	4.740E+02	1.209E-02	7.730E-04	141.8
218	P(94)	PIN(47)	8.830E+02	2.245E-02	3.485E-04	268.8
219	P(95)	PIN(48)	8.830E+02	2.245E-02	3.487E-04	29.2
220	P(96)	PIN(49)	8.830E+02	2.245E-02	3.456E-04	150.1
221	P(97)	PIN(50)	2.458E+03	6.286E-02	3.165E-05	278.1
222	P(98)	PIN(51)	2.458E+03	6.286E-02	3.084E-05	38.9
223	P(99)	PIN(52)	2.458E+03	6.286E-02	3.115E-05	160.8

AEROJET OME INJECTOR
FUEL SIDE, NO RING DAMS, TEMP=230 F
SPINNING FIRST TANGENTIAL MODE

	LB/SEC/PSI	% FLOW/% PC
TOTAL INJECTOR FLOW=	1.9386E-02	3.3704E-01
TOTAL VECTOR INJECTOR FLOW=	1.6699E-02	2.9031E-01
TOTAL INJECTOR FLOW PROPORTIONED BY PC AMPLITUDES=	1.4869E-02	2.5851E-01
TOTAL VECTOR INJECTOR FLOW PROPORTIONED BY PC AMPLITUDES=	1.2977E-02	2.2562E-01

Figure C-3. (Concluded)

PRESSURE NODE	VOLUME CU IN	AC. VEL. IN/SEC	MAGNITUDE PSI/PSI	PHASE DEGREES	FLOWS IN		FLOWS OUT				
1	2.756E+00	4.788E+04	2.394E-01	83.1	2		3	17			
2	2.756E+00	4.788E+04	1.116E-01	25.6	3		4	18			
3	2.756E+00	4.788E+04	1.342E-01	289.0	4		5	19			
4	2.756E+00	4.788E+04	2.322E-01	240.9	5		6	20			
5	2.756E+00	4.788E+04	2.907E-01	213.5	6		7	21			
6	2.756E+00	4.788E+04	2.583E-01	189.1	7		8	22			
7	2.756E+00	4.788E+04	1.497E-01	154.3	8		9	23			
8	2.756E+00	4.788E+04	7.678E-02	40.7	1	9	10	24			
9	2.756E+00	4.788E+04	2.890E-01	354.8	10		11	25			
10	2.756E+00	4.788E+04	3.896E-01	341.5	11		12	26			
11	2.756E+00	4.788E+04	3.110E-01	328.7	12		13	27			
12	2.756E+00	4.788E+04	1.101E-01	297.9	13		14	28			
13	2.756E+00	4.788E+04	1.335E-01	150.6	14		15	29			
14	2.756E+00	4.788E+04	2.921E-01	122.4	15		16	30			
15	2.756E+00	4.788E+04	3.318E-01	105.2	16		2	31			
16	1.813E-01	4.788E+04	2.874E-01	351.0	17	32	33				
17	2.383E-01	4.788E+04	8.565E-01	334.0	18	33	34	47			
18	2.383E-01	4.788E+04	8.529E-01	331.8	19	34	35	48			
19	1.813E-01	4.788E+04	3.433E-01	315.2	20	35	36				
20	1.813E-01	4.788E+04	4.323E-02	221.6	21	36	37				
21	1.813E-01	4.788E+04	3.350E-01	111.4	22	37	38				
22	2.383E-01	4.788E+04	8.653E-01	94.6	23	38	39	49			
23	2.383E-01	4.788E+04	8.488E-01	91.8	24	39	40	50			
24	1.813E-01	4.788E+04	3.520E-01	66.3	25	40	41				
25	1.813E-01	4.788E+04	1.299E-01	356.4	26	41	42				
26	1.813E-01	4.788E+04	2.769E-01	241.8	27	42	43				
27	2.383E-01	4.788E+04	8.430E-01	215.2	28	43	44	51			
28	2.383E-01	4.788E+04	8.467E-01	212.0	29	44	45	52			
29	1.813E-01	4.788E+04	3.685E-01	190.2	30	45	46				
30	1.813E-01	4.788E+04	8.982E-02	134.5	31	46	32				
31	1.195E+00	4.788E+04	9.956E-01	333.2	48		53	56	75	81	87
32	5.272E-01	4.788E+04	8.982E-01	331.9	56		57	54	93	99	
33	1.576E-01	4.788E+04	8.338E-01	329.2	57		55	105	111	117	
34	1.195E+00	4.788E+04	1.015E+00	332.8	47	53	58	74	80	86	
35	5.272E-01	4.788E+04	9.454E-01	330.2	58	54	59	92	98		
36	1.576E-01	4.788E+04	8.398E-01	329.0	59	55	104	110	116		
37	1.195E+00	4.788E+04	9.979E-01	93.4	50		60	63	77	83	89
38	5.272E-01	4.788E+04	9.012E-01	92.1	63		61	64	95	101	
39	1.576E-01	4.788E+04	8.367E-01	89.4	64		62	107	113	119	
40	1.195E+00	4.788E+04	1.020E+00	93.1	49	60	65	76	82	88	

Figure C-4. Input and Output Data for Pressure Nodes

41	5.272E-01	4.788E+04	9.490E-01	90.4	61	65		66	94	100			
42	1.576E-01	4.788E+04	8.428E-01	89.1	62	66		106	112	118			
43	1.195E+00	4.788E+04	9.922E-01	213.9	52			67	70	79	85	91	
44	5.272E-01	4.788E+04	8.973E-01	212.6	70			68	71	97	103		
45	1.576E-01	4.788E+04	8.335E-01	210.0	71			69	109	115	121		
46	1.195E+00	4.788E+04	1.010E+00	213.6	51	67		72	78	84	90		
47	5.272E-01	4.788E+04	9.436E-01	210.9	68	72		73	96	102			
48	1.576E-01	4.788E+04	8.394E-01	209.7	69	73		108	114	120			
49	6.416E-02	4.788E+04	1.009E+00	310.4	122			123	173				
50	6.420E-02	4.788E+04	1.012E+00	332.3	74	123		124	174				
51	6.420E-02	4.788E+04	9.399E-01	335.3	75	124		125	175				
52	6.416E-02	4.788E+04	8.384E-01	40.8	125			126	176				
53	6.416E-02	4.788E+04	1.011E+00	70.5	126			127	177				
54	6.420E-02	4.788E+04	1.016E+00	92.5	76	127		128	178				
55	6.420E-02	4.788E+04	9.425E-01	95.4	77	128		129	179				
56	6.416E-02	4.788E+04	8.387E-01	160.9	129			130	180				
57	6.416E-02	4.788E+04	1.009E+00	190.8	130			131	181				
58	6.420E-02	4.788E+04	1.008E+00	213.1	78	131		132	182				
59	6.420E-02	4.788E+04	9.380E-01	216.0	79	132		133	183				
60	6.416E-02	4.788E+04	8.416E-01	280.8	133			122	184				
61	1.192E-01	4.788E+04	9.664E-01	313.0	134			135	185				
62	1.192E-01	4.788E+04	9.745E-01	333.9	80	81	135	136	186				
63	1.192E-01	4.788E+04	8.987E-01	37.5	136			137	187				
64	1.192E-01	4.788E+04	9.676E-01	73.1	137			138	188				
65	1.192E-01	4.788E+04	9.781E-01	94.1	82	83	138	139	189				
66	1.192E-01	4.788E+04	8.991E-01	157.5	139			140	190				
67	1.192E-01	4.788E+04	9.672E-01	193.3	140			141	191				
68	1.192E-01	4.788E+04	9.716E-01	214.6	84	85	141	142	192				
69	1.192E-01	4.788E+04	9.014E-01	277.5	142			134	193				
70	8.940E-02	4.788E+04	8.842E-01	314.4	143			144	194				
71	8.940E-02	4.788E+04	9.639E-01	333.8	86	87	144	145	195				
72	8.940E-02	4.788E+04	7.837E-01	38.2	145			146	196				
73	8.940E-02	4.788E+04	8.855E-01	74.5	146			147	197				
74	8.940E-02	4.788E+04	9.675E-01	94.0	88	147	89	148	198				
75	8.940E-02	4.788E+04	7.842E-01	158.2	148			149	199				
76	8.940E-02	4.788E+04	8.849E-01	194.7	149			150	200				
77	8.940E-02	4.788E+04	9.612E-01	214.5	90	91	150	151	201				
78	8.940E-02	4.788E+04	7.869E-01	278.1	151			143	202				
79	9.369E-02	4.788E+04	8.886E-01	327.2	92	152		153	203				
80	9.370E-02	4.788E+04	6.987E-01	334.7	93	153		154	204				
81	9.369E-02	4.788E+04	8.918E-01	87.4	94	154		155	205				
82	9.370E-02	4.788E+04	7.015E-01	94.8	95	155		156	206				
83	9.369E-02	4.788E+04	8.884E-01	208.0	96	156		157	207				

Figure C-4. (Continued)

84	9.370E-02	4.788E+04	7.007E-01	215.5	97	157		152	208
85	5.724E-02	4.788E+04	8.333E-01	324.8	98	158		159	209
86	5.720E-02	4.788E+04	6.662E-01	333.6	99	159		160	210
87	5.724E-02	4.788E+04	8.362E-01	84.9	100	160		161	211
88	5.720E-02	4.788E+04	6.688E-01	93.6	101	161		162	212
89	5.724E-02	4.788E+04	8.329E-01	205.5	102	162		163	213
90	5.720E-02	4.788E+04	6.683E-01	214.4	103	163		158	214
91	1.172E-01	4.788E+04	6.798E-01	324.9	104	105	164	165	215
92	1.172E-01	4.788E+04	6.823E-01	85.0	106	107	165	166	216
93	1.172E-01	4.788E+04	6.814E-01	205.6	108	109	166	164	217
94	6.414E-02	4.788E+04	4.985E-01	321.5	110	111	167	168	218
95	6.414E-02	4.788E+04	4.997E-01	81.7	112	113	168	169	219
96	6.414E-02	4.788E+04	4.996E-01	202.4	114	115	169	167	220
97	2.318E-02	4.788E+04	1.290E-01	325.8	116	117	170	171	221
98	2.318E-02	4.788E+04	1.276E-01	86.7	118	119	171	172	222
99	2.318E-02	4.788E+04	1.295E-01	207.7	120	121	172	170	223

Figure C-4. (Concluded)

APPENDIX D

COMPUTER MODEL DOCUMENTATION OF AEROJET

OME TECHNOLOGY INJECTOR

OXIDIZER SYSTEM FREQUENCY RESPONSE

```
AEROJET OME INJECTOR
OXIDIZER SIDE, NO RING DAMS
SPINNING FIRST TANGENTIAL MODE
   71    51     6
    1    -2    -3    -4   -74          2    -5    -6   -72   -73
    3    -7    -8   -70   -71          4    -9   -10   -68   -69
    6   -11   -14   -57   -63         14   -12   -15   -45   -51
   15   -13   -33   -39               5    11   -16   -56   -62
   12    16   -17   -44   -50         13    17   -32   -38
    8   -18   -21   -59   -65         21   -19   -22   -47   -53
   22   -20   -35   -41               7    18   -23   -58   -64
   23    19   -24   -46   -52         20    24   -34   -40
   10   -25   -28   -61   -67         28   -29   -26   -49   -55
   29   -27   -37   -43               9    25   -30   -60   -66
   26    30   -31   -48   -54         27    31   -36   -42
   75   -76  -123                    76   -77  -124
   32    77   -78  -125               33    78   -79  -126
   79   -80  -127                    80   -81  -128
   81    34   -82  -129               35    82   -83  -130
   83   -84  -131                    84   -85  -132
   36    85  -133   -86               86    37   -75  -134
   87   -88  -135                    38    39    88   -89  -136
   89   -90  -137                    90   -91  -138
   40    41    91   -92  -139         92   -93  -140
   93   -94  -141                    42    43    94   -95  -142
   95   -87  -143                    96   -97  -144
   44    45    97   -98  -145         98   -99  -146
   99  -100  -147                    47   100    46  -101  -148
  101  -102  -149                   102  -103  -150
   48    49   103  -104  -151        104   -96  -152
   50   105  -106  -153               51   106  -107  -154
   52   107  -108  -155               53   108  -109  -156
   54   109  -110  -157               55   110  -105  -158
   56   111  -112  -159               57   112  -113  -160
   58   113  -114  -161               59   114  -115  -162
   60   115  -116  -163               61   116  -111  -164
   62    63   117  -118  -165         64    65   118  -119  -166
   66    67   119  -117  -167         68    69   120  -121  -168
   70    71   121  -122  -169         72    73   122  -120  -170
   74  -171
    1  -123  -124  -125  -126  -127  -128  -129  -130  -131  -132  -133
 -134  -135  -136  -137  -138  -139  -140  -141  -142  -143  -144  -145
 -146  -147  -148  -149  -150  -151  -152  -153  -154  -155  -156  -157
 -158  -159  -160  -161  -162  -163  -164  -165  -166  -167  -168  -169
 -170  -171
```

Figure D-1, Data Deck for Aerojet Injector Oxidizer Side

```
          1         2600
          1           2           1
 0.         3.706      345.       3.706      15.        3.706
 45.        3.706      75.        3.706     105.        3.706
135.        3.706      165.       3.706     195.        3.706
225.        3.706      255.       3.706     285.        3.706
315.        3.181       20.       3.181      60.        3.181
100.        3.181      140.       3.181     180.        3.181
220.        3.181      260.       3.181     300.        3.181
340.        2.656       20.       2.656      60.        2.656
100.        2.656      140.       2.656     180.        2.656
220.        2.656      260.       2.656     300.        2.656
340.        2.131       30.       2.131      90.        2.131
150.        2.131      210.       2.131     270.        2.131
330.        1.606       30.       1.606      90.        1.606
150.        1.606      210.       1.606     270.        1.606
3360.       1.081       0.        1.081     180.        1.081
300.         .556      300.        .556     180.         .556
60.         0.          0.
0.0         0.0
0.0         0.0
&D1 R=0.,3*1.49,6*0.,21*0.,6*.318,6*.323,6*.403,6*.53,6*.945,
6*2.31,6*12.,22.5,0.0,0.0,3*0.0,0.0,3*0.0,0.0,2*0.,0.0,
2*0.,0.0,2*0.,0.0,2*0.,0.0,2*0.,0.0,2*0.,0.0,
2*0.0,0.0,0.0,0.0,0.0,0.0,0.0,0.0,0.0,0.0,0.0,
0.0,0.0,6*0.0,12*411.,9*358.,9*443.,6*352.,6*461.,3*370.,
3*738.,2600.,Z=4*.005978,6*.000824,.001576,.003933,.006185,.006625,
.003674,.006625,.003674,.001576,.003933,.006185,.006625,.003674,
.006625,.003674,.001576,.003933,.006185,.006625,.003674,.006625,
.003674,6*.006055,6*.00722,6*.008928,6*.01178,6*.01711,6*.03183,
6*.06082,.124,12*.08256,9*.109,9*.1071,6*.1568,6*.1599,3*.2821,
3*.1449,12*.01747,9*.01522,9*.01887,6*.01496,6*.01964,3*.01571,
3*.03131,.1048,
V=17.6,3*.364,.565,1.224,1.59,.565,1.224,1.59,.565,1.224,1.59,.565,
1.224,1.59,.565,1.224,1.59,.565,1.224,1.59,2*.118,2*.118,2*.118,2*.118,
2*.118,2*.118,.117,2*.117,.117,2*.117,.117,2*.117,.0832,.0832,.0832,
.0832,2*.0832,.0832,2*.0832,6*.148,6*.101,3*.123,3*.0802,.0152,
C=71*39612., &END
11.86       125.
    7     1
   23    35    44    53    59    65    68     2    14    23    32    38
   44    47   123   135   144   153   159   165   168    75    87    96
  105   111   117   120    12     9     9     6     6     3     4
```

Figure D-1. (Continued)

```
REAL INPUT MATRIX AMPLITUDES - PSI
   0.0          9.6593E-01   9.6593E-01   7.0711E-01   2.5882E-01 -2.5882E-01
  -7.0711E-01  -9.6593E-01  -9.6593E-01  -7.0711E-01  -2.5882E-01  2.5882E-01
   7.0711E-01   9.2022E-01   4.8964E-01  -1.7005E-01  -7.5017E-01 -9.7927E-01
  -7.5017E-01  -1.7005E-01   4.8964E-01   9.2022E-01   8.4783E-01  4.5112E-01
  -1.5667E-01  -6.9116E-01  -9.0224E-01  -6.9116E-01  -1.5667E-01  4.5112E-01
   8.4783E-01   6.7431E-01   0.0         -6.7431E-01  -6.7431E-01  0.0
   6.7431E-01   5.3531E-01   0.0         -5.3531E-01  -5.3531E-01  0.0
  -3.0906E-01   4.3048E-01  -4.3048E-01   2.1524E-01   1.1270E-01 -2.2540E-01
   1.1270E-01   0.0          0.0

IMAGINARY INPUT MATRIX AMPLITUDES - PSI
   0.0         -2.5882E-01   2.5882E-01   7.0711E-01   9.6593E-01  9.6593E-01
   7.0711E-01   2.5882E-01  -2.5882E-01  -7.0711E-01  -9.6593E-01 -9.6593E-01
  -7.0711E-01   3.3493E-01   8.4808E-01   9.6440E-01   6.2947E-01  0.0
  -6.2947E-01  -9.6440E-01  -8.4808E-01  -3.3493E-01   3.0858E-01  7.8136E-01
   8.8853E-01   5.7995E-01   0.0         -5.7995E-01  -8.8853E-01 -7.8136E-01
  -3.0859E-01   3.8931E-01   7.7862E-01   3.8931E-01  -3.8931E-01 -7.7862E-01
  -3.8931E-01   3.0906E-01   6.1813E-01   3.0906E-01  -3.0906E-01 -6.1813E-01
   5.3531E-01   0.0          0.0         -3.7281E-01  -1.9520E-01  0.0
   1.9520E-01   0.0          0.0

1.
AEROJET CME INJECTOR
OXIDIZER SIDE, NO RING DAMS
SPINNING FIRST TANGENTIAL MODE

INPUT FREQUENCY= 2600.0
```

Figure D-2. Real and Imaginary Input Matrix Amplitudes

FLOW	UPSTREAM PRESSURE	DOWNSTREAM PRESSURE	RESISTANCE SEC/IN SQ	INERTANCE SEC SQ/IN SQ	AMPLITUDE LB/SEC/PSI	PHASE DEGREES
1	PIN(1)	P(1)	0.0	5.978E-03	7.646E-05	46.5
2	P(1)	P(2)	1.490E+00	5.978E-03	5.633E-03	53.7
3	P(1)	P(3)	1.490E+00	5.978E-03	5.614E-03	175.6
4	P(1)	P(4)	1.490E+00	5.978E-03	5.649E-03	290.2
5	P(2)	P(8)	0.0	8.240E-04	2.876E-03	56.9
6	P(2)	P(5)	0.0	8.240E-04	2.583E-03	51.6
7	P(3)	P(14)	0.0	8.240E-04	2.890E-03	178.7
8	P(3)	P(11)	0.0	8.240E-04	2.546E-03	173.4
9	P(4)	P(20)	0.0	8.240E-04	2.628E-03	297.1
10	P(4)	P(17)	0.0	8.240E-04	2.875E-03	285.3
11	P(5)	P(8)	0.0	1.576E-03	2.023E-04	95.1
12	P(6)	P(9)	0.0	3.933E-03	4.983E-04	88.4
13	P(7)	P(10)	0.0	6.185E-03	4.686E-04	82.4
14	P(5)	P(6)	0.0	6.625E-03	2.784E-03	50.9
15	P(6)	P(7)	0.0	3.674E-03	1.340E-03	52.8
16	P(8)	P(9)	0.0	6.625E-03	2.988E-03	53.7
17	P(9)	P(10)	0.0	3.674E-03	2.093E-03	55.0
18	P(11)	P(14)	0.0	1.576E-03	2.210E-04	212.2
19	P(12)	P(15)	0.0	3.933E-03	4.984E-04	208.9
20	P(13)	P(16)	0.0	6.185E-03	4.693E-04	202.6
21	P(11)	P(12)	0.0	6.625E-03	3.039E-03	173.6
22	P(12)	P(13)	0.0	3.674E-03	2.007E-03	175.3
23	P(14)	P(15)	0.0	6.625E-03	3.242E-03	176.0
24	P(15)	P(16)	0.0	3.674E-03	2.266E-03	177.0
25	P(17)	P(20)	0.0	1.576E-03	3.215E-04	44.8
26	P(18)	P(21)	0.0	3.933E-03	4.857E-04	330.9
27	P(19)	P(22)	0.0	6.185E-03	4.646E-04	323.2
28	P(17)	P(18)	0.0	6.625E-03	2.411E-03	298.1
29	P(18)	P(19)	0.0	3.674E-03	1.622E-03	300.1
30	P(20)	P(21)	0.0	6.625E-03	2.676E-03	299.8
31	P(21)	P(22)	0.0	3.674E-03	1.895E-03	301.3
32	P(10)	P(25)	3.180E-01	6.055E-03	2.220E-03	225.4
33	P(7)	P(26)	3.180E-01	6.055E-03	3.368E-03	238.0
34	P(16)	P(29)	3.180E-01	6.055E-03	2.198E-03	347.3
35	P(13)	P(30)	3.180E-01	6.055E-03	3.364E-03	359.4
36	P(22)	P(33)	3.180E-01	6.055E-03	2.128E-03	103.3
37	P(19)	P(34)	3.180E-01	6.055E-03	3.260E-03	117.1
38	P(10)	P(36)	3.230E-01	7.220E-03	1.985E-03	234.3
39	P(7)	P(36)	3.230E-01	7.220E-03	1.642E-03	227.6
40	P(16)	P(39)	3.230E-01	7.220E-03	1.981E-03	355.7
41	P(13)	P(39)	3.230E-01	7.220E-03	1.633E-03	349.3
42	P(22)	P(42)	3.230E-01	7.220E-03	1.913E-03	113.3
43	P(19)	P(42)	3.230E-01	7.220E-03	1.581E-03	106.1
44	P(9)	P(45)	4.030E-01	8.928E-03	1.503E-03	231.6
45	P(6)	P(45)	4.030E-01	8.928E-03	1.334E-03	225.9
46	P(15)	P(48)	4.030E-01	8.928E-03	1.495E-03	352.9
47	P(12)	P(48)	4.030E-01	8.928E-03	1.324E-03	347.2

Figure D-3. Input and Output Data for Flowrates

48	P(21)	P(51)	4.030E-01	8.928E-03	1.457E-03	110.5
49	P(18)	P(51)	4.030E-01	8.928E-03	1.302E-03	104.4
50	P(9)	P(53)	5.300E-01	1.178E-02	1.735E-03	226.5
51	P(6)	P(54)	5.300E-01	1.178E-02	2.584E-03	243.7
52	P(15)	P(55)	5.300E-01	1.178E-02	1.723E-03	348.3
53	P(12)	P(56)	5.300E-01	1.178E-02	2.577E-03	5.2
54	P(21)	P(57)	5.300E-01	1.178E-02	1.682E-03	104.9
55	P(18)	P(58)	5.300E-01	1.178E-02	2.505E-03	122.9
56	P(8)	P(59)	9.450E-01	1.711E-02	1.057E-03	219.9
57	P(5)	P(60)	9.450E-01	1.711E-02	1.419E-03	239.1
58	P(14)	P(61)	9.450E-01	1.711E-02	9.305E-04	336.9
59	P(11)	P(62)	9.450E-01	1.711E-02	1.372E-03	359.2
60	P(20)	P(63)	9.450E-01	1.711E-02	8.748E-04	98.8
61	P(17)	P(64)	9.450E-01	1.711E-02	8.534E-04	194.5
62	P(8)	P(65)	2.310E+00	3.183E-02	2.980E-04	222.6
63	P(5)	P(65)	2.310E+00	3.183E-02	2.921E-04	221.1
64	P(14)	P(66)	2.310E+00	3.183E-02	6.208E-04	356.2
65	P(11)	P(66)	2.310E+00	3.183E-02	6.120E-04	355.6
66	P(20)	P(67)	2.310E+00	3.183E-02	6.319E-04	112.1
67	P(17)	P(67)	2.310E+00	3.183E-02	6.383E-04	110.7
68	P(4)	P(68)	1.200E+01	6.082E-02	3.160E-04	116.3
69	P(4)	P(68)	1.200E+01	6.082E-02	3.160E-04	116.3
70	P(3)	P(69)	1.200E+01	6.082E-02	3.078E-04	359.3
71	P(3)	P(69)	1.200E+01	6.082E-02	3.078E-04	359.3
72	P(2)	P(70)	1.200E+01	6.082E-02	3.189E-04	238.2
73	P(2)	P(70)	1.200E+01	6.082E-02	3.189E-04	238.2
74	P(1)	P(71)	2.250E+01	1.240E-01	1.612E-06	269.6
75	P(34)	P(23)	0.0	8.256E-02	1.008E-03	97.5
76	P(23)	P(24)	0.0	8.256E-02	9.332E-05	138.4
77	P(24)	P(25)	0.0	8.256E-02	4.012E-04	341.9
78	P(25)	P(26)	0.0	8.256E-02	1.301E-04	260.5
79	P(26)	P(27)	0.0	8.256E-02	1.042E-03	217.5
80	P(27)	P(28)	0.0	8.256E-02	9.843E-05	249.9
81	P(28)	P(29)	0.0	8.256E-02	3.903E-04	104.5
82	P(29)	P(30)	0.0	8.256E-02	1.303E-04	20.6
83	P(30)	P(31)	0.0	8.256E-02	1.050E-03	338.8
84	P(31)	P(32)	0.0	8.256E-02	1.081E-04	16.4
85	P(32)	P(33)	0.0	8.256E-02	3.877E-04	218.0
86	P(33)	P(34)	0.0	8.256E-02	1.298E-04	140.8
87	P(43)	P(35)	0.0	1.090E-01	1.668E-04	176.4
88	P(35)	P(36)	0.0	1.090E-01	3.560E-04	343.6
89	P(36)	P(37)	0.0	1.090E-01	8.729E-04	215.7
90	P(37)	P(38)	0.0	1.090E-01	1.627E-04	293.4
91	P(38)	P(39)	0.0	1.090E-01	3.465E-04	106.3
92	P(39)	P(40)	0.0	1.090E-01	8.785E-04	336.9
93	P(40)	P(41)	0.0	1.090E-01	1.720E-04	53.7
94	P(41)	P(42)	0.0	1.090E-01	3.432E-04	219.9
95	P(42)	P(43)	0.0	1.090E-01	8.449E-04	95.5

Figure D-3. (Continued)

96	P(52)	P(44)	0.0	1.071E-01	1.263E-04	173.5
97	P(44)	P(45)	0.0	1.071E-01	3.204E-04	344.3
98	P(45)	P(46)	0.0	1.071E-01	7.653E-04	218.3
99	P(46)	P(47)	0.0	1.071E-01	1.252E-04	289.9
100	P(47)	P(48)	0.0	1.071E-01	3.119E-04	106.1
101	P(48)	P(49)	0.0	1.071E-01	7.674E-04	339.4
102	P(49)	P(50)	0.0	1.071E-01	1.326E-04	51.3
103	P(50)	P(51)	0.0	1.071E-01	3.143E-04	221.1
104	P(51)	P(52)	0.0	1.071E-01	7.450E-04	98.0
105	P(58)	P(53)	0.0	1.568E-01	3.553E-04	73.4
106	P(53)	P(54)	0.0	1.568E-01	9.198E-05	271.9
107	P(54)	P(55)	0.0	1.568E-01	3.766E-04	194.6
108	P(55)	P(56)	0.0	1.568E-01	9.164E-05	32.7
109	P(56)	P(57)	0.0	1.568E-01	3.588E-04	317.1
110	P(57)	P(58)	0.0	1.568E-01	9.063E-05	152.4
111	P(64)	P(59)	0.0	1.599E-01	3.498E-04	79.6
112	P(59)	P(60)	0.0	1.599E-01	6.031E-05	278.4
113	P(60)	P(61)	0.0	1.599E-01	2.013E-04	199.7
114	P(61)	P(62)	0.0	1.599E-01	6.852E-05	33.5
115	P(62)	P(63)	0.0	1.599E-01	1.941E-04	315.1
116	P(63)	P(64)	0.0	1.599E-01	1.402E-04	236.8
117	P(67)	P(65)	0.0	2.821E-01	1.377E-04	75.2
118	P(65)	P(66)	0.0	2.821E-01	1.312E-04	213.9
119	P(66)	P(67)	0.0	2.821E-01	9.496E-05	320.9
120	P(70)	P(68)	0.0	1.449E-01	1.794E-04	254.2
121	P(68)	P(69)	0.0	1.449E-01	1.696E-04	135.6
122	P(69)	P(70)	0.0	1.449E-01	1.784E-04	17.6
123	P(23)	PIN(2)	4.110E+02	1.747E-02	5.786E-04	98.3
124	P(24)	PIN(3)	4.110E+02	1.747E-02	4.812E-04	206.9
125	P(25)	PIN(4)	4.110E+02	1.747E-02	2.348E-03	234.1
126	P(26)	PIN(5)	4.110E+02	1.747E-02	2.852E-03	245.4
127	P(27)	PIN(6)	4.110E+02	1.747E-02	6.046E-04	218.7
128	P(28)	PIN(7)	4.110E+02	1.747E-02	4.760E-04	328.7
129	P(29)	PIN(8)	4.110E+02	1.747E-02	2.336E-03	355.8
130	P(30)	PIN(9)	4.110E+02	1.747E-02	2.854E-03	6.8
131	P(31)	PIN(10)	4.110E+02	1.747E-02	6.146E-04	339.5
132	P(32)	PIN(11)	4.110E+02	1.747E-02	4.462E-04	84.5
133	P(33)	PIN(12)	4.110E+02	1.747E-02	2.251E-03	112.6
134	P(34)	PIN(13)	4.110E+02	1.747E-02	2.747E-03	124.6
135	P(35)	PIN(14)	3.580E+02	1.522E-02	5.296E-04	211.8
136	P(36)	PIN(15)	3.580E+02	1.522E-02	3.081E-03	242.1
137	P(37)	PIN(16)	3.580E+02	1.522E-02	4.727E-04	210.4
138	P(38)	PIN(17)	3.580E+02	1.522E-02	5.280E-04	333.4
139	P(39)	PIN(18)	3.580E+02	1.522E-02	3.074E-03	3.6
140	P(40)	PIN(19)	3.580E+02	1.522E-02	4.786E-04	331.6
141	P(41)	PIN(20)	3.580E+02	1.522E-02	4.980E-04	90.6
142	P(42)	PIN(21)	3.580E+02	1.522E-02	2.962E-03	121.0
143	P(43)	PIN(22)	3.580E+02	1.522E-02	4.492E-04	89.6

Figure D-3. (Continued)

144	P(44)	PIN(23)	4.430E+02	1.887E-02	4.157E-04	199.5
145	P(45)	PIN(24)	4.430E+02	1.887E-02	2.224E-03	240.6
146	P(46)	PIN(25)	4.430E+02	1.887E-02	5.067E-04	211.9
147	P(47)	PIN(26)	4.430E+02	1.887E-02	4.101E-04	220.7
148	P(48)	PIN(27)	4.430E+02	1.887E-02	2.210E-03	1.9
149	P(49)	PIN(28)	4.430E+02	1.887E-02	5.101E-04	332.8
150	P(50)	PIN(29)	4.430E+02	1.887E-02	3.996E-04	77.1
151	P(51)	PIN(30)	4.430E+02	1.887E-02	2.160E-03	119.4
152	P(52)	PIN(31)	4.430E+02	1.887E-02	4.920E-04	91.0
153	P(53)	PIN(32)	3.520E+02	1.496E-02	1.706E-03	221.1
154	P(54)	PIN(33)	3.520E+02	1.496E-02	2.651E-03	248.4
155	P(55)	PIN(34)	3.520E+02	1.496E-02	1.683E-03	342.7
156	P(56)	PIN(35)	3.520E+02	1.496E-02	2.660E-03	9.6
157	P(57)	PIN(36)	3.520E+02	1.496E-02	1.647E-03	98.6
158	P(58)	PIN(37)	3.520E+02	1.496E-02	2.571E-03	127.8
159	P(59)	PIN(38)	4.610E+02	1.964E-02	8.999E-04	205.8
160	P(60)	PIN(39)	4.610E+02	1.964E-02	1.395E-03	244.8
161	P(61)	PIN(40)	4.610E+02	1.964E-02	8.738E-04	328.9
162	P(62)	PIN(41)	4.610E+02	1.964E-02	1.376E-03	5.5
163	P(63)	PIN(42)	4.610E+02	1.964E-02	9.688E-04	89.2
164	P(64)	PIN(43)	4.610E+02	1.964E-02	1.044E-03	204.1
165	P(65)	PIN(44)	3.700E+02	1.571E-02	5.578E-04	221.7
166	P(66)	PIN(45)	3.700E+02	1.571E-02	1.180E-03	354.3
167	P(67)	PIN(46)	3.700E+02	1.571E-02	1.203E-03	112.8
168	P(68)	PIN(47)	7.380E+02	3.131E-02	4.159E-04	122.7
169	P(69)	PIN(48)	7.380E+02	3.131E-02	4.022E-04	5.9
170	P(70)	PIN(49)	7.380E+02	3.131E-02	4.099E-04	245.3
171	P(71)	PIN(50)	2.600E+03	1.048E-01	1.773E-06	259.6

AEROJET CME INJECTOR
OXIDIZER SIDE, NO RING DAMS
SPINNING FIRST TANGENTIAL MODE

	LB/SEC/PSI	% FLOW/% PC
TOTAL INJECTOR FLOW=	6.3636E-02	6.7070E-01
TOTAL VECTOR INJECTOR FLOW=	5.8723E-02	6.1891E-01
TOTAL INJECTOR FLOW PROPORTIONED BY PC AMPLITUDES=	5.4482E-02	5.7422E-01
TOTAL VECTOR INJECTOR FLOW PROPORTIONED BY PC AMPLITUDES=	5.0354E-02	5.3071E-01

Figure D-3. (Continued)

PRESSURE NODE	VOLUME CU IN	AC. VEL. IN/SEC	MAGNITUDE PSI/PSI	PHASE DEGREES	FLOWS IN			FLOWS OUT			
1	1.760E+01	3.961E+04	7.467E-03	316.5	1			2	3	4	74
2	3.640E-01	3.961E+04	5.576E-01	322.7	2			5	6	72	73
3	3.640E-01	3.961E+04	5.437E-01	84.1	3			7	8	70	71
4	3.640E-01	3.961E+04	5.484E-01	200.0	4			9	10	68	69
5	5.650E-01	3.961E+04	5.924E-01	322.7	6			11	14	57	63
6	1.224E+00	3.961E+04	8.936E-01	322.1	14			12	15	45	51
7	1.590E+00	3.961E+04	1.004E+00	322.2	15			13	33	39	
8	5.650E-01	3.961E+04	5.962E-01	323.0	5	11		16	56	62	
9	1.224E+00	3.961E+04	9.196E-01	323.3	12	16		17	44	50	
10	1.590E+00	3.961E+04	1.045E+00	323.5	13	17		32	38		
11	5.650E-01	3.961E+04	5.780E-01	84.0	8			18	21	59	65
12	1.224E+00	3.961E+04	9.069E-01	83.9	21			19	22	47	53
13	1.590E+00	3.961E+04	1.027E+00	84.0	22			20	35	41	
14	5.650E-01	3.961E+04	5.825E-01	84.4	7	18		23	58	64	
15	1.224E+00	3.961E+04	9.333E-01	85.0	23	19		24	46	52	
16	1.590E+00	3.961E+04	1.069E+00	85.2	20	24		34	40		
17	5.650E-01	3.961E+04	5.869E-01	199.7	10			25	28	61	67
18	1.224E+00	3.961E+04	8.459E-01	202.3	28			29	26	49	55
19	1.590E+00	3.961E+04	9.425E-01	203.1	29			27	37	43	
20	5.650E-01	3.961E+04	5.835E-01	200.5	9	25		30	60	66	
21	1.224E+00	3.961E+04	8.705E-01	203.6	26	30		31	48	54	
22	1.590E+00	3.961E+04	9.834E-01	204.5	27	31		36	42		
23	1.180E-01	3.961E+04	7.697E-01	356.5	75			76	123		
24	1.180E-01	3.961E+04	8.531E-01	3.1	76			77	124		
25	1.180E-01	3.961E+04	8.284E-01	325.6	32	77		78	125		
26	1.180E-01	3.961E+04	6.733E-01	319.3	33	78		79	126		
27	1.180E-01	3.961E+04	7.587E-01	117.0	79			80	127		
28	1.180E-01	3.961E+04	8.607E-01	123.0	80			81	128		
29	1.180E-01	3.961E+04	8.546E-01	87.3	81	34		82	129		
30	1.180E-01	3.961E+04	6.966E-01	81.6	35	82		83	130		
31	1.180E-01	3.961E+04	7.523E-01	237.1	83			84	131		
32	1.180E-01	3.961E+04	8.544E-01	244.5	84			85	132		
33	1.180E-01	3.961E+04	7.780E-01	207.5	36	85		133	86		
34	1.180E-01	3.961E+04	6.211E-01	201.1	86	37		75	134		
35	1.170E-01	3.961E+04	8.376E-01	8.5	87			88	135		
36	1.170E-01	3.961E+04	8.111E-01	323.3	38	39	88	89	136		
37	1.170E-01	3.961E+04	8.186E-01	108.3	89			90	137		
38	1.170E-01	3.961E+04	8.434E-01	128.3	90			91	138		
39	1.170E-01	3.961E+04	8.356E-01	85.2	40	41	91	92	139		
40	1.170E-01	3.961E+04	8.138E-01	228.2	92			93	140		
41	1.170E-01	3.961E+04	8.412E-01	249.4	93			94	141		

Figure D-4. Input and Output Data for Pressure Nodes

```
42   1.170E-01 3.961E+04  7.578E-01  204.9  42  43  94     95 142
43   1.170E-01 3.961E+04  8.280E-01  347.9  95             87 143
44   8.320E-02 3.961E+04  7.282E-01   10.0  96             97 144
45   8.320E-02 3.961E+04  7.005E-01  323.8  44  45  97     98 145
46   8.320E-02 3.961E+04  6.899E-01  112.5  98             99 146
47   8.320E-02 3.961E+04  7.334E-01  129.9  99            100 147
48   8.320E-02 3.961E+04  7.155E-01   85.7  47 100  46    101 148
49   8.320E-02 3.961E+04  6.858E-01  232.4 101            102 149
50   8.320E-02 3.961E+04  7.282E-01  251.0 102            103 150
51   8.320E-02 3.961E+04  6.584E-01  204.6  48  49 103    104 151
52   8.320E-02 3.961E+04  6.985E-01  352.3 104             96 152
53   1.480E-01 3.961E+04  5.895E-01  327.2  50 105        106 153
54   1.480E-01 3.961E+04  4.180E-01  308.4  51 106        107 154
55   1.480E-01 3.961E+04  6.054E-01   88.7  52 107        108 155
56   1.480E-01 3.961E+04  4.313E-01   71.0  53 108        109 156
57   1.480E-01 3.961E+04  5.529E-01  208.7  54 109        110 157
58   1.480E-01 3.961E+04  3.819E-01  189.1  55 110        105 158
59   1.010E-01 3.961E+04  3.160E-01  335.4  56 111        112 159
60   1.010E-01 3.961E+04  2.027E-01  310.4  57 112        113 160
61   1.010E-01 3.961E+04  3.438E-01   97.6  58 113        114 161
62   1.010E-01 3.961E+04  1.988E-01   74.5  59 114        115 162
63   1.010E-01 3.961E+04  3.479E-01  208.8  60 115        116 163
64   1.010E-01 3.961E+04  6.123E-01  176.9  61 116        111 164
65   1.230E-01 3.961E+04  4.448E-01  326.7  62  63 117    118 165
66   1.230E-01 3.961E+04  2.600E-01   82.4  64  65 118    119 166
67   1.230E-01 3.961E+04  2.551E-01  198.7  66  67 119    117 167
68   8.020E-02 3.961E+04  2.379E-01  192.6  68  69 120    121 168
69   8.020E-02 3.961E+04  2.401E-01   78.3  70  71 121    122 169
70   8.020E-02 3.961E+04  2.432E-01  316.5  72  73 122    120 170
71   1.520E-02 3.961E+04  5.520E-03  292.9  74             171

AEROJET CME INJECTOR
OXIDIZER SIDE, NO RING DAMS
SPINNING FIRST TANGENTIAL MODE
```

Figure D-4. (Continued)

APPENDIX E

COMPUTER MODEL DOCUMENTATION OF ROCKETDYNE

OME TECHNOLOGY INJECTOR

FUEL SYSTEM FREQUENCY RESPONSE

```
ROCKETDYNE OME INJECTOR
FUEL SIDE, NO RING DAMS
STANDING FIRST TANGENTIAL MODE
   78     39     12
    1    130    -10    -28    -46    -64    -73   -131
    2    131    -11    -29    -47    -48    -65    -74   -132
    3    132    -12    -30    -49    -66    -75   -133
    4    133    -13    -31    -50    -67    -76   -134
    5    134    -14    -32    -51    -52    -68    -77   -135
    6    135    -15    -33    -53    -69    -78   -136
    7    136    -16    -34    -54    -70    -79   -137
    8    137    -17    -35    -55    -56    -71    -80   -138
    9    138    -18    -36    -57    -72    -81   -130
   10    -19
   11    -20
   12    -21
   13    -22
   14    -23
   15    -24
   16    -25
   17    -26
   18    -27
   19    100   -101   -139
   20    101   -102   -140
   21    102   -103   -141
   22    103   -104   -142
   23    104   -105   -143
   24    105   -106   -144
   25    106   -107   -145
   26    107   -108   -146
   27    108   -100   -147
   28    -37
   29    -38
   30    -39
   31    -40
   32    -41
   33    -42
   34    -43
   35    -44
   36    -45
   37    109   -110   -148
   38    110   -111   -149
   39    111   -112   -150
   40    112   -113   -151
   41    113   -114   -152
   42    114   -115   -153
   43    115   -116   -154
   44    116   -117   -155
```

Figure E-1. Data Deck for Rocketdyne OME Technology Injector Fuel Side

```
 45   117  -109  -156
 46    47   -58
 48    49   -59
 50    51   -60
 52    53   -61
 54    55   -62
 56    57   -63
 58   118  -119  -157
 59   119  -120  -158
 60   120  -121  -159
 61   121  -122  -160
 62   122  -123  -161
 63   123  -118  -162
 64    65    66   -89
 67    68    69   -91
 70    71    72   -93
 73    74    75   -82   -88
 76    77    78   -83   -90
 79    80    81   -84   -92
 82   -85
 83   -86
 84   -87
 85   124  -125  -163
 86   125  -126  -164
 87   126  -124  -165
 88   -94
 89   -95
 90   -96
 91   -97
 92   -98
 93   -99
 94    95   127  -128  -166
 96    97   128  -129  -167
 98    99   129  -127  -168
  1     2     3     4     5     6     7     8     9  -139  -140  -141
-142  -143  -144  -145  -146  -147  -148  -149  -150  -151  -152  -153
-154  -155  -156  -157  -158  -159  -160  -161  -162  -163  -164  -165
-166  -167  -168
          1          2600
          1            10             0
          0          3.93           340          3.93           20          3.93
         60          3.93           100          3.93          140          3.93
        180          3.93           220          3.93          260          3.93
        300          3.17           340          3.17           20          3.17
         60          3.17           100          3.17          140          3.17
        180          3.17           220          3.17          260          3.17
        300          2.43           350          2.43           50          2.43
```

Figure E-1. (Continued)

```
        110         2.43          170         2.43          230         2.43
        290         1.69           20         1.69          140         1.69
        260         .945           20         .945          140         .945
        260
          0            0            0            0            0            0
          0            0            0            0            0            0
&D1 R=9*0.0,18*5.99,18*1.87,5.29,2*10.6,2*5.29,2*10.6,
2*5.29,2*10.6,5.29,6*3.52,18*7.07,3*4.03,3*6.99,
6*5.31,6*3.55,30*0.0,0.0,2*0.0,0.0,2*0.0,0.0,2*0.0,
9*681.,9*389.,6*351.,3*480.,3*275.,
V=9*1.34,9*.0443,9*.0434,9*.0941,9*.0503,6*.094,
6*.0935,3*.078,3*.167,3*.068,3*.0507,6*.0442,
3*.0776,
Z=9*.0103,18*.0303,18*.0198,.0453,2*.0906,2*.0453
2*.0906,2*.0453,2*.0906,.0453,6*.0303,9*.1121,
9*.0523,3*.0481,3*.0305,.0386,.0585,.0386,.0585,
.0386,.0585,6*.0211,9*.443,9*.251,6*.1787,3*.2,3*.4154,
9*.0112,9*.0802,9*.0575,6*.05,3*.0686,3*.0392,
C=81*50400., &END
7.25          125.
    5     1
   19    37    52    67    76    10    19    28    34    37   142   151
  160   166   169   100   109   118   124   127     9     9     6     3
    3
```

Figure E-1. (Continued)

```
REAL INPUT MATRIX AMPLITUDES - PSI
   0.0          0.0          0.0          0.0          0.0          0.0
   0.0          0.0          0.0          9.3969E-01   9.3969E-01   5.0000E-01
  -1.7365E-01  -7.6604E-01  -1.0000E+00  -7.6604E-01  -1.7365E-01   5.0000E-01
   8.9944E-01   8.9944E-01   4.7858E-01  -1.6621E-01  -7.3323E-01  -9.5716E-01
  -7.3323E-01  -1.6621E-01   4.7858E-01   8.0831E-01   5.2758E-01  -2.8072E-01
  -8.0831E-01  -5.2758E-01   2.8072E-01   5.7697E-01  -4.7035E-01  -1.0662E-01
   3.3624E-01  -2.7411E-01  -6.2135E-02

IMAGINARY INPUT MATRIX AMPLITUDES - PSI
   0.0          0.0          0.0          0.0          0.0          0.0
   0.0          0.0          0.0          0.0          0.0          0.0
   0.0          0.0          0.0          0.0          0.0          0.0
   0.0          0.0          0.0          0.0          0.0          0.0
   0.0          0.0          0.0          0.0          0.0          0.0
   0.0          0.0          0.0          0.0          0.0          0.0
   0.0          0.0          0.0
ROCKETDYNE OME INJECTOR
FUEL SIDE, NO RING DAMS
STANDING FIRST TANGENTIAL MODE

  INPUT FREQUENCY= 2600.0
```

Figure E-2. Real and Imaginary Input Matrix Amplitudes

FLOW	UPSTREAM PRESSURE	DOWNSTREAM PRESSURE	RESISTANCE SEC/IN SQ	INERTANCE SEC SQ/IN SQ	AMPLITUDE LB/SEC/PSI	PHASE DEGREES
1	PIN(1)	P(1)	0.0	1.030E-02	1.223E-03	100.3
2	PIN(2)	P(2)	0.0	1.030E-02	1.251E-03	100.2
3	PIN(3)	P(3)	0.0	1.030E-02	7.325E-04	100.1
4	PIN(4)	P(4)	0.0	1.030E-02	3.363E-04	279.8
5	PIN(5)	P(5)	0.0	1.030E-02	1.020E-03	280.2
6	PIN(6)	P(6)	0.0	1.030E-02	1.258E-03	280.4
7	PIN(7)	P(7)	0.0	1.030E-02	8.864E-04	280.5
8	PIN(8)	P(8)	0.0	1.030E-02	2.312E-04	280.2
9	PIN(9)	P(9)	0.0	1.030E-02	5.252E-04	100.7
10	P(1)	P(10)	5.990E+00	3.030E-02	3.541E-04	102.8
11	P(2)	P(11)	5.990E+00	3.030E-02	3.533E-04	102.6
12	P(3)	P(12)	5.990E+00	3.030E-02	1.828E-04	102.5
13	P(4)	P(13)	5.990E+00	3.030E-02	5.795E-05	281.4
14	P(5)	P(14)	5.990E+00	3.030E-02	2.880E-04	282.6
15	P(6)	P(15)	5.990E+00	3.030E-02	3.797E-04	282.9
16	P(7)	P(16)	5.990E+00	3.030E-02	2.961E-04	283.0
17	P(8)	P(17)	5.990E+00	3.030E-02	6.529E-05	282.6
18	P(9)	P(18)	5.990E+00	3.030E-02	1.969E-04	103.2
19	P(10)	P(19)	5.990E+00	3.030E-02	3.121E-04	103.0
20	P(11)	P(20)	5.990E+00	3.030E-02	3.109E-04	102.9
21	P(12)	P(21)	5.990E+00	3.030E-02	1.593E-04	102.7
22	P(13)	P(22)	5.990E+00	3.030E-02	4.857E-05	281.6
23	P(14)	P(23)	5.990E+00	3.030E-02	2.535E-04	282.9
24	P(15)	P(24)	5.990E+00	3.030E-02	3.358E-04	283.1
25	P(16)	P(25)	5.990E+00	3.030E-02	2.636E-04	283.2
26	P(17)	P(26)	5.990E+00	3.030E-02	5.746E-05	282.9
27	P(18)	P(27)	5.990E+00	3.030E-02	1.765E-04	103.4
28	P(1)	P(28)	1.870E+00	1.980E-02	4.986E-04	100.3
29	P(2)	P(29)	1.870E+00	1.980E-02	4.980E-04	100.2
30	P(3)	P(30)	1.870E+00	1.980E-02	2.572E-04	100.0
31	P(4)	P(31)	1.870E+00	1.980E-02	8.120E-05	278.9
32	P(5)	P(32)	1.870E+00	1.980E-02	4.060E-04	280.2
33	P(6)	P(33)	1.870E+00	1.980E-02	5.350E-04	280.4
34	P(7)	P(34)	1.870E+00	1.980E-02	4.175E-04	280.6
35	P(8)	P(35)	1.870E+00	1.980E-02	9.202E-05	280.2
36	P(9)	P(36)	1.870E+00	1.980E-02	2.778E-04	100.8
37	P(28)	P(37)	1.870E+00	1.980E-02	4.128E-04	100.3
38	P(29)	P(38)	1.870E+00	1.980E-02	4.111E-04	100.2
39	P(30)	P(39)	1.870E+00	1.980E-02	2.089E-04	100.0
40	P(31)	P(40)	1.870E+00	1.980E-02	6.183E-05	278.8
41	P(32)	P(41)	1.870E+00	1.980E-02	3.351E-04	280.2

Figure E-3. Input and Output Data for Flowrates

42	P(33)	P(42)	1.87CE+CO	1.980E-02	4.450E-04	280.4
43	P(34)	P(43)	1.870E+00	1.980E-02	3.510E-04	280.6
44	P(35)	P(44)	1.87CE+00	1.980E-02	7.596E-05	280.2
45	P(36)	P(45)	1.870E+00	1.980E-02	2.361E-04	100.8
46	P(1)	P(46)	5.290E+00	4.530E-02	2.475E-04	98.1
47	P(2)	P(46)	1.060E+01	9.060E-02	1.205E-04	98.1
48	P(2)	P(47)	1.060E+01	9.060E-02	3.776E-05	94.7
49	P(3)	P(47)	5.290E+00	4.530E-02	1.932E-04	98.4
50	P(4)	P(48)	5.290E+00	4.530E-02	1.287E-04	278.7
51	P(5)	P(48)	1.060E+01	9.060E-02	1.367E-05	111.1
52	P(5)	P(49)	1.060E+01	9.060E-02	1.423E-04	278.6
53	P(6)	P(49)	5.290E+00	4.530E-02	2.306E-04	278.0
54	P(7)	P(50)	5.290E+00	4.530E-02	1.188E-04	277.5
55	P(8)	P(50)	1.060E+01	9.060E-02	1.338E-04	279.5
56	P(8)	P(51)	1.060E+01	9.060E-02	1.046E-04	100.1
57	P(9)	P(51)	5.290E+00	4.530E-02	3.741E-05	95.8
58	P(46)	P(52)	3.520E+00	3.030E-02	2.772E-04	97.8
59	P(47)	P(53)	3.520E+00	3.030E-02	1.688E-04	97.4
60	P(48)	P(54)	3.520E+00	3.030E-02	7.992E-05	276.5
61	P(49)	P(55)	3.520E+00	3.030E-02	2.836E-04	278.0
62	P(50)	P(56)	3.520E+00	3.030E-02	1.973E-04	278.3
63	P(51)	P(57)	3.520E+00	3.030E-02	1.149E-04	98.8
64	P(1)	P(58)	7.070E+00	1.121E-01	1.489E-05	86.7
65	P(2)	P(58)	7.070E+00	1.121E-01	1.231E-05	84.5
66	P(3)	P(58)	7.070E+00	1.121E-01	5.960E-05	97.3
67	P(4)	P(59)	7.070E+00	1.121E-01	7.252E-05	278.5
68	P(5)	P(59)	7.070E+00	1.121E-01	1.003E-05	264.5
69	P(6)	P(59)	7.070E+00	1.121E-01	1.255E-05	114.5
70	P(7)	P(60)	7.070E+00	1.121E-01	5.802E-05	101.5
71	P(8)	P(60)	7.070E+00	1.121E-01	2.274E-06	264.5
72	P(9)	P(60)	7.070E+00	1.121E-01	7.168E-05	280.3
73	P(1)	P(61)	7.070E+00	5.230E-02	3.881E-05	94.5
74	P(2)	P(61)	7.070E+00	5.230E-02	3.316E-05	94.1
75	P(3)	P(61)	7.070E+00	5.230E-02	1.352E-04	99.2
76	P(4)	P(62)	7.070E+00	5.230E-02	1.615E-04	279.8
77	P(5)	P(62)	7.070E+00	5.230E-02	2.703E-05	274.1
78	P(6)	P(62)	7.070E+00	5.230E-02	2.026E-05	111.3
79	P(7)	P(63)	7.070E+00	5.230E-02	1.230E-04	101.4
80	P(8)	P(63)	7.070E+00	5.230E-02	6.127E-06	274.1
81	P(9)	P(63)	7.070E+00	5.230E-02	1.550E-04	280.8
82	P(61)	P(64)	4.030E+00	4.810E-02	6.019E-05	105.9
83	P(62)	P(65)	4.030E+00	4.810E-02	4.907E-05	285.9
84	P(63)	P(66)	4.030E+00	4.810E-02	1.112E-05	285.9

Figure E-3. (Continued)

85	P(64)	P(67)	6.950E+00	3.050E-02	1.296E-05	126.7
86	P(65)	P(68)	6.950E+00	3.050E-02	1.057E-05	306.7
87	P(66)	P(69)	6.950E+00	3.050E-02	2.395E-06	306.7
88	P(61)	P(70)	5.310E+00	3.860E-02	4.989E-05	83.4
89	P(58)	P(71)	5.310E+00	5.850E-02	4.174E-05	88.2
90	P(62)	P(72)	5.310E+00	3.860E-02	4.067E-05	263.4
91	P(59)	P(73)	5.310E+00	5.850E-02	3.402E-05	268.2
92	P(63)	P(74)	5.310E+00	3.860E-02	9.218E-06	263.4
93	P(60)	P(75)	5.310E+00	5.850E-02	7.713E-06	268.2
94	P(70)	P(76)	3.550E+00	2.110E-02	2.242E-05	64.6
95	P(71)	P(76)	3.550E+00	2.110E-02	1.310E-05	67.6
96	P(72)	P(77)	3.550E+00	2.110E-02	1.828E-05	244.6
97	P(73)	P(77)	3.550E+00	2.110E-02	1.068E-05	247.6
98	P(74)	P(78)	3.550E+00	2.110E-02	4.143E-06	244.6
99	P(75)	P(78)	3.550E+00	2.110E-02	2.421E-06	247.7
100	P(27)	P(19)	0.0	4.430E-01	3.625E-05	100.9
101	P(19)	P(20)	0.0	4.430E-01	5.586E-07	84.6
102	P(20)	P(21)	0.0	4.430E-01	3.409E-05	281.6
103	P(21)	P(22)	0.0	4.430E-01	5.553E-05	280.9
104	P(22)	P(23)	0.0	4.430E-01	4.565E-05	281.7
105	P(23)	P(24)	0.0	4.430E-01	1.742E-05	282.3
106	P(24)	P(25)	0.0	4.430E-01	1.929E-05	100.9
107	P(25)	P(26)	0.0	4.430E-01	4.512E-05	101.9
108	P(26)	P(27)	0.0	4.430E-01	5.152E-05	101.8
109	P(45)	P(37)	0.0	2.510E-01	5.995E-05	99.7
110	P(37)	P(38)	0.0	2.510E-01	1.011E-06	87.4
111	P(38)	P(39)	0.0	2.510E-01	5.624E-05	280.2
112	P(39)	P(40)	0.0	2.510E-01	9.190E-05	279.7
113	P(40)	P(41)	0.0	2.510E-01	7.524E-05	280.3
114	P(41)	P(42)	0.0	2.510E-01	2.860E-05	280.8
115	P(42)	P(43)	0.0	2.510E-01	3.192E-05	99.7
116	P(43)	P(44)	0.0	2.510E-01	7.426E-05	100.5
117	P(44)	P(45)	0.0	2.510E-01	8.483E-05	100.4
118	P(57)	P(52)	0.0	1.787E-01	1.210E-04	98.4
119	P(52)	P(53)	0.0	1.787E-01	6.037E-05	278.9
120	P(53)	P(54)	0.0	1.787E-01	1.653E-04	278.4
121	P(54)	P(55)	0.0	1.787E-01	1.135E-04	278.9
122	P(55)	P(56)	0.0	1.787E-01	6.436E-05	98.4
123	P(56)	P(57)	0.0	1.787E-01	1.738E-04	98.9
124	P(69)	P(67)	0.0	2.000E-01	1.058E-04	101.0
125	P(67)	P(68)	0.0	2.000E-01	1.620E-04	281.0
126	P(68)	P(69)	0.0	2.000E-01	5.627E-05	101.0
127	P(78)	P(76)	0.0	4.154E-01	4.810E-05	96.7

Figure E-3. (Continued)

128	P(76)	P(77)	0.0	4.154E-01	7.370E-05	276.7
129	P(77)	P(78)	0.0	4.154E-01	2.559E-05	96.7
130	P(9)	P(1)	0.0	1.120E-02	6.415E-04	100.0
131	P(1)	P(2)	0.0	1.120E-02	2.641E-05	96.7
132	P(2)	P(3)	0.0	1.120E-02	4.772E-04	280.4
133	P(3)	P(4)	0.0	1.120E-02	9.828E-04	280.0
134	P(4)	P(5)	0.0	1.120E-02	6.289E-04	280.5
135	P(5)	P(6)	0.0	1.120E-02	2.184E-04	281.0
136	P(6)	P(7)	0.0	1.120E-02	3.413E-04	100.0
137	P(7)	P(8)	0.0	1.120E-02	6.026E-04	100.6
138	P(8)	P(9)	0.0	1.120E-02	6.956E-04	100.6
139	P(10)	PIN(10)	6.810E+02	8.020E-02	2.901E-04	103.1
140	P(20)	PIN(11)	6.810E+02	8.020E-02	2.874E-04	103.0
141	P(21)	PIN(12)	6.810E+02	8.020E-02	1.492E-04	102.6
142	P(22)	PIN(13)	6.810E+02	8.020E-02	4.666E-05	281.0
143	P(23)	PIN(14)	6.810E+02	8.020E-02	2.343E-04	283.0
144	P(24)	PIN(15)	6.810E+02	8.020E-02	3.115E-04	283.2
145	P(25)	PIN(16)	6.810E+02	8.020E-02	2.435E-04	283.5
146	P(26)	PIN(17)	6.810E+02	8.020E-02	5.311E-05	283.0
147	P(27)	PIN(18)	6.810E+02	8.020E-02	1.623E-04	103.7
148	P(37)	PIN(19)	3.890E+02	5.750E-02	4.092E-04	100.3
149	P(38)	PIN(20)	3.890E+02	5.750E-02	4.052E-04	100.2
150	P(39)	PIN(21)	3.890E+02	5.750E-02	2.103E-04	99.8
151	P(40)	PIN(22)	3.890E+02	5.750E-02	6.565E-05	278.2
152	P(41)	PIN(23)	3.890E+02	5.750E-02	3.303E-04	280.2
153	P(42)	PIN(24)	3.890E+02	5.750E-02	4.394E-04	280.4
154	P(43)	PIN(25)	3.890E+02	5.750E-02	3.436E-04	280.7
155	P(44)	PIN(26)	3.890E+02	5.750E-02	7.488E-05	280.2
156	P(45)	PIN(27)	3.890E+02	5.750E-02	2.291E-04	101.0
157	P(52)	PIN(28)	3.510E+02	5.000E-02	3.363E-04	97.9
158	P(53)	PIN(29)	3.510E+02	5.000E-02	2.125E-04	97.4
159	P(54)	PIN(30)	3.510E+02	5.000E-02	1.074E-04	276.5
160	P(55)	PIN(31)	3.510E+02	5.000E-02	3.400E-04	278.1
161	P(56)	PIN(32)	3.510E+02	5.000E-02	2.290E-04	278.6
162	P(57)	PIN(33)	3.510E+02	5.000E-02	1.276E-04	99.3
163	P(67)	PIN(34)	4.800E+02	6.860E-02	2.428E-04	102.3
164	P(68)	PIN(35)	4.800E+02	6.860E-02	1.979E-04	282.3
165	P(69)	PIN(36)	4.800E+02	6.860E-02	4.486E-05	282.3
166	P(76)	PIN(37)	2.750E+02	3.920E-02	1.008E-04	86.2
167	P(77)	PIN(38)	2.750E+02	3.920E-02	8.217E-05	266.2
168	P(78)	PIN(39)	2.750E+02	3.920E-02	1.863E-05	266.2

ROCKETDYNE OME INJECTOR
FUEL SIDE, NO RING DAMS
STANDING FIRST TANGENTIAL MODE

	LB/SEC/PSI	% FLOW/% PC
TOTAL INJECTOR FLOW=	6.3257E-03	1.0906E-01
TOTAL VECTOR INJECTOR FLOW=	6.3160E-03	1.0890E-01
TOTAL INJECTOR FLOW PROPORTIONED BY PC AMPLITUDES=	4.4153E-03	7.6126E-02
TOTAL VECTOR INJECTOR FLOW PROPORTIONED BY PC AMPLITUDES=	4.4111E-03	7.6053E-02

Figure E-3. (Continued)

PRESSURE NODE	VOLUME CU IN	AC. VEL. IN/SEC	MAGNITUDE PSI/PSI	PHASE DEGREES	FLOWS IN	FLOWS OUT
1	1.340E+00	5.040E+04	2.057E-01	10.3	1 130	10 28 46 64 73 131
2	1.340E+00	5.040E+04	2.106E-01	10.2	2 131	11 29 47 48 65 74 132
3	1.340E+00	5.040E+04	1.232E-01	10.1	3 132	12 30 49 66 75 133
4	1.340E+00	5.040E+04	5.658E-02	189.8	4 133	13 31 50 67 76 134
5	1.340E+00	5.040E+04	1.716E-01	190.2	5 134	14 32 51 52 68 77 135
6	1.340E+00	5.040E+04	2.116E-01	190.4	6 135	15 33 53 69 78 136
7	1.340E+00	5.040E+04	1.492E-01	190.5	7 136	16 34 54 70 79 137
8	1.340E+00	5.040E+04	3.891E-02	190.2	8 137	17 35 55 56 71 80 138
9	1.340E+00	5.040E+04	8.836E-02	10.7	9 138	18 36 57 72 81 130
10	4.430E-02	5.040E+04	3.810E-01	11.1	10	19
11	4.430E-02	5.040E+04	3.854E-01	11.0	11	20
12	4.430E-02	5.040E+04	2.137E-01	10.8	12	21
13	4.430E-02	5.040E+04	8.527E-02	190.1	13	22
14	4.430E-02	5.040E+04	3.142E-01	191.0	14	23
15	4.430E-02	5.040E+04	3.995E-01	191.2	15	24
16	4.430E-02	5.040E+04	2.957E-01	191.4	16	25
17	4.430E-02	5.040E+04	7.122E-02	191.0	17	26
18	4.430E-02	5.040E+04	1.858E-01	11.7	18	27
19	4.340E-02	5.040E+04	5.355E-01	11.5	19 100	101 139
20	4.340E-02	5.040E+04	5.393E-01	11.3	20 101	102 140
21	4.340E-02	5.040E+04	2.926E-01	11.1	21 102	103 141
22	4.340E-02	5.040E+04	1.093E-01	190.3	22 103	104 142
23	4.340E-02	5.040E+04	4.397E-01	191.3	23 104	105 143
24	4.340E-02	5.040E+04	5.657E-01	191.6	24 105	106 144
25	4.340E-02	5.040E+04	4.262E-01	191.8	25 106	107 145
26	4.340E-02	5.040E+04	9.966E-02	191.3	26 107	108 146
27	4.340E-02	5.040E+04	2.732E-01	12.0	27 108	100 147
28	9.410E-02	5.040E+04	3.670E-01	10.2	28	37
29	9.410E-02	5.040E+04	3.716E-01	10.1	29	38
30	9.410E-02	5.040E+04	2.064E-01	9.9	30	39
31	9.410E-02	5.040E+04	8.284E-02	189.4	31	40
32	9.410E-02	5.040E+04	3.030E-01	190.1	32	41
33	9.410E-02	5.040E+04	3.847E-01	190.2	33	42
34	9.410E-02	5.040E+04	2.842E-01	190.4	34	43
35	9.410E-02	5.040E+04	6.868E-02	190.1	35	44
36	9.410E-02	5.040E+04	1.782E-01	10.6	36	45
37	5.030E-02	5.040E+04	5.005E-01	10.1	37 109	110 148
38	5.030E-02	5.040E+04	5.046E-01	10.0	38 110	111 149
39	5.030E-02	5.040E+04	2.740E-01	9.9	39 111	112 150
40	5.030E-02	5.040E+04	1.028E-01	189.2	40 112	113 151
41	5.030E-02	5.040E+04	4.113E-01	190.0	41 113	114 152

Figure E-4. Input and Output Data for Pressure Nodes

```
42   5.030E-02 5.040E+04   5.286E-01   190.2   42 114        115 153
43   5.030E-02 5.040E+04   3.977E-01   190.4   43 115        116 154
44   5.030E-02 5.040E+04   9.325E-02   190.0   44 116        117 155
45   5.030E-02 5.040E+04   2.546E-01    10.5   45 117        109 156
46   9.400E-02 5.040E+04   3.888E-01     9.1   46  47         58
47   9.400E-02 5.040E+04   2.662E-01     9.0   48  49         59
48   9.400E-02 5.040E+04   1.518E-01   188.8   50  51         60
49   9.400E-02 5.040E+04   3.872E-01   189.1   52  53         61
50   9.400E-02 5.040E+04   2.370E-01   189.2   54  55         62
51   9.400E-02 5.040E+04   1.160E-01     9.5   56  57         63
52   9.350E-02 5.040E+04   5.259E-01     8.6   58 118        119 157
53   9.350E-02 5.040E+04   3.497E-01     8.5   59 119        120 158
54   9.350E-02 5.040E+04   1.913E-01   188.3   60 120        121 159
55   9.350E-02 5.040E+04   5.275E-01   188.7   61 121        122 160
56   9.350E-02 5.040E+04   3.346E-01   188.9   62 122        123 161
57   9.350E-02 5.040E+04   1.728E-01     9.1   63 123        118 162
58   7.800E-02 5.040E+04   2.323E-01     8.7   64  65  66     89
59   7.800E-02 5.040E+04   1.894E-01   188.7   67  68  69     91
60   7.800E-02 5.040E+04   4.293E-02   188.7   70  71  72     93
61   1.670E-01 5.040E+04   2.387E-01     9.4   73  74  75     82  88
62   1.670E-01 5.040E+04   1.946E-01   189.4   76  77  78     83  90
63   1.670E-01 5.040E+04   4.411E-02   189.4   79  80  81     84  92
64   6.800E-02 5.040E+04   2.856E-01    10.5   82             85
65   6.800E-02 5.040E+04   2.330E-01   190.5   83             86
66   6.800E-02 5.040E+04   5.281E-02   190.5   84             87
67   5.070E-02 5.040E+04   2.916E-01    11.0   85 124        125 163
68   5.070E-02 5.040E+04   2.377E-01   191.0   86 125        126 164
69   5.070E-02 5.040E+04   5.389E-02   191.0   87 126        124 165
70   4.420E-02 5.040E+04   2.690E-01     7.5   88             94
71   4.420E-02 5.040E+04   2.716E-01     7.1   89             95
72   4.420E-02 5.040E+04   2.193E-01   187.5   90             96
73   4.420E-02 5.040E+04   2.214E-01   187.1   91             97
74   4.420E-02 5.040E+04   4.972E-02   187.5   92             98
75   4.420E-02 5.040E+04   5.019E-02   187.1   93             99
76   7.760E-02 5.040E+04   2.755E-01     6.7   94  95 127    128 166
77   7.760E-02 5.040E+04   2.246E-01   186.7   96  97 128    129 167
78   7.760E-02 5.040E+04   5.091E-02   186.7   98  99 129    127 168
ROCKETDYNE OME INJECTOR
FUEL SIDE, NO RING DAMS
STANDING FIRST TANGENTIAL MODE
```

Figure E-4. (Continued)

APPENDIX F

COMPUTER MODEL DOCUMENTATION OF ROCKETDYNE OME TECHNOLOGY INJECTOR OXIDIZER SYSTEM FREQUENCY RESPONSE

```
ROCKETDYNE OME INJECTOR
OXIDIZER SIDE, NO RING DAMS
STANDING FIRST TANGENTIAL MODE
   69     51     12
    1    -10    -19
    2    -11    -20
    3    -12    -21
    4    -13    -22
    5    -14    -23
    6    -15    -24
    7    -16    -25
    8    -17    -26
    9    -18    -27
   10    -37
   11    -38
   12    -39
   13    -40
   14    -41
   15    -42
   16    -43
   17    -44
   18    -45
   19    -28
   20    -29
   21    -30
   22    -31
   23    -32
   24    -33
   25    -34
   26    -35
   27    -36
   28     70    -71   -100
   29     71    -72   -101
   30     72    -73   -102
   31     73    -74   -103
   32     74    -75   -104
   33     75    -76   -105
   34     76    -77   -106
   35     77    -78   -107
   36     78    -70   -108
   37     79    -80   -109
   38     80    -81   -110
   39     81    -82   -111
   40     82    -83   -112
   41     83    -84   -113
   42     84    -85   -114
   43     85    -86   -115
```

Figure F-1. Data Deck for Rocketdyne OME Technology Injector Oxidizer Side

```
 44    86   -87  -116
 45    87   -79  -117
 46   -52
 47   -53
 48   -54
 49   -55
 50   -56
 51   -57
 52    88   -89  -118
 53    89   -90  -119
 54    90   -91  -120
 55    91   -92  -121
 56    92   -93  -122
 57    93   -88  -123
 58   -61
 59   -62
 60   -63
 61    94   -95  -124
 62    95   -96  -125
 63    96   -94  -126
 64   -67
 65   -68
 66   -69
 67    97   -98  -127
 68    98   -99  -128
 69    99   -97  -129
  1     2     3     4     5     6     7     8     9    46    47    48
 49    50    51    58    59    60    64    65    66  -100  -101  -102
-103  -104  -105  -106  -107  -108  -109  -110  -111  -112  -113  -114
-115  -116  -117  -118  -119  -120  -121  -122  -123  -124  -125  -126
-127  -128  -129
          1          2600
          1            22             0
          0          7.11           320          7.11           360          7.11
         40          7.11            80          7.11           120          7.11
        160          7.11           200          7.11           240          7.11
        280          7.11           320          5.59           360          5.59
         40          5.59            80          5.59           120          5.59
        160          5.59           200          5.59           240          5.59
        280          4.11           330          4.11            30          4.11
         90          4.11           150          4.11           210          4.11
        270          2.63           360          2.63           120          2.63
        240          1.21           360          1.21           120          1.21
        240
          0             0             0             0             0             0
          0             0             0             0             0             0
          0             0             0             0             0             0
          0             0             0             0             0             0
```

Figure F-1. (Continued)

```
&D1 R=9*1.35,9*4.65,9*8.26,9*3.3,9*4.65,12*3.32,6*2.29,6*8.4,
30*0.0,9*179.,9*228.,6*231.,3*189.,3*693.,
V=9*0.202,9*0.0459,9*0.085,9*0.0374,9*0.0199,6*0.0828,
6*0.0315,3*0.0948,3*0.0239,3*0.0262,3*0.0058,
Z=9*0.0137,9*0.0503,9*0.0513,9*0.0254,9*0.0229,12*0.0277,
6*0.021,6*0.0759,9*0.399,9*0.459,6*0.345,3*0.702,3*0.560,
9*0.0389,15*0.049,3*0.0402,3*0.147,
C=69*39610.,&END
```

```
12.          125.
    5     1
   28    37    52    61    67    22    31    40    46    49   100   109
  118   124   127    70    79    88    94    97     9     9     6     3
    3
```

Figure F-1. (Continued)

```
REAL INPUT MATRIX AMPLITUDES - PSI
   0.0           0.0           0.0           0.0           0.0           0.0
   0.0           0.0           0.0           0.0           0.0           0.0
   0.0           0.0           0.0           0.0           0.0           0.0
   0.0           0.0           0.0          7.6604E-01    1.0000E+00    7.6604E-01
   1.7365E-01 -5.0000E-01 -9.3969E-01 -9.3969E-01 -5.0000E-01  1.7365E-01
   7.6604E-01   9.4648E-01   7.2505E-01   1.6435E-01 -4.7324E-01 -8.8940E-01
  -8.8940E-01 -4.7324E-01   1.6435E-01   6.7697E-01   6.7697E-01   0.0
  -6.7697E-01 -6.7697E-01   0.0          5.3686E-01 -2.6843E-01 -2.6843E-01
   2.5528E-01 -1.2764E-01 -1.2764E-01

IMAGINARY INPUT MATRIX AMPLITUDES - PSI
   0.0           0.0           0.0           0.0           0.0           0.0
   0.0           0.0           0.0           0.0           0.0           0.0
   0.0           0.0           0.0           0.0           0.0           0.0
   0.0           0.0           0.0           0.0           0.0           0.0
   0.0           0.0           0.0           0.0           0.0           0.0
   0.0           0.0           0.0           0.0           0.0           0.0
   0.0           0.0           0.0           0.0           0.0           0.0
   0.0           0.0           0.0           0.0           0.0           0.0
   0.0           0.0           0.0
ROCKETDYNE OME INJECTOR
OXIDIZER SIDE, NO RING DAMS
STANDING FIRST TANGENTIAL MODE
   | CENTERLINE
INPUT FREQUENCY= 2600.0
```

Figure F-2. Real and Imaginary Input Matrix Amplitudes

FLOW	UPSTREAM PRESSURE	DOWNSTREAM PRESSURE	RESISTANCE SEC/IN SQ	INERTANCE SEC SQ/IN SQ	AMPLITUDE LB/SEC/PSI	PHASE DEGREES
1	PIN(1)	P(1)	1.350E+00	1.370E-02	9.200E-04	93.3
2	PIN(2)	P(2)	1.350E+00	1.370E-02	1.176E-03	93.3
3	PIN(3)	P(3)	1.350E+00	1.370E-02	8.998E-04	93.3
4	PIN(4)	P(4)	1.350E+00	1.370E-02	2.040E-04	93.3
5	PIN(5)	P(5)	1.350E+00	1.370E-02	5.872E-04	273.3
6	PIN(6)	P(6)	1.350E+00	1.370E-02	1.104E-03	273.3
7	PIN(7)	P(7)	1.350E+00	1.370E-02	1.104E-03	273.3
8	PIN(8)	P(8)	1.350E+00	1.370E-02	5.871E-04	273.3
9	PIN(9)	P(9)	1.350E+00	1.370E-02	2.054E-04	93.2
10	P(1)	P(10)	4.650E+00	5.030E-02	3.335E-04	94.6
11	P(2)	P(11)	4.650E+00	5.030E-02	4.124E-04	94.4
12	P(3)	P(12)	4.650E+00	5.030E-02	3.150E-04	94.5
13	P(4)	P(13)	4.650E+00	5.030E-02	7.140E-05	94.5
14	P(5)	P(14)	4.650E+00	5.030E-02	2.056E-04	274.5
15	P(6)	P(15)	4.650E+00	5.030E-02	3.864E-04	274.5
16	P(7)	P(16)	4.650E+00	5.030E-02	3.863E-04	274.5
17	P(8)	P(17)	4.650E+00	5.030E-02	2.055E-04	274.5
18	P(9)	P(18)	4.650E+00	5.030E-02	7.264E-05	94.3
19	P(1)	P(19)	8.260E+00	5.130E-02	4.193E-04	92.5
20	P(2)	P(20)	8.260E+00	5.130E-02	5.498E-04	92.6
21	P(3)	P(21)	8.260E+00	5.130E-02	4.212E-04	92.6
22	P(4)	P(22)	8.260E+00	5.130E-02	9.548E-05	92.6
23	P(5)	P(23)	8.260E+00	5.130E-02	2.749E-04	272.6
24	P(6)	P(24)	8.260E+00	5.130E-02	5.167E-04	272.6
25	P(7)	P(25)	8.260E+00	5.130E-02	5.167E-04	272.6
26	P(8)	P(26)	8.260E+00	5.130E-02	2.749E-04	272.6
27	P(9)	P(27)	8.260E+00	5.130E-02	9.544E-05	92.5
28	P(19)	P(28)	3.300E+00	2.540E-02	2.287E-04	92.7
29	P(20)	P(29)	3.300E+00	2.540E-02	3.022E-04	92.7
30	P(21)	P(30)	3.300E+00	2.540E-02	2.316E-04	92.7
31	P(22)	P(31)	3.300E+00	2.540E-02	5.250E-05	92.7
32	P(23)	P(32)	3.300E+00	2.540E-02	1.512E-04	272.7
33	P(24)	P(33)	3.300E+00	2.540E-02	2.841E-04	272.7
34	P(25)	P(34)	3.300E+00	2.540E-02	2.841E-04	272.7
35	P(26)	P(35)	3.300E+00	2.540E-02	1.512E-04	272.7
36	P(27)	P(36)	3.300E+00	2.540E-02	5.236E-05	92.7
37	P(10)	P(37)	4.650E+00	2.290E-02	2.449E-04	94.9
38	P(11)	P(38)	4.650E+00	2.290E-02	3.012E-04	94.8
39	P(12)	P(39)	4.650E+00	2.290E-02	2.301E-04	94.8
40	P(13)	P(40)	4.650E+00	2.290E-02	5.214E-05	94.8
41	P(14)	P(41)	4.650E+00	2.290E-02	1.501E-04	274.8
42	P(15)	P(42)	4.650E+00	2.290E-02	2.821E-04	274.8
43	P(16)	P(43)	4.650E+00	2.290E-02	2.821E-04	274.8
44	P(17)	P(44)	4.650E+00	2.290E-02	1.501E-04	274.8
45	P(18)	P(45)	4.650E+00	2.290E-02	5.313E-05	94.6
46	PIN(10)	P(46)	3.320E+00	2.770E-02	4.326E-04	97.7
47	PIN(11)	P(47)	3.320E+00	2.770E-02	4.326E-04	97.7

Figure F-3. Input and Output Data for Flowrates

48	PIN(12)	P(48)	3.320E+00	2.770E-02	1.842E-11	75.5
49	PIN(13)	P(49)	3.320E+00	2.770E-02	4.326E-04	277.7
50	PIN(14)	P(50)	3.320E+00	2.770E-02	4.326E-04	277.7
51	PIN(15)	P(51)	3.320E+00	2.770E-02	3.640E-11	266.4
52	P(46)	P(52)	3.320E+00	2.770E-02	3.673E-04	97.8
53	P(47)	P(53)	3.320E+00	2.770E-02	3.673E-04	97.8
54	P(48)	P(54)	3.320E+00	2.770E-02	1.565E-11	75.6
55	P(49)	P(55)	3.320E+00	2.770E-02	3.673E-04	277.8
56	P(50)	P(56)	3.320E+00	2.770E-02	3.673E-04	277.8
57	P(51)	P(57)	3.320E+00	2.770E-02	3.091E-11	266.5
58	PIN(16)	P(58)	2.290E+00	2.100E-02	4.144E-04	98.4
59	PIN(17)	P(59)	2.290E+00	2.100E-02	2.072E-04	278.4
60	PIN(18)	P(60)	2.290E+00	2.100E-02	2.072E-04	278.4
61	P(58)	P(61)	2.290E+00	2.100E-02	3.602E-04	98.4
62	P(59)	P(62)	2.290E+00	2.100E-02	1.801E-04	278.4
63	P(60)	P(63)	2.290E+00	2.100E-02	1.801E-04	278.4
64	PIN(19)	P(64)	8.400E+00	7.590E-02	4.118E-05	100.4
65	PIN(20)	P(65)	8.400E+00	7.590E-02	2.059E-05	280.4
66	PIN(21)	P(66)	8.400E+00	7.590E-02	2.059E-05	280.4
67	P(64)	P(67)	8.400E+00	7.590E-02	3.580E-05	100.4
68	P(65)	P(68)	8.400E+00	7.590E-02	1.790E-05	280.4
69	P(66)	P(69)	8.400E+00	7.590E-02	1.790E-05	280.4
70	P(36)	P(28)	0.0	3.990E-01	7.741E-05	92.3
71	P(28)	P(29)	0.0	3.990E-01	3.024E-05	92.4
72	P(29)	P(30)	0.0	3.990E-01	3.051E-05	272.3
73	P(30)	P(31)	0.0	3.990E-01	7.717E-05	272.3
74	P(31)	P(32)	0.0	3.990E-01	8.775E-05	272.3
75	P(32)	P(33)	0.0	3.990E-01	5.728E-05	272.3
76	P(33)	P(34)	0.0	3.990E-01	3.363E-10	52.0
77	P(34)	P(35)	0.0	3.990E-01	5.728E-05	92.3
78	P(35)	P(36)	0.0	3.990E-01	8.779E-05	92.3
79	P(45)	P(37)	0.0	4.590E-01	5.948E-05	93.8
80	P(37)	P(38)	0.0	4.590E-01	1.910E-05	93.2
81	P(38)	P(39)	0.0	4.590E-01	2.246E-05	273.6
82	P(39)	P(40)	0.0	4.590E-01	5.634E-05	273.7
83	P(40)	P(41)	0.0	4.590E-01	6.406E-05	273.7
84	P(41)	P(42)	0.0	4.590E-01	4.181E-05	273.7
85	P(42)	P(43)	0.0	4.590E-01	1.063E-09	65.8
86	P(43)	P(44)	0.0	4.590E-01	4.182E-05	93.7
87	P(44)	P(45)	0.0	4.590E-01	6.427E-05	93.7
88	P(57)	P(52)	0.0	3.450E-01	6.423E-05	97.4
89	P(52)	P(53)	0.0	3.450E-01	1.076E-11	280.6
90	P(53)	P(54)	0.0	3.450E-01	6.423E-05	277.4
91	P(54)	P(55)	0.0	3.450E-01	6.423E-05	277.4
92	P(55)	P(56)	0.0	3.450E-01	4.231E-11	269.1
93	P(56)	P(57)	0.0	3.450E-01	6.423E-05	97.4
94	P(63)	P(61)	0.0	7.020E-01	3.476E-05	98.0
95	P(61)	P(62)	0.0	7.020E-01	3.476E-05	278.0
96	P(62)	P(63)	0.0	7.020E-01	5.551E-12	69.4

Figure F-3. (Continued)

97	P(69)	P(67)	0.0	5.60CE-01	1.565E-05	100.0
98	P(67)	P(68)	0.0	5.60CE-01	1.565E-05	280.0
99	P(68)	P(69)	0.0	5.60CE-01	5.759E-13	315.0
100	P(28)	PIN(22)	1.790E+02	3.890E-02	1.777E-04	92.7
101	P(29)	PIN(23)	1.790E+02	3.890E-02	2.352E-04	92.9
102	P(30)	PIN(24)	1.790E+02	3.890E-02	1.804E-04	92.9
103	P(31)	PIN(25)	1.790E+02	3.890E-02	4.090E-05	92.9
104	P(32)	PIN(26)	1.790E+02	3.890E-02	1.178E-04	272.9
105	P(33)	PIN(27)	1.790E+02	3.890E-02	2.213E-04	272.9
106	P(34)	PIN(28)	1.790E+02	3.890E-02	2.213E-04	272.9
107	P(35)	PIN(29)	1.790E+02	3.890E-02	1.178E-04	272.9
108	P(36)	PIN(30)	1.790E+02	3.890E-02	4.052E-05	92.9
109	P(37)	PIN(31)	2.280E+02	4.900E-02	2.395E-04	95.0
110	P(38)	PIN(32)	2.280E+02	4.900E-02	2.856E-04	94.8
111	P(39)	PIN(33)	2.280E+02	4.900E-02	2.202E-04	94.8
112	P(40)	PIN(34)	2.280E+02	4.900E-02	4.994E-05	94.8
113	P(41)	PIN(35)	2.280E+02	4.900E-02	1.438E-04	274.8
114	P(42)	PIN(36)	2.280E+02	4.900E-02	2.703E-04	274.8
115	P(43)	PIN(37)	2.280E+02	4.900E-02	2.703E-04	274.8
116	P(44)	PIN(38)	2.280E+02	4.900E-02	1.440E-04	274.8
117	P(45)	PIN(39)	2.280E+02	4.900E-02	4.787E-05	94.5
118	P(52)	PIN(40)	2.310E+02	4.900E-02	3.857E-04	97.8
119	P(53)	PIN(41)	2.310E+02	4.900E-02	3.857E-04	97.8
120	P(54)	PIN(42)	2.310E+02	4.900E-02	1.851E-11	271.2
121	P(55)	PIN(43)	2.310E+02	4.900E-02	3.857E-04	277.8
122	P(56)	PIN(44)	2.310E+02	4.900E-02	3.857E-04	277.8
123	P(57)	PIN(45)	2.310E+02	4.900E-02	3.656E-11	102.1
124	P(61)	PIN(46)	1.890E+02	4.020E-02	4.042E-04	98.4
125	P(62)	PIN(47)	1.890E+02	4.020E-02	2.021E-04	278.4
126	P(63)	PIN(48)	1.890E+02	4.020E-02	2.021E-04	278.4
127	P(67)	PIN(49)	6.930E+02	1.470E-01	6.487E-05	100.2
128	P(68)	PIN(50)	6.930E+02	1.470E-01	3.243E-05	280.2
129	P(69)	PIN(51)	6.930E+02	1.470E-01	3.243E-05	280.2

ROCKETDYNE OME INJECTOR
OXIDIZER SIDE, NO RING DAMS
STANDING FIRST TANGENTIAL MODE

	LB/SEC/PSI	% FLOW/% PC
TOTAL INJECTOR FLOW=	5.5053E-03	5.7347E-02
TOTAL VECTOR INJECTOR FLOW=	5.5012E-03	5.7304E-02
TOTAL INJECTOR FLOW PROPORTIONED BY PC AMPLITUDES=	3.6987E-03	3.8528E-02
TOTAL VECTOR INJECTOR FLOW PROPORTIONED BY PC AMPLITUDES=	3.6961E-03	3.8501E-02

Figure F-3. (Continued)

PRESSURE NODE	VOLUME CU IN	AC. VEL. IN/SEC	MAGNITUDE PSI/PSI	PHASE DEGREES	FLOWS IN		FLOWS OUT	
1	2.020E-01	3.961E+04	2.059E-01	3.0	1		10	19
2	2.020E-01	3.961E+04	2.632E-01	2.9	2		11	20
3	2.020E-01	3.961E+04	2.014E-01	3.0	3		12	21
4	2.020E-01	3.961E+04	4.565E-02	3.0	4		13	22
5	2.020E-01	3.961E+04	1.314E-01	183.0	5		14	23
6	2.020E-01	3.961E+04	2.470E-01	183.0	6		15	24
7	2.020E-01	3.961E+04	2.470E-01	183.0	7		16	25
8	2.020E-01	3.961E+04	1.314E-01	183.0	8		17	26
9	2.020E-01	3.961E+04	4.598E-02	2.9	9		18	27
10	4.590E-02	3.961E+04	4.799E-01	3.7	10		37	
11	4.590E-02	3.961E+04	6.020E-01	3.6	11		38	
12	4.590E-02	3.961E+04	4.602E-01	3.6	12		39	
13	4.590E-02	3.961E+04	1.043E-01	3.6	13		40	
14	4.590E-02	3.961E+04	3.003E-01	183.6	14		41	
15	4.590E-02	3.961E+04	5.645E-01	183.6	15		42	
16	4.590E-02	3.961E+04	5.644E-01	183.6	16		43	
17	4.590E-02	3.961E+04	3.002E-01	183.6	17		44	
18	4.590E-02	3.961E+04	1.057E-01	3.5	18		45	
19	8.500E-02	3.961E+04	5.573E-01	2.3	19		28	
20	8.500E-02	3.961E+04	7.239E-01	2.3	20		29	
21	8.500E-02	3.961E+04	5.544E-01	2.3	21		30	
22	8.500E-02	3.961E+04	1.257E-01	2.3	22		31	
23	8.500E-02	3.961E+04	3.618E-01	182.3	23		32	
24	8.500E-02	3.961E+04	6.800E-01	182.3	24		33	
25	8.500E-02	3.961E+04	6.800E-01	182.3	25		34	
26	8.500E-02	3.961E+04	3.618E-01	182.3	26		35	
27	8.500E-02	3.961E+04	1.260E-01	2.3	27		36	
28	3.740E-02	3.961E+04	6.522E-01	2.3	28	70	71	100
29	3.740E-02	3.961E+04	8.493E-01	2.3	29	71	72	101
30	3.740E-02	3.961E+04	6.505E-01	2.3	30	72	73	102
31	3.740E-02	3.961E+04	1.474E-01	2.3	31	73	74	103
32	3.740E-02	3.961E+04	4.246E-01	182.3	32	74	75	104
33	3.740E-02	3.961E+04	7.979E-01	182.3	33	75	76	105
34	3.740E-02	3.961E+04	7.979E-01	182.3	34	76	77	106
35	3.740E-02	3.961E+04	4.245E-01	182.3	35	77	78	107
36	3.740E-02	3.961E+04	1.477E-01	2.3	36	78	70	108
37	1.990E-02	3.961E+04	5.716E-01	3.8	37	79	80	109
38	1.990E-02	3.961E+04	7.147E-01	3.7	38	80	81	110
39	1.990E-02	3.961E+04	5.463E-01	3.7	39	81	82	111
40	1.990E-02	3.961E+04	1.238E-01	3.7	40	82	83	112
41	1.990E-02	3.961E+04	3.565E-01	183.7	41	83	84	113

Figure F-4. Input and Output Data for Pressure Nodes

```
42    1.990E-02 3.961E+04   6.700E-01   183.7  42  84        85 114
43    1.990E-02 3.961E+04   6.700E-01   183.7  43  85        86 115
44    1.990E-02 3.961E+04   3.564E-01   183.7  44  86        87 116
45    1.990E-02 3.961E+04   1.255E-01     3.6  45  87        79 117
46    8.280E-02 3.961E+04   1.957E-01     7.3  46            52
47    8.280E-02 3.961E+04   1.957E-01     7.3  47            53
48    8.280E-02 3.961E+04   8.337E-09   345.1  48            54
49    8.280E-02 3.961E+04   1.957E-01   187.3  49            55
50    8.280E-02 3.961E+04   1.957E-01   187.3  50            56
51    8.280E-02 3.961E+04   1.647E-08   176.0  51            57
52    3.150E-02 3.961E+04   3.620E-01     7.4  52  88        89 118
53    3.150E-02 3.961E+04   3.620E-01     7.4  53  89        90 119
54    3.150E-02 3.961E+04   1.542E-08   345.1  54  90        91 120
55    3.150E-02 3.961E+04   3.620E-01   187.4  55  91        92 121
56    3.150E-02 3.961E+04   3.620E-01   187.4  56  92        93 122
57    3.150E-02 3.961E+04   3.046E-08   176.0  57  93        88 123
58    9.480E-02 3.961E+04   1.422E-01     8.0  58            61
59    9.480E-02 3.961E+04   7.109E-02   188.0  59            62
60    9.480E-02 3.961E+04   7.109E-02   188.0  60            63
61    2.390E-02 3.961E+04   2.657E-01     8.0  61  94        95 124
62    2.390E-02 3.961E+04   1.329E-01   188.0  62  95        96 125
63    2.390E-02 3.961E+04   1.329E-01   188.0  63  96        94 126
64    2.620E-02 3.961E+04   5.106E-02    10.0  64            67
65    2.620E-02 3.961E+04   2.553E-02   190.0  65            68
66    2.620E-02 3.961E+04   2.553E-02   190.0  66            69
67    5.800E-03 3.961E+04   9.544E-02    10.0  67  97        98 127
68    5.800E-03 3.961E+04   4.772E-02   190.0  68  98        99 128
69    5.800E-03 3.961E+04   4.772E-02   190.0  69  99        97 129

ROCKETDYNE OME INJECTOR
OXIDIZER SIDE, NO RING DAMS
STANDING FIRST TANGENTIAL MODE
```

Figure F-4. (Continued)

APPENDIX G

COMPUTER MODEL DOCUMENTATION OF LANCE

XRL FUEL SYSTEM FREQUENCY RESPONSE

```
XRL INJECTOR
FUEL SIDE, NO RING DAMS
ANOMOLOUS SECOND TANGENTIAL MODE
   53    28     6                                  2    -6
    1    -5                                       4    -8
    3    -7                                       6   -14   -74
    5   -13   -73                                 8   -16   -76
    7   -15   -75                                18   -19   -46
    9    17   -18   -45                           20   -21   -48
   19   -20   -47                                 22   -23   -50
   21    10   -22   -49                           24   -25   -52
   23   -24   -51                                 26   -27   -54
   25    11   -26   -53                           28   -29   -56
   27   -28   -55                                 30   -31   -58
   29    12   -30   -57                           32   -17   -60
   31   -32   -59                                 34   -35   -62
   33    13   -34   -61                           36    14   -37   -64
   35   -36   -63                                 38   -39   -66
   37   -38   -65                                 40   -41   -68
   39    15   -40   -67                           42    16   -43   -70
   41   -42   -69                                 44   -33   -72
   43   -44   -71                                 74   -10   -77
   73    -9                                       76   -12   -83
   75   -11                                       78   -79
   77   -78                                       80   -81
   79   -80                                       82
   81   -82
```

```
   83   -84                                       84   -85
   85   -86                                       86   -87
   87   -88                                       88
   -1    -2    -3    -4
  -45   -46   -47   -48   -49   -50   -51   -52   -53   -54   -55   -56
  -57   -58   -59   -60   -61   -62   -63   -64   -65   -66   -67   -68
  -69   -70   -71   -72
```

Figure G-1. Data Deck for XRL Fuel Side

```
            1          1300
            0
+1.0         -1.0         -1.0         -1.0         -1.0         +1.0
+1.0         +1.0         +1.0         -1.0         -1.0         -1.0
-1.0         +1.0         +1.0         +1.0         +1.0         -1.0
-1.0         -1.0         +1.0         +1.0         +1.0         -1.0
-1.0         -1.0         +1.0         +1.0
 &D1 R=4*0.293,4*0.090,8*1.06,0.0,0.0,3*0.0,0.0,3*0.0,0.0,
 3*0.0,0.0,3*0.0,0.0,2*0.0,0.0,2*0.0,0.0,
 2*0.0,0.0,0.0,16*203.,12*221.,4*0.090,12*0.0
 V=4*3.20,4*3.025,1.06,3*0.754,1.06,3*0.754,1.06,3*0.754,
 1.06,3*0.754,0.762,2*.506,0.762,2*0.506,0.762,2*0.506,0.762,2*0.506,
 4*3.74,12*4.42,100.
 Z=4*0.0045,4*0.0075,4*0.0025,4*0.0019,16*0.0178,12*0.0271,16*0.0242,
 12*0.026,4*.0065,12*0.1756
 C=53*47700., &END
 39.          950.
     2     1
     9    25    1    17    45    61    17    33    16    12
```

Figure G-1. (Continued)

```
XRL INJECTOR
FUEL SIDE, NO RING DAMS
ANOMOLOUS SECOND TANGENTIAL MODE

REAL INPUT MATRIX AMPLITUDES - PSI
   1.0000E+00 -1.0000E+00 -1.0000E+00 -1.0000E+00 -1.0000E+00  1.0000E+00
   1.0000E+00  1.0000E+00  1.0000E+00 -1.0000E+00 -1.0000E+00 -1.0000E+00
  -1.0000E+00  1.0000E+00  1.0000E+00  1.0000E+00  1.0000E+00 -1.0000E+00
  -1.0000E+00 -1.0000E+00  1.0000E+00  1.0000E+00  1.0000E+00 -1.0000E+00
  -1.0000E+00 -1.0000E+00  1.0000E+00  1.0000E+00

IMAGINARY INPUT MATRIX AMPLITUDES - PSI
   0.0         0.0         0.0         0.0         0.0         0.0
   0.0         0.0         0.0         0.0         0.0         0.0
   0.0         0.0         0.0         0.0         0.0         0.0
   0.0         0.0         0.0         0.0         0.0         0.0
   0.0         0.0         0.0         0.0
XRL INJECTOR
FUEL SIDE, NO RING DAMS
ANOMOLOUS SECOND TANGENTIAL MODE


   INPUT FREQUENCY= 1300.0
```

Figure G-2. Real and Imaginary Input Matrix Amplitudes

FLOW	UPSTREAM PRESSURE	DOWNSTREAM PRESSURE	RESISTANCE SEC/IN SQ	INERTANCE SEC SQ/IN SQ	AMPLITUDE LB/SEC/PSI	PHASE DEGREES
1	P(53)	P(1)	2.930E-01	4.500E-03	4.160E-03	113.2
2	P(53)	P(2)	2.930E-01	4.500E-03	3.959E-03	295.7
3	P(53)	P(3)	2.930E-01	4.500E-03	4.160E-03	113.2
4	P(53)	P(4)	2.930E-01	4.500E-03	3.959E-03	295.7
5	P(1)	P(5)	9.000E-02	7.500E-03	3.494E-03	113.1
6	P(2)	P(6)	9.000E-02	7.500E-03	3.300E-03	296.0
7	P(3)	P(7)	9.000E-02	7.500E-03	3.494E-03	113.1
8	P(4)	P(8)	9.000E-02	7.500E-03	3.300E-03	296.0
9	P(37)	P(9)	1.060E+00	2.500E-03	6.461E-04	307.0
10	P(38)	P(13)	1.060E+00	2.500E-03	4.111E-04	131.0
11	P(39)	P(17)	1.060E+00	2.500E-03	6.461E-04	307.0
12	P(40)	P(21)	1.060E+00	2.500E-03	4.111E-04	131.0
13	P(5)	P(25)	1.060E+00	1.900E-03	3.027E-04	154.7
14	P(6)	P(28)	1.060E+00	1.900E-03	3.913E-04	324.7
15	P(7)	P(31)	1.060E+00	1.900E-03	3.027E-04	154.7
16	P(8)	P(34)	1.060E+00	1.900E-03	3.913E-04	324.7
17	P(24)	P(9)	0.0	1.780E-02	1.902E-03	284.1
18	P(9)	P(10)	0.0	1.780E-02	5.292E-03	294.3
19	P(10)	P(11)	0.0	1.780E-02	2.454E-03	284.0
20	P(11)	P(12)	0.0	1.780E-02	2.096E-04	273.2
21	P(12)	P(13)	0.0	1.780E-02	1.985E-03	104.4
22	P(13)	P(14)	0.0	1.780E-02	5.208E-03	114.3
23	P(14)	P(15)	0.0	1.780E-02	2.428E-03	104.0
24	P(15)	P(16)	0.0	1.780E-02	2.353E-04	94.3
25	P(16)	P(17)	0.0	1.780E-02	1.902E-03	284.1
26	P(17)	P(18)	0.0	1.780E-02	5.292E-03	294.3
27	P(18)	P(19)	0.0	1.780E-02	2.454E-03	284.0
28	P(19)	P(20)	0.0	1.780E-02	2.096E-04	273.2
29	P(20)	P(21)	0.0	1.780E-02	1.985E-03	104.4
30	P(21)	P(22)	0.0	1.780E-02	5.208E-03	114.3
31	P(22)	P(23)	0.0	1.780E-02	2.428E-03	104.0
32	P(23)	P(24)	0.0	1.780E-02	2.353E-04	94.3
33	P(36)	P(25)	0.0	2.710E-02	1.090E-03	291.6
34	P(25)	P(26)	0.0	2.710E-02	3.437E-03	296.1
35	P(26)	P(27)	0.0	2.710E-02	9.658E-04	285.8
36	P(27)	P(28)	0.0	2.710E-02	1.122E-03	111.4
37	P(28)	P(29)	0.0	2.710E-02	3.405E-03	116.2
38	P(29)	P(30)	0.0	2.710E-02	9.658E-04	105.8
39	P(30)	P(31)	0.0	2.710E-02	1.090E-03	291.6
40	P(31)	P(32)	0.0	2.710E-02	3.437E-03	296.1
41	P(32)	P(33)	0.0	2.710E-02	9.658E-04	285.8
42	P(33)	P(34)	0.0	2.710E-02	1.122E-03	111.4
43	P(34)	P(35)	0.0	2.710E-02	3.405E-03	116.2
44	P(35)	P(36)	0.0	2.710E-02	9.658E-04	105.8
45	P(9)	PIN(1)	2.030E+02	2.420E-02	2.150E-03	120.3
46	P(10)	PIN(2)	2.030E+02	2.420E-02	2.569E-03	303.6
47	P(11)	PIN(3)	2.030E+02	2.420E-02	1.544E-03	282.4

Figure G-3. Input and Output Data for Flowrates

48	P(12)	PIN(4)	2.030E+02	2.420E-02	1.459E-03	279.9
49	P(13)	PIN(5)	2.030E+02	2.420E-02	2.251E-03	300.3
50	P(14)	PIN(6)	2.030E+02	2.420E-02	2.505E-03	124.3
51	P(15)	PIN(7)	2.030E+02	2.420E-02	1.482E-03	103.0
52	P(16)	PIN(8)	2.030E+02	2.420E-02	1.388E-03	100.0
53	P(17)	PIN(9)	2.030E+02	2.420E-02	2.150E-03	120.3
54	P(18)	PIN(10)	2.030E+02	2.420E-02	2.569E-03	303.6
55	P(19)	PIN(11)	2.030E+02	2.420E-02	1.544E-03	282.4
56	P(20)	PIN(12)	2.030E+02	2.420E-02	1.459E-03	279.9
57	P(21)	PIN(13)	2.030E+02	2.420E-02	2.251E-03	300.3
58	P(22)	PIN(14)	2.030E+02	2.420E-02	2.505E-03	124.3
59	P(23)	PIN(15)	2.030E+02	2.420E-02	1.482E-03	103.0
60	P(24)	PIN(16)	2.030E+02	2.420E-02	1.386E-03	100.0
61	P(25)	PIN(17)	2.210E+02	2.600E-02	2.217E-03	123.6
62	P(26)	PIN(18)	2.210E+02	2.600E-02	2.216E-03	300.2
63	P(27)	PIN(19)	2.210E+02	2.600E-02	1.664E-03	287.5
64	P(28)	PIN(20)	2.210E+02	2.600E-02	2.271E-03	303.4
65	P(29)	PIN(21)	2.210E+02	2.600E-02	2.182E-03	120.7
66	P(30)	PIN(22)	2.210E+02	2.600E-02	1.627E-03	107.8
67	P(31)	PIN(23)	2.210E+02	2.600E-02	2.217E-03	123.6
68	P(32)	PIN(24)	2.210E+02	2.600E-02	2.216E-03	300.2
69	P(33)	PIN(25)	2.210E+02	2.600E-02	1.664E-03	287.5
70	P(34)	PIN(26)	2.210E+02	2.600E-02	2.271E-03	303.4
71	P(35)	PIN(27)	2.210E+02	2.600E-02	2.182E-03	120.7
72	P(36)	PIN(28)	2.210E+02	2.600E-02	1.627E-03	107.8
73	P(5)	P(37)	9.000E-02	6.500E-03	1.753E-03	106.3
74	P(6)	P(38)	9.000E-02	6.500E-03	1.496E-03	289.6
75	P(7)	P(39)	9.000E-02	6.500E-03	1.753E-03	106.3
76	P(8)	P(40)	9.000E-02	6.500E-03	1.496E-03	289.6
77	P(38)	P(41)	0.0	1.756E-01	3.446E-04	114.1
78	P(41)	P(42)	0.0	1.756E-01	5.187E-05	294.1
79	P(42)	P(43)	0.0	1.756E-01	7.808E-06	114.1
80	P(43)	P(44)	0.0	1.756E-01	1.175E-06	294.1
81	P(44)	P(45)	0.0	1.756E-01	1.768E-07	114.1
82	P(45)	P(46)	0.0	1.756E-01	2.602E-08	294.1
83	P(40)	P(47)	0.0	1.756E-01	3.446E-04	114.1
84	P(47)	P(48)	0.0	1.756E-01	5.187E-05	294.1
85	P(48)	P(49)	0.0	1.756E-01	7.808E-06	114.1
86	P(49)	P(50)	0.0	1.756E-01	1.175E-06	294.1
87	P(50)	P(51)	0.0	1.756E-01	1.768E-07	114.1
88	P(51)	P(52)	0.0	1.756E-01	2.602E-08	294.1

XRL INJECTOR
FUEL SIDE, NO RING DAMS
ANOMOLOUS SECOND TANGENTIAL MODE

	LB/SEC/PSI	% FLOW/% PC
TOTAL INJECTOR FLOW=	5.5052E-02	1.3410E+00
TOTAL VECTOR INJECTOR FLOW=	5.4374E-02	1.3245E+00
TOTAL INJECTOR FLOW PROPORTIONED BY PC AMPLITUDES=	5.5052E-02	1.3410E+00
TOTAL VECTOR INJECTOR FLOW PROPORTIONED BY PC AMPLITUDES=	5.4374E-02	1.3245E+00

Figure G-3. (Continued)

PRESSURE NODE	VOLUME CU IN	AC. VEL. IN/SEC	MAGNITUDE PSI/PSI	PHASE DEGREES	FLOWS IN		FLOWS OUT	
1	3.200E+00	4.770E+04	1.500E-01	23.7	1		5	
2	3.200E+00	4.770E+04	1.484E-01	204.2	2		6	
3	3.200E+00	4.770E+04	1.500E-01	23.7	3		7	
4	3.200E+00	4.770E+04	1.484E-01	204.2	4		8	
5	3.025E+00	4.770E+04	3.640E-01	23.3	5		13	73
6	3.025E+00	4.770E+04	3.505E-01	205.2	6		14	74
7	3.025E+00	4.770E+04	3.640E-01	23.3	7		15	75
8	3.025E+00	4.770E+04	3.505E-01	205.2	8		16	76
9	1.060E+00	4.770E+04	4.436E-01	21.5	9	17	18	45
10	7.540E-01	4.770E+04	3.270E-01	208.1	18		19	46
11	7.540E-01	4.770E+04	6.787E-01	200.8	19		20	47
12	7.540E-01	4.770E+04	7.078E-01	200.0	20		21	48
13	1.060E+00	4.770E+04	4.215E-01	203.9	21	10	22	49
14	7.540E-01	4.770E+04	3.357E-01	25.0	22		23	50
15	7.540E-01	4.770E+04	6.856E-01	19.4	23		24	51
16	7.540E-01	4.770E+04	7.187E-01	18.6	24		25	52
17	1.060E+00	4.770E+04	4.436E-01	21.5	25	11	26	53
18	7.540E-01	4.770E+04	3.270E-01	208.1	26		27	54
19	7.540E-01	4.770E+04	6.787E-01	200.8	27		28	55
20	7.540E-01	4.770E+04	7.078E-01	200.0	28		29	56
21	1.060E+00	4.770E+04	4.215E-01	203.9	29	12	30	57
22	7.540E-01	4.770E+04	3.357E-01	25.0	30		31	58
23	7.540E-01	4.770E+04	6.856E-01	19.4	31		32	59
24	7.540E-01	4.770E+04	7.187E-01	18.6	32		17	60
25	7.620E-01	4.770E+04	3.678E-01	23.7	33	13	34	61
26	5.060E-01	4.770E+04	3.936E-01	208.2	34		35	62
27	5.060E-01	4.770E+04	6.041E-01	203.9	35		36	63
28	7.620E-01	4.770E+04	3.560E-01	205.6	36	14	37	64
29	5.060E-01	4.770E+04	3.976E-01	26.7	37		38	65
30	5.060E-01	4.770E+04	6.089E-01	22.9	38		39	66
31	7.620E-01	4.770E+04	3.678E-01	23.7	39	15	40	67
32	5.060E-01	4.770E+04	3.936E-01	208.2	40		41	68
33	5.060E-01	4.770E+04	6.041E-01	203.9	41		42	69
34	7.620E-01	4.770E+04	3.560E-01	205.6	42	16	43	70
35	5.060E-01	4.770E+04	3.976E-01	26.7	43		44	71
36	5.060E-01	4.770E+04	6.089E-01	22.9	44		33	72
37	3.740E+00	4.770E+04	4.565E-01	21.8	73		9	
38	3.740E+00	4.770E+04	4.296E-01	204.1	74		10	77
39	3.740E+00	4.770E+04	4.565E-01	21.8	75		11	
40	3.740E+00	4.770E+04	4.296E-01	204.1	76		12	83
41	4.420E+00	4.770E+04	6.467E-02	24.1	77		78	

Figure G-4. Input and Output Data for Pressure Nodes

```
42    4.420E+00 4.770E+04   9.734E-03   204.1  78     79
43    4.420E+00 4.770E+04   1.465E-03    24.1  79     80
44    4.420E+00 4.770E+04   2.205E-04   204.1  80     81
45    4.420E+00 4.770E+04   3.308E-05    24.1  81     82
46    4.420E+00 4.770E+04   4.245E-06   204.1  82
47    4.420E+00 4.770E+04   6.467E-02    24.1  83     84
48    4.420E+00 4.770E+04   9.734E-03   204.1  84     85
49    4.420E+00 4.770E+04   1.465E-03    24.1  85     86
50    4.420E+00 4.770E+04   2.205E-04   204.1  86     87
51    4.420E+00 4.770E+04   3.308E-05    24.1  87     88
52    4.420E+00 4.770E+04   4.245E-06   204.1  88
53    1.000E+02 4.770E+04   3.888E-03   162.7        1    2    3    4
 XRL INJECTOR
 FUEL SIDE, NO RING DAMS
 ANOMOLOUS SECOND TANGENTIAL MODE
```

Figure C-4. (Continued)

APPENDIX H

COMPUTER MODEL DOCUMENTATION OF LANCE XRL OXIDIZER SYSTEM FREQUENCY RESPONSE

```
XRL INJECTOR
OXIDIZER SIDE, NO RING DAMS
ANOMOLOUS SECOND TANGENTIAL MODE
   61    36     6
    1    -3                                    2    -4
    3    -5                                    4    -6
    5    -7                                    6    -8
    7    -9                                    8   -10
    9   -11                                   10   -12
   11   -13                                   12   -14
   13   -15                                   14   -16
   15   -21                                   16   -24
   17   -19                                   18   -20
   19   -22                                   20   -23
   21   -25   -29   -33                       22   -26   -30   -34
   23   -27   -31   -35                       24   -28   -32   -36
   25    37   -38   -73                       38   -39   -74
   39   -40   -75                             40   -41   -76
   41    26   -42   -77                       42   -43   -78
   43   -44   -79                             44   -45   -80
   45    27   -46   -81                       46   -47   -82
   47   -48   -83                             48   -49   -84
   49    28   -50   -85                       50   -51   -86
   51   -52   -87                             52   -37   -88
   53    29   -54   -89                       54   -55   -90
   55   -56   -91                             56    30   -57   -92
   57   -58   -93                             58   -59   -94
   59    31   -60   -95                       60   -61   -96
   61   -62   -97                             62    32   -63   -98
   63   -64   -99                             64   -53  -100
   65    33   -66  -101                       66   -67  -102
   67    34   -68  -103                       68   -69  -104
   69    35   -70  -105                       70   -71  -106
   71    36   -72  -107                       72   -65  -108
   -1    -2   -17   -18
  -73   -74   -75   -76   -77   -78   -79   -80   -81   -82   -83   -84
  -85   -86   -87   -88   -89   -90   -91   -92   -93   -94   -95   -96
  -97   -98   -99  -100  -101  -102  -103  -104  -105  -106  -107  -108
```

Figure H-1. Data Deck for XRL Oxidizer Side

```
                1          1300
                0
+1.0            +1.0       +1.0        -1.0        -1.0        -1.0
-1.0            +1.0       +1.0        +1.0        +1.0        -1.0
-1.0            -1.0       -1.0        +1.0        +1.0        +1.0

+1.0            -1.0       -1.0        -1.0        +1.0        +1.0
+1.0            -1.0       -1.0        -1.0        +1.0        +1.0
-1.0            -1.0       +1.0        +1.0        -1.0        -1.0
 &D1 R=16*0.0188,4*0.0299,0.0179,2*0.0327,0.0179,4*0.602,4*0.636,4*2.50,
 3*0.0,0.0,3*0.0,0.0,3*0.0,0.0,3*0.0,2*0.0,2*0.0,
 0.0,2*0.0,0.0,2*0.0,0.0,2*0.0,0.0,0.0,0.0,0.0,
 0.0,0.0,0.0,0.0,16*154.,12*75.7,8*128.,
 V=16*4.04,4*4.20,4*7.53,1.19,3*0.977,1.19,3*0.977,1.19,3*0.977,1.19,
 3*0.977,12*1.37,0.866,0.666,0.866,0.666,0.866,0.666,0.866,0.666,4.0
 Z=16*0.0044,4*0.0038,4*0.0041,4*0.0017,4*0.0,4*0.0045,16*0.0155,
 12*0.0114,8*0.0290,16*0.0237,12*0.0117,8*0.0199,
 C=61*53100., &END
 130.          950.
     3     1
    25    41    53     1    17    29    73    89   101    37    53    65
    16    12     8
```

Figure H-1. (Continued)

```
XRL INJECTOR
OXIDIZER SIDE, NO RING DAMS
ANOMOLOUS SECOND TANGENTIAL MODE

REAL INPUT MATRIX AMPLITUDES - PSI
   1.0000E+00  1.0000E+00  1.0000E+00 -1.0000E+00 -1.0000E+00 -1.0000E+00
  -1.0000E+00  1.0000E+00  1.0000E+00  1.0000E+00  1.0000E+00 -1.0000E+00
  -1.0000E+00 -1.0000E+00 -1.0000E+00  1.0000E+00  1.0000E+00  1.0000E+00
   1.0000E+00 -1.0000E+00 -1.0000E+00 -1.0000E+00  1.0000E+00  1.0000E+00
   1.0000E+00 -1.0000E+00 -1.0000E+00 -1.0000E+00  1.0000E+00  1.0000E+00
  -1.0000E+00 -1.0000E+00  1.0000E+00  1.0000E+00 -1.0000E+00 -1.0000E+00

IMAGINARY INPUT MATRIX AMPLITUDES - PSI
   0.0         0.0         0.0         0.0         0.0         0.0
   0.0         0.0         0.0         0.0         0.0         0.0
   0.0         0.0         0.0         0.0         0.0         0.0
   0.0         0.0         0.0         0.0         0.0         0.0
   0.0         0.0         0.0         0.0         0.0         0.0
   0.0         0.0         0.0         0.0         0.0         0.0


  INPUT FREQUENCY= 1300.0
```

Figure H-2. Real and Imaginary Input Matrix Amplitudes

FLOW	UPSTREAM PRESSURE	DOWNSTREAM PRESSURE	RESISTANCE SEC/IN SQ	INERTANCE SEC SQ/IN SQ	AMPLITUDE LB/SEC/PSI	PHASE DEGREES
1	P(61)	P(1)	1.880E-02	4.400E-03	7.939E-03	296.3
2	P(61)	P(2)	1.880E-02	4.400E-03	7.939E-03	116.3
3	P(1)	P(3)	1.880E-02	4.400E-03	6.649E-03	296.3
4	P(2)	P(4)	1.880E-02	4.400E-03	6.649E-03	116.3
5	P(3)	P(5)	1.880E-02	4.400E-03	4.278E-03	296.3
6	P(4)	P(6)	1.880E-02	4.400E-03	4.278E-03	116.3
7	P(5)	P(7)	1.880E-02	4.400E-03	1.212E-03	296.4
8	P(6)	P(8)	1.880E-02	4.400E-03	1.212E-03	116.4
9	P(7)	P(9)	1.880E-02	4.400E-03	2.051E-03	116.2
10	P(8)	P(10)	1.880E-02	4.400E-03	2.051E-03	296.2
11	P(9)	P(11)	1.880E-02	4.400E-03	4.981E-03	116.2
12	P(10)	P(12)	1.880E-02	4.400E-03	4.981E-03	296.2
13	P(11)	P(13)	1.880E-02	4.400E-03	7.101E-03	116.3
14	P(12)	P(14)	1.880E-02	4.400E-03	7.101E-03	296.3
15	P(13)	P(15)	1.880E-02	4.400E-03	8.067E-03	116.3
16	P(14)	P(16)	1.880E-02	4.400E-03	8.067E-03	296.3
17	P(61)	P(17)	2.990E-02	3.800E-03	6.238E-03	288.6
18	P(61)	P(18)	2.990E-02	3.800E-03	6.238E-03	108.6
19	P(17)	P(19)	2.990E-02	3.800E-03	5.328E-03	288.6
20	P(18)	P(20)	2.990E-02	3.800E-03	5.328E-03	108.6
21	P(15)	P(21)	1.790E-02	4.100E-03	7.722E-03	116.3
22	P(19)	P(22)	3.270E-02	4.100E-03	3.640E-03	288.6
23	P(20)	P(23)	3.270E-02	4.100E-03	3.640E-03	108.6
24	P(16)	P(24)	1.790E-02	4.100E-03	7.722E-03	296.3
25	P(21)	P(25)	6.020E-01	1.700E-03	3.296E-03	115.4
26	P(22)	P(29)	6.020E-01	1.700E-03	1.898E-03	295.0
27	P(23)	P(33)	6.020E-01	1.700E-03	1.898E-03	115.0
28	P(24)	P(37)	6.020E-01	1.700E-03	3.296E-03	295.4
29	P(21)	P(41)	6.360E-01	0.0	1.020E-03	116.2
30	P(22)	P(44)	6.360E-01	0.0	1.817E-03	118.0
31	P(23)	P(47)	6.360E-01	0.0	1.817E-03	298.0
32	P(24)	P(50)	6.360E-01	0.0	1.020E-03	296.2
33	P(21)	P(53)	2.500E+00	4.500E-03	5.862E-04	121.9
34	P(22)	P(55)	2.500E+00	4.500E-03	5.141E-04	98.6
35	P(23)	P(57)	2.500E+00	4.500E-03	5.141E-04	278.6
36	P(24)	P(59)	2.500E+00	4.500E-03	5.861E-04	301.9
37	P(40)	P(25)	0.0	1.550E-02	1.143E-03	104.1
38	P(25)	P(26)	0.0	1.550E-02	1.183E-03	106.9
39	P(26)	P(27)	0.0	1.550E-02	1.635E-03	288.4
40	P(27)	P(28)	0.0	1.550E-02	4.905E-03	294.1
41	P(28)	P(29)	0.0	1.550E-02	1.660E-03	284.5
42	P(29)	P(30)	0.0	1.550E-02	6.663E-04	288.2
43	P(30)	P(31)	0.0	1.550E-02	1.915E-03	105.3
44	P(31)	P(32)	0.0	1.550E-02	5.039E-03	112.7
45	P(32)	P(33)	0.0	1.550E-02	1.757E-03	101.0
46	P(33)	P(34)	0.0	1.550E-02	7.608E-04	99.6
47	P(34)	P(35)	0.0	1.550E-02	1.768E-03	288.8

Figure H-3. Input and Output Data for Flowrates

48	P(35)	P(36)	0.0	1.550E-02	4.771E-03	294.2
49	P(36)	P(37)	0.0	1.550E-02	1.241E-03	279.2
50	P(37)	P(38)	0.0	1.550E-02	1.277E-03	281.9
51	P(38)	P(39)	0.0	1.550E-02	1.495E-03	112.9
52	P(39)	P(40)	0.0	1.550E-02	4.641E-03	115.8
53	P(52)	P(41)	0.0	1.140E-02	7.915E-03	113.2
54	P(41)	P(42)	0.0	1.140E-02	2.589E-03	106.3
55	P(42)	P(43)	0.0	1.140E-02	2.506E-03	283.9
56	P(43)	P(44)	0.0	1.140E-02	3.838E-03	292.3
57	P(44)	P(45)	0.0	1.140E-02	1.659E-03	287.1
58	P(45)	P(46)	0.0	1.140E-02	2.960E-03	100.9
59	P(46)	P(47)	0.0	1.140E-02	9.058E-03	110.9
60	P(47)	P(48)	0.0	1.140E-02	1.906E-03	101.0
61	P(48)	P(49)	0.0	1.140E-02	2.506E-03	283.9
62	P(49)	P(50)	0.0	1.140E-02	8.132E-03	291.6
63	P(50)	P(51)	0.0	1.140E-02	3.836E-03	282.3
64	P(51)	P(52)	0.0	1.140E-02	2.062E-03	108.2
65	P(60)	P(53)	0.0	2.900E-02	3.222E-03	114.9
66	P(53)	P(54)	0.0	2.900E-02	9.475E-05	143.7
67	P(54)	P(55)	0.0	2.900E-02	3.532E-03	293.0
68	P(55)	P(56)	0.0	2.900E-02	2.759E-04	79.6
69	P(56)	P(57)	0.0	2.900E-02	3.668E-03	111.2
70	P(57)	P(58)	0.0	2.900E-02	1.034E-04	272.2
71	P(58)	P(59)	0.0	2.900E-02	3.354E-03	292.8
72	P(59)	P(60)	0.0	2.900E-02	2.253E-04	275.8
73	P(25)	PIN(1)	1.540E+02	2.370E-02	2.740E-03	114.4
74	P(26)	PIN(2)	1.540E+02	2.370E-02	2.242E-03	106.4
75	P(27)	PIN(3)	1.540E+02	2.370E-02	2.929E-03	117.1
76	P(28)	PIN(4)	1.540E+02	2.370E-02	2.957E-03	299.8
77	P(29)	PIN(5)	1.540E+02	2.370E-02	2.202E-03	291.1
78	P(30)	PIN(6)	1.540E+02	2.370E-02	1.935E-03	285.2
79	P(31)	PIN(7)	1.540E+02	2.370E-02	2.769E-03	298.0
80	P(32)	PIN(8)	1.540E+02	2.370E-02	3.023E-03	119.2
81	P(33)	PIN(9)	1.540E+02	2.370E-02	2.202E-03	111.1
82	P(34)	PIN(10)	1.540E+02	2.370E-02	1.863E-03	105.6
83	P(35)	PIN(11)	1.540E+02	2.370E-02	2.609E-03	119.0
84	P(36)	PIN(12)	1.540E+02	2.370E-02	3.332E-03	298.7
85	P(37)	PIN(13)	1.540E+02	2.370E-02	2.740E-03	294.4
86	P(38)	PIN(14)	1.540E+02	2.370E-02	2.171E-03	286.8
87	P(39)	PIN(15)	1.540E+02	2.370E-02	2.769E-03	298.0
88	P(40)	PIN(16)	1.540E+02	2.370E-02	3.266E-03	119.2
89	P(41)	PIN(17)	7.570E+01	1.170E-02	5.860E-03	116.5
90	P(42)	PIN(18)	7.570E+01	1.170E-02	4.222E-03	103.7
91	P(43)	PIN(19)	7.570E+01	1.170E-02	5.842E-03	115.5
92	P(44)	PIN(20)	7.570E+01	1.170E-02	4.642E-03	292.6
93	P(45)	PIN(21)	7.570E+01	1.170E-02	3.644E-03	281.7
94	P(46)	PIN(22)	7.570E+01	1.170E-02	5.608E-03	295.9
95	P(47)	PIN(23)	7.570E+01	1.170E-02	4.642E-03	112.6

Figure H-3. (Continued)

96	P(48)	PIN(24)	7.570E+01	1.170E-02	3.406E-03	101.5
97	P(49)	PIN(25)	7.570E+01	1.170E-02	5.014E-03	115.9
98	P(50)	PIN(26)	7.570E+01	1.170E-02	5.860E-03	296.5
99	P(51)	PIN(27)	7.570E+01	1.170E-02	3.984E-03	283.6
100	P(52)	PIN(28)	7.570E+01	1.170E-02	5.248E-03	295.4
101	P(53)	PIN(29)	1.280E+02	1.990E-02	3.375E-03	115.2
102	P(54)	PIN(30)	1.280E+02	1.990E-02	3.334E-03	113.4
103	P(55)	PIN(31)	1.280E+02	1.990E-02	2.818E-03	293.2
104	P(56)	PIN(32)	1.280E+02	1.990E-02	3.132E-03	293.6
105	P(57)	PIN(33)	1.280E+02	1.990E-02	2.818E-03	113.2
106	P(58)	PIN(34)	1.280E+02	1.990E-02	2.931E-03	113.9
107	P(59)	PIN(35)	1.280E+02	1.990E-02	3.375E-03	295.2
108	P(60)	PIN(36)	1.280E+02	1.990E-02	3.132E-03	293.6

XRL INJECTOR
OXIDIZER SIDE, NO RING DAMS
ANOMOLOUS SECOND TANGENTIAL MODE

	LB/SEC/PSI	% FLOW/% PI
TOTAL INJECTOR FLOW=	1.2464E-01	9.1079E-01
TOTAL VECTOR INJECTOR FLOW=	1.2416E-01	9.0729E-01
TOTAL INJECTOR FLOW PROPORTIONED BY PC AMPLITUDES=	1.2464E-01	9.1079E-01
TOTAL VECTOR INJECTOR FLOW PROPORTIONED BY PC AMPLITUDES=	1.2416E-01	9.0729E-01

Figure H-3. (Continued)

PRESSURE NODE	VOLUME CU IN	AC. VEL. IN/SEC	MAGNITUDE PSI/PSI	PHASE DEGREES	FLOWS IN		FLOWS OUT		
1	4.040E+00	5.310E+04	2.853E-01	206.3	1		3		
2	4.040E+00	5.310E+04	2.853E-01	26.3	2		4		
3	4.040E+00	5.310E+04	5.243E-01	206.3	3		5		
4	4.040E+00	5.310E+04	5.243E-01	26.3	4		6		
5	4.040E+00	5.310E+04	6.780E-01	206.3	5		7		
6	4.040E+00	5.310E+04	6.780E-01	26.3	6		8		
7	4.040E+00	5.310E+04	7.216E-01	206.3	7		9		
8	4.040E+00	5.310E+04	7.216E-01	26.3	8		10		
9	4.040E+00	5.310E+04	6.479E-01	206.3	9		11		
10	4.040E+00	5.310E+04	6.479E-01	26.3	10		12		
11	4.040E+00	5.310E+04	4.688E-01	206.3	11		13		
12	4.040E+00	5.310E+04	4.688E-01	26.3	12		14		
13	4.040E+00	5.310E+04	2.136E-01	206.4	13		15		
14	4.040E+00	5.310E+04	2.136E-01	26.4	14		16		
15	4.040E+00	5.310E+04	7.631E-02	25.8	15		21		
16	4.040E+00	5.310E+04	7.632E-02	205.8	16		24		
17	4.200E+00	5.310E+04	1.936E-01	198.5	17		19		
18	4.200E+00	5.310E+04	1.936E-01	18.5	18		20		
19	4.200E+00	5.310E+04	3.590E-01	198.5	19		22		
20	4.200E+00	5.310E+04	3.590E-01	18.5	20		23		
21	7.530E+00	5.310E+04	3.349E-01	26.2	21		25	29	33
22	7.530E+00	5.310E+04	4.809E-01	198.5	22		26	30	34
23	7.530E+00	5.310E+04	4.809E-01	18.5	23		27	31	35
24	7.530E+00	5.310E+04	3.349E-01	206.2	24		28	32	36
25	1.190E+00	5.310E+04	3.807E-01	25.8	25	37	38	73	
26	9.770E-01	5.310E+04	5.292E-01	23.3	38		39	74	
27	9.770E-01	5.310E+04	3.235E-01	26.4	39		40	75	
28	9.770E-01	5.310E+04	2.981E-01	201.8	40		41	76	
29	1.190E+00	5.310E+04	5.072E-01	198.7	41	26	42	77	
30	9.770E-01	5.310E+04	5.916E-01	198.7	42		43	78	
31	9.770E-01	5.310E+04	3.498E-01	201.0	43		44	79	
32	9.770E-01	5.310E+04	2.885E-01	24.7	44		45	80	
33	1.190E+00	5.310E+04	5.072E-01	18.7	45	27	46	81	
34	9.770E-01	5.310E+04	6.025E-01	17.3	46		47	82	
35	9.770E-01	5.310E+04	3.788E-01	16.4	47		48	83	
36	9.770E-01	5.310E+04	2.344E-01	216.8	48		49	84	
37	1.190E+00	5.310E+04	3.807E-01	205.8	49	28	50	85	
38	9.770E-01	5.310E+04	5.390E-01	201.6	50		51	86	
39	9.770E-01	5.310E+04	3.498E-01	201.0	51		52	87	
40	9.770E-01	5.310E+04	2.407E-01	32.7	52		37	88	
41	1.370E+00	5.310E+04	3.349E-01	26.0	53	29	54	89	

Figure H-4, Input and Output Data for Pressure Nodes

```
42   1.37CE+00 5.310E+04  5.74CE-01   22.0  54       55  90
43   1.37CE+00 5.310E+04  3.446E-01   27.5  55       56  91
44   1.37CE+00 5.310E+04  4.807E-01  198.7  56  30   57  92
45   1.37CE+00 5.310E+04  6.351E-01  198.3  57       58  93
46   1.37CE+00 5.310E+04  3.636E-01  203.9  58       59  94
47   1.37CE+00 5.310E+04  4.807E-01   18.7  59  31   60  95
48   1.37CE+00 5.310E+04  6.571E-01   16.6  60       61  96
49   1.37CE+00 5.310E+04  4.241E-01   18.1  61       62  97
50   1.37CE+00 5.310E+04  3.349E-01  206.0  62  32   63  98
51   1.37CE+00 5.310E+04  5.948E-01  200.0  63       64  99
52   1.37CE+00 5.310E+04  4.029E-01  200.8  64       53 100
53   8.660E-01 5.310E+04  3.565E-01   26.3  65  33   66 101
54   6.660E-01 5.310E+04  3.766E-01   27.8  66       67 102
55   8.660E-01 5.310E+04  4.626E-01  199.1  67  34   68 103
56   6.660E-01 5.310E+04  4.069E-01  203.6  68       69 104
57   8.660E-01 5.310E+04  4.626E-01   19.1  69  35   70 105
58   6.660E-01 5.310E+04  4.392E-01   20.0  70       71 106
59   8.660E-01 5.310E+04  3.565E-01  206.3  71  36   72 107
60   6.660E-01 5.310E+04  4.069E-01  203.6  72       65 108
61   4.000E+00 5.310E+04  1.101E-06  331.2            1   2  17  18

XRL INJECTOR
OXIDIZER SIDE, NO RING DAMS
ANOMOLOUS SECOND TANGENTIAL MODE
```

Figure H-4. (Continued)